P383-207696

NBS: Processing/Microstructure/Property Relationships ir 2024 Aluminum Alloy Plates

(U.S.) National Bureau of Standards
Washington, DC

Prepared for

National Aeronautics and Space Administration
Washington, DC

Jan 83

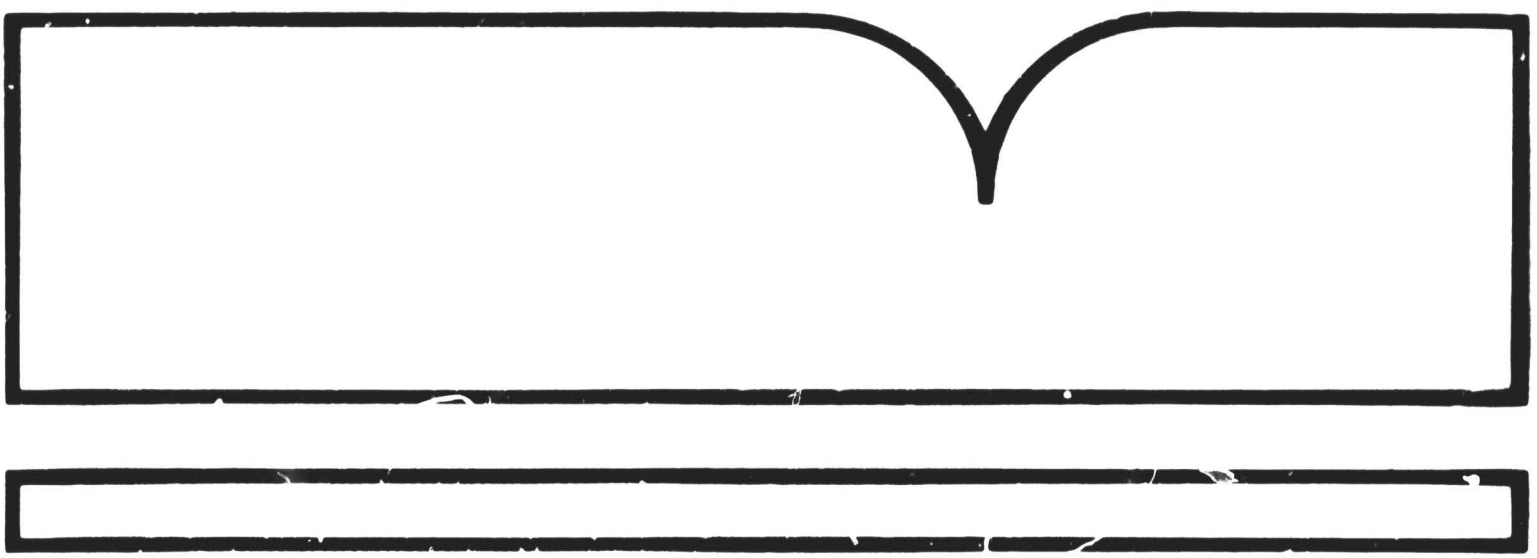

NBSIR 83-2669

NBS: Processing/Microstructure/Property Relationships in 2024 Aluminum Alloy Plates

U.S. DEPARTMENT OF COMMERCE
National Bureau of Standards
National Measuremen[illegible]boratory
Center for Materials S[illegible]g
Washington, DC 2023[illegible]
Phone: (301) 921-2891

January 1983

Technical Report

Joint Sponsorship by NBS/NASA
NASA Government Order W-14,637; Modification 3

U.S DEPARTMENT OF COMMERCE
National Bureau of Standards

NBSIR 83-2669

NBS: PROCESSING/MICROSTRUCTURE/PROPERTY RELATIONSHIPS IN 2024 ALUMINUM ALLOY PLATES

L. K. Ives, L. J. Swartzendruber, W. J. Boettinger, M. Rosen,
S. D. Ridder, F. S. Biancaniello, R. C. Reno, D. B. Ballard and
R. Mehrabian

U.S. DEPARTMENT OF COMMERCE
National Bureau of Standards
National Measurement Laboratory
Center for Materials Science
Washington, DC 20234
Phone: (301) 921-2891

January 1983

Technical Report

Joint Sponsorship by NBS/NASA
NASA Government Order W-14,637; Modification 3

U.S. DEPARTMENT OF COMMERCE, Malcolm Baldrige, *Secretary*
NATIONAL BUREAU OF STANDARDS, Ernest Ambler, *Director*

PROCESSING/MICROSTRUCTURE/PROPERTY RELATIONSHIPS IN 2024 ALUMINUM ALLOY PLATES

ABSTRACT

Nondestructive evaluation (NDE) using eddy-current conductivity and hardness measurements form an essential part of the quality control of aluminum alloy plates used for aerospace vehicles. The relationships between the NDE measurements and the important mechanical properties are affected by a large number of variables including: chemical composition, cast structure, ingot scalping, solution heat treatment and quenching, mechanical working, and aging treatment. At the request of the National Aeronautics and Space Administration, a number of these relationships has been explored for 2024 aluminum alloy. This work is a continuation of our previous efforts on 2219 aluminum alloy and is motivated by a concern that a number of improperly treated plates with "soft spots" may have been incorporated into aerospace structures. A major result of our research has been a delineation of which alloy tempers and plate thicknesses are most likely to contain "soft spots" due to specific processing errors.

The investigation included the following:

- Studies on as-received material. This included a 15.24 cm (6 in.) thick plate of 2024-T851, an 0.635 cm (1/4 in.) thick plate of 2024-F, and a direct chill cast ingot for 2024, all obtained from industry.

  Investigation of the phases and inclusions present in cast 2024 aluminum alloy with the aim of determining the degree of micro- and macro-segregation and identifying the inclusions present in the as-cast ingots.

- Determination of a set of C-curves which can predict the mechanical and NDE properties for any type of quench following the solution heat treatment. Two tempers, T851 and T351, were investigated.

- Transmission electron microscope studies of the stable and metastable phases present and an attempt to relate the observed microstructural changes to the measured changes in mechanical properties and NDE measurements.

- A study of the ultrasonic wave propagation as a function of thermomechanical treatment of the alloy with the objective of establishing a correlation between ultrasonic data and mechanical properties and of providing an additional NDE method to improve the characterization of the material.

- A nondestructive evaluation of the age hardening sequence by means of dynamic eddy-current conductivity measurements.

- Use of a heat flow model to calculate almost all conceivable heat flow conditions anticipated during the quench of 2024 aluminum alloy plate from the solution heat treatment temperature of 495 °C. The calculated time-temperature data were then coupled to the C-curves and the variations in properties across different thickness plates for the "worst case" heat flow conditions were predicted.

Predictable macrosegregation was obtained in laboratory ingots of 2024 aluminum alloy. It was found that macrosegregation of copper and other alloying additions in direct chill cast ingots of 2024 aluminum alloy cannot be completely eliminated by chill face scalping and subsequent thermomechanical treatment. Although good scalping practice should maintain compositions within specified limits with no deterioration in mechanical properties, the macrosegregation remaining in the finished plate product will contribute to the scatter observed in NDE measurements. Further, because of the large copper content variation near the chill face, surface hardness and eddy-current conductivity measurements are necessarily very sensitive to scalping depth in their ability to evaluate the condition of finished alloy plates.

A large number of samples were taken from a 0.635 cm thick plate of 2024 aluminum alloy in the F temper and processed to the T851, T351 or T4 temper. During processing to these tempers, the quench following solution heat treatment was varied, giving a series of samples with a wide range of microstructures and hence mechanical properties. Two types of "pre-aging" treatment, labeled sequence A and sequence B, were used. The hardness, eddy-current conductivity, yield strength, ultimate tensile strength, elongation, and area reduction of these samples were measured. The accumulated data were used to establish a set of approximate C-curves from which the alloy properties can be established for any time-temperature cycle of the quench following heat treatment. The C-curves can also be used to generate correlations between mechanical and NDE properties. It was found that eddy-current conductivity alone cannot be used as a reliable predictor of the mechanical properties of 2024-T351 or 2024-T851. It must be combined with other information such as hardness and yield strength measurements on the same lot (same ingot or plate) of material.

The C-curves were combined with time-temperature data from a computerized heat flow model to predict the variations in properties across plates of different thicknesses for both sequence A and sequence B type "pre-aging" heat treatments. It was found that the T851 temper is quite "quench sensitive" in the sense that the ultimate tensile strength falls below specification for the "worst case" quench conditions for rather thin plates ($\sim$ 1 cm thick).

TEM studies were carried out on a large number of specimens in an 120 kV instrument equipped to operate in the scanning transmission (STEM) mode as well as in the conventional transmission mode. The instrument was equipped with an x-ray energy dispersive spectrometer. A major objective was to identify those microstructural changes that were responsible for the mechanical and physical properties

delineated in the C-curve representations. Although the microstructure as a function of "pre-aging" treatment is complex, it appears that "pre-aging" induced precipitates can contribute to the strength and are subject to overaging during further heat treatment. This provides a mechanism for the loss of strength which can account for the fact that the strength of the T851 temper is actually reduced below that of the T351 temper given the same "pre-aging" heat treatment (rather than being raised as occurs for properly quenched material).

The objective of the ultrasonic studies was to determine the extent to which a correlation exists between the mechanical and ultrasonic properties. For this purpose, the absolute, rather than the relative, values of the sound velocity and ultrasonic attenuation are required. The absolute values of sound velocity and ultrasonic attenuation were determined to within ± 1 ms ^{1} and ± 0.02 dB, respectively. A parabolic relationship was found between hardness and sound-wave velocity, whereas ultrasonic attenuation decreases with increasing hardness.

TABLE OF CONTENTS

I. INTRODUCTION

This is a comprehensive technical report of our investigations in the past two years on 2024 aluminum alloy. The overall aim of this work was to develop specific relationships between process variables during casting, working and heat treatment of the alloy and the resulting microstructures, mechanical properties and various nondestructive evaluations (NDE), eddy-current (electrical) conductivity, hardness, and ultrasonic measurements.

This work is a follow-up to a similar study on 2219 aluminum alloy (1). Both investigations were carried out at the request of the National Aeronautics and Space Administration. The initial motivation was government and industry concerns that substrength aluminum alloys may have been used in aircraft and space vehicle structures[1]. The concerns originated from the discovery of "soft" spots[2] in an anodized 2124-T851 aluminum alloy machined part in July 1979. The "soft" spots were apparently due to improper processing of the plate (1). Furthermore, it was established that the same plant had produced a variety of other aluminum plates including 2024 and 2219 aluminum alloys. Serious concerns were also expressed about the variability of test techniques used for quality assurance or finding the suspect plates[1].

In our earlier work (1), we determined the effect of improper quenching on the mechanical properties and NDE (eddy-current conductivity, and hardness) measurements of 2219 aluminum alloy. The kinetics of precipitation for two types of cooling sequences from the solution heat

---

1 Aviation Week and Space Technology, August 1980, p. 14, and August 13, 1980, p. 17.

2 "Soft" spots denote areas of a plate with mechanical properties below federal specifications.

treatment temperature were investigated. Emphasis was placed on the reliability of eddy-current conductivity and hardness as NDE tools to detect variations in microstructure, hence in mechanical properties, introduced by the various cooling sequences. An important result from this work was that under the "worst case" quench conditions plates of 2219 aluminum alloy with thicknesses less than about 5 cm (2 in.) will not suffer yield strength degradation below levels in federal specification QQ-A-250/30. Qualitatively speaking, the results showed that 2219 aluminum alloy is much less sensitive to improper heat treatment than are other aluminum alloys. This is largely the result of the high copper content in this alloy that gives a "C curve" with a "nose" at a relatively high temperature.

Very evident from the results of this work (1) was the need to always double check eddy-current conductivity measurements by periodic hardness measurements or better, by direct mechanical property measurements when possible. Furthermore, a need also exists for better NDE techniques which can scan aluminum plates rapidly and observe the entire plate thickness rather than a thin surface layer. Because of this, in the work described in the present report, the feasibility of using ultrasonic techniques were also investigated as a corollary method to available NDE tools for quality assurance.

The specific aims of the investigations carried out on 2024 aluminum alloy included the following:

- To establish processing conditions and mechanisms responsible for the occurrence of "soft" spots;

- To establish correlations between process variables during solidification and thermomechanical treatment and the composition and microstructures of the plates;
- To identify the constituent phases in the alloy and to determine the kinetics of precipitation and relate the microstructures to mechanical properties and NDE measurements;
- To develop correlations between heat flow during quench from solution heat treatment temperature and time-temperature precipitation models in order to determine the ranges of possible degradation in mechanical properties due to improper heat treatment.

In this report we describe the details of our work on the 2024 aluminum alloy under the following subheadings:

- Studies on as-received plates of 2024 aluminum alloy;
- Solidification-segregation studies, microsegregation and macrosegregation in laboratory and commercially cast ingots;
- C-curves and nondestructive evaluation, time-temperature precipitation diagrams and the relationships between mechanical properties and NDE measurements;
- Transmission electron microscopy studies, and the relationship between microstructure and properties;
- Ultrasonic characterization;
- Eddy-current conductivity characterization, the study of aging process by means of dynamic eddy current measurements, and
- Heat flow--property predictions, property degradations due to improper quench from the solution heat treatment temperature.

II. STUDIES ON AS-RECEIVED PLATES OF 2024 ALUMINUM ALLOY

Two plates of 2024 aluminum alloy were used in this investigation. They were:

1. A 15.24 cm (6 in.) thick plate of 2024 in the T851 temper obtained from the Reynolds Metals Corp. Average composition of this plate[3] was determined to be 3.95 wt.% Cu, 1.47 wt.% Mg, 0.57 wt.% Mn, 0.20 wt.% Fe, 0.05 wt.% Si, and 0.025 wt.% Zn.
2. A 0.635 cm (1/4 in.) thick plate of 2024 in the F temper also obtained from the Reynolds Metals Corp. The chemical composition of this plate[3] was determined to be 4.3 wt % Cu, 1.44 wt.% Mg, 0.57 wt.% Mn, 0.28 wt.% Fe, 0.11 wt.% Si and 0.1 wt.% Zn.

In addition, segregation in a direct chill (DC) cast ingot of 2024, obtained from the Reynolds Metals McCook plant, was studied. The average composition of this ingot was determined to be 4.54 wt.% Cu, 1.5 wt.% Mg, 0.52 wt.% Mn, 0.32 wt.% Fe, 0.11 wt.% Si and 0.1 wt.% Zn.

Note that there is some variation in the composition of the three pieces of 2024 aluminum alloy used in this study. In particular, the two 2024 plates appear to meet the composition specification for 2124 (with respect to the Fe and Si contents), whereas for the DC cast ingot the Fe content exceeds the 2124 specification by a small amount. The

---

[3] The composition of 2024 aluminum alloy according to ASTM Spec. B209 is 3.8 to 4.9 wt.% Cu, 1.2 to 1.8 wt.% Mg, 0.3 to 0.9 wt.% Mn, 0.50 wt.% Fe max, 0.50 wt.% Si max, 0.25 wt.% Zn max, 0.10 wt.% Cr max, 0.15 wt.% Ti max (0.20 wt.% Ti + Zr max), each other 0.05 max (total other 0.15 wt.% max). The composition of 2124 aluminum alloy according to ASTM Spec. B209 is 3.8 to 4.9 wt.% Cu, 1.2 to 1.8 wt.% Mg, 0.3 to 0.9 wt.% Mn, 0.30 wt.% Fe max, 0.20 wt.% Si max, 0.25 wt.% Zn max, 0.10 wt.% Cr max, 0.15 wt.% Ti max (0.20 wt.% Ti + Zr max), each other 0.05 wt.% max (total other 0.15 wt.% max). The Cu, Fe, Mg, and Mn contents of the 0.635 cm plate and the Cu contents of the 15.24 cm plate and the DC ingot were determined by atomic absorption spectrometry.

effect of these compositional differences is not determined herein and would require a more extensive study. Because of iron's ability to tie up large amounts of Cu and Mn under certain conditions, results could be expected to be affected by the iron content.

It was expected that across the thickness variations in properties due to macrosegregation in the original DC cast ingot or due to a cooling rate gradient, because of normal thermal resistance of the plate during quench from the solution temperature, would be most pronounced in very thick plates. Therefore, the 15.24 cm thick plate in the T851 temper was carefully examined for chemical, microstructural and property variation across its thickness.

The data obtained for the composition, hardness, and electrical conductivity of the 15.24 cm thick plate are shown in Figure 1. These data essentially establish the variations in properties due to the normal variation in cooling rate experienced during quench from the solution heat treatment temperature, and the macrosegregation remaining in the plate from the original DC cast ingot. The first plot in Figure 1 shows that there is approximately 0.2 wt.% variation in copper content across the plate. This was determined by molecular absorption spectrometry (wet chemistry). The abrupt changes in copper content at the edges of the plate are due to the depleted region (negatively segregated region) next to the chill face in the original DC cast ingot[4]. The scalping apparently removed the positive chill face segregation leaving some of the depleted region intact which ended up in the plate. The negative segregation at the plate centerline is due to the

---

[4] Macrosegregation across the DC cast ingot of 2024 aluminum alloy produced at the Reynolds McCook plant is shown in a subsequent section.

same type of segregation noted in the DC cast ingot[4]. Rockwell B hardness measurements were made according to ASTM E-18 on a Wilson bench model Rockwell hardness tester[5]. Eddy-current conductivity measurements were made using a Verimet M4900B conductivity meter. This conductivity meter was checked before each use with three standards with nominal conductivities of 30, 40, and 50 percent IACS (International Annealed Copper Standard). These standards had in turn been calibrated at a temperature of 23.0 ± 0.2 °C using the NBS conductivity bridge with the standards. During use, the standards and the sample to be measured were placed on a large aluminum block at room temperature (20 to 25 °C) and allowed to equilibrate to the same temperature within better than ± 0.5 °C. All conductivity measurements herein refer to the value at 23 °C. Repeatability at any location on a given specimen was ± 0.1 percent IACS. Although no detailed statistical analysis was made, spot checks indicate that they were accurate to ± 0.5 percent IACS.

---

5 All references to commercial equipment in this report are for identification purposes only and in no way constitute any endorsement or evaluation of the relative merits of such equipment.

III. SOLIDIFICATION-SEGREGATION STUDIES

A series of calculations and experiments have been performed to determine the phases present in cast 2024 aluminum alloy with the ultimate aim of determining the degree of micro- and macrosegregation and identifying the inclusions present in the as-cast ingots. Such segregation could have effects on the heat treatment response of this alloy and its properties, including nondestructive measurements made for quality control.

1. Microsegregation in Cast 2024 Aluminum Alloy

(a) Calculation of Microsegregation for Al-Cu-Mg-Mn-Fe-Si Alloy System

Calculation of expected microsegregation for the n-component alloy was performed using the assumption of local equilibrium at the interface, complete diffusion in the liquid phase, no diffusion in the solid phase and no fluid flow in the interdendritic "mushy" region. During solidification of primary α-aluminum, the situation is governed by (n-1) differential equations (2)

$$\frac{df_L}{dC_{Li}} = -\frac{1}{1-k_i^{\alpha}} \frac{f_L}{C_{Li}} \qquad i = 1, \ldots n-1 \qquad [1]$$

where f_L is the weight fraction liquid, C_{Li} is the liquid concentration of the i-th alloying element, and k_i^{α} is the i-th equilibrium partition coefficient for the solidification of the α-aluminum phase. In general, k_i^{α} is a function of C_{L1}, C_{L2}, ... $C_{L(n-1)}$, but because the tie lines of the phase diagram are not known we have assumed that k_i^{α} are constant and are determined from the binary diagrams of aluminum with each alloying addition.

Solution to equation [1] in this case is:

$$\frac{C_{Li}}{C_{oi}} = (1-f_s)^{k_i^{\alpha}-1} \qquad [2]$$

where C_{oi} is the original composition of the i-th component and f_s is the weight fraction solid ($1-f_L$). We calculate the solidification "path" (C_{Li} vs f_s) to determine at what fraction solid the interdendritic liquid becomes saturated with respect to a second solid phase, i.e., when the solidification "path" encounters a multivariant eutectic (or peritectic). After this point, the solidification is governed by a different set of differential equations.

Segregation studies in 2024 aluminum alloy requires the examination of the Al-Cu-Mg-Mn-Fe-Si senary system. Other alloying additions are present in small quantities or act as grain refiners and have been neglected. Values of the k_i^{α} used are given in Table I. As an example, Table II shows the calculated solidification "path" (concentration of the interdendritic liquid as a function of f_s) for an alloy Al-4.0 wt.% Cu-1.4 wt.% Mg-0.65 wt.% Mn-0.2 wt.% Fe-0.1 wt.% Si. The maximum levels in 2024 for Fe and Si are 0.5 wt.%. The relatively low values for Si and Fe used here are close to the ingots and plates characterized in this study, and are more typical of a 2124 alloy.

Determination of the solidification "path" in the six component phase diagram is extremely difficult and can only be done approximately. In general, many possibilities exist, depending on the initial alloy composition, for the formation of second phases in the interdendritic region. If we examine the solidification "path" (Table II) in various ternary system combinations of these different components the possibilities become

apparent. Figures 2 and 3 show the solidification "paths" plotted in the Al-Cu-Mg, and Al-Cu-Fe ternary systems.

In the Al-Cu-Mg system, the solidification "path" intersects the monovariant eutectic through $L \rightarrow \alpha\text{-Al}+CuMgAl_2$ at $f_s = 0.91$ at about 513 °C. Hence, in this ternary system $CuMgAl_2$ is the second phase to form and the third phase to form would be $CuAl_2$ by way of the ternary eutectic $L \rightarrow \alpha\text{-Al}+CuAl_2+ CuMgAl_2$ at 508 °C.

In the Al-Cu-Fe ternary system, the solidification "path" would intersect the monovariant eutectic through $L \rightarrow \alpha\text{-Al}+(Fe,Cu)(Al,Cu)_6$ at $f_s = 0.83$ at about 600 °C. Hence, in this case $(Fe,Cu)(Al,Cu)_6$ is the second phase to form. The third phase to form would be Cu_2FeAl_7 by way of the ternary peritectic $L + (Fe,Cu)(Al,Cu)_6 \rightarrow \alpha\text{-Al} + Cu_2FeAl_7$ at 590 °C. During dendritic solidification it is unlikely that this ternary peritectic occurs to any extent and hence, $(Fe,Cu)(Al,Cu)_6$ would probably remain in the microstructure. The interdendritic liquid composition would continue on the monovariant eutectic through $L \rightarrow \alpha\text{-Al}+Cu_2FeAl_7$ until complete solidification at the ternary eutectic point $L \rightarrow \alpha\text{-Al}+Cu_2FeAl_7+CuAl_2$ at 548 °C. It should be noted that a slight reduction in the initial Fe content or small increases in the equilibrium partition coefficient used for Fe will cause the solidification "path" to first intersect the monovariant eutectic $L \rightarrow \alpha\text{-Al}+Cu_2FeAl_7$ and hence the phase $(Fe,Cu)(Al,Cu)_6$ will not form.

Examination of the Al-Fe-Si ternary system indicates that the solidification "path" would intersect the binary eutectic through $L \rightarrow \alpha\text{-Al}+FeAl_3$. Between 629 and 611 °C, solidification would continue as $L \rightarrow \alpha\text{-Al}+Fe_3Si_2Al_{12}$. This phase is often designated α-Al(Fe)Si or α-Al(Fe,Mn)Si when Mn is present.

From these ternaries, we note the eutectics involving $FeAl_3$, α-Al(Fe)Si and $(Fe,Cu)(Al,Cu)_6$ occur at temperatures above 600 °C. This fact makes one of these phases a likely candidate for the second phase to solidify in the six component alloy. Such an analysis is consistent with the microstructural observations of Sperry (3) on cast 2024 aluminum alloy.

An examination of the quaternary phase diagram data of Phragmen (4) was performed to attempt to make the above predictions more specific. Figure 4 shows a projection of the quaternary tetrahedron Al-Cu-Mg-Fe into the Al-rich corner (2). The coordinates of this diagram are based on the relative percentages of Mg, Fe, and Cu. In this figure α-aluminum is always present and hence regions represent the solidification of two solid phases and lines represent the solidification of three solid phases (ternary eutectic, single arrow and ternary peritectic, double arrow). Examination of the compositions reached in the interdendritic liquid shows that $(Fe,Cu)(Al,Cu)_6$ is the second phase to form followed by Cu_2FeAl_7. During the subsequent freezing of α-aluminum and Cu_2FeAl_7, the liquid composition moves toward the line representing the ternary eutectic $L \rightarrow \alpha\text{-Al } Cu_2FeAl_7 + CuMgAl_2$. Solidification will be completed at the quaternary eutectic point D $L \rightarrow \alpha\text{-Al} + Cu_2FeAl_7 + CuMgAl_2 + CuAl_2$.

In the Al-Cu-Mg-Si system shown in Figure 5, after the solidification of α-Al, freezing continues with the binary eutectic $L \rightarrow \alpha\text{-Al} + CuMgAl_2$. Subsequently, the liquid composition encounters the ternary eutectic $L \rightarrow \alpha\text{-Al} + CuMgAl_2 + CuAl_2$. Solidification is completed at the quarternary eutectic point C, $L \rightarrow \alpha\text{-Al} + CuMgAl_2 + CuAl_2 + Mg_2Si$.

In the Al-Cu-Fe-Si system, the solidification "path", Figure 6, is far removed from the phase $Fe_3Si_2Al_{12}$ also designated α-Al(Fe)Si.

However, as will be seen in the next section, this phase is commonly found in both cast and solution heat treated 2024 aluminum alloy.

(b) Second Phase Particles Formed During Solidification of 2024 Aluminum Alloy

Two ingots of 2024 aluminum alloy were examined by optical, SEM and TEM microscopy to determine the phases present in the as-cast condition. The first ingot was laboratory cast from alloy taken from the 15.24 cm plate. It was solidified in a graphite crucible with a cooling rate of approximately 0.15 K/s. The second ingot was a section of the DC (direct chill) cast 2024 aluminum alloy obtained from the Reynolds McCook plant.

The determination of the phases present in as-cast 2024 aluminum alloy and related multi-component aluminum based alloy systems has been the subject of numerous studies. The most relevant work to this study is that of Sperry (3) and more recently of Munitz et al. (5) which deal specifically with phases present in as-cast 2024 aluminum alloy. Sperry (3) in particular has identified phases in their order of appearance during solidification by means of optical and x-ray methods. The reported composition of Sperry's alloy was 4.90 wt.% Cu, 1.40 wt.% Mg, 0.70 wt.% Mn, 0.30 wt.% Fe, and 0.15 wt.% Si which compares closely with the compositions studied here. Sperry (3) investigated cooling rates in the range 0.06 to 0.92 K/s. A list of the phases he observed together with their crystal structures is given in Table III. An important observation made by Sperry concerned the fact that the major Fe bearing phase at the slower cooling rates was Cu_2FeAl_7 while at the higher cooling rates cubic α-Al(Fe,Mn)Si was the predominant Fe bearing phase. The phases present in the slow cooled laboratory and DC cast

ingots were determined by optical and scanning electron microscopy using the known etching response and morphologies of the phases. TEM (transmission electron microscopy) was used to confirm the identification of phases by means of electron diffraction and EDS (x-ray energy dispersive spectrometry) and to study submicrometer sized structures.

Laboratory Cast Ingot. As previously noted, the average cooling rate during solidification of this ingot was ~ 0.15 K/s. The measured segregate spacings, i.e., secondary dendrite arm spacings, were in the range between 70 and 90 μm. Optical and SEM examinations indicated the presence of small second phase particles within the primary α-Al dendrites concentrated around the border. A TEM micrograph[6] of these particles is shown in Figure 7. They are readily identified as the S' phase[7] by means of electron diffraction. These precipitates develop through a solid state reaction during cooling. The higher concentration of precipitates at the dendrite borders is a consequence of microsegregation.

The interdendritic regions in this ingot consisted typically of a fine coupled eutectic structure along with other coarser phases. Examples are shown in Figures 8 and 9. Three phases are present in the coupled eutectic and are identified as α-Al, Θ-$CuAl_2$ and S-$CuMgAl_2$ in Figure 8. A tentative identification was first made by EDS and then confirmed by electron diffraction. In addition to this ternary eutectic, a blade shaped phase was also frequently observed, Figure 9. The shape immediately suggests that it is Cu_2FeAl_7 and, indeed, this was found to be correct by means of electron diffraction and EDS. The three secondary

---

6 Details describing TEM specimen preparation are given in Section V.

7 The S' phase has approximately the same composition and structure as S-$CuMgAl_2$. A more detailed discussion of this phase is presented in the description of "pre-aging" microstructures in Section V.

phases, θ-$CuAl_2$, S-$CuMgAl_2$ and Cu_2FeAl_7 together with the primary α-Al phase were the major constituents in this relatively slow cooled ingot. Observation of these phases is in accord with Sperry's (3) results. In particular, the presence of Cu_2FeAl_7 is consistent with Sperry's finding that this phase is promoted by a slow cooling rate. Other phases listed in Table III may have been present but with a much lower frequency. An exhaustive search for them was not made.

DC Cast Ingot Samples for detailed microstructural characterization were taken from the one-quarter position across the short transverse direction. The measured secondary dendrite arm spacings in this location were in the range between 30 and 50 μm. This indicates a substantially higher average cooling rate during solidification than that measured in the laboratory cast ingot. Primary α-Al dendrites in the DC cast ingot contained S' precipitates as was found in the laboratory ingot. In contrast to the laboratory ingot, the precipitates were present at a higher density and were distributed more uniformly throughout the dendrites rather than being located primarily at the borders. An example of the S' precipitates in an α-Al dendrite is shown in Figure 10.

The interdendritic structures in the DC ingot shown in Figure 11 were predominantly of two types: a fine multi-phase eutectic structure and a single phase constituent sometimes with a polyhedral shape that often entirely filled the interdendritic gap. An example of the eutectic structure is shown in Figure 12. Four phases were present. They were identified as α-Al, θ-$CuAl_2$, S-$CuMgAl_2$ and Mg_2Si. According to the analysis of the solidification "path" in this report and also in Sperry (3), this comprises the quarternary eutectic which is expected to be the last structure to solidify. In many instances, the Mg_2Si phase was

not found, possibly because it was present at a lower concentration than the other phases. The eutectic would then be identified as the ternary structure which was found in the more slowly cooled laboratory ingot. Occasionally, a blade of the Cu_2FeAl_7 phase was also noted in he structure, Figure 11(b).

An example of the polyhedrally shaped single phase interdendritic structure is shown in Figure 13(a). Apparently this phase forms a divorced eutectic with α-Al. Electron diffraction patterns from the phase could be indexed in a way that was consistent with a bcc unit cell having a lattice parameter of a_o 1.25 nm. On this basis and with composition information obtained by EDS, Figure 13(b), the phase was identified as cubic α-Al(Fe,M)Si where M in this case designates Cu and Mn. With the exception of a somewhat lower Si concentration in the present samples, the composition agrees closely with results obtained by Munitz et al. (5). The presence of α-Al(Fe,M)Si and not Cu_2FeAl_7 agrees with Sperry's (3) finding that the former phase is favored by higher cooling rates. None of the other phases listed in Table III appeared to be present to a significant extent at this location in the DC cast ingot.

2. Macrosegregation in Cast 2024 Aluminum Alloy

A series of experiments and measurements were performed to determine the degree of macrosegregation in semi-continuous DC cast and laboratory cast ingots of 2024 aluminum alloy. The former gives an indication of the maximum composition variations expected in the final plate product while the latter will be used in the preparation of control specimens to establish the effect of composition on properties including the NDE measurements.

(a) DC Cast Ingot

A sketch of the section of DC cast 2024 alumimum alloy ingot used in this study is shown in Figure 14. It extends from chill face to chill face of the casting in the short transverse direction and from chill face to centerline in the long transverse direction. Measurement of macrosegregation was performed initially in a direction perpendicular to the chill face in the short transverse direction (position B1) shown in Figure 14. Chemical analysis was performed by the Center for Analytical Chemistry at NBS by spectrophotometric measurement at 435 nm of a copper complex. The chemistry data should be considered accurate to ± 0.04 wt.%.

As seen in Figure 15, very high positive copper segregation is noted at the chill face (∿ 12 wt.% Cu) followed by a region of rapidly varying composition that extends almost 3 cm into the ingot. Two minimums in composition (∿ 4.25 wt.% Cu) occur at ∿ 0.2 cm and 2 cm from the chill face. A relatively uniform composition region (∿ 4.6 wt.% Cu) extends from ∿ 3 cm to 15 cm from the chill face followed by a region of negative segregation at the ingot centerline where the composition drops to ∿ 4.1 wt.% Cu. These variations are caused by interdendritic fluid flow during solidification (6). The inset in Figure 15 shows the drastic reduction in the volume fraction of eutectic which occurs about 0.2 cm from the chill face. This reduction is the origin of the rapid drop in copper content near the chill face. Figures 16 and 17 show optical and SEM views respectively, of the relative change in the volume fraction of the eutectic present at various distances from the chill face. These photos can be qualitatively correlated to the measured copper contents at these positions shown in Figure 15.

The occurrence of the two minimums in copper content near the chill face was considered to be rather unusual. In the previous study of macrosegregation in DC cast 2219 aluminum alloy (1) only a single minimum in copper content was observed near the chill face. Although for the 2024 ingot these composition excursions failed to take the ingot outside of the specification for copper, the second minimum at 2 cm is substantially further from the chill face than is the comparable minimum for copper (0.8 cm) observed in the previous studies of 2219 aluminum alloy. To establish whether this behavior was an exception to normal in this ingot, further macrosegregation profiles were performed at different positions in the ingot section shown in Figure 14. Data near the chill face for sections A1 and A2 along with B1 are shown in Figure 18. Note that the magnitude of the minima have changed but their existence is quite evident. Figure 19 shows data in the long transverse direction labeled LT in Figure 14. Here it might be argued that the first minimum is not significant, however, the second minimum is present and exists at the 2 cm position.

One can only speculate about the origins of this unusual macrosegregation profile. Depressions in average copper content are caused by sudden air gap formations and subsequent reheating of the ingot surface during solidification. For example, it may be postulated that after the initial air gap formation, adequate cooling was re-established and interrupted for a second time. It is expected, however, that in most ingots a single "dip" in copper content near the chill face will be observed.

(b) Laboratory Cast Ingot

Following the work of Mehrabian and Flemings on macrosegregation in multicomponent systems (6), a special geometry unidirectional ingot

was cast with the 2024 aluminum alloy to demonstrate the mechanisms responsible for the positive and the negative macrosegregation noted in the DC cast ingot and to obtain controlled composition samples differing from the nominal. These samples were used for thermomechanical treatments and nondestructive evaluation.

The geometry of the casting is shown in the inset of Figure 20 and employs a reduction in area of approximately 10 to 1 to cause macrosegregation. The bottom section of the casting is 9.2 cm square and 9.0 cm high while the top section of the casting is 2.7 cm square and 21 cm high. An investment mold of plaster was preheated to 500 °C and placed directly on a water cooled chill block. The mold has an open bottom so that molten metal comes into direct contact with the chill. This, coupled with the preheated mold, guaranteed directional solidification of the ingot. The mold was filled with molten 2024 aluminum alloy (obtained from the full cross section of the DC Ingot) at about 720 °C after being degassed with chlorine. The casting was analyzed for average composition variation (macrosegregation) in the direction perpendicular to the chill. The variation in copper and magnesium content determined by atomic absorption spectrometry as a function of distance from the bottom chill in the as-cast ingot is shown in Figure 20. As expected from previous studies of macrosegregation noted above, high positive segregation (5.35 wt.% Cu) is observed at the chill face while negative segregation (~ 3.1 wt.% Cu) occurs in the region of the cross section change. To a lesser extent, magnesium also shows a high level at the chill face, drops to a minimum near the cross section change and rises again in the rest of the ingot. This similarity of shapes of the composition profiles is an indication that

the equilibrium partition coefficients for Cu and Mg (0.17, and 0.30 respectively) are less than one. Because the partition coefficient for Mg is larger, macrosegregation of Mg is less than Cu. The relative levels of Cu and Mg are important because they are the major components in the hardening phase, $CuMgAl_2$, in heat treated 2024 aluminum alloy.

Chill face and cross-section-change segregation both result from the flow of segregated interdendritic liquid to feed solidification shrinkage. It should be noted that the laboratory ingot exhibits a lower positive chill face segregation and no adjacent negative segregation compared to the DC cast ingot. The occurrence of these phenomena near the chill face of the DC cast ingot can be readily ascribed to the formation of an extensive air gap which results in the abrupt reheating of the ingot surface during solidification and the exudation of the solute rich interdendritic liquid from the adjacent region. On the other hand, the negative segregation at the DC ingot center line and at the section reduction of the laboratory ingot are due to the extensive flow of interdendritic liquid from the hotter to the cooler regions of the ingots at these locations.

A second laboratory ingot of 2024 aluminum alloy with a 10 to 1 reduction in cross section was also cast in a manner identical with the first ingot with eight thermocouples inserted through the mold at different distances from the bottom chill face. Figure 21 shows the temperature-time curves for the eight thermocouples and the distance from the chill face to each. The liquidus and solidus temperatures for this alloy are approximately 638 (± 5) and 502 (± 5) °C respectively and hence, from these curves the local solidification time as a function of position has been determined. Additionally, secondary dendrite arm

spacings were obtained from metallographic sections at various distances from the chill face. These spacings are correlated with the local solidification time in Figure 22.

3. Thermomechanical Treatment and Evaluation of Laboratory Ingot

The effect of variations in alloy composition due to macrosegregation on the heat treatment response of 2024 aluminum alloy and its properties including nondestructive measurements used for quality assurance has been evaluated using samples taken from the reduced-cross-section laboratory ingot.

Samples, ~ 2.7 cm square and ~ 2 cm thick in the solidification direction, were cut from the ingot at different distances from the bottom chill face to obtain specimens with differing compositions. The samples, of course, contained composition gradients through their thickness, but were relatively uniform in perpendicular directions due to the unidirectional solidification. As a reference point, eddy-current measurements were conducted on as-cast samples. Measurements were made with the coil on the surfaces which were perpendicular to the solidification direction. The conductivity along with the previously determined copper content is shown in Figure 23. These data indicate that wide variations in the conductivity can exist depending on composition and structure unrelated to subsequent thermomechanical treatment.

The samples were then thermomechanically treated to the T851 condition as follows:

(a) homogenization heat treated for 48 hours at 495 °C,

(b) hot rolled at 495 °C to 1/6 of their initial thickness (0.32 cm, ~ 1/8"),

(c) solution heat treated at 495 °C for 75 minutes,

(d) stretched 2.5% and aged at 190 °C for 12 hours.

Hardness measurements were carried out on both surfaces of these 0.3 cm thick samples. In Figure 24 hardness is plotted as a function of the original distance of these surfaces from the bottom chill face along with the copper content.

The hardness levels obtained in the bottom section of the casting are relatively insensitive to changes in Cu and Mg content between 4.4 to 5.3 wt.% Cu and 1.3 to 1.5 wt.% Mg. The hardness level of 77 HRB is typical of correctly processed commercially cast 2024 aluminum alloy in the T851 condition. Near the cross section change of the ingot, the hardness drops to below 64 HRB, a value normally considered below specification. The composition at this point in the casting was 3.1 wt.% Cu, and 1.1 wt.% Mg, values which are below the minimum specification for these alloying additions (3.8 wt.% Cu and 1.2 wt.% Mg). After the cross section change, the hardness rises to $\sim$ 78 HRB as the compositions rise to normal levels. The low hardnesses obtained at the very top of the ingot are due to excess porosity which occurred there due to shrinkage. Although the limited number of samples obtained preclude precise conclusions, the ranges of compositions seen in the as-received plate (3.85 to 4.00 wt.% Cu) should not be the major cause of the hardness variation across that plate.

IV C-CURVES AND NONDESTRUCTIVE EVALUATION

A large number of samples taken from the 0.635 cm (1/4 in.) thick plate of 2024 aluminum alloy in the F temper condition were processed to the T851 and T351 tempers. During the processing to these tempers, the quench following solution heat treatment was varied. This gave a series of samples with a wide range of microstructures and hence mechanical properties. The hardness, eddy-current conductivity, yield strength, ultimate tensile strength, elongation, and area reduction of these samples were measured. The data accumulated were used to establish a set of approximate C-curves from which the alloy properties can be estimated for any time-temperature cycle of the quench following solution heat treatment. The data are also presented in a number of correlation plots to show the relationship between the mechanical properties and the nondestructive evaluation (NDE) parameters. The measured changes in physical and mechanical properties are related to microstructural observations in the next section.

Some comparisons are also made with data from other sources and with our previous study of 2219-T87* aluminum alloy (1). In particular, it appears that 2024 aluminum alloy is a more "complex" system than the 2219 aluminum alloy. This complexity has a number of consequences. In particular, it is seen that the simple C-curve shapes used in the analysis, which worked well for the case of 2219-T87* aluminum alloy, give much more approximate results for the case of 2024-T851 and 2024-T351 aluminum alloys. Further, relationships between mechanical properties and NDE measurements (i.e. hardness and eddy-current conductivity) have considerably more scatter, making the task of testing the 2024 aluminum alloys more difficult. This is especially true for the

case of the naturally aged T351 material, and should be taken into account in the specifications for this material.

1. Thermomechanical Treatment

Specimens 0.635 cm thick and measuring 2.5 cm by 18 cm were cut from the plate, supplied by the Reynolds Aluminum Company, such that the long dimension was aligned in the rolling direction. The plate was received in an F temper condition. As previously noted, the chemical composition of the plate represents approximately the middle of the specified range for Cu, Mg and Mn contents for both 2024 and 2124 aluminum alloys (3.8 to 4.9 wt.% Cu, 1.2 to 1.8 wt.% Mg, and 0.3 to 0.9 wt.% Mn). The amount of Si and Fe are also within specification of both alloys (0.5 max. wt.% Fe and 0.5 max. wt.% Si for 2024 aluminum alloy; 0.3 max. wt.% Fe and 0.2 max. wt.% Si for 2124 aluminum alloy) with the Fe content being, however, only slightly below the maximum specified for the 2124 aluminum alloy. Since the presence of iron is expected to have a deleterious effect on the yield and ultimate tensile strengths of these alloys, the results obtained here might be considered applicable in the sense of a lower bound for 2124 aluminum alloys with mid-range Cu, Mg, and Mn contents and with similar other elemental contents. The effect of compositional variations on the C-curves was not investigated and the degree to which such variations would alter the C-curve parameters and contribute to interlaboratory disagreement on the effect of heat treatment on alloy properties is not fully known at present.

The 0.635 by 2.5 by 18 cm specimens were subjected to a systematic thermomechanical processing schedule involving a 75 minute solution heat treatment at 495 °C followed by a specially designed "pre-aging" heat treatment using a salt bath. The term "pre-aging" heat treatment

is being used in this report in place of "interrupted quench" or "slack quench" because the definition of the latter two terms does not appear to be fully established. We use "pre-aging sequence A" or simply "sequence A" to refer to a monotonic quench from solution heat treatment and "pre-aging sequence B" or simply "sequence B" to refer to a quench with reheating to an intermediate temperature.

During the "pre-aging" treatment, thermal data were continuously acquired and manipulated by an automated high speed data acquisition system for later use in C-curve determination. Following the solution heat treatment at 495 °C for 75 minutes and "pre-aging", the specimens were stretched from 2.25% to 2.5% permanent strain and either artifically aged at 190 °C for 12 hours (T851) or aged at room temperature (T351). A schematic of this thermomechanical treatment is given in Figure 25. The alloys thus produced consist of four sets: 2024-T351 sequence A; 2024-T351 sequence B; 2024-T851 sequence A; and 2024-T851 sequence B.

2. Mechanical and Electrical Measurements

Following final aging, the hardness and eddy-current conductivity were measured for each sample. Approximately one-half the samples were machined into tensile specimens of the shape shown in Figure 26. The yield strength (0.2% offset), ultimate tensile strength, elongation, and reduction in area, as well as hardness and eddy-current conductivity, were determined for each of these machined specimens.

Hardness measurements were made on the Rockwell B scale according to ASTM E-18 on a Wilson bench model Rockwell hardness tester. Each time hardness was measured, two measurements were taken on the sample surface at a random location, excluding 5 cm from the sample ends where the sample was gripped during the stretching operation and, for the

tensile test specimens, excluding the gage. The yield strength (0.2% offset) and ultimate tensile strength were determined on a calibrated Satec System Inc. Baldwin Model 60 CG Universal Testing System. Eddy-current conductivity measurements were made using the instrument and procedure described in the previous section.

Hardness and conductivity measurements were made both before and after machining the samples into tensile test specimens. Approximately 0.5 mm was milled from each sample surface during the machining operation. Comparison of these measurements gives an indication of any possible effect of a machining operation on these measurements, as well as an indication of the measurement scatter that might be expected due to the combined influences of measurement precision and "normal" sample variations. The variations obtained for hardness and conductivity were ± 0.57% IACS (two sigma level) and ± 3.7 HRB (two sigma level), respectively. This comparison is illustrated in Figures 27 and 28.

The time-temperature quench history and the measured properties for the thermomechanically processed samples are summarized in Table IV for both tempers and both "pre-aging" sequences. These data are used below to calculate C-curves and compare the mechanical properties with the hardness and electrical conductivity.

3. Calculation of C-curves

The data on hardness, eddy-current conductivity, yield strength, ultimate tensile strength and time-temperature history have been used to determine a set of C-curves for both sequence A and sequence B alloys and for tempers T851 and T351.

The C-curves are a family of C-shaped curves used to characterize the effects of quench rate on the final properties of the finished material. Their use for aluminum alloys was pioneered by W. L. Fink

and L. A. Willey (7). These curves represent the effect of "pre-aging" time at a given temperature (intermediate between the solution heat treatment temperature and the quench water temperature) on the final properties of the material. In using these curves to determine the effect of an arbitrary time-temperature history during the quench from solution heat treatment temperature, a "rule of additivity" developed by Cahn (8) is used. Basically, this rule states that the degradation in, for example, yield strength that occurs in a given temperature interval is independent of that which occurred during previous temperature intervals passed through during the quench. The total degradation is taken as the simple sum of the degradations occurring in each temperature interval during the quench. This rule is also used in determination of the C-curve but is much less important there because the "pre-aging" is made as nearly isothermal as possible.

The extent to which the "rule of additivity" is applicable to aluminum alloys has not been established. However, previous experience by Staley (9) indicates that it can be applied with good approximation at least to some aluminum alloys. One might expect the rule to apply approximately when the degradation in properties is small and when the temperature decreases monotonically. The differences we find in the present study between the sequence A and sequence B heat treatments gives some indication as to how closely this rule is followed. As in the previous study (1), we use the results from these two sequences in section VIII to calculate limits on what properties might be obtained under "best" and "worst" quenching conditions in 2024-T351 and 2024-T851 aluminum alloy plates.

Following Evancho and Staley (10) and Cahn (8,11), we assume that the resulting value of a property, σ, can be represented as

$$\sigma = (\sigma_m - \sigma_o) \exp(-K_{1x}\tau_x) + \sigma_o \qquad [3]$$

where σ_m is the maximum achievable property, σ_o is the minimum or "intrinsic" value of the property achieved under given conditions, and τ_x is given by

$$\tau_x = \int_{t_s}^{t_o} \frac{dt}{C_x(T(t))} \qquad [4]$$

with t_s being the time at which the quench from solution heat treatment temperature is started, t_o the time to achieve a temperature less than about 120 °C, T(t) the temperature as a function of time, and $C_x(T)$ the C-curve. The C-curve is represented by the equation

$$C_x(T) = K_{1x}K_2 \exp\left(\frac{K_3K_4^2}{RT(K_4 - T)^2}\right) \exp\left(\frac{K_5}{RT}\right) \qquad [5]$$

where K_2, K_3, K_4, and K_5 are constants to be determined, T is the absolute temperature, and K_{1x}, is a constant given the value

$$K_{1x} = -\ln\left(\frac{\sigma_x - \sigma_o}{\sigma_m - \sigma_o}\right). \qquad [6]$$

This value of K_{1x} is chosen so that for $\tau_x > 1$, $\sigma < \sigma_x$. Thus τ_x becomes a critical parameter for achieving some given value, σ_x, of the property in question. The curve $C_x(T)$ has the dimensions of time and, when plotted as a function of temperature (normally with the temperature as the vertical axis and $C_x(T)$ as the horizontal axis), represents the

isothermal holding time (or critical time) at any temperature needed to degrade the property to the value of σ_x, with $\sigma_m > \sigma_x > \sigma_o$.

To determine the parameters σ_m, σ_o, K_2, K_3, K_4, and K_5 the following procedure was used:

(i) The temperature from 110 °C to 496.5 °C (1.5 °C above the solution heat treatment temperature) was divided into 32 temperature intervals,

(ii) The time, t_i, spent in each of the temperature intervals during the "pre-aging" treatment was stored in a datalogger,

(iii) These time data were used to numerically calculate the integral of Equation [4] according to

$$\tau_x \approx \sum_{i=1}^{32} \frac{ti}{C_x(T_i)} \qquad [7]$$

where T_i is the average temperature in the interval, and

(iv) Using an iterative, non-linear fitting routine, values of the parameters which minimize the least squares deviation between measured and calculated values were obtained.

The computer program used in the least squares fitting has been listed and described in a previous report (1). For each iteration in the fitting procedure, an "estimated standard deviation", defined by

$$\text{e.s.d.} = \sqrt{\frac{\Sigma(\sigma_i - \sigma_{ci})^2}{N - 6}} \qquad [8]$$

where σ_i is the measured value of the property in question for the i^{th} sample, σ_{ci} is the calculated value of that property, and N is the total number of samples, is determined. The program allows one or more parameters to be fixed while the remainder vary to establish a constrained

minimum value of the estimated standard deviation. This is useful because the values of K_5, K_4, and K_3 can often be varied over a considerable range without significant changes in the estimated standard deviation. A "significant change" in the e.s.d. was considered to be a change greater than 10 percent of the "normal scatter" as determined previously for the hardness and conductivity. It was found that the value of K_5 was indeterminate over a range of about 20,000 to 40,000 cal/mol in the sense that, for any value of K_5 in this range, the other parameters could be adjusted to give an essentially equivalent value of the estimated standard deviation. A value of 32,000 cal/mol was selected for this parameter on the grounds that it is close to the known activation energy for the diffusion of copper in aluminum. Having chosen K_5, values of K_4 and K_3 were selected for each temper and "pre-aging" sequence in a similar manner. Given these values of K_5, K_4, and K_3, the remaining parameters were varied for each property to arrive at a final set of parameters with the constraint that the σ_m of each property must be identical for the A and B sequences of each temper. The final set of parameters is listed in Table V. For the T351 alloys, samples "pre-aged" below 250 °C were not included in the fit. "Pre-aging" below 250 °C is in some ways equivalent to an artificial aging and, for T351, increased the values of yield strength and hardness above those obtained for a direct quench.

The C-curves obtained from these parameters are displayed in Figures 29-44. With each C-curve is a plot of the measured property versus the value of that property calculated from the C-curve parameters using the rule of additivity and the data of Table IV. In these plots, the data have been divided into six groups: (1) those alloys given a direct quench (no "pre-aging"); (2) those alloys "pre-aged" at an average

temperature between 200 and 250 °C; (3) between 250 and 300 °C; (4) between 300 and 350 °C; (5) between 350 and 400 °C; and (6) between 400 and 450 °C. These groups are given the symbols, respectively, of asterisk, plus sign, x, circle, square, and triangle.

4. Discussion and Comparison of C-curves

The C-curves presented in Figures 29-44 represent the isothermal holding time for a property to degrade to a given value. The most critical temperature, i.e. the temperature at which the most rapid degradation occurs, is represented by the minimum or "nose" of the C-curves. The parameterization of Equations 3-6 gives a curve of approximately the correct shape for a single precipitation process. However, as explained in more detail in section V, there are several precipitation processes, with each process probably requiring a separate and different C-curve.

The justification for using a single C-curve to describe what in reality is a much more complicated process lies in the fact that this empirical approach appears to give a fairly good approximation of the effect of "pre-aging" on the properties of the material after it has been fully processed. The estimated standard deviations for the hardnesses, see Table V, are only slightly greater than the single sample deviation of 1.85 HRB (one-sigma level) determined on the machined samples as discussed above. Much more data would be required to sensibly utilize a model with two or more individual C-curves (and hence a larger number of adjustable parameters). Inspection of the measured vs calculated plots of Figures 29-44 shows the predictive value of the single C-curve approach fails most noticeably in two areas. First, the large degradation that occurs for long "pre-aging"

times around 350 °C and above are not suitably predicted. In this case, the C-curves have been adjusted to slightly overpredict the degradation that does occur. Second, for the T351 alloys, "pre-aging" in the temperature range of about 200 to 250 °C actually increases the yield strength, ultimate tensile strength and hardness, rather than decreasing these properties as predicted by the C-curves. This is because "pre-aging" these alloys, which later receive only a natural aging, in this temperature range accomplishes some artificial aging which enhances the hardness of the final product. Thus, in fitting the model C-curves for the T351 alloys, data on "pre-aging" in the temperature range of 200 to 275 °C was ignored. For both cases, prediction of the mechanical properties which result from a particular quench following solution heat treatment made using the C-curves presented here should tend to slightly underestimate these properties. Further, the predicted values are expected to have their greatest validity at the upper end of the property value range, i.e. between σ_m and about $(\sigma_m + \sigma_o)/2$.

Figure 45 gives a comparison of the yield strength C-curves of 2024-T851, 2024-T351 and 2219-T87[8] aluminum alloys for both sequence A and sequence B "pre-aging" treatments. The curves are drawn to represent isothermal times required for a reduction to 90% of the maximum attainable yield strength. During the quench from solution heat treatment, degradation of properties occurs most rapidly at temperatures near the "nose" of the C-curve. During normal quenching, the time spent reaching a given temperature increases with decreasing temperatures. Hence, for two C-curves identical except for the nose temperature, the one with the nose at higher temperature will be less "quench sensitive".

---

[8] This is a modified T87 treatment practiced at the Reynolds McCook plant (1).

Comparing the A and B sequences of 2024-T351 aluminum alloy it is seen that the B sequence nose is at a higher temperature. The B sequence is, however, slightly shifted towards shorter times. This gives the A and B sequences of T351 nearly the same yield strength quench sensitivities (compare the section below on heat flow property predictions). Comparing the 2024-T851 aluminum alloy sequence A and B C-curves it is seen that, at all temperatures, the B sequence C-curve lies at shorter times than the A sequence curve and hence the B sequence has greater quench sensitivity. Comparing the 2024-T851 and 2024-T351 C-curves it is seen that in almost all cases T851 is more quench sensitive. Further, comparing 2219-T87* with 2024 it can be seen that, unless large amounts of time are spent above 400°C during the quench, 2219-T87* aluminum alloy is generally less "quench sensitive" than either 2024-T851 or 2024-T351 aluminum alloy.

5. Correlation Plots

Plots showing the correlation of ultimate tensile strength and yield strength with the NDE properties of hardness and eddy-current conductivity are displayed in Figures 46-57. The solid and dotted lines in each figure, denoting sequence A and sequence B, respectively, were calculated from their appropriate C-curves. It is seen that the correlation predicted by the C-curves fits the data well. Inspection of the scatter bands (which were drawn independently of the C-curves using only the data itself) shows the difficulty in using conductivity as an independent NDE tool. The scatter bands are very broad, especially for the T351 alloys.

In Figures 53 and 55, which plot ultimate tensile strength and yield strength, respectively, vs hardness for 2024-T351 aluminum alloy, it can be seen that many yield strengths and hardnesses lie above the

terminus of the C-curve correlation. These represent samples which were "pre-aged" at temperatures around 250 °C and below. The scatter in the yield strength vs hardness for T351 (Figure 55) is very large. Much of this scatter represents a real difference between the sequence A and sequence B specimens, with the sequence B specimens generally lying higher in yield strength and having considerably more scatter. This difference can be related to the difference in precipitation mechanism for the naturally aged 2024-T4 alloy as discussed in section V. For example, the θ phase found in sequence A specimens was not found in sequence B specimens of 2024-T4.

6. Comparison With Other Data

A large amount of data on the ultimate tensile strength, yield strength, hardness, and eddy-current conductivity has been presented by Petrak and Gunderson (12). These data were taken from specimens cut from a (5-1/2 in.) thick plate of 2124-T851, from a (2-3/4 in.) thick plate of 2124-T851, and from a (2 in.) thick plate of 2024-T351 which had been found to have or were suspected of having improperly quenched regions. Petrak and Gunderson (12) plotted the ultimate tensile and yield strengths vs hardnesses and conductivities for both the 2124-T851 and 2024-T351 data. For each plot, they have least squares fitted the data to provide a mean line and a lower 90% confidence line for each data set. In Figures 58-65 we have superimposed their lines (heavy solid and dashed, representing the least squares mean and the lower 90% confidence, respectively) on our own data.

Inspection of Figures 58-61 shows generally good agreement between the data of this report and the data of Petrak and Gunderson (12) for strength vs hardness of 2024-T851. There is also some agreement, over

at least a portion of the conductivity range, in the strength vs conductivity of 2024-T851. For 2024-T351 (Figures 62-65) the agreement is less satisfactory. In every case, the strength vs hardness plots of Petrak and Gunderson (12) lie lower than our own data, with a truly large difference in the yield strength vs hardness data for 2024-T351 (Figure 64). This large difference is difficult to rationalize. Considering the much closer agreement on the T851 temper, it could not be simply a measuring instrument calibration problem. It may be due to a difference in composition of the materials represented. For example, as previously mentioned, the Fe and Si content of the 2024 alloy we used met the specifications for 2124. However, no compositional analysis is given by Petrak and Gunderson (12). Further investigation of the reasons for these differences would undoubtedly be useful.

V. TRANSMISSION ELECTRON MICROSCOPY STUDIES AND THE RELATIONSHIP BETWEEN MICROSTRUCTURE AND PROPERTIES

1. Introduction

Changes in physical and mechanical properties of 2024 aluminum alloy brought about by an improper quench or a "pre-aging" treatment subsequent to solution heat treatment are related to the development of stable and metastable phases. These phases either do not form or do so to a negligible extent during a "proper" quench from the solution heat treatment temperature. The main objective of the TEM (transmission electron microscopy) investigation was to reveal the nature of the "pre-aging" induced phases. The results of that investigation will be presented in this section. As a natural corollary to the TEM investigation, an attempt has been made to relate the observed microstructural changes to the measured changes in physical and mechanical properties. Part of this discussion, particularly as it relates to mechanical properties, will be included in the present section. Some additional considerations will be presented in the following sections describing NDE evaluations.

TEM studies were carried out on a large number of specimens from the 0.635 cm (1/4 in.) thick plate. Some of these specimens were "pre-aged" and processed to T351 and T851 conditions as described in Section IV. The majority of the specimens, however, were prepared specifically for the TEM investigation. These specimens were subjected to "pre-aging" treatments which in many cases were identical to those given specimens prepared for physical and mechanical property measurements, but subsequent processing to T351 and T851 conditions was not carried out. In this way, microstructural changes associated with stretching

and final aging operations which might change or confuse the observation of "pre-aging" induced phases was avoided.

Strictly speaking, the microstructure was not necessarily identical to that immediately after "pre-aging". The 2024 aluminum alloy, especially when quenched directly into ice water from the solution treatment temperature or when "pre-aging" does not result in a significant reduction in solute supersaturation, is subject to fairly rapid aging at room temperature. Therefore, examination was carried out after room temperature aging to an essentially stable condition, i.e. after what may be referred to as a T4 temper treatment. The so-called natural aging response in this alloy is believed to be a direct result of the formation of G.P. zones, or G.P.B. zones as they are frequently referred to in Al-Mg-Cu alloys (13). In principle, valuable information with respect to the level of solute supersaturation and the effect of solute segregation could be obtained by studying G.P.B. zones, however, as will be pointed out later, zones exhibiting the expected characteristics were not imaged in the TEM. In any case, the presence of G.P.B. zones has no effect on the observation in the TEM of the various precipitates formed during thermal processing. Indirect evidence of G.P.B. zones and, more importantly, the concentration of available solute can be obtained from room temperature aging experiments. Such experiments were carried out on many of the specimens used for TEM examination. The results are presented in this section in connection with the discussion of the relationship between microstructure and properties.

After a brief description of the experimental procedure, the major portion of this section will be concerned with the identification in the TEM of various precipitates and constituent phases found in the

"pre-aged" specimens. A discussion of the influence of "pre-aging" induced precipitation on mechanical and physical properties will be presented at the end of this section.

2. Experimental Procedure

Specimens for TEM examination were prepared by cutting with a low speed diamond saw a thin slice approximately 0.25 mm thick from bulk material. Disks 3 mm in diameter were then punched from the slice and electropolished with a dual jet polishing device to obtain electron transparent areas. The electropolishing solution consisted of 70% methyl alcohol and 30% concentrated nitric acid. Satisfactory results were obtained when the solution was maintained in the temperature range 18 to 20 °C and the applied cell voltage was approximately 20 V. The presence of relatively large constituent phase particles in all materials and porosity in the as-cast materials described earlier had an adverse effect on the quality of the foils obtained. Preferential attack at these features often led to foils that were thicker than was desirable so that several attempts were sometimes required before a satisfactory specimen was obtained. For the as-cast ingot, where the principal objective was the identification of constituent phases, preferential chemical attack and the possibility of a systematic loss of a particular phase species was most undesirable. Therefore, some specimens were thinned by argon ion milling. With this method, it is often possible to achieve the simultaneous thinning of specimen areas which differ widely in composition and crystal structure. Ion milling was also carried out on some specimens subsequent to electropolishing to remove or minimize the presence of an electrochemically induced corrosion film or otherwise chemically depleted or enriched layer (14) that might

interfere with the accuracy of energy dispersive x-ray analyses in the electron microscope.

Most of the TEM studies were conducted at 120 kV in an instrument equipped to operate in the scanning transmission (STEM) mode as well as in the conventional transmission mode. The instrument was also equipped with an x-ray energy dispersive spectrometer (EDS). With this system it is, in principle, possible to determine the chemical composition of a column of material as small as 10 nm in diameter traversed by the electron beam. The analysis is limited to elements with atomic numbers $\geq$ 11 (Na). In general, an accurate analysis requires a knowledge of the foil thickness, lack of an interfering layer of material having a different composition and an appropriate calibration of the EDS system. In this investigation, the analyses were primarily qualitative or semi-quantitative in nature for the purpose of identifying the phases present. Identification of a particular phase generally involved the use of both electron diffraction and elemental composition determination by EDS.

3. Microstructure of 0.635 cm Thick Plate Specimens

A chart showing the "pre-aged" specimens that were studied by means of TEM is presented in Figure 66. The "pre-aging" times and temperatures indicated are nominal values in each case. Because of the finite heating and cooling rates, some of the "pre-aging" time interval was spent at temperatures other than those shown. Typical "pre-aging" temperature vs time curves are shown in Figure 26. A departure from the ideal "isothermal" cycle would probably have the most significant effect on the microstructures observed in specimens given short "pre-aging" treatments, particularly 20 s, where a considerable fraction of

the time shown was spent at higher than indicated temperatures in the case of sequence A specimens and at lower temperatures for the sequence B specimens. Even with the longer "pre-aging" treatments any time spent at a temperature which might be critical to a nucleation process has the potential of producing a microstructure that is different from that which would occur for a strictly isothermal treatment at the designated target temperature. The specimens in Figure 66 were selected to provide a survey of the microstructural changes that occurred over the range of "pre-aging" treatments covered in this investigation. A major objective was to identify those microstructural changes that were responsible for the mechanical and physical properties delineated in the C-curve representations. In addition to the specimens shown in Figure 66, several others were examined. These are listed in Table VI. They include a specimen quenched directly into ice water from the solution treatment temperature and aged at room temperature to provide a reference microstructure against which "pre-aged" specimens could be compared. Directly quenched specimens processed to the T351 and T851 tempers were also included to provide examples of "properly" quenched and processed microstructures with those tempers. The remaining two specimens included in Table VI were "pre-aged" and then processed to the T851 temper.

The TEM specimens in each case were prepared from thin slices cut perpendicular to the longitudinal plate direction. The specimen plane was therefore perpendicular to the longitudinal direction. Since it was usually necessary to tilt the specimen in the electron microscope to obtain the desired crystallographic orientation with respect to the electron beam, the normal to the electron micrographs shown in this

report may deviate from the longitudinal direction by up to 30°. The region examined was always approximately 1.6 mm in from the plate surface. Variations in the number densities, both relative and absolute, of different precipitate types were also observed on the scale of a few tenths of micrometers in a given specimen. This was taken as evidence for composition fluctuations on the same scale, indicating that homogenization of the intially segregated ingot structure had not been completely achieved. In the following two subsections, the nature of the constituent phases and of the "pre-aging" induced precipitates in the plate specimens will be described.

(a) Constituent Phases

Constituent phases found in wrought 2024 aluminum alloy materials can generally be classified into two size ranges, large particles having a major dimension > 1 μm in length and small particles whose major dimension is less than 1 μm. The large particles are in general from the as-cast ingot structures. They may be broken up and redistributed during mechanical stages of processing and perhaps suffer a phase change or diffusion related compositional modification during thermal processing steps following casting. In contrast, the majority of the small constituent particles are not present in the as-cast structure and probably develop during thermomechanical processing as a result of dissolution of interdendritic phases and subsequent precipitation. The small particles, so formed, are stable at the solution treatment temperature and are usually referred to as dispersoids. They play a major role in reducing grain growth during processing but also have a critical effect on the nucleation of other phases during quenching and aging treatments as will be discussed later.

The permissible concentrations of the various elements in 2024 aluminum alloy cover a sufficiently wide range that a rather large variety of constituent phases are possible. Many of the interdendritic phases listed by Sperry (3) (see Table III) will be retained even if complete homogenization and equilibration are achieved at the solution treatment temperature, 495 °C. This is especially true with respect to phases containing Fe and Si because of the low solubilities of these elements. Whether or not θ-$CuAl_2$ or S-$CuMgAl_2$ are present as constituent phases will depend on the available concentrations of Cu and Mg at the solution treatment temperature. With reference to the phase diagram shown in Figure 67 it can be seen that if the concentration of Cu exceeds approximately 4.0 wt.% and Mg is < 1.5 wt.% the excess Cu will be taken up by the θ phase. As the concentration of Mg is raised above 1.5 wt.% an increasing amount of the excess Cu will appear in the S phase. The level of available Cu is particularly sensitive to the concentrations of Fe and Mn, mainly because of the formation of Cu_2FeAl_7 and $Mn_3Cu_2Al_{20}$ and to some extent because of the solubility of Cu in the phases α-Al(Fe,M)Si and $MnAl_6$ (3,5).

During the course of examining a great many specimens listed in Figure 66 and Table VI, large constituent phase particles were frequently encountered. Most often, these were found to be the α-Al(Fe,M)Si phase. It may be recalled that this was also determined to be the predominant Fe bearing phase in the DC cast ingot. An example of one of these particles is shown in Figure 68(a) together with its diffraction pattern in Figure 68(b). EDS analyses of several particles gave an average composition of about 70% Al, 12% Fe, 5% Mn, 5% Cu, and 4% Si (atomic percent) similar to that obtained for this phase in the DC cast

ingot. There was no evidence to indicate decomposition of the α-Al(Fe,M)Si phase. Sperry (3) reported that α-Al(Fe,M)Si and Cu_2FeAl_7 might serve as a rough index to the degree of homogenization. Since there was no evidence of decomposition of α-Al(Fe,M)Si and the phase, Cu_2FeAl_7, was not found, it is apparent that other factors must be important. While large constituent particles of the θ phase were occasionally seen, particles of the S phase were not found in directly quenched specimens studied in the TEM. As will be described later, these phases were present after certain "pre-aging" experiments. It should be emphasized, of course, that due to the relatively small volume studied in the TEM, low concentrations of widely dispersed particles might not have been detected.

Dispersoid particles were observed in all the 0.635 cm thick plate specimens examined. They were typically equi-axed in shape with faceted sides, although rod shaped particles were frequently present. The equi-axed particles ranged in size from approximately 30 to 80 nm; however, much larger particles about 500 nm in diameter were often observed at grain boundaries. Particle spacing was of the order of 10 nm. Typical distributions of dispersoid particles from a directly quenched specimen are shown in Figure 69. In Figure 69(a) at low magnification it can be seen that the particles are arranged in bands with particle free regions between bands. This effect is almost certainly associated with segregation in the original as-cast ingot. Particle free zones were also present at some grain boundaries. No reference was found in the literature giving a detailed identification of the dispersoid phase. The fact that Mn does contribute to the formation of dispersoid particles has been mentioned by several investigators in connection with corrosion and mechanical properties studies of 2024

aluminum alloy (15-21). That Mn can be implicated in the formation of dispersoid particles is demonstrated by the investigations of Robinson and Hunter (18) and Stolz and Pelloux (19). Both examined Al-Cu-Mg alloys with no measurable Mn or at a concentration of Mn below the solubility limit and found that dispersoids were not present. Robinson and Hunter mention the $Cu_2Mn_3Al_{20}$ phase but do not indicate that the dispersoid particles are that phase. Kaufman and Low (20) referred to rod shaped precipitates 0.1 to 0.2 μm in size at grain boundaries in 2124 aluminum alloy as $Cu_2Mn_3Al_{20}$ but did not indicate how the identification of that phase was made. Van Stone et al. (21) indicate that dispersoid particles in 2000 series alloys have been identified as $Al_{12}(FeMn)_3Si$. Petri (22) and others (23,24) have determined that the solid solubility of Mn in Al-Cu-Mn alloys is approximately 0.2 wt.% at 500 °C. At a composition of Al-4wt.% Cu-0.6wt.% Mn according to Petri's phase diagram, which is confirmed by Day and Phillips (23) and Hofmann (25), the two phases α-Al and $Cu_2Mn_3Al_{20}$ (referred to as "T" by Petri) are present. The work of Phragman (26) indicates that the additional presence of 1.5 wt.% Mg in 2024 aluminum alloy probably does not change this result. It might also be noted that Robinson and Hunter (18) show qualitatively similar electron micrographs of dispersoid particles in Al-Cu-Mn and Al-Cu-Mg-Mn alloys.

With respect to the material studied here, an average Mn concentration of 0.6 wt.% was determined by chemical analyses. However, some of the available Mn (0.4 wt.%) is lost through the formation of the insoluble α-Al(Fe,M)Si phase formed during solidification. It is therefore reasonable to assume that a large fraction of the dispersoid particles in 2024 aluminum alloy are the $Cu_2Mn_3Al_{20}$ phase. Analyses of

the $Cu_2Mn_3Al_{20}$ phase have determined that it may differ from the ideal composition, 80 at.% Al, 8 at.% Cu, and 12 at.% Mn. Petri obtained a variable composition ranging from 80.1 at.% Al, 7.8 at.% Cu, and 12.1 at.% Mn to 78.1 at.% Al, 6.9 at.% Cu, and 15.0 at.% Mn. Day and Philips (23) found a single composition, 11 at.% Cu and 15 at.% Mn.

EDS analyses were carried out on a number of dispersoid particles in the directly quenched specimen as well as in several "pre-aged" specimens. A composition of about 80 to 90 wt.% Al and 5 to 10 wt.% each of Cu and Mn was obtained in each case. The uncertainty in this analysis was due to the different thicknesses of the particles examined and to the fact that some thickness of the α-Al matrix probably covered many of the particles. Electron diffraction studies of the particles were also carried out. Petri determined that $Cu_2Mn_3Al_{20}$ has an orthorhombic unit cell. A detailed x-ray crystallographic study by Robinson (27) gave unit cell dimensions of $a_o = 24.2\mathring{A}$, $b_o = 12.5\mathring{A}$ and $c_o = 7.72\mathring{A}$, quite consistent with results obtained by Petri. Robinson also determined on the basis of systematically absent reflections that the space group was either Bbmm, Bbm2 or Bb2m. Several characteristics of the dispersoid particles and of the $Cu_2Mn_3Al_{20}$ crystal structure complicate its identification by means of electron diffraction. They are the small particle size, twinning within individual particles, a large unit cell size and the fact that most of the strongly reflecting planes have very nearly the same spacings (27). These factors may explain why previous investigators have not offered a specific identification of this phase. It was possible in this investigation, however, to obtain microdiffraction patterns from individual particles and to index these patterns consistent with the $Cu_2Mn_3Al_{20}$ structure. An example is shown in Figure 70.

(b) T4, T351 and T851 Microstructures

It is widely accepted that age hardening at room temperature of supersaturated Al-Cu-Mg alloys having a Cu:Mg ratio of approximately 2.2:1 occurs by the formation of so called G.P.B. zones (13) which presumably are clusters rich in Cu and Mg. Age hardening at room temperature of the more complicated 2024 aluminum alloy is [illegible] to occur by the same means. Silcock (13) on the basis of x-ray measurements has proposed that the G.P.B. zones are rods parallel to the <100> matrix direction with an estimated length of 40 Å and diameter of 10 to 20 Å. Although TEM has proved to be very valuable for the direct observation of zones in a number of systems (Al-Cu is an especially good example (28)), no reference was found providing a detailed study of G.P.B. zones formed at room temperature in Al-Cu-Mg alloys. In fact, it was noted in several cases that G.P.B. zones could not be resolved (29-31). G.P. zones in general can be revealed in the TEM by diffraction contrast as a result of surrounding strain fields (coherency strains) in the matrix, in dark field due to non-matrix diffraction contributions, by structure factor contrast, or through lattice imaging (32). During the normal course of examining a number of specimens in this investigation, conclusive evidence of G.P.B. zones, consistent with the description of Silcock (13), was not obtained despite a marked room temperature age hardening response. This was true both with respect to images obtained under a variety of diffraction conditions, and particularly in diffraction patterns. There was no obvious contribution in addition to the α-Al matrix pattern to suggest the presence of zones which one might expect on the basis of the x-ray diffraction results. It must be concluded that zones in Al-Cu-Mg alloys differ significantly from those in the

binary Al-Cu system, especially with respect to the development of coherency strains.

The microstructure of a directly quenched specimen in the T4 condition shown in Figure 69 has already been discussed. An additional micrograph of this specimen is shown in Figure 71 with dislocations in contrast. The dislocations were either retained after solution treatment or were introduced during the quench. Migration of excess vacancies to dislocations and subsequent climb of screw segments has led to the formation of helices (33). As will be seen later, these dislocations can act as sites for the heterogeneous nucleation of precipitates.

The T351 temper is similar to T4 with the exception of an intermediate plastic deformation step after quenching in which the material is stretched to a strain of ~ 2.5%. The resulting microstructure is shown in Figure 72. The relatively high dislocation density is a consequence of the stretching operation, otherwise the microstructure does not appear to differ from the T4 condition.

The effect of artifical aging of 2024 aluminum alloys and similar Al-Cu-Mg alloys has been extensively studied (34,35). Three different stages of precipitation are recognized. They are generally represented by the scheme,

$$\text{supersaturated } \alpha\text{-Al} \rightarrow \text{G.P.B. zones} \rightarrow S' \rightarrow S.$$

It does not follow however that G.P.B. zones necessarily preceed the formation of S' or that S is preceeded by S'.

The S' phase is thought to be nearly identical to S in composition ($CuMgAl_2$) and structure (orthorhombic with $a_o = 4.04$ Å, $b_o = 9.25$ Å, and $c_o = 7.18$Å) (36). The two phases differ mainly in that S' is

semi-coherent and S is incoherent. Both S' and S have the same orientation relationship with the matrix:

$$[100]_S \quad [100]_\alpha;\ [010]_S \quad [021]_\alpha;\ [001]_S \quad [01\bar{2}]_\alpha.$$

Individual S' precipitates grow in the form of laths on $\{210\}_\alpha$ planes with their long axis parallel to $\langle 001\rangle_\alpha$; thus there are 12 different orientation variants in the α-Al matrix. Adjacent S' precipitates are often arranged to form corrigated sheets.

The effect of aging time and temperature on the development of the various precipitate species has been studied by Silcock (13) in the ternary alloy Al-3.15 wt.% Cu-1.52 wt.% Mg which closely corresponds to 2024 aluminum alloy. At temperatures between 110 and 260 °C, G.P.B. zones were the first species to be observed. After approximately 10 days at 130 °C and in much shorter times at higher temperatures, S' precipitates were also detected. At 260 °C only the S' phase was found.

The T851 temper is achieved by exposing T351 material to artificial aging at 195 °C for 12 hrs. The resulting precipitates are predominantly S'. Grain boundary precipitates form also and these are considered to be the S phase on account of their non-lath like shape. An example of the T851 microstructure is shown in Figure 73(a). The diffraction pattern from this area is shown in Figure 73(b) and the corresponding indexed pattern is shown schematically in Figure 73(c). That the majority of the S' precipitates probably nucleate heterogeneously at dispersoid particles and dislocations will be demonstrated later.

(c) "Pre-aged" Microstructures

During quenching from solution treatment it has been found that a cooling rate of less than approximately 550 °C/s through a

critical temperature range extending from about 400 °C to 290 °C is detrimental to many of the properties of 2024 aluminum alloy (37). Corrosion is one of the most sensitive properties to quench rate, and degradation in corrosion behavior is the first effect to be noted when the rate is reduced below 550 °C/s. Mechanical properties are not affected until the quench rate is reduced below about 10 °C/s--corresponding to a dwell time of 8 s in the critical temperature range. Note that the nose of the yield strength C-curve, Figure 30(a), occurs at about 8 s. Materials in the naturally aged condition are in general more susceptible to corrosion than those subjected to artificial aging. The major microstructural consequence of a reduced quench rate is to permit the nucleation and growth of precipitates that not only do not improve the mechanical properties but consume solute elements that otherwise would contribute to the desired age-hardening G.P.B. zones and precipitates. Furthermore precipitates formed during a slow quench may produce sites for enhanced corrosion activity.

As already described two different "pre-aging" treatments were employed to develop C-curves which can serve to predict the effect of an improper quench on properties. Because two separate processes are involved, one being nucleation and the other growth, a single "pre-aging" sequence is not adequate to explore behavior under conditions where an improper quench treatment may result in a non-monotonic cooling curve. Thus the sequence A "pre-aging" treatment consists of rapidly cooling from the solution temperature to an intermediate "pre-aging" temperature where the specimen is held for a prescribed length of time before quenching into ice water. Nucleation and growth is then confined to temperatures above or at the "pre-aging" temperature. In the sequence

B, "pre-aging" treatment, the specimen is first quenched to ice water and then rapidly reheated to the "pre-aging" temperature. Here nucleation and growth occur mainly below or at the "pre-aging" temperature. In what follows, the results of TEM studies of sequence A "pre-aged" specimens will be described first followed by the presentation of sequence B results.

Sequence A Microstructures. Representative examples of sequence A microstructures from specimens "pre-aged" at 400 °C, 350 °C, and 300 °C are shown in Figure 74 at a relatively low magnification and in Figure 75 at a higher magnification. In each case, structures corresponding to "pre-aging" times of 20 s and 500 s are included. Specimens were examined after 100 s and the microstructures were found to be intermediate between those at 20 s and 500 s. Consider first the series at 400 °C. After 20 s of "pre-aging", Figures 74(a) and 75(a), the only detectable change from the directly quenched structure was the presence of slightly larger, and perhaps more frequent, grain boundary precipitates. 'Pre-aging" for 100 s and 500 s led to a substantial change. Not only were the grain boundary precipitates very large but large precipitates were also present in the grain interiors. An electron diffraction analysis of the grain boundary precipitates indicated that they were S-$CuMgAl_2$. An example of one of these precipitates with its electron diffraction pattern is shown in Figure 76. This and other S phase grain boundary precipitates examined exhibited the reported orientation relationship,

$$[100]_S \quad [100]_\alpha;\ [010]_S \quad [021]_\alpha;\ [001]_S \quad [01\bar{2}]_\alpha,$$

with at least one adjacent grain at the boundary.

Precipitates present within grain interiors were of two types. One type had an irregular but more-or-less equi-axed shape. The other was disk shaped. An example of an irregular shaped precipitate is shown in Figure 77. From its diffraction pattern it was determined to be the S phase obeying the orientation relationship noted above. That is, these precipitates were essentially identical to the grain boundary precipitates.

The disk shaped precipitates were determined by electron diffraction to be the θ phase. Analysis of diffraction patterns indicated the orientation relationship,

$$(110)_\theta \quad (1\bar{1}\bar{1})_\alpha; \; [\bar{1}\bar{1}0]_\theta \quad [0\bar{1}\bar{1}]_\alpha.$$

Furthermore, the face of the precipitate disks was $(110)_\theta$ and was parallel to $(1\bar{1}\bar{1})_\alpha$. An example of a θ precipitate with important matrix and precipitate crystallographic directions indicated is shown in Figure 78(a). The corresponding diffraction pattern is presented in Figure 78(b). It is interesting that the orientation relationship determined here was not one of the several relationships that have been reported for the θ phase in Al-Cu alloys. The latter relationships have been summarized by Lorimer (36). All have a common feature in that $[001]_\theta$ is either parallel to $[001]_\alpha$ (within ± 4° in one case) or parallel to $[110]_\alpha$. The θ phase observed in these "pre-aged" specimens was oriented with $[001]_\theta$ parallel to $[2\bar{1}1]_\alpha$.

It might be hypothesized that the presence of both θ and S phases after "pre-aging" at 400 °C is a manifestation of the approach to equilibrium. The equilibrium conditions under which both θ and S may coexist in a ternary Al-Cu-Mg alloy comparable to 2024 aluminum alloy

are indicated in the phase diagram shown in Figure 67. On cooling, the path indicated in Figure 67 is followed and is approximately coincident with a 2.2:1 ratio of Cu to Mg. If Cu is available in excess of this ratio the θ phase will form until the excess Cu is consumed and thereafter the alloy will behave as a pseudobinary of α + S. Observing both the θ and S phases after "pre-aging" suggests there may in fact have been an overbalance of Cu. To test this hypothesis, a specimen was "pre-aged" at 400 °C for 7200 min. to allow time for equilibrium to be reached. Examination of this specimen revealed only the S phase. It may be concluded, therefore, that the presence of the θ phase at short "pre-aging" times was not the result of the suggested equilibrium reaction and that the θ phase is metastable.

The series of specimens "pre-aged" at 350 °C were similar in many respects to those exposed at 400 °C. For short "pre-aging" times, θ was the major precipitate phase with increasing amounts of the S phase appearing as the duration of "pre-aging" was increased. Some S' precipitates were also observed. The distinction between S and S' is based on the shape of the precipitates. Thin rod or lath shaped precipitates parallel to $\langle 100 \rangle_{\alpha}$ directions are considered to be S' while the much thicker precipitates without this characteristic shape are referred to as S. A relatively high concentration of precipitates was already present after 20 s as is shown in Figure 74(c). Most of the precipitates in Figure 74(c) are θ.

The S phase precipitates here and in other examples can often be recognized by the region of light contrast that surrounds them. The light contrast is the result of a local reduction in thickness caused by preferential attack during electro-chemical thinning in preparation

of the specimen. Figure 75(c) clearly demonstrates that the θ precipitates are heterogeneously nucleated at dispersoid particles. Here the precipitates have a distinct hexagonal shape with straight sides parallel to $\langle 112 \rangle_\alpha$. An example is shown in Figure 79 where the $(111)_\alpha$ plane and a θ precipitate in that plane are approximately parallel to the viewing plane. The relationship between the S phase and the other precipitates was not obvious although it appeared that they developed in association with the dispersoid particles and perhaps the θ phase precipitates. As Cu is consumed by the θ phase, the relative proportion of Mg increases and, according to the phase diagram, the tendency for the formation of the S phase should be enhanced. Nucleation of the S' precipitates was at dislocations and possibly at dispersoid particles. After "pre-aging" for 500 s, θ was no longer the predominant precipitate phase. The majority of the precipitates were found to be the S phase. "Pre-aging" at 350 °C for 1000 min led almost entirely to the loss of the θ phase with only S and possibly S' being present. Therefore, it must be concluded that the θ phase is not an equilibrium phase at 350 °C.

"Pre-aging" at 300 °C also led to the formation of θ phase precipitates at dispersoid particles. The dispersoid particles were also identified as the sites for the formation of S' precipitates. After "pre-aging" for 20 s, Figure 75(e), the precipitates have grown out only a short distance from the dispersoid particles. When the duration of "pre-aging" was extended to 500 s the precipitates were distributed uniformly throughout the matrix, Figure 75(f). Prolonged "pre-aging" for 1000 min as at 400 °C and 350 °C again led to the disappearance of the θ phase with only S and S' remaining. As a further observation it was noted that S' was increasingly present at dispersoid particles as the "pre-aging" temperature was reduced.

A single specimen "pre-aged" at 250 °C was studied. The duration of "pre-aging" was 400 s. Both θ and S' precipitates were observed at dispersoid particles, similar to specimens "pre-aged" at 300 °C. In addition, however, much smaller S' precipitates were distributed homogeneously in the matrix, with precipitate free zones in the vicinity of the larger S' and θ precipitates at dispersoid particles. These different types of precipitates are shown in Figure 80. The observation of homogeneously distributed precipitates is important here because it is an indication that the "pre-aging" temperature, 250 °C, is in the temperature range where G.P.B. zones may form. The assumption is made that G.P.B. zones must precede the development of homogeneously distributed S' precipitates. Beton and Rollason (38) have determined the G.P.B. zone solvus for Al-Cu-Mg alloys by means of a reversion method. At a composition corresponding to the 2024 aluminum alloy, they obtained a dissolution temperature of about 260 °C for G.P.B. zones which tends to support the observation made here.

The precipitation processes resulting from the sequence A "pre-aging" treatments can be conveniently summarized by means of a nucleation or transformation diagram. Such a diagram has been drawn in Figure 81. Each curve represents the estimated time and temperature dependences for the onset of a particular transformation. The representation shown in Figure 81 should be regarded as largely schematic, since in no case was an exact determination made to fix the position of a curve. The first phase observed at elevated temperatures was S at grain boundaries. In time, this was followed by θ and then S'. Both θ and S' nucleated heterogeneously at dispersoid particles, and in addition, S' nucleated at dislocations. One might speculate that in the absence of dispersoid

particles and dislocations neither of these phases would have formed. At low temperatures, G.P.B. zones, possibly preceeded by spinodal decomposition, occur first and then transform to homogeneously distributed S' precipitates. For longer "pre-aging" times the θ phase disappears to be replaced by equilibrium S. The precise nature of that transformation is not understood. Prolonged aging also results in the disappearance of S' and an accompanying increase in the amount of S. Observations also indicate that the homogeneous S' precipitates disappear in the presence of larger heterogeneously nucleated S' precipitates. Whether the latter transformation is simply a consequence of Ostwald ripening or represents a more fundamental difference between homogeneous S' and heterogeneous S' is not known.

The C-curves presented in Section IV can, of course, be related to the nucleation curves. If a single time and temperature dependent transformation process is involved and the property (hardness, electrical conductivity, etc.) for which the C-curve is drawn is sufficiently sensitive to that transformation process, then the first C-curve, indicating an initial change in the property, should coincide with the nucleation curve. When several interdependent processes are involved, the determination of C-curves is essentially a curve fitting exercise. If the processes are well separated in time and temperature, a single family of C-curves will probably fit the data poorly. If the processes overlap and are interdependent as is apparently the case here, a better fit may be achieved.

Sequence B Microstructures. The microstructures of specimens subjected to sequence B "pre-aging" treatments at 400 °C, 350 °C, and 300 °C for 20 s and 500 s are shown in Figures 82 and 83. In each

case, S' was the only precipitate phase that formed within the grains. Precipitates of the S phase were observed at grain boundaries under all conditions, much as was found in the sequence A specimens. The change in precipitate size and concentration can be followed in Figures 82 and 83 as a function of "pre-aging" time and temperature. In general, the size of the precipitates increases with increasing time at each temperature. After only 20 s of "pre-aging" at 400 °C, Figures 82(a) and 83(a), precipitates are uniformly distributed throughout the matrix. Here and in all examples shown in Figures 82 and 83 the direction normal to the micrograph is within a few degrees of $[001]_{\alpha}$. Therefore, eight orientation variants of the rod shaped S' precipitates are present having their long axis parallel to the plane of the micrograph and four variants are present with their long axis perpendicular to the plane of the micrograph. When viewed end-on, it was evident that many of the rods were nearly circular in cross-sectional shape. Other rods were elongated with an aspect ratio of about 2:1 or less. At 400 °C, the diameter of the rods determined in the end-on orientation is approximately 10 to 30 nm after 20 s and 20 to 90 nm after 500 s of "pre-aging". Thus, the growth rate of the average precipitate varies approximately as $d \propto t^{\frac{1}{2}}$ where d is the precipitate diameter and t is the time. This suggests that the process is diffusion controlled. Undoubtedly, factors other than volume diffusion were involved in determining the growth rate; for example, impingement of precipitates has certainly occurred in many instances in Figures 82 and 83. Although the precipitate concentrations were not measured, it was apparent that fewer precipitates were present at 500 s than at 20 s, indicating that coarsening had occurred. As the precipitates become larger and fewer in number with

longer "pre-aging" times due to coarsening, the obvious relationship between precipitates and dispersoid particles is lost. For example, the S' precipitates after "pre-aging" at 400 °C for 500 s, Figure 83(b), appear to be relatively independent of dispersoid particles.

"Pre-aging" at 350 °C led to a precipitate morphology which appears similar to that at 400 °C. S phase precipitates are formed at grain boundaries and S' within grains. Typical microstructures are shown in Figures 82(c), 82(d), 83(c) and 83(d). The precipitates formed at 350 °C are smaller than those at 400 °C for the same "pre-aging" times. After "pre-aging" for 20 s and 500 s, the end-on diameters of the S' precipitates are 3 to 10 nm and 20 to 75 nm, respectively. Comparing Figures 83(c) and 83(d) at 20 s and 500 s, respectively, the number density of precipitates doesn't appear to be significantly different, although the precipitates are considerably larger at 500 s. The increase in size is probably due to growth from solution rather than coarsening due to the dissolution of smaller precipitates as observed at 400 °C.

The heterogeneous nature of the precipitation process is very clearly demonstrated by the specimen "pre-aged" for 20 s at 350 °C. The rod shaped S' precipitates all seem to radiate out from each dispersoid particle along <200> directions. Precipitates clustered along short dislocation lines can also be seen.

The trend in the precipitation process observed at 350 °C and 400 °C was also found at 300 °C. After "pre-aging" for 20 s the precipitates at dispersoid particles are very small, Figure 83(e). With 500 s of "pre-aging" the precipitates have grown substantially, Figure 83(f). In addition to precipitates at dispersoid particles, some very small homogeneously distributed S' precipitates are present in the matrix.

These as well as precipitates at dispersoid particles and dislocations are shown in the dark field image in Figure 84. The presence of homogeneously distributed precipitates at 300 °C seems not to be consistent with the reaction G.P.B. zones → S' since 300 °C is probably above the G.P.B. zone solvus. However, the reaction may have taken place during the temperature rise to 300 °C from the ice water quench. To support this suggestion, it may be noted that homogeneously distributed S' precipitates were not observed after the sequence A "pre-aging" treatment at 300 °C.

One specimen was "pre-aged" at 250 °C for 400 s. This temperature is below the G.P.B. solvus bourdary and homogeneously distributed S' precipitates were present in the matrix as might be expected. Much larger S' precipitates were observed at dispersoid particles and dislocations. The microstructure was similar to that observed in the specimen "pre-aged" at 300 °C for 20 s, Figures 83(e) and 84.

Specimens were also examined after prolonged "pre-aging" treatments. At 400 °C after 7200 min large S phase precipitates were present along grain boundaries. A few very large precipitates of either the S or S' phase were observed within grains. Because of their rod-like shape with their long axis parallel to $[100]_{\alpha}$, they are assumed to be S'. The corresponding sequence A specimen exhibited a higher concentration of S precipitates without the rod-like shape. Optical micrographs of these two specimens are shown for comparison in Figure 85.

Nucleation curves can be drawn for reactions occurring during the sequence B treatment as was done for the sequence A treatment. The representation, shown in Figure 86, is much simpler than for the sequence A case since the θ phase was not detected. In common with the sequence

A treatment, the first phase to be observed after "pre-aging" at elevated temperatures was the S phase at grain boundaries. Almost simultaneously, however, the S' phase was found at dispersoid particles and dislocations. Continued "pre-aging" led to the transformation, S' → S. However, the process was relatively slow even at 400 °C and was apparently a result of the dissolution of S' precipitates within grains and the diffusion of solute to S precipitates at grain boundaries. At lower temperatures, the formation of G.P.B. zones and homogeneously distributed S' was similar to that after sequence A treatments.

As might be expected on the basis of the different transformation processes, the sequence B C-curves differ from those for the sequence A "pre-aging" treatments. While the sequence A treatment resulted in the nucleation of θ, S and S' phases within grains, only the S' phase was observed after a sequence B treatment. Differences in the nucleation, growth, coarsening and transformation kinetics of the various phases explain the differences in the C-curves.

Effect of "Pre-aging" on T851 Microstructure. Two sequence A specimens "pre-aged" at 350 °C were examined after being subjected to a T851 temper treatment. The "pre-aging" treatments were carried out for 20 s and 109 s each; the microstructures are shown in Figures 87(a) and (b), respectively. Large precipitates at dispersoid particles are readily identified as being produced during the "pre-aging" treatment by comparison with Figure 73 given a T851 treatment without "pre-aging" and Figure 75(c) which was subject to "pre-aging" and not processed to the T851 condition. The "pre-aging" induced precipitates were determined to be the θ and S phases. The small needle shaped precipitates are, of course, the S' phase which was formed during final aging at 190 °C.

The low density of S' precipitates around "pre-aging" induced precipitates is indicative of the extent to which solute was lost during "pre-aging".

4. Discussion: Relationship Between Microstructure and Properties

Property changes associated with "pre-aging" are a result of the nucleation, growth, and coarsening of precipitates during the "pre-aging" treatment. TEM studies have demonstrated that the precipitates may differ significantly in type, size, concentration, distribution and coherence depending on the nature of the "pre-aging" treatment. The changes in properties are strongly time dependent indicating that transformation kinetics are of critical importance. "Pre-aging" induced precipitates may have both a direct effect on properties and an indirect effect. The indirect effect is a result of the consumption of solute elements (Cu and Mg) by the "pre-aging" induced precipitates. This reduces or in the worst case precludes the formation of G.P.B. zones and precipitates which normally develop during the final natural or artificial aging treatment.

Although no attempt will be made to develop quantitative relationships between properties and microstructural quantities such as precipitate type, size and concentration, an effort will be made to provide a qualitative explanation of the effect that "pre-aging" has on properties. In addition to the TEM studies, the discussion will depend strongly on the results of the room temperature aging experiments presented below, on measurements of the age hardening behavior of Al-Cu-Mg alloys from Hardy (35) and Beton and Rollason (38), and on phase diagram information, also from Hardy. A major part of the discussion is concerned with the T4 condition since most of the TEM specimens examined were in that condition. Also, in the T4 condition, the effects of "pre-aging" can

be related directly to property changes without the need to account for additional modifications brought about by deformation and elevated temperature aging which accompanies processing to the T351 and T851 conditions. The effect of "pre-aging" on these temper conditions will, however, be considered in the final part of this section.

(a) T4 Condition

In general, the T4 condition refers to materials that have been allowed to age at room temperature after the quench from solution treatment without intervening or subsequent treatments. In the present investigation, the T4 appellation is also applied to specimens given a "pre-aging" treatment prior to room temperature aging. The room temperature age hardening responses of many of the specimens prepared for TEM study (Figure 66) are shown in Figure 88. For reference, the age hardening behavior of a specimen quenched directly into ice water from the solution treatment temperature is shown in Figure 89. The data plotted in Figures 88 and 89 were obtained as follows. After quenching in ice water at the end of the "pre-aging" cycle for Figure 88 or after the direct quench for Figure 89, the specimen was immediately immersed in liquid nitrogen for storage until room temperature aging was commenced. The specimen was brought quickly to room temperature by agitating in a bath of water. Hardness measurements were made according to the Rockwell "B" method noted earlier. The first determination was obtained at 1 to 2 mins after the specimen had reached room temperature. Hardness measurements were made periodically thereafter until no further change was observed. In many cases, an initial increase in hardness was observed during the first 2 or 3 mins followed by an incubation period and then hardening to the final value. The initial change in hardness will not

be considered further here, however it is thought that it may be associated with spinodal decomposition. The effect would be better studied at lower temperatures.

Consider first the effect on hardness of the sequence A "pre-aging" treatments. Final hardness, post quench incubation hardness and the difference between final and incubation hardness values are plotted in Figures 90(a), (b) and (c) respectively. The plotted results were taken from room temperature aging curves in Figures 88 and 89 after converting from Rockwell "B" to the Vickers hardness scale by utilizing a table from Mondolfo (39). The Vickers scale bears a more nearly linear relationship to strength than the Rockwell "B" scale. To explain the variation in hardness shown in Figure 90 the following must be considered:

1. Hardening by G.P.B. zones
2. Solid solution hardening
3. Precipitation hardening
4. Grain size effects

Age hardening of Al-Cu-Mg alloys with a Cu:Mg ratio of 2.2:1 occurs at room temperature by the formation of G.P.B. zones. A maximum increase in hardness for a given Cu and Mg composition is obtained when the concentration of G.P.B. zones is maximized. This is achieved by solution heat treatment above the S+α boundary and quenching at a sufficiently high cooling rate to retain all the Cu and Mg in solution. A reduced quench rate, or "pre-aging" treatment as was done in this investigation at a temperature below the S+α boundary can lead to a reduction in the solute concentration through the precipitation of the S, S', and θ phases and a diminished concentration of G.P.B. zones upon

subsequent aging. The effect of "pre-aging" on the incremental increase in hardness associated with G.P.B. zone formation after room temperature aging to a stable condition is clearly demonstrated in Figure 90(c). On "pre-aging" at 400 °C, the hardness increment falls until a constant value is reached after 100 s. The behavior is similar for 350 °C but the constant level which is obtained after 500 s is only about 10 N/mm^2. At 300 °C, extended "pre-aging" eventually eliminates any observable room temperature age hardening effect. Since G.P.B. zone formation probably requires some minimal level of solute supersaturation, Figure 90(c) demonstrates that aging for a sufficient time ($\gtrsim$ 500 s) at a temperature between 300 and 350 °C reduces the supersaturation below the minimum value. The TEM studies determined that the loss of solute was primarily a result of the formation of the θ and S phases within grains and the S phase at grain boundaries. In effect, the material behaves like an alloy with a lower solute concentration. For the Al-Cu-Mg system according to Hardy (35) the $\alpha/(\alpha+S)$ boundary is given by $\log_{10}$ [Cu][Mg] = 5.603-3975/T, where [Cu] and [Mg] are concentrations in atomic percent and T is the absolute temperature. Using this equation the equilibrium concentration of Cu+Mg at 400 °C is approximately 2.2 wt.% while at 300 °C it is only 0.6 wt.%. The relationship between the hardness change produced by G.P.B. zone formation and solute concentration for the Al-Cu-Mg system plotted from the data of Beton and Rollason is shown in Figure 91. The relationship is not linear, particularly at concentrations above ~ 3.5 wt.% (Cu+Mg). Between 1 wt.% (the minimum value for which data was reported and 3.5 wt.% the change in hardness is approximately proportional to the concentration. Temperatures corresponding to the $\alpha/(\alpha+S)$ phase boundary location are also indicated

in Figure 91. It can be seen that the hardness increment at concentrations below 1 wt.% (Cu+Mg) attained by equilibration at temperatures < 326 °C is very small. Thus, it may be inferred that by "pre-aging" 2024 aluminum alloy for a sufficiently long period of time at temperatures close to 300 °C the concentration of solute remaining in solution would be reduced to a point where few G.P.B. zones would form. A direct comparison between 2024 aluminum alloy and ternary Al-Cu-Mg alloys, of course suffers from the fact that 2024 aluminum alloy contains additional elements that can effect its aging behavior.

Figure 90(c) also provides information on the rate at which equilibration occurs. The rate is determined by the nucleation and growth kinetics of "pre-aging" induced precipitates. At 400 °C where nucleation is comparatively difficult as is demonstrated by the absence of precipitates after "pre-aging" for 20 s, there is little change in solute supersaturation. After 100 s large precipitates were observed throughout the matrix and according to Figure 90(c) an equilibrium concentration of solute had been reached. There is a complication here, of course, because the θ phase, the major phase within grains, consumes mainly Cu leaving a surplus of Mg. What effect this may have on G.P.B. zone formations is not known, although it is not expected to be large.

At 300 °C nucleation occurs more rapidly as evidenced by a high concentration of θ precipitates. The initial rate of approach to equilibrium was also the most rapid for the temperatures studied.

The final hardness shown in Figure 90(a) can be regarded as the sum of the incremental increase associated with G.P.B. zone formation and an incubation hardness value that varies with "pre-aging" time and

temperature. At 400 °C there is no change in hardness before 20 s and a logarithmic decrease thereafter. Initially, a rapid drop in incubation hardness is observed at 350 °C and 300 °C which is followed by a slower logarithmic decay at about the same rate as at 400 °C. The difference between the initial behavior at 400 °C and that at the two lower temperatures is consistent with differences in the microstructures. After aging for 20 s at 400 °C there was no evidence that precipitation had occurred except at grain boundaries where very small S precipitates were observed. In contrast relatively large precipitates were present after "pre-aging" for 20 s at 350 and 300 °C. The initial large rate of decrease in incubation hardness can be attributed to a decrease in solid solution hardening as a result of the nucleation and growth of the Θ and S phases. A measure of the extent to which Cu and Mg in solution can affect hardness is indicated by the as-quenched hardness vs (Cu + Mg) concentration curve obtained by Hardy (35), Figure 92. The period during which the rapid loss of solute from the matrix takes place corresponds to the portion of the curves in Figure 90(c) showing a rapid change in hardness increment due to G.P.B. zone formation. The Θ and S phase precipitates may increase the hardness but apparently not nearly enough to offset the effect associated with the loss of solute. The continued decay in hardness with increasing time at all temperatures can be attributed in part to a further loss of solute from the matrix due to the gradual approach to equilibrium. Eventually, this involves the slow dissolution of Θ and the growth of S, where it will be recalled that the S phase consumes both Cu and Mg and the Θ phase only Cu, i.e. the change would mainly be associated with the loss of Mg from solution. Loss of other elements in solution, for example Mn and Cu to the

$Cu_2Mn_3Al_{20}$ dispersoid phase may also contribute to the reduction in plateau hardness. Part of the decay in hardness can also be attributed to precipitate coarsening, a reduction in the number density of precipitates due to Ostwald ripening, and transformation of S' to S.

Finally, prolonged "pre-aging" especially at temperatures close to the solution treatment temperature could lead to grain growth and a reduction in hardness. However, grain growth was not observed after 7200 min at 400 °C and is made unlikely by the closely spaced S precipitates at the grain boundaries.

Turning to the sequence B treatment, a similar approach can be taken to relate the effects of "pre-aging" induced phase transformation to property changes. Figure 93(a), (b), and (c) summary the room temperature age hardening response of specimens "pre-aged" at 300 °C, 350 °C and 400 °C. Figure 93(a) presents the final hardness values, Figure 93(b) gives the incubation values and Figure 93(c) shows the incremental change in hardness. The room temperature age hardening response after sequence B treatment at 400 and 350 °C differs from that observed for a sequence A treatment. After "pre-aging" for 20 s at 400 °C, the incremental change in hardness, Figure 93(c), has dropped to $\sim$ 200 N/mm^2 from 330 N/mm^2, the directly quenched value. No change was observed after a sequence A treatment for the same period of "pre-aging". The initial rapid decrease in hardness increment after the sequence B treatment is consistent with the presence of a high concentration of S' precipitates within grains and S at grain boundaries observed in the TEM. It may be recalled that precipitation was just beginning at grain boundaries after the sequence A treatments at 400 °C for 20 s. The low rate of nucleation at 400 °C is overcome in the sequence B treatment during the quench-reheat portion of the cycle.

"Pre-aging" at 400 °C for 100 s and 500 s resulted in increasingly larger S' precipitates with little change in hardness increment. Thus the process during this period was mainly one of coarsening and did not involve a change in the volume fraction of the S' phase, i.e. the concentration of solute in solution did not change appreciably. "Pre-aging" for 7200 min led to an increase in the hardness increment and resulted in a microstructure that consisted of only a few large S' precipitates within grains and very large S precipitates at grain boundaries. Thus, prolonged aging apparently resulted in the dissolution of much of the S' phase within grains and a corresponding growth of the S phase at grain boundaries. The reason for the increase in hardness increment after 7200 min at 400 °C is not understood. The same effect was not observed for the corresponding sequence A treatment. The difference may be associated with the much lower incubation hardness after the sequence B treatment.

The hardness increment vs "pre-aging" time curves at 350 °C and 300 °C, Figure 93(c), are similar to the companion sequence A curves, Figure 90(c), although the decrease occurs more rapidly at 350 °C than was obtained for the sequence A treatment.

The incubation hardness curves, Figure 93(b) for the sequence B treatments at 400 °C and 300 °C show an approximate decrease in hardness with logarithmic time from the onset of "pre-aging". At 300 °C, however, there is an initial rise during approximately the first 100 s followed by a decrease at about the same rate as for 350 °C and 400 °C. The incubation hardness over the range of "pre-aging" times studied is greatest at 300 °C and smallest at 400 °C. This differs from the sequence A treatment results where the highest hardness

was found at 400 °C and the lowest at 350 °C. On the basis of the TEM studies, it appears that the incubation hardness behavior of the sequence B specimens is strongly dependent on the formation and subsequent coarsening of heterogeneously nucleated S' precipitates. The initial rise in hardness observed at 300 °C can be attributed to the presence of very small, homogeneously distributed S' precipitates. Since the hardness increment curves, particularly at 300 °C and 350 °C, indirectly indicate a decreasing concentration of (Cu and Mg) in solution until "pre-aging" times of 500 s and 100 s, respectively, have been reached, solid solution hardening must also contribute during that period to the observed incubation hardness. Comparing sequence A and B final and incubation hardness curves, Figures 90 and 93, at 350 °C and 300 °C, it is seen that after a "pre-aging" time of 500 s the sequence A curves fall more rapidly to considerably lower hardness valves. This is apparently a result of the considerable stability of the S' phase in the sequence B specimens against coarsening and transformation to the S phase.

(b) T351 and T851 Conditions

The foregoing discussion of the influence of "pre-aging" on T4 microstructure and properties is directly applicable to the T351 condition. It is only necessary to include the effect on properties of an incremental increase in the dislocation density. To a first approximation, the difference between T4 and T351 properties should be constant, independent of the "pre-aging" treatment. This does not necessarily hold true for the T851 condition. The microstructure of a specimen that has been directly quenched to ice water from the solution treatment temperature and processed according to T851 specifications consists of

a uniform distribution of heterogeneously nucleated S' precipitates. To obtain this structure, it is necessary that solute be available for the nucleation and growth of the S' precipitates at dislocations during final aging. The solute may be supplied either directly from a supersaturated solid solution or by G.P.B. zones and possibly from subsequently formed homogeneously distributed S' precipitates. Because of the high rate at which G.P.B. zones form, its unlikely that much solute is supplied directly from the supersaturated solid solution.

Solute that has been consumed by the relatively stable "pre-aging" induced precipitates is no longer available for the formation of S' precipitates during subsequent aging treatments. Moreover, the "pre-aging" induced precipitates may continue to consume solute during the final aging treatment. Finally, the "pre-aging" induced precipitates, as already discussed, contribute to strength and are subject to overaging during further heat treatment and provide an additional mechanism for the loss of strength. It is therefore not surprising that the strength of specimens given a T851 treatment was actually reduced below that of the T351 condition as opposed to the properly quenched material.

VI. ULTRASONIC CHARACTERIZATION

Correlation of Ultrasonic Data with Hardness after Aging to T4, T351, and T851 Conditions

1. Introduction

The study of ultrasonic wave propagation can provide information about the elastic properties and absorption characteristics of the material in which the wave propagates. These properties are intimately related to microstructure, hence the thermomechanical treatment that the material underwent prior to the ultrasonic measurements, thus enabling a nondestructive evaluation and characterization of the materials properties.

The speed of sound in a solid is most often used in nondestructive testing as a constant programmed into an ultrasonic thickness gauge. However, in the realm of nondestructive characterization of materials, the absolute measurement of longitudinal and shear wave velocities can be used to calculate many useful material parameters, e.g., Young's modulus (E), shear modulus (G), bulk modulus (B), and Poisson's ratio (ν). The determination of these effective moduli is based on the assumption that the material is isotropic. The calculation of the moduli requires knowledge of the value for the density of the material.

The energy loss, or ultrasonic attenuation, of elastic waves propagating in a solid, may be divided into contributions from geometrical and intrinsic effects. Geometrical effects include reflection and refraction at a free surface, grain or phase boundary, beam divergence due to diffraction, as well as waveguide effects due to multiple boundary surfaces. Intrinsic effects include scattering of the ultrasonic wave at inhomogeneities, interaction with thermal phonons, dislocation damping, and conversion of sound energy to heat as a result of elastic deformation.

Unlike geometric effects, intrinsic effects may change in time if the internal crystal lattice or defect structure undergoes change. During precipitation hardening of 2024 aluminum alloy the main contribution to the attenuation is believed to be scattering of the ultrasonic wave by newly precipitating phases. The magnitude of the absorption will be determined by the magnitude of the stress field at the boundary between the precipitate and the matrix which, in turn, is determined by the precipitate size and the degree of coherency of the precipitate with the matrix (41). An attenuation peak should be observed when the size of the precipitate and associated stress field around it reach a magnitude that produces the maximal interaction with the ultrasonic wave. This value of attenuation will also depend on the wavelength of the ultrasonic wave relative to the size of the scattering center. As frequency increases, the wavelength decreases, and hence the size of an effective scattering center will also decrease.

With continuous monitoring, the relationship between aging time and change in sound velocity and ultrasonic attenuation can be determined. The information may provide an insight into the kinetics and mechanism of precipitate formation and growth in the age-hardening aluminum alloys. Several investigations (41-43) have demonstrated that the ultrasonic method is operationally feasible for monitoring the precipitation process in aluminum alloys in real time, over a wide temperature interval. The calculated activation energies and characteristic kinetic parameters could be related to the mechanism of the formation and growth of the precipitates, and their effect on the ultimate mechanical properties of the alloy. The extension of techniques for ultrasonic NDE to industrial applications requiring on-line, real-time monitoring

during thermomechanical treatment would necessitate modifications of the experimental approach for the specific technological application.

The objective of the present study was to establish the existence of a correlation between ultrasonic data and mechanical properties (e.g. hardness, yield strength) of 2024 aluminum alloy specimens after they had been subjected to carefully controlled thermomechanical treatments. For this purpose, the absolute, rather than the relative, values of the sound velocity and ultrasonic attenuation are required. The data have to be determined, consistently, to a high degree of accuracy so as to enable a comparison to be made between specimens of unknown thermal history, and to correlate these data with the ultimate mechanical properties of the material. Ideally, as an NDE technique the ultrasonic measurement should provide the necessary information in order to specify, nondestructively, the mechanical properties of the alloy.

As will be shown, a correlation between the absolute values of the sound velocity and ultrasonic attenuation, and the hardness data was found. Regardless of the thermal sequence of the aging process, maximal hardness (and strength) of the 2024 aluminum alloy was found to be related to a definite range in the values of the sound velocity. A consistent difference between the sequence A and B "pre-aging" heat treatments was revealed. Furthermore, a difference was also noted in the values of the sound velocity between the T851 and T351 tempers of 2024 aluminum alloy.

2. Experimental Procedure

A systematic ultrasonic examination was carried out on a total of about 140 specimens that underwent the variety of controlled "pre-aging"

heat treatments reported in earlier sections of this report. The samples were subjected to "pre-aging" sequences A and B, after solution treatment at 495 °C, and prior to T4 or the stretching operation that precedes the aging to T351 and T851. The specimens were flat and parallel and had the following dimensions: 150 x 25.4 x 6.35 mm (in thickness). The measurements were performed by means of conventional ultrasonic equipment (MATEC pulse generator and receiver and delta-time HEWLETT-PACKARD oscilloscope).

Specimens and ultrasonic sensors were immersed in a distilled-water tank to avoid complications caused by variations in couplant thickness. Constant separation between the transducer and the specimen surface was maintained. The specimen mounting stage was designed to allow adjustment of the parallelism between the surface of the transducer and the insonated surface of the sample. Before making velocity and attenuation measurements the ultrasonic pulse train was adjusted to obtain an exponential decay of the successive echoes combined with a maximal number of echoes in the pulse train. The pulse superposition technique was employed for sound wave velocity determination. Attenuation was monitored by means of a MATEC Automatic Attenuation Recorder which provides analog processing of the video output of the MATEC pulser/receiver.

The absolute values of the sound velocity and ultrasonic attenuation were determined to within ± 1 $m.s^{-1}$ and ± 0.02 dB, respectively, It should be pointed out, in this context, that both the precision and accuracy of velocity and attenuation determination can be markedly improved by increasing commensurately, the specimen thickness since the accuracy in velocity and attenuation depends also on the accuracy of the thickness measurement.

3. Results and Discussion

Figure 94 shows the variation of the ultimate sound velocity in 2024-T4 aluminum alloy as a function of "pre-aging" time for various "pre-aging" temperatures, between 300 and 400 °C, for both sequences A and B.

For long "pre-aging" times, exceeding 2000 min the sound velocities converge at the same value. Apparently, the "pre-aging" temperatures are sufficiently elevated to allow the operation of a diffusional process for the formation of a precipitate morphology that yields a similar average sound velocity.

Figure 94 shows that sequence A yields lower initial sound-wave velocities than sequence B. The main reason for this behavior is the fact that the sequence B samples exposed to low temperatures contain a high concentration of S' precipitates. TEM evidence for 20 s "pre-aging" at 400 °C following sequences A and B are shown in Figures 75(a) and 83(a), respectively. In the sequence A treatment, there is essentially no difference in microstructure compared with the direct quench from the solutionizing temperature. In contrast, sequence B treatment results in relatively high concentration of S' precipitates throughout the matrix (Figure 83(a)). This difference in microstructure appears to be the cause of the significant change in the initial sound-wave velocity, Figure 94.

Figure 95 exhibits the change in ultimate hardness of 2024-T4 aluminum alloy as a function of "pre-aging" time for various "pre-aging" temperatures, between 300 and 400 °C, for both A and B sequences.

"Pre-aging" at the temperatures indicated, for both sequences, reduces the ultimate hardness values determined after completion of the aging process at room temperature. In general, sequence A leads to a

greater reduction in hardness than sequence B. For long "pre-aging" times the least detrimental "pre-aging" temperature was found to be 400 °C. It can be reasoned that at 400 °C, much of the Cu and Mg is retained in solution in the aluminum matrix. When the alloy "pre-aged" at 400 °C is quenched to room temperature, conditions are quite favorable for formation of G.P.B. zones typical of natural aging. The expected microstructure is, therefore, a mixture of low temperature precipitates (G.P.B. zones) as well as some θ', S' and S that formed at 400 °C prior to aging, Figures 75(a) and 75(b).

The lowest ultimate hardness values after prolonged "pre-aging" times were obtained for the sequence A "pre-aging" treatment at 300 °C. These specimens were not exposed to room temperature before aging. Therefore, one should expect an extensive formation (by volume) of θ and S precipitates that are responsible for the drastic decrease in hardness. This line of reasoning is compatible with the observed high values in the sound velocity (Figure 94). The incoherent intermetallic solute-rich compounds θ and S have a significantly higher specific velocity than the aluminum matrix, thus contributing to a net increase in the measured sound velocity (50).

Figure 96 shows the influence of the "pre-aging" time, for various temperatures and heat treatment sequences, on the ultrasonic attenuation.

The highest attenuation value, for all "pre-aging" times, was found for sequence A and 350 °C. As was mentioned earlier, 350 °C is apparently the most efficient "pre-aging" holding temperature for the formation of the incoherent θ and S as well as of the semi-coherent S' precipitates, Figures 75(c) and 75(d). The size distribution and concentration of these precipitates is particularly conducive to an

enhanced attenuation effect obtained by ultrasonic measurements at frequencies of about 10 MHz. In addition, dislocation loops formed around precipitates, that have lost coherency with the aluminum matrix (41), interact most effectively with the propagating ultrasonic waves, thus yielding a high attenuation value. As previously noted (41) this behavior of the ultrasonic attenuation is compatible with the substantial decrease in hardness, shown in Figure 95.

The lowest absolute values as well as the smallest changes of attenuation, were observed in specimens that were "pre-aged" at 400 °C, for both A and B sequences. The behavior of the ultrasonic attenuation is in agreement with the behavior of the sound velocity and hardness (Figures 94 and 95) in the sense that at 400 °C only a small volume fraction of θ and S and S' is formed. The final fully aged microstructure for this specific "pre-aging" holding temperature consists mainly of G.P.B. zones that were formed upon subsequent aging at room temperature. These low temperature precipitates are apparently too small in size to significantly contribute to the observed ultrasonic attenuation.

For zero "pre-aging" time, the attenuation curves seem to extrapolate to a common low value. For prolonged "pre-aging" times, the attenuation values are significantly different due to the differing microstructures and size distribution of the precipitates.

Figure 97 exhibits the effect of "pre-aging" (sequence A and B) on the velocity, attenuation, hardness and electrical conductivity when specimens were held for 60 minutes at different "pre-aging" temperatures, prior to the natural aging process.

Sequence A yields a lower hardness for each of the "pre-aging" temperatures, between 300 and 400 °C. The lowest hardness values are

found at 300 and 350 °C. The reason that the B sequence yields consistently higher hardness values than A sequence is because the S' precipitates formed during sequence B "pre-aging" make an effective contribution to hardness.

The sound velocity, for both A and B sequences, exhibits a maximum for the 350 °C "pre-aging" temperature. This behavior is in agreement with the fact that at 350 °C, a substantial volume fraction of θ, S' and S is observed, Figures 82 and 83 thus contributing to the observed increase in the sound velocity. The 400 °C "pre-aging" temperature is too close to the solution temperature of 495 °C to form an appreciable volume fraction of incoherent precipitates that may contribute to an increase in the sound velocity. Therefore, the velocity values for the 400 °C "pre-aging" temperature are more typical of the low temperature precipitates (G.P. zones) formed at room temperature aging, after "pre-aging," since they constitute the major volume fraction of the precipitated phase.

The difference in the observed sound velocities between B and A sequences is consistent with the high concentration of S' precipitates that are nucleated during the quench and reheat cycle in the B sequence treatment. The nucleation process is less efficient in the A sequence.

The behavior of the ultrasonic attenuation is compatible with the behavior of the hardness. Higher attenuation values are indicative of lower hardness (Figures 98 and 99). The attenuation behavior confirms the model that at this temperature the majority of the precipitates are apparently of the semi-coherent and incoherent character surrounded by dislocation loops that strongly interact with the propagating sound

wave, thus yielding high attenuation values. The higher attenuation values of B sequence, relative to A sequence, as seen in Figure 98, may again be explained by the larger amount of low temperature precipitates that cause scattering of the ultrasonic waves.

The electrical conductivity (Fig. 97), as obtained from eddy current measurements after completion of aging, shows that A sequence treatment leads to higher electrical conductivity than the corresponding B sequence treatment. Moreover, conductivity increases, for both A and B, with increasing "pre-aging" temperature.

In section VII of this report, it will be shown that the electrical conductivity increases with the "purification" of the aluminum matrix by mean of segregation of the solute atoms (mainly Cu and Mg) and formation of solute-rich precipitates. Also, the electrical conductivity decreases by the presence of small precipitates (e.g. G.P.B. zones) that are quite effective scatterers of electrons. However, this negative contribution to the conductivity is offset by the "purification" process, particularly at temperatures where an enhanced diffusion of the solute species from the supersaturated aluminum matrix is possible.

The conductivities of A and B sequences converge at a value of about 41.0% IACS, at 400 °C "pre-aging" similar to non "preaged" 2024 Al alloy (51). This experimental observation may be explained in terms of the equal amount of Cu and Mg atoms that left the aluminum matrix. This does not necessarily imply that the microstructure of the precipitation must also be similar or identical. In fact, TEM observations (Section V) point quite to the contrary, as do sound velocity, attenuation, and hardness measurements. The effect of microstructure on the measured electrical conductivity is complex, and depends quite insignificantly on the morphology.

Figure 98 shows the influence of the "pre-aging" sequence (A and B) on the relationship between hardness and ultrasonic attenuation in T4 heat treated 2024 steel. For each sequence, separately, a good correlation was observed: high hardness is directly related with low attenuation values.

The correlation between hardness and attenuation is very important from an NDE point of view. This correlation suggests that within a limited range of thermomechanical treatments the hardness can be uniquely determined by means of ultrasonic attenuation. This correlation could be quite useful for in-process monitoring where small deviations from the norm of a well-specified thermomechanical treatment is encountered. On the cortrary, Figure 98 indicates that substantial deviations from the norm, as obtained for example for sequence A relative to B, renders such predictive capability rather difficult.

Figure 98 indicates that sequence B exhibits consistently higher hardness values, than sequence A for a given value of attenuation. Consequently, sequence B should contain a higher volume fraction of the low temperature GP zones an intermediate (S') precipitates that are known to contribute substantially to hardness and enhance the attenuation of ultrasonic waves.

Figure 99 shows hardness versus ultrasonic attenuation for 2024-T351 temper, "pre-aged" by the sequence A scheme, for various "pre-aging" temperatures between 300 and 400 °C. The observed change in hardness is between 65 and 80 HRB. The ultrasonic attenuation varies linearly and inversely with hardness. For this range of hardness (between 65 and 80 HRB) an approximately linear decrease in attenuation was also observed for 2024-T4 (Figure 98).

Figure 99, similar to Figure 98, does not differentiate between "pre-aging" times and "pre-aging" temperatures. This figure represents a strictly NDE correlation giving a qualitative change between two properties, hardness and ultrasonic attenuation. The behavior of these two properties is a consequence of differing microstructures, precipitate sizes, states of coherency etc., but the integral effect yields a linear correlation that may be utilized in qualitative NDE characterization.

Figures 100-102 depict the correlation between sound velocity and hardness for 2024 Al alloy of different tempers, namely; T4, T351, and T851.

Analogous with Figures 98 and 99, Figures 100-102 present an NDE correlation. Neither "pre-aging" times nor "pre-aging" temperatures, nor heat treatment sequences are specified. This emphasizes the potency of the correlation between sound-wave velocity and hardness of the completely aged alloy. The correlation (Figures 100-102) is parabolic, where the maximal hardness (or yield strength) is attained for a narrow window of sound-wave velocities. When maximal strength is required, the NDE technique employing ultrasonic sound velocity measurements would probe and monitor for a definite predetermined range of sound-wave velocities. The absolute values of these velocities may change slightly with the selected temper or state of plastic deformation prior to aging. Plastic deformation prior to aging (e.g. T351 compared with T4 temper) increases the absolute value of the ultimate sound velocity, at the peak hardness, 6369 versus 6363 $m.s^{-1}$, respectively. Larger volume fractions of precipitated phases will also contribute to an increase in the absolute value of the sound velocity.

VII. EDDY-CURRENT CONDUCTIVITY VERSUS HARDNESS DURING AGING

1. Introduction

The kinetics and mechanism of the precipitation hardening process in pseudo-binary aluminum alloys has been extensively investigated (43). A discussion of the nature of the nucleation and growth of precipitates in binary aluminum alloys was developed by Lorimer and Nicholson (44). However, relatively little work has been reported on studies involving nondestructive characterization of the technologically important 2024 aluminum alloy during the aging process. This alloy acquires high strength and hardness when subjected to controlled thermo-mechanical treatments involving natural or artificial age hardening.

Electrical conductivity measurements, employing a.c., d.c., and eddy currents are often utilized to determine the kinetic behavior of the precipitation process, or to evaluate nondestructively the progress of the age hardening sequence (46-48). The variation of electrical conductivity as a function of aging is complex and results from a number of factors (49), a major contribution is associated with changes in the scattering of conduction electrons. Such scattering can be caused by:

a. vacancies quenched-in during rapid cooling following solution heat treatment
b. alloying atoms present in the matrix
c. G.P. zones with dimensions comparable with the electron wavelength
d. coherency strains and dislocations at boundaries of the zones or clusters.

During aging at lo temperatures, as for example, below 50 °C, two competing processes are operative. There is a decrease in the number of quenched-in vacancies, and a clustering of Cu and Mg, which are the major additions to Al in the 2024 alloy. These processes tend to increase the measured electrical conductivity but simultaneously there is a more significant decrease in the electrical conductivity due to the appearance of newly formed precipitates which are small enough to be effective as scatterers of electrons. At higher temperatures, precipitates of larger size are formed, which are not as effective scatterers resulting in an increase of conductivity to an ultimate value determined by the solubility of impurity atoms at the specific aging temperature. The absolute value of electrical conductivity achieved after any given aging time is dependent on the aging temperature due to the fact that the geometry and size distribution, and type of the precipitates are governed by a thermally-activated process (35).

Addition of trace elements to the Al-Cu-Mg system may have a profound effect on the kinetics and mechanism of the precipitation process. Some elements may suppress one stage of the aging process while stimulating another. At low aging temperatures, zone formation may be retarded, apparently due to a strong vacancy-trace element interaction which prevents vacancies from enhancing the diffusion of Cu atoms in the α-Al matrix. At higher aging temperatures these elements may accelerate the formation of intermediate precipitates (θ', S') by reducing interfacial energies.

The influence of precipitation kinetics on eddy-current conductivity and hardness during the aging of 2024 aluminum alloy was investigated by means of dynamic eddy-current conductivity measurements. Aging

temperatures between 21 and 190 °C were used, and measurements were made on both unstretched and plastically deformed samples (three percent permanent strain). The two measurement techniques, electrical conductivity and hardness, respond in a complementary manner to the varying microstructures that form during different stages of the aging process.

2. Experimental Procedure

The specimens used in this investigation were prepared from the 0.635 cm thick 2024 aluminum alloy plate supplied in the F condition. Results of the chemical analysis were given in an earlier section.

Prior to the thermomechanical treatment, the specimens were machined into rectangular bars 170 x 25.4 x 6.35 mm. Solution heat treatment at 495 °C for 75 minutes was followed by ice-water quenching. The specimens were then stored in liquid nitrogen to protect them against changes in microstructure. Hardness measurements, carried out at subzero temperatures, before and after storage, verified no natural aging had occurred during storage.

Some of the specimens were plastically deformed to 3 percent elongation in a tensile testing machine. This stretching process was used to simulate the T351 and T851 tempers. The stretching was performed while the specimens were kept at subzero temperatures in order to avoid natural aging during the plastic deformation procedure.

The specimens were then aged in a thermostatic bath containing heated oil kept in continuous circulation. The bath could be maintained within 0.05 °C at any temperature between ambient and 200 °C.

Electrical conductivity measurements were performed on the specimens by means of SUPERHALEC (England) and VERIMET (USA) eddy current monitors and probes.

Each eddy-current conductivity measurement was preceded and followed by calibration of the eddy current monitors against NBS secondary standards. These standards are calibrated at 20 °C; hence all reported conductivity values herein refer to the conductivity value at 20 °C. The measured values were considered accurate to within ± 0.05 percent IACS[9].

Hardness measurements were made using a WILSON hardness tester. The precision of the hardness values on the Rockwell B scale was approximately ± 1 units.

Room temperature measurements of hardness were made at prescribed intervals throughout the aging treatment. The specimens were removed from the isothermal bath, cooled rapidly to room temperature, and subjected to electrical conductivity and hardness measurements. Whenever necessary due to the time delays in making a measurement, the specimens were temporarily stored in liquid nitrogen.

3. Experimental Results

Figure 103 shows the variation of the electrical conductivity as a function of aging time of 2024 aluminum alloy at different isothermal holding temperatures. This series of specimens did not undergo plastic deformation (stretching) prior to aging. The value of electrical conductivity, before aging, was found to be 31.5% IACS. The salient features in Figure 103 are:

a. An initial decrease in conductivity at each of the isothermal aging temperatures in the range between 21 and 190 °C. The rate of initial decrease in conductivity depends on the aging

---

9 International Annealed Copper Standard

temperature, increasing with increased aging temperature. In the temperature range between 150 and 190 °C, the rate of initial decrease in conductivity is relatively large and virtually identical within this set.

b. A sigmoidal decrease in conductivity with aging time was observed for the 21, 35, and 50 °C isotherms. For these aging temperatures, the ultimate value of the fully aged alloy was found to be 29.5% IACS.

c. In contrast to the variation of electrical conductivity as a function of aging time at low temperature (below 50 °C), the conductivity above 150 °C increases with increasing isothermal aging temperature, after the initial decrease during the first five minutes of the aging process. The change in conductivity with aging time is extremely sluggish at 150 °C, exhibiting a nearly constant value for about 30 hours of aging.

d. For unstretched specimens aged at 170, 180, and 190 °C, the most pronounced rate of increase in electrical conductivity occurs at the highest aging temperature. The ultimate value of the electrical conductivity, ~ 40% IACS, was attained after about 50 hours at 190 °C, and after somewhat longer times at the lower isothermal holding temperatures.

Figure 104 exhibits the variation of hardness as a function of aging time for the unstretched specimens at aging temperatures within the range of 150 and 190 °C. In general, the rate of increase of hardness with aging time increases as aging temperature increases. Overaging was observed at aging temperatures of 180 and 190 °C, in the former case occurring at about 1,000 min and at approximately half that

value at the higher temperature. With decreasing aging temperatures, the peak value of hardness increases, and occurs after a longer aging time.

Figures 105 and 106 compare the variation of hardness and electrical conductivity of unstretched and stretched specimens at 190 °C (Figure 105) and 150 °C (Figure 106). The initial hardness of the stretched specimens is higher by about 5 units of the Rockwell B scale. The change in hardness with aging time is quite similar for both sets, and the initial difference in hardness is essentially preserved. In Figure 105, the stretched specimens show the same response to overaging as the unstretched ones.

The initial electrical conductivity, before aging, of the 3 percent stretched specimens is lower by about 0.4% IACS than that of the unstretched specimens. However, at 190 °C, (Figure 105), the rate of change of conductivity with aging time after about 100 hours is higher in the stretched specimens but the two curves begin to converge after an aging period of about 100 hours.

At 150 °C (Figure 106), the initial shape of the conductivity curves for stretched and unstretched specimens is in general accord with the curves shown in Figure 105, but at the lower temperature the electrical conductivity values remain about the same over an aging span of 1000 minutes.

The hardness values, before aging of the 3 percent stretched and unstretched specimens, were 60 and 55 units on the Rockwell B scale, respectively. Thus, while higher initial values for hardness were obtained on stretched specimens prior to aging, as compared to unstretched specimens, the opposite relationship was observed in electrical conductivity measurements. Table VII gives the hardness values

attained after aging at different temperatures. It should be noted that continuous aging, somewhat beyond 6 hours, at temperatures of 150, 170, and 180 °C yielded higher values than those tabulated. After 16 hours of aging at 150, 170, and 180 °C, the average hardnesss values of the unstretched specimens were found to be 76, 78.5, and 82 HRB, respectively, indicating an increasing trend in hardness values with time. However, after 30 hours of aging, well beyond the overaging point on the 180 and 190 °C isotherms, the hardness values for the unstretched specimens aged at 150, 170, 180, and 190 °C were found to be 79, 80, 77, and 71 HRB, respectively. The increased values at 150 and 170 °C reveal that overaging has not yet set in at these temperatures in the specified time period. Furthermore, it is noteworthy that the overaging phenomenon at 180 and 190 °C present on the hardness isotherms was not at all apparent in the electrical conductivity.

4. Discussion

The initial decrease in conductivity of the alloy, during the first few minutes of the aging process at all isothermal holding temperatures between 21 and 190 °C (Figure 103) is apparently due to the formation of G.P.B. zones. The kinetics of their formation is governed by the mobility of Cu and Mg atoms which may be enhanced by the presence of quenched-in vacancies. The interaction is particularly strong with Mg atoms (47). Under favorable nucleation conditions, these zones rapidly nucleate in a homogeneous fashion throughout the lattice. The formation of zones is a thermally activated process; therefore, their rate of formation increases with increasing temperature and the hardness of the lattice increases accordingly (48). However the zones rapidly formed at temperatures above 100 °C cannot persist in the presence of

more stable precipitates (35). Consequently, they dissolve back into the matrix by a diffusional process or become nuclei for the formation of intermediate, semi-coherent, precipitates of well-defined crystallographic identity.

The initial decrease in the electrical conductivity of the alloy is due mainly to the appearance of zones which are effective scatterers of electrons. The zone formation process segregates the Cu and Mg atoms, as well as the frozen-in vacancies, thus purifying the aluminum matrix of potential scatterers of electrons. However, the purification achieved by the formation of zones is not sufficient to compensate for the opposite effect, namely the effective scattering of electrons by zones. This very mechanism continues to operate at 21, 35, and 50 °C (Figure 103) thus contributing to the decrease in measured electrical conductivity. The sigmoidal behavior is suggestive of a thermally activated process. The logarithmic aging-time dependence of the conductivity is qualitatively similar to the kinetics in other ternary aluminum alloys (35), except for the absence of a conductivity minimum in 2024 aluminum alloy. The minimum is generally related to the appearance of critical-size precipitates (44). Noteworthy is the fact that the sigmoids (Figure 103) for 21, 35, and 50 °C achieve an identical electrical conductivity value at long times. From the isothermal reaction kinetics, using these three isotherms, the activation energy of the process can be calculated. The time to achieve 50 percent of the aging process is indicated by the intersection of the tangent and each sigmoid curve at the inflection point. In this manner, the aging time for 50 percent reaction at 21, 35, and 50 °C, are 135, 25, and 7.5 minutes, respectively. Plotting 1000/T, where T is the absolute temperature of

these isotherms, as a function of the aging times for 50 percent reaction, yields a straight line whose slope is proportional to an activation energy for the diffusional process governing the kinetics of formation of both G.P. and G.P.B. zones in 2024 aluminum alloy at relatively low temperatures. The activation energy obtained by this procedure is 20 kcal/mol. Formation of both zones requires the simultaneous transport of Cu and Mg atoms as Cu-Mg-vacancy groups by a reshuffling process (47).

At temperatures above 100 °C, intermediate precipitates, rather than zones, begin to appear with the approximate composition $CuMgAl_2$. They are predominantly S' with S along the grain boundaries, Figure 75. The precipitation process of the S' particles is thermally activated. The process is rather sluggish at 150 °C (Figure 103). Since the hardness increases at 150 °C, though more slowly than at the higher temperatures, (Figure 104) it is conjectured that the contribution to hardness is due to G.P.B. zones, rather than nucleation and growth of S'. As aging temperature increases, the rate of increase in both conductivity and hardness increases in accordance with the rate of formation of S' particles. The conductivity at 180 and 190 °C levels off (not shown in Figure 103) at a value of about 40% IACS. This asymptotic value was achieved after isothermal holding for 60 hours at 180 °C. Hardness, Figure 104, increases at a higher rate as aging temperature increases. However, the 190 and 180 °C isotherms reveal overaging after 5.5 and 16 hours of aging, respectively.

The increase in electrical conductivity, after the initial decrease, at aging above 150 °C, can be explained in terms of purification of the aluminum matrix. Above 150 °C, G.P.B. zones desolve while S' and S

precipitates nucleate and grow. In contrast to zones, the relatively large particles, S' and S precipitates, scatter electrons to a lesser degree. The net effect is an increase in conductivity.

Plastic deformation, induced by stretching the 2024 aluminum alloy prior to age hardening, is meant to have a beneficial effect on the ultimate mechanical properties. The stretching deformation induces a high dislocation density, homogeneously distributed. Consequently, nucleation of S' precipitates can be controlled and made predominantly homogeneous as was demonstrated in the TEM studies. Figures 105 and 106 show the effect of plastic deformation on hardness and electrical conductivity of 2024 aluminum alloy aged at 190 and 150 °C, respectively. The additional hardness of the stretched specimens, about 5 units on the Rockwell B scale, is preserved during the entire precipitation hardening process. This indicates that the dislocations are retained during the aging process. As expected, the increased population of dislocations in the lattice of the stretched specimens causes the initial conductivity to be lower than in the unstretched ones. The dislocations in the stretched matrix provide nucleation sites for S' precipitates, thus enhancing the precipitation process. Figure 105 depicts this behavior where it is seen that the curve for electrical conductivity for the stretched specimen crosses over the curve for the unstretched specimen at a time period of less than 100 minutes.

The results of the present study illustrate that in 2024 aluminum alloy a given property, such as hardness, can be associated with a wide range of eddy current conductivities in the final aged condition. The differing conductivities are a reflection of differences in the microstructure of the material. Hence, a single nondestructive measurement,

Page intentionally left blank

VIII. HEAT FLOW-PROPERTY PREDICTIONS

A heat flow model developed earlier for 2219 aluminum alloy (1) was used here to calculate almost all conceivable heat flow conditions anticipated during the quench of 2024 aluminum alloy plates from the solutionizing temperature of 495 °C. The calculated time-temperature data was then coupled to the C-curves established in section IV. The variations in properties across different thickness plates for the worst and the best heat flow conditions were thus predicted.

1. Heat Flow Model

The heat flow calculations carried out for the various "pre-aging" treatments during cooling of a flat plate from an initial temperature of T_o were identical to those previously described (1). They included the following:

(a) Asymmetric cooling of plates, where heat is withdrawn from only the top surface for all times.

(b) Symmetric cooling of plates from both top and bottom followed by an abrupt variation in the heat transfer coefficient on the bottom surface of the plate, at different times.

Time-temperature data from the computer program was then combined with equations (3) to (5) for the determination of C-curves using the values of the constants reported in Table V. The numerical procedure for the determination of a given property, e.g., yield strength, was as follows. Equation (4) is integrated, using the calculated time-temperature data and equation (5) for a given position in the plate, and the quantity $K_{1\chi}\tau_\chi$ is determined. Using the values of σ_m and σ_o from Table V, the value of σ, in this case yield strength, is established. These computations are carried out numerically and simultaneously with the heat flow calculations.

Finally, for a given sequence (A or B) and a given heat treatment, the values of the constants K_3, K_4 and K_5 are identical for all properties in question, while σ_m, σ_o and K_2 differ according to Table V. Under these conditions, it follows from equations (3) to (5) that the quantity $K_2 \ln[(\sigma-\sigma_o)/(\sigma_m-\sigma_o)]$ remains the same for all properties, e.g. hardness, tensile strength, and conductivity, for a given sequence. Thus, from the yield strength results one can readily obtain all the other properties without further heat flow calculations.

The thermophysical properties used in the calculations were:

Initial temperature T_o = 495 °C

Water temperature T_f = 40 °C

Thermal conductivity k = 1.2 W/cm K

Thermal diffusivity α = 0.5 cm^2/s

Heat transfer coefficient[10] h = 0.8 W/cm^2K

It was found that minimum strength properties predicted were always at locations near the bottom surface (where quench interruptions were induced) for the cooling conditions described under (b) above. The data for the worst properties (e.g. lowest yield strength), were established using a computer model and the trial and error methodology described earlier (1).

The predicted "worst possible case" yield strength data for both "pre-aged" sequences in the T351 and T851 conditions are plotted versus plate thickness in Figure 107. Noted on the same plot are the ASTM B209 specifications (which are the same as those given in Military

---

[10] As before (1), this heat transfer coefficient was deduced from simulation of temperature-time data on the computer and comparison of same with actual data obtained in laboratory and commercial practice. This value approximates the normal condition during water quench from the solution heat treatment temperature.

Specifications QQ-A-250/4E and QQ-A-250/29A) for 2024 and 2124 aluminum alloys, respectively. The 2124 specifications are listed because the iron and silicon contents of the 0.635 cm (1/4 in.) thick plate, 0.27 wt.% Fe and 0.11 wt.% Si, are within the 2124 composition specification. The minimum specification for yield strength in the T351 condition is quite low and is not available for the 2124 alloy in the T351 condition or for the complete range of plate thicknesses (up to 6 inches) considered. The predictions show that under the "worst" heat flow conditions, the T851 plates subjected to a sequence B "pre-aging" treatment suffer significant deterioration in yield strength. T851 plates as thin as 1.2 cm (1/2 in.) thick can fall out of specification. This behavior might be expected when one considers the relative location of the "nose" of the C-curves in Figures 30 and 34. Unlike the T851, the minimum yield strengths for the T351 do not differ significantly for the A and B sequences. It should be noted, however, that the precision of the T351 predictions (compare the least squares deviations shown in Table V) is less than the precision of the T851 predictions so that the T351 results are less reliable than the T851 results.

Figure 108 is similar to Figure 107 except that the "worst possible case" ultimate tensile strength is shown as a function of plate thickness. It is seen that the T351B curve can be slightly below the minimum specification for 2024-T351. Thus a plate of T351 might, according to Figure 107, meet the yield strength specification yet fail the ultimate tensile strength specification. As for the yield strength, T851 plates as thin as 1.2 cm (1/2 in.) can fall out of specification for the "worst case" of one-sided quench water flow interruption considered here.

In Figures 109 and 110, the "worst case" hardness and eddy-current conductivity respectively, are plotted as a function of plate thickness. Typical minimum hardness and allowable eddy-current conductivity ranges from current industrial practice are indicated on these two plots. It can be seen that, for the T351 temper, these results predict that for thin plates the hardness and conductivity fall out of range while the yield strength and ultimate tensile strength are within specification.

IX. CONCLUSIONS

1. As-received plate

1.1 A 15.24 cm (6 inch) thick 2024-T851 aluminum plate was found to contain moderate variations in composition, hardness and eddy-current conductivity across its thickness. Macrosegregation present in the original ingot is responsible for the composition variations. The variations in hardness are mainly due to changes in cooling rate across the plate during the quench from solution heat treatment and are probably influenced to some extent by inhomogeneous mechanical deformation during processing.

2. Solidification-Segregation Studies

2.1 The phases present in cast 2024 aluminum alloy due to solidification-microsegregation, determined by metallography, electron diffraction and x-ray energy dispersive spectroscopy, were α-Al solid solution, Θ-$CuAl_2$, S-$CuMgAl_2$, Cu_2FeAl_7, Mg_2Si, and α-Al(Fe,M)Si where M in this case designates Cu and Mn. The formation of the latter two phases is a function of alloy composition and it is favored by higher cooling rates during solidification.

2.2 Macrosegregation of copper and other alloying additions in DC cast ingots of 2024 aluminum alloy cannot be completely eliminated by chill face scalping and subsequent thermomechanical treatment. Macrosegregation does remain in the finished plate product. However, good scalping practice should maintain compositions to within specified limits for 2024 with no deterioration in mechanical properties.

2.3 Positive and negative macrosegregation was obtained in a unidirectionally cast ingot. The negative segregation was intentionally introduced by an abrupt cross-section change in the ingot which resulted in excessive flow of segregated interdendritic liquid.

2.4 Eddy-current conductivity of cast 2024 aluminum alloy is approximately inversely related to copper content in a complex manner. This fact complicates the relationship of conductivity to mechanical properties used for nondestructive evaluation of the finished plate product.

2.5 Because of large copper content variation near the chill face of DC cast ingots, surface hardness and eddy-current conductivity measurements may be very sensitive tc scalping depth in their ability to evaluate the condition of finished alloy plate.

2.6 Based on a limited number of samples obtained from the laboratory cast ingot designed to cause macrosegregation, the hardness of properly heat treated 2024-T851 is below specification when the average composition is below 3.1 wt.%Cu and 1.1 wt.%Mg.

3. C-Curves and Nondestructive Evaluation

3.1 The C-curves developed in this report provide a good description of the effect of time-temperature quench history on the mechanical and NDE properties of 2024-T351 and 2024-T851.

3.2 Eddy-current conductivity alone cannot be used as a reliable predictor of the mechanical properties of 2024-T351 or 2024-T851. It must be combined with other information such as

hardness and yield strength measurements on the same lot (same ingot or plate) of material.

3.3 For any given thermomechanical treatment of 2024 aluminum alloy, there will be a large amount of scatter in the final mechanical properties and NDE measurements, both within a given lot of material and between different lots of materials. This scatter is much greater for 2024-T351 than for 2024-T851.

3.4 Comparison of the C-curves for 2024-T351, 2024-T851, and 2219-T87* shows that: (1) 2024-T851 is more quench sensitive than 2024-T351, (2) 2024-T851 is more sensitive to a B-sequence quench (i.e. "pre-aging" with reheating of the material) than to an A-sequence quench (i.e. one in which no reheating occurs), and (3) both tempers of 2024 are more quench sensitive than 2219-T87*.

4. TEM Studies: Relationship Between Microstructure and Properties

4.1 Constituent phase particles in the 0.635 cm thick 2024 aluminum alloy plate, in agreement with other investigations, consist of two types; large particles > 1 μm in size retained from the cast structure and small dispersoid particles < 1 μm.

4.2 The majority of the large particles retained from the cast structure were found to be the cubic phase α-Al(FeCuMn)Si. Other constituent phase particles would probably be present in 2024 aluminum alloy plate material having a composition different from that studied here.

4.3 Dispersoid particles are not present in the as-cast ingot and are formed during thermomechanical processing treatments subsequent to casting. These particles were determined by

means of electron diffraction and energy dispersive x-ray analysis to be the orthorhombic phase $Cu_2Mn_3Al_{20}$. They are insoluble at the solution treatment temperature of 495 °C.

4.4 Quenching from the solution heat treatment temperature (495 °C) and holding at an intermediate temperature above approximately 300 °C (sequence A "pre-aging" treatment) results in the heterogeneous nucleation and growth of θ-$CuAl_2$, S-$CuMgAl_2$ and S' phases at dispersoid particles and S-$CuMgAl_2$ precipitates at grain boundaries.

4.5 An ice water quench from the solution heat treatment temperature followed by aging at a temperature between 300 °C and 495 °C (sequence B "pre-aging" treatment) leads to the formation of the S' phase heterogeneously nucleated at dispersoid particles and dislocations and S phase precipitates at grain boundaries.

4.6 Prolonged "pre-aging" results in the disappearance of all phases initially induced by "pre-aging" with the exception of S-$CuMgAl_2$ which was apparently the equilibrium phase in the 2024 aluminum alloy plate studied.

4.7 Precipitate phases formed during "pre-aging" or alternatively as a result of an abnormal or slow quench from solution heat treatment consume Cu and Mg solute, required during final aging for the development of zones and precipitates, resulting in the degradation of properties.

4.8 C-curves which indicate the degradation of properties due to an abnormal quench are also a measure of the amount and type of second phase constituents formed during quenching.

5. Ultrasonic Characterization

5.1 A parabolic relationship was found between hardness and sound wave velocity in 2024 aluminum alloy for T4, T351, and T851 tempers. Maximum hardness (or yield strength) values are related to an intermediate, well determined, range of values of sound velocity for each temper.

5.2 Ultrasonic attenuation decreases as hardness increases. A linear relationship was found for the range of hardness values between 60 and 80 HRB.

5.3 "Pre-aging" at 350 °C for 60 minutes yields the greatest reduction in hardness, and corresponding maxima in sound velocity and ultrasonic attenuation.

6. Eddy-Current Conductivity vs Hardness During Aging

6.1 Eddy-current conductivity and hardness measurements during aging of 2024 aluminum alloy show that the two measurements are not a single valued function of one another.

7. Heat Flow--Property Predictions

7.1 Yield strength, tensile strength, hardness, and eddy-current conductivity for 2024-T351 and 2024-T851 were calculated from the appropriate C-curves for interrupted (abnormal) cooling, in which the heat transfer coefficient at the bottom plate surface changes from the same value as at the top surface to a zero value. The "worst case" properties occur near the bottom surface of the plate. These calculations are subject to the uncertainties found in the determination of the C-curve parameters.

7.2 For the T851 alloy sequence B "pre-aging" treatment gives considerably poorer "worst case" properties than sequence A for all properties (yield strength, tensile strength, hardness, and eddy-current conductivity). For example, for a 5.08 cm (.) thick plate, T851-sequence A has a "worst case" yield s . . h of 58.4 ksi compared with 38.4 ksi for the sequence B "pre-aging" treatment. Under the "worst" heat flow conditions, T851 plates subjected to sequence B "pre-aging" treatment suffer significant deterioration in properties and fall below ASTM specifications.

7.3 For the T351 alloy, there is little difference in yield strength, tensile strength, and hardness between sequence A and B "pre-aging" treatments. The sequence B "pre-aging" treatment gives higher values of the "worst case" conductivity. Even the "worst case" yield strength lies above minimum specifications and the "worst case" tensile strength lies above or only slightly below the minimum specifications.

REFERENCES

1. L. Swartzendruber, W. Boettinger, L. Ives, S. Coriell, D. Ballard, D. Laughlin, R. Clough, F. Biancaniello, P. Blau, J. Cahn, R. Mehrabian, G. Free, H. Berger and L. Mordfin, NBS: Nondestructive Evaluation of Nonuniformities in 2219 Aluminum Alloy Plate - Relationship to Process ng, NBSIR 80-2069, December 1980.

2. M. C. Flemings, Solidification Processing, McGraw-Hill, New York, (1974).

3. P. R. Sperry, Trans. ASM, 48, p. 904 (1965).

4. G. Phragmen, J. Inst. Metals, 77, p. 489 (1950).

5. A. Munitz, A. Zangvil and M. Metzger, Met. Trans. A, 11A, p. 1863 (1980).

6. R. Mehrabian and M. C. Flemings, Met. Trans., 1, p. 455 (1970).

7. W. L. Fink and L. A. Willey, Trans. AIME, 175, p. 414 (1948).

8. J. W. Cahn, Acta Met., 4, p. 572 (1956).

9. J. T. Staley, Ind. Heating, 44, p. 6 (1977).

10. J. W. Evancho and J. T. Staley, Met. Trans., 1, p. 455 (1970).

11. J. W. Cahn, Acta Met., 4, p. 449 (1956).

12. G. J. Petrak and A. W. Gunderson, AFWAL-TR-81-4032, Materials Laboratory, Air Force Wright Aeronautical Laboratories, Air Force Systems Command, Wright-Patterson AFB, Ohio 45433, July 1981.

13. J. M. Silcox, J. Inst. Metals, 89, p. 203 (1960-61).

14. M. N. Thompson, P. Doig, J. W. Edington and P. E. J. Flewitt, Phil. Mag., 35, p. 1537 (1977).

15. M. S. Hunter, G. P. Frank, Jr. and D. L. Robinson, Proc. of Second International Congress on Metallic Corrosion, New York, March 11-15, 1963, NACE, p. 102.

16. M. O. Speidel and M. V. Hyatt, Advances in Corrosion Science and Technology, 2, Chapter 3, M. G. Fontana and R. W. Staele, eds., Plenum Press, New York, (1972).

17. M. S. Hunter, A. M. Montgomery and G. W. Wilcox, Aluminum, 1, Chapter 3, ASM, (1967).

18. D. L. Robinson and M. S. Hunter, Met. Trans., 3, p. 1147 (1972).

19. R. E. Stoltz and R. M. Pelloux, Met. Trans. A, 7A, p. 1295 (1976).

20. J. G. Kaufman and J. R. Low, Jr., Proc. of the Second International Conf. on Mech. Behavior of Materials, Special Volume, N. Promisel and V. Weiss, es., ASM, p. 415 (1976).

21. R. H. VanStone, R. H. Merchant and J. R. Low, Jr., Fatigue and Fracture Toughness - Cryogenic Behavior, ASTM STP 556, p. 93 (1974).

22. H. G. Petri, Aluminum-Archiv, 14 (1938).

23. M. K. B. Day and H. W. L. Phillips, J. Inst. Metals, 74, p. 33 (1948).

24. A. Chitty, J. Inst. Metals, 86, p. 65 (1957-58).

25. W. Hofmann, Z. Metallkunde, 41, p. 477 (1950).

26. K. Robinson, Phil. Mag., 43, p. 775 (1952).

27. R. B. Nicholson and J. Nutting, Phil. Mag., 3, p. 531 (1958).

28. R. N. Wilson, D. M. Moore and P. J. E. Forsyth, J. Inst. Metals, 95, p. 177 (1967).

29. M. O. Speidel, Proc. of Conf. on Fundamental Aspects of Stress Corrosion Cracking, Ohio State University, NACE, p. 561 (1969).

30. G. Lutjering, H. Doker and D. Munz, Proc. of Third Intl. Conf. on Strength of Metals and Alloys, Cambridge, England, p. 427 (1973).

31. P. B. Hirsch, A. Howie, R. B. Nicholson, D. W. Pashley and M. J. Whelan, Electron Microscopy of Thin Crysta s, Butterworths, London, (1975).

32. G. Thomas and M. J. Whelan, Phil. Mag., 4, p. 511 (1959).

33. W. A. Anderson, Precipitation from Solid Solution, ASM, p. 150 (1959

34. H. K. Hardy, J. Inst. Metals, 83, p. 17 (1954-55).

35. G. W. Lorimer, Precipitation Processes in Solids, K. C. Russell and H. I. Aaronson, eds., Met. Soc. AIME, p. 87 (1976).

36. H. Y. Hunsicker, Aluminum, 1, Chapter 5, ASM, (1967).

37. R. H. Beton and E. C. Rollason, J. Inst. Metals, 86, p. 77 (1957-58).

38. L. F. Mondolfo, Aluminum Alloys: Structure and Properties, Butterworths, London, p. 70 (1976).

39. Metallorgraphy, Structures and Phase Diagrams, Metals Handbook, 8, 8th Ed., ASM, p. 386 (1973).

40. M. Rosen, S. Fick, R. Reno, E. Horowitz and R. Mehrabian, Matls. Sci. Eng., 53, p. 163 (1982).

41. M. Rosen, C. L. Friant, S. Fick and E. Horowitz, NDE of the Precipitation Hardening Process in 2024 Aluminum Alloy, Part 2, The Johns Hopkins University Center for Materials Research Report CMR-NDE2 (Nov. 1981).

42. Y. Gefen, M. Rosen and A. Rosen, Matls. Sci. Engr., 8, p. 246 (1971).

43. A. Kelly and R. B. Nicholson, Prog. Mater. Sci., 10, p. 149 (1963).

44. G. W. Lorimer and R. B. Nicholson, The Mechanism of Phase Transformations in Crystalline Solids, Monograph No. 33, Inst. of Metals, London, p. 36 (1969).

45. D. Turnbull, M. S. Rosenbaum and H. N. Treaftis, Acta Met., 8, p. 277 (1960).

46. K. M. Entwistle, J. H. Fall and K. I. Koo, J. Inst. Metals, 91, p. 84 (1962-63).

47. Y. Gefen, M. Rosen and A. Rosen, Mater. Sci. Engr., 8, p. 181 (1971).

48. P. L. Rossiter and P. Wells, Phil. Mag., 24, p. 425 (1971).

49. G. Panseri and T. Federighi, Acta Met., 8, p. 217 (1960).

50. Y. C. Waung, D. E. Beskos and W. Sachse, J. Mater. Sci., 10 p. 109 (1975).

51. M. Rosen, E. Horowitz, L. Swartzendruber, S. Fick and R. Mehrabian, Mater. Sci. Engr., 53, p. 191 (1982).

TABLE I

Equilibrium Partition Coefficients for Solidification of Primary α-Aluminum Phase

	k_i^{α}
Al-Cu	0.17
Al-Mg	0.30
Al-Mn	0.95
Al-Fe	0.02
Al-Si	0.13

TABLE II

Solidification "Path" for Al-Cu-Mg-Mn-Fe-Si

f_s	wt% Cu	wt% Mg	wt% Mn	wt% Fe	wt% Si
0.0	4.00	1.40	0.65	0.20	0.10
0.1	4.36	1.51	0.65	0.22	0.10
0.2	4.80	1.64	0.66	0.25	0.12
0.3	5.36	1.79	0.66	0.27	0.14
0.4	6.12	2.00	0.67	0.33	0.16
0.5	7.12	2.27	0.68	0.39	0.28
0.6	8.52	2.66	0.68	0.49	0.22
0.7	10.8	3.25	0.69	0.65	0.30
0.8	15.2	4.33	0.70	0.97	0.40
0.85	19.3	5.28	0.72	1.28	0.52
0.90	27.0	7.01	0.73	1.91	0.74
0.91	29.3	7.55	0.73	2.12	0.81

TABLE III

Phases Identified in As-Cast 2024 Aluminum Alloy Ingots by Sperry (3)

α-Al	Face Centered Cubic
Mg_2Si	Cubic
$CuAl_2$	Tetragonal
$CuMgAl_2$	Orthorhombic
$MnAl_6$	Orthorhombic
$FeAl_3$	Orthorhombic
α-Al(Fe,Mn)Si	Body Centered Cubic
Cu_2FeAl_7	Tetragonal

TABLE IV

Data for sequence A and sequence B heat treatments are used to determine C-curves for 2024-T851 and 2024-T351 in this report. The range between the solution heat treatment temperature (495°C) and 110°C was divided into intervals. First given is the list of the bracketing temperatures for these intervals. Next, sample numbers are given followed, on the same line, by the Rockwell B hardness, the conductivity in % IACS, the yield strength (0.2% offset) in ksi, the ultimate tensile strength in ksi, the % elongation and the % reduction in area, respectively for the fully processed alloy. For each sample, the following four lines give a list of times, in seconds (± 0.1 second), spent between each of the temperatures listed, respectively. For sequence A alloys, the cooling cycle from the solution heat treatment temperature was performed by a direct transfer from the solution heat treatment furnace to a salt bath and then to an ice water quench. For sequence B alloys, a quench into ice water from the solution heat treatment temperature was followed by an immediate transfer to a salt bath at elevated temperature and then by another ice water quench.

2024-T851 SEQUENCE A

TEMP RANGES

10	488.5	485.0	473.0	461.5	450.0	438.0	426.0	414.0	402.5	390.5
10	378.0	367.5	355.0	343.0	331.0	319.0	307.0	295.0	283.0	270.5
10	258.5	246.5	234.0	221.5	209.0	197.0	184.0	172.0	159.0	147.0
3	134.0	122.0	110.0							

END

1000	83.2	38.4	.0	.0	.0	.0				
	.0	.0	.0	.0	.0	.0	.0	.0	.0	.0
	.0	.0	.0	.0	.0	.0	.0	.0	.0	.0
	.0	.0	.0	.0	.0	.0	.0	.0	.0	.0
1010	86.1	38.2	69.3	78.5	13.0	23.0				
	.0	.0	.0	.0	.0	.0	.0	.0	.0	.0
	.0	.0	.0	.0	.0	.0	.0	.0	.0	.0
	.0	.0	.0	.0	.0	.0	.0	.0	.0	.0
1011	81.7	38.4	.0	.0	.0	.0				
	.0	.0	.0	.0	.0	.0	.0	.0	.0	.0
	.0	.0	.0	.0	.0	.0	.0	.0	.0	.0
	.0	.0	.0	.0	.0	.0	.0	.0	.0	.0
1012	84.9	38.2	68.1	71.9	12.0	22.0				
	.0	.0	.0	.0	.0	.0	.0	.0	.0	.0
	.0	.0	.0	.0	.0	.0	.0	.0	.0	.0
	.0	.0	.0	.0	.0	.0	.0	.0	.0	.0
1013	83.9	38.7	67.9	72.8	13.0	24.0				
	.0	.0	.0	.0	.0	.0	.0	.0	.0	.0
	.0	.0	.0	.0	.0	.0	.0	.0	.0	.0
	.0	.0	.0	.0	.0	.0	.0	.0	.0	.0
1016	85.0	38.2	68.6	71.9	11.0	22.0				
	.0	.0	.0	.0	.0	.0	.0	.0	.0	.0
	.0	.0	.0	.0	.0	.0	.0	.0	.0	.0
	.0	.0	.0	.0	.0	.0	.0	.0	.0	.0

1017	84.5	38.4	67.9	71.5	11.0	20.0				
	.0	.0	.0	.0	.0	.0	.0	.0	.0	.0
	.0	.0	.0	.0	.0	.0	.0	.0	.0	.0
	.0	.0	.0	.0	.0	.0	.0	.0	.0	.0
	.0	.0								
1018	78.9	40.6	59.0	66.1	12.0	21.0				
	.3	.1	.1	.2	.2	.2	.1	.1	.1	.1
	.1	.3	.3	.3	.3	.6	.6	.1	2.0	93.1
	.0	.0	.0	.0	.0	.0	.0	.0	.0	.0
	.0	.0								
1019	77.5	40.0	.0	.0	.0	.0				
	.3	.1	.1	.2	.2	.2	.1	.1	.1	.1
	.1	.3	.3	.3	.3	.6	.6	.1	2.0	93.1
	.0	.0	.0	.0	.0	.0	.0	.0	.0	.0
	.0	.0								
1020	78.0	39.8	.0	.0	.0	.0				
	.3	.1	.1	.2	.2	.2	.1	.1	.1	.1
	.1	.3	.3	.3	.3	.6	.6	.1	2.0	93.1
	.0	.0	.0	.0	.0	.0	.0	.0	.0	.0
	.0	.0								
1021	79.8	39.7	59.9	67.0	13.0	22.0				
	.3	.1	.1	.2	.2	.2	.1	.1	.1	.1
	.1	.3	.3	.3	.3	.6	.6	.1	2.0	93.1
	.0	.0	.0	.0	.0	.0	.0	.0	.0	.0
	.0	.0								
1022	81.0	39.2	63.7	68.1	13.0	23.0				
	.4	.1	.2	.1	.2	.2	.1	.3	.3	.3
	.3	.3	.6	.6	1.2	2.0	2.0	.0	.0	.0
	.0	.0	.0	.0	.0	.0	.0	.0	.0	.0
	.0	.0								
1023	79.7	39.5	.0	.0	.0	.0				
	.4	.1	.2	.1	.2	.2	.1	.3	.3	.3
	.3	.3	.6	.6	1.2	2.0	2.0	.0	.0	.0
	.0	.0	.0	.0	.0	.0	.0	.0	.0	.0
	.0	.0								
1024	79.0	39.3	.0	.0	.0	.0				
	.4	.1	.2	.1	.2	.2	.1	.3	.3	.3
	.3	.3	.6	.6	1.2	2.0	2.0	.0	.0	.0
	.0	.0	.0	.0	.0	.0	.0	.0	.0	.0
	.0	.0								
1025	80.5	39.2	62.8	67.7	12.0	21.0				
	.4	.1	.2	.1	.2	.2	.1	.3	.3	.3
	.3	.3	.6	.6	1.2	2.0	2.0	.0	.0	.0
	.0	.0	.0	.0	.0	.0	.0	.0	.0	.0
	.0	.0								
1026	79.3	39.6	60.9	66.1	12.0	22.0				
	.3	.1	.2	.1	.2	.2	.1	.3	.3	.3
	.3	.3	.6	.6	1.2	2.6	16.0	.0	.0	.0
	.0	.0	.0	.0	.0	.0	.0	.0	.0	.0
	.0	.0								
1027	77.0	40.0	.0	.0	.0	.0				
	.4	.1	.2	.1	.2	.2	.1	.3	.3	.3
	.3	.3	.6	.6	1.2	2.6	16.0	.0	.0	.0
	.0	.0	.0	.0	.0	.0	.0	.0	.0	.0
	.0	.0								
1028	77.5	39.9	.0	.0	.0	.0				
	.4	.1	.2	.1	.2	.2	.1	.3	.3	.3
	.3	.3	.6	.6	1.2	2.6	16.0	.0	.0	.0
	.0	.0	.0	.0	.0	.0	.0	.0	.0	.0
	.0	.0								
1029	78.8	39.8	59.9	65.2	13.0	21.0				
	.4	.1	.2	.1	.2	.2	.1	.3	.3	.3
	.3	.3	.6	.6	1.2	2.6	16.0	.0	.0	.0
	.0	.0	.0	.0	.0	.0	.0	.0	.0	.0
	.0	.0								
1031	42.3	44.2	.0	.0	.0	.0				
	.2	.1	.1	.2	.2	.2	.4	.1	.3	.3
	.4	.4	.6	.6	1.7	4.0	194.4	.0	.0	.0
	.0	.0	.0	.0	.0	.0	.0	.0	.0	.0
	.0	.0								
1032	43.6	43.7	34.8	46.7	17.0	29.0				
	.2	.1	.1	.2	.2	.2	.4	.1	.3	.3
	.4	.4	.6	.6	1.7	4.0	194.4	.0	.0	.0
	.0	.0	.0	.0	.0	.0	.0	.0	.0	.0
	.0	.0								

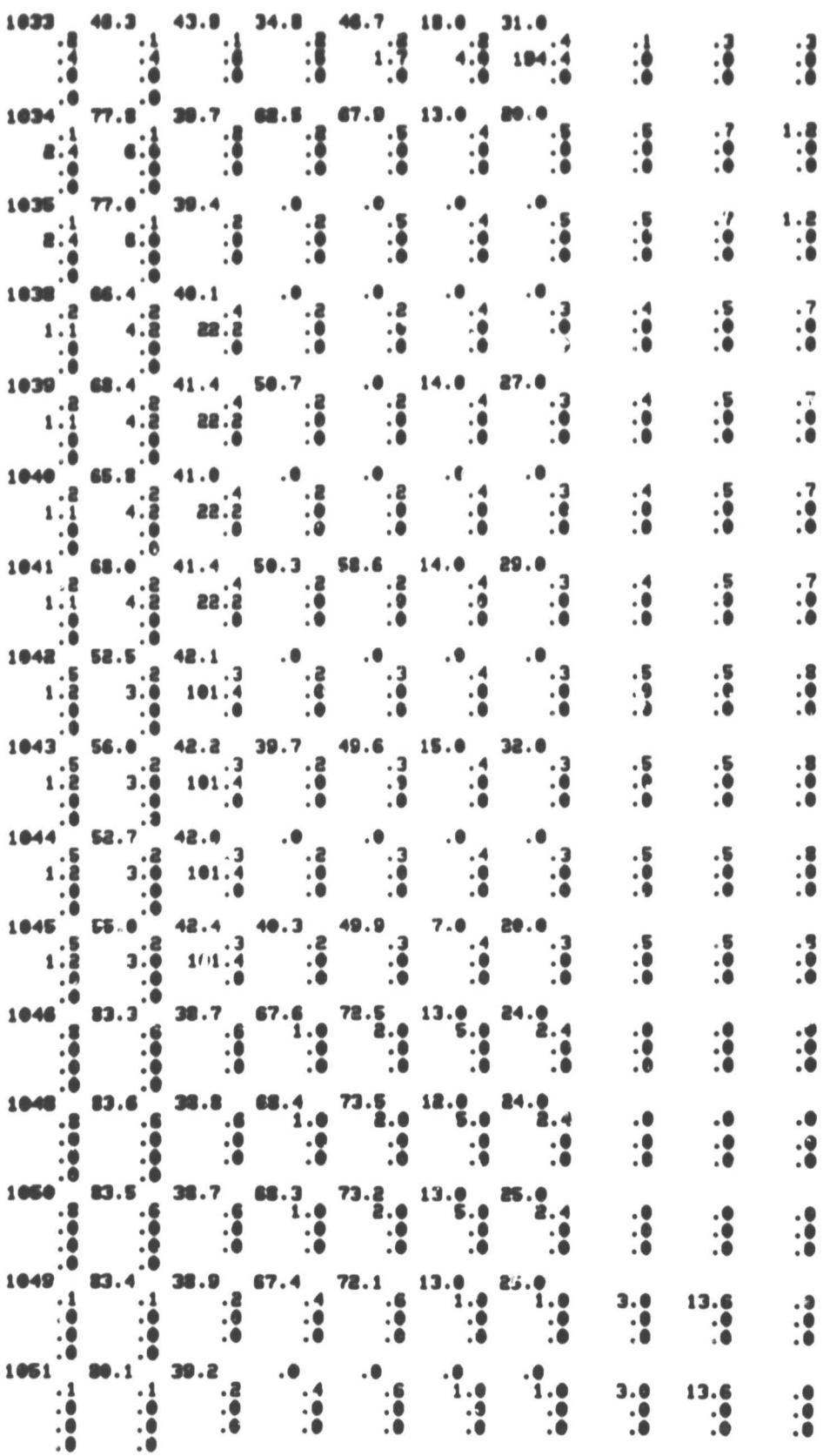

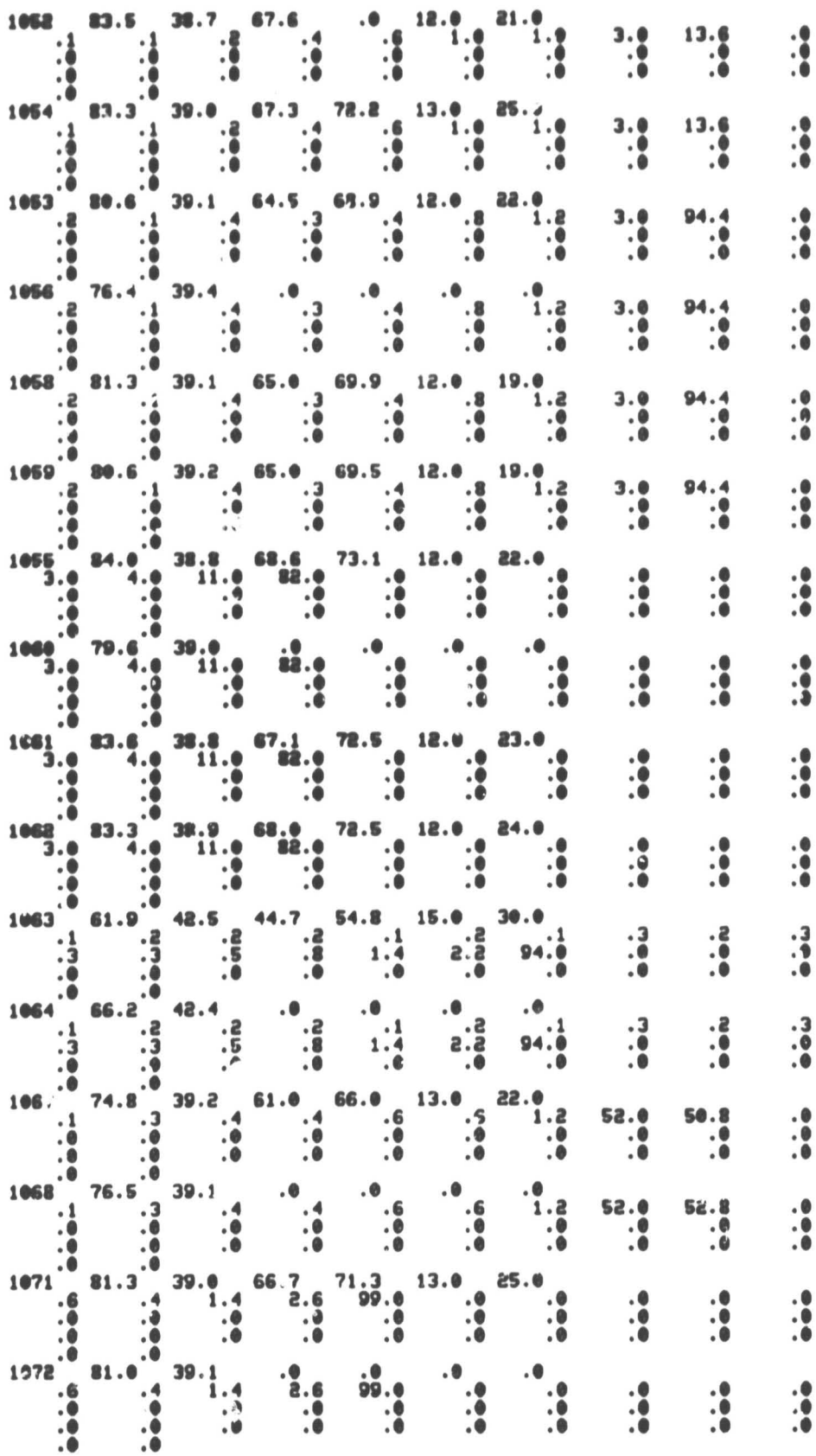

1099	57.5	43.2	.0	.0	.0	.0				
.2	.2	.2	.2	.2	.2	.2	.2	.4	.4	
.4	.4	.6	.6	1.2	2.9	104.5	.0	.0	.0	
.0	.0	.0	.0	.0	.0	.0	.0	.0	.0	
.0	.0									
1100	58.5	43.2	42.2	52.8	16.0	29.0				
.2	.2	.2	.2	.2	.2	.2	.2	.4	.4	
.4	.4	.6	.6	1.2	2.9	104.5	.0	.0	.0	
.0	.0	.0	.0	.0	.0	.0	.0	.0	.0	
.0	.0									
1138	73.5	40.8	57.6	64.2	13.0	26.0				
.3	.3	.3	.3	.5	.5	.5	.5	1.0	1.0	
8.8	8.9	3.8	.0	.0	.0	.0	.0	.0	.0	
.0	.0	.0	.0	.0	.0	.0	.0	.0	.0	
.0	.1									
1133	74.0	40.3	.0	.0	.0	.0				
.3	.3	.3	.3	.5	.5	.5	.5	1.0	1.0	
8.8	8.9	3.8	.0	.0	.0	.0	.0	.0	.0	
.0	.0	.0	.0	.0	.0	.0	.0	.0	.0	
.0	.1									
1154	76.0	40.3	.0	.0	.0	.0				
.2	.2	.2	.2	.2	.2	.2	.2	.2	.2	
.2	.2	.2	.4	.4	.4	.4	.6	.6	1.2	
1.9	4.6	727.0	.3	.3	.3	.3	.3	.3	.3	
.3	.3									
1155	78.3	40.2	57.4	66.8	13.0	16.0				
.2	.2	.2	.2	.2	.2	.2	.2	.2	.2	
.2	.2	.2	.4	.4	.4	.4	.6	.6	1.2	
1.9	4.6	727.0	.3	.3	.3	.3	.3	.3	.3	
.3	.3									
1159	71.8	41.2	51.9	62.3	14.0	26.0				
.7	.6	.2	.0	.1	.1	.2	.2	.2	.4	
.3	.3	.3	.5	.6	.6	.9	1.1	1.6	9.9	
315.9	68.2	.2	.0	.0	.0	.0	.0	.0	.0	
.0	.1									
1160	72.0	41.1	.0	.0	.0	.0				
.7	.6	.2	.0	.1	.1	.2	.2	.2	.4	
.3	.3	.3	.5	.5	.6	.9	1.1	1.6	9.9	
315.9	68.2	.2	.0	.0	.0	.0	.0	.0	.0	
.0	.1									
1163	78.8	40.0	59.4	67.9	12.0	26.0				
.1	.1	.1	.2	.2	.1	.1	.2	.4	.3	
.2	.3	.3	.4	.4	.3	.7	.7	1.0	1.5	
2.0	5.0	337.9	.1	.1	.1	.1	.1	.1	.1	
.1	.1									
1164	77.7	39.9	.0	.0	.0	.0				
.1	.1	.1	.2	.2	.1	.1	.2	.4	.3	
.2	.3	.3	.4	.4	.3	.7	.7	1.0	1.5	
2.0	5.0	337.9	.1	.1	.1	.1	.1	.1	.1	
.1	.1									
1166	75.0	40.3	.0	.0	.0	.0				
2.0	.6	.1	.1	.3	.2	.2	.2	.2	.2	
.2	.3	.3	.3	.3	.6	.5	.8	1.8	5.7	
132.3	56.3	.0	.0	.0	.0	.0	.0	.0	.0	
.0	.1									
1167	75.8	43.6	57.1	66.0	13.0	24.0				
2.0	.6	.1	.1	.3	.2	.2	.2	.2	.2	
.2	.3	.3	.3	.3	.6	.5	.8	1.8	5.7	
132.3	56.3	.0	.0	.0	.0	.0	.0	.0	.0	
.0	.1									
1182	74.0	41.2	.0	.0	.0	.0				
.3	.3	.3	.3	.3	.3	.3	.3	.3	.4	
.5	.6	.8	1.0	2.6	25.2	8.3	.1	.0	.0	
.0	.0	.0	.0	.0	.0	.0	.0	.0	.0	
.0	.0									
1183	70.0	41.8	52.2	61.2	15.0	28.0				
.3	.3	.3	.3	.3	.3	.3	.3	.3	.4	
.5	.5	.8	1.0	2.6	25.2	8.3	.1	.0	.0	
.0	.0	.0	.0	.0	.0	.0	.0	.0	.0	
.0	.0									
1190	74.5	40.3	56.8	64.5	14.0	27.0				
.1	.1	.1	.1	.2	.1	.2	.3	.2	.2	
.7	.7	1.0	1.4	12.6	2.1	.3	.1	.0	.0	
.0	.0	.0	.0	.0	.0	.0	.0	.0	.0	
.0	.0									

1191	74.5	40.3	.0	.0	.0	.0				
	.1	.1	.1	.1	.2	.1	.2	.3	.2	.2
	.7	.7	1.0	1.4	12.6	2.1	.3	.1	.0	.0
	.0	.0	.0	.0	.0	.0	.0	.0	.0	.0
	.0	.0								
1194	65.5	41.7	42.4	57.6	15.0	27.0				
	1.5	.9	.3	.3	.3	.2	.4	.5	.6	.6
	.9	1.0	1.3	28.6	5.2	.8	.8	.1	.0	.0
	.0	.0	.0	.0	.0	.0	.0	.0	.0	.0
	.0	.1								
1195	69.0	41.5	.0	.0	.0	.0				
	1.5	.9	.3	.3	.3	.2	.4	.5	.6	.6
	.9	1.0	1.3	28.6	5.2	.8	.8	.1	.0	.0
	.0	.0	.0	.0	.0	.0	.0	.0	.0	.0
	.0	.1								
1198	78.0	39.8	60.0	67.4	14.0	28.0				
	1.0	.6	.3	.2	.2	.2	.3	.3	.3	.3
	.6	.8	1.3	3.2	1.4	1.1	1.1	.1	.0	.0
	.0	.0	.0	.0	.0	.0	.0	.0	.0	.0
	.0	.1								
1199	77.5	39.6	.0	.0	.0	.0				
	1.0	.6	.3	.2	.2	.2	.3	.3	.3	.3
	.6	.8	1.3	3.2	1.4	1.1	1.1	.1	.0	.0
	.0	.0	.0	.0	.0	.0	.0	.0	.0	.0
	.0	.1								
1214	72.8	39.6	58.4	63.5	11.0	22.0				
	.3	.5	.6	1.3	2.6	3.2	6.4	18.5	92.3	77.8
	.0	.0	.0	.0	.0	.0	.0	.0	.0	.0
	.0	.0	.0	.0	.0	.0	.0	.0	.0	.1
	.1	.1								
1215	72.7	39.4	.0	.0	.0	.0				
	.3	.5	.6	1.3	2.6	3.2	6.4	18.5	92.3	77.8
	.0	.0	.0	.0	.0	.0	.0	.0	.0	.0
	.0	.0	.0	.0	.0	.0	.0	.0	.0	.1
	.1	.1								
1228	67.0	40.2	52.2	58.1	12.9	21.0				
	1.2	.6	.5	.3	.6	.5	1.2	6.0	443.1	48.3
	.1	.1	.1	.1	.0	.0	.0	.0	.0	.0
	.0	.0	.0	.0	.3	.0	.0	.0	.0	.0
	.0	.1								
1229	69.7	40.2	.0	.0	.0	.0				
	1.2	.6	.5	.3	.6	.5	1.2	6.0	443.1	48.3
	.1	.1	.1	.1	.0	.0	.0	.0	.0	.0
	.0	.0	.0	.0	.0	.0	.0	.0	.0	.0
	.0	.1								
1302	27.4	44.4	28.7	40.2	.0	.0				
	3.5	2.9	.1	.1	.6	.1	.1	.3	.3	.7
	.5	.4	.4	.4	1.2	4.2	490.2	20.1	1.6	.6
	.1	.0	.0	.0	.0	.0	.0	.0	.0	.0
	.1	.1								
1303	28.7	44.3	29.0	40.5	.0	.0				
	3.5	2.9	.1	.1	.6	.1	.1	.3	.3	.7
	.5	.4	.4	.4	1.2	4.	490.2	20.1	1.6	.6
	.1	.0	.0	.0	.0	.0	.0	.0	.0	.0
	.1	.1								
1316	71.4	40.4	54.5	62.5	.0	.0				
	1.9	1.1	1.0	1.6	.6	.3	.3	.3	.4	1.1
	8.1	8.0	6.5	.3	.2	.1	.0	.0	.0	.0
	.0	.0	.0	.0	.0	.0	.0	.0	.0	.1
	.1	.1								
1317	71.5	40.3	54.8	63.1	.0	.0				
	1.9	1.1	1.0	1.0	.6	.3	.3	.3	.4	1.1
	2.1	8.8	6.5	.3	.2	.1	.0	.0	.0	.0
	.0	.0	.0	.0	.0	.0	.0	.0	.0	.1
	.1	.1								
1319	55.5	41.9	45.7	56.7	.0	.0				
	1.5	1.0	.3	.3	.3	.4	.4	.5	.6	.7
	1.1	2.2	35.8	47.5	12.7	.0	.0	.0	.0	.0
	.0	.0	.0	.0	.0	.0	.0	.0	.0	.0
	.0	.1								
1320	54.2	41.9	48.2	50.3	.0	.0				
	1.5	1.0	.3	.3	.3	.4	.4	.5	.6	.7
	1.1	2.2	35.8	47.5	12.7	.0	.0	.0	.0	.0
	.0	.0	.0	.0	.0	.0	.0	.0	.0	.0
	.0	.1								
1323	43.2	43.1	34.2	44.5	.0	.0				
	1.7	.4	.1	.1	.3	.4	.4	.4	.5	.6
	.9	2.2	346.5	148.5	.1	.1	.0	.0	.0	.0
	.0	.0	.0	.0	.0	.0	.0	.0	.0	.9
	.0	.1								

```
 1304   44.8    42.8    34.1    44.5      .0      .0
    1.7     .4      .1      .1      .3      .4      .4      .5      .6
     .9    2.0   346.5   148.5      .1      .1      .0      .0      .0
     .0      .0      .0      .0      .0      .0      .0      .0      .0
     .0      .1
 1338   88.8    38.7    66.7    72.6      .0      .0
    1.2      .3      .5      .5      .6      .7    1.4    6.5    10.5      .1
     .0      .0      .1      .1      .0      .0      .0      .0      .0      .0
     .0      .0      .0      .0      .0      .0      .0      .0      .0      .0
     .0      .1
 1341   82.6    38.6    66.0    72.5      .0      .0
    1.2      .3      .5      .5      .6      .7    1.4    6.5    10.5      .1
     .0      .0      .1      .1      .0      .0      .0      .0      .0      .0
     .0      .0      .0      .0      .0      .0      .0      .0      .0      .0
     .0      .1
 1343   77.2    38.9    62.2    67.6      .0      .0
    2.2      .3      .3      .4      .5      .7    1.2   43.4    53.2      .1
     .0      .0      .0      .0      .0      .0      .0      .0      .0      .0
     .0      .0      .0      .0      .0      .0      .0      .0      .0      .0
     .0      .1
 1344   76.2    38.8    61.8    67.1      .0      .0
    2.2      .3      .3      .4      .5      .7    1.2   43.4    53.2      .1
     .0      .0      .0      .0      .0      .0      .0      .0      .0      .0
     .0      .0      .0      .0      .0      .0      .0      .0      .0      .0
     .0      .1
END
```

2024-T851 SEQUENCE B

```
TEMP RANGES
10   498.5   485.0   473.0   461.5   450.0   438.0   426.0   414.0   402.5   390.5
10   379.0   367.0   355.0   343.0   331.0   319.0   307.0   295.0   283.0   270.5
10   258.5   246.0   234.0   221.5   209.0   197.0   184.0   172.0   159.0   147.0
 3   134.0   122.0   110.0
END
 1899   83.2    38.4      .0      .0      .0      .0      .0
     .0      .0      .0      .0      .0      .0      .0      .0      .0      .0
     .0      .0      .0      .0      .0      .0      .0      .0      .0      .0
     .0      .0      .0      .0      .0      .0      .0      .0      .0      .0
     .0      .0
 1910   85.1    38.2    69.3    72.5    12.0    23.0
     .0      .0      .0      .0      .0      .0      .0      .0      .0      .0
     .0      .0      .0      .0      .0      .0      .0      .0      .0      .0
     .0      .0      .0      .0      .0      .0      .0      .0      .0      .0
     .0      .0
 1911   81.7    38.4      .0      .0      .0      .0      .0
     .0      .0      .0      .0      .0      .0      .0      .0      .0      .0
     .0      .0      .0      .0      .0      .0      .0      .0      .0      .0
     .0      .0      .0      .0      .0      .0      .0      .0      .0      .0
     .0      .0
 1912   84.9    38.2    68.1    71.9    12.0    22.0
     .0      .0      .0      .0      .0      .0      .0      .0      .0      .0
     .0      .0      .0      .0      .0      .0      .0      .0      .0      .0
     .0      .0      .0      .0      .0      .0      .0      .0      .0      .0
     .0      .0      .0      .0      .0      .0      .0      .0      .0      .0
     .0      .0
 1915   83.9    38.7    67.9    72.8    13.0    24.0
     .0      .0      .0      .0      .0      .0      .0      .0      .0      .0
     .0      .0      .0      .0      .0      .0      .0      .0      .0      .0
     .0      .0      .0      .0      .0      .0      .0      .0      .0      .0
     .0      .0      .0      .0      .0      .0      .0      .0      .0      .0
     .0      .0
 1916   85.0    38.2    68.6    71.9    11.0    22.0
     .0      .0      .0      .0      .0      .0      .0      .0      .0      .0
     .0      .0      .0      .0      .0      .0      .0      .0      .0      .0
     .0      .0      .0      .0      .0      .0      .0      .0      .0      .0
     .0      .0      .0      .0      .0      .0      .0      .0      .0      .0
     .0      .0
 1917   84.5    38.4    67.9    71.5    11.0    20.0
     .0      .0      .0      .0      .0      .0      .0      .0      .0      .0
     .0      .0      .0      .0      .0      .0      .0      .0      .0      .0
     .0      .0      .0      .0      .0      .0      .0      .0      .0      .0
     .0      .0      .0      .0      .0      .0      .0      .0      .0      .0
     .0      .0
```

1075	68.8	41.8	51.9	59.9	14.0	23.0				
.0	.2	.0	.0	.0	94.9	8.7	1.2	.0	.0	
.6	.5	.4	.4	.3	.3	.4	.4	.3	.3	
.5	.7	.6	.5	.5	.5	.2	.5	.2	.2	
.2	.2									
1076	78.0	41.5	.0	.0	.0	.0				
.0	.0	.0	.0	.0	94.9	8.7	1.2	.0	.0	
.6	.5	.4	.4	.3	.3	.4	.4	.3	.3	
.5	.7	.6	.5	.5	.5	.2	.5	.2	.2	
.2	.2									
1079	72.3	41.3	54.1	64.1	12.0	22.0				
.0	.0	.0	.0	.0	.0	.0	.0	.0	.0	
2.7	1.5	.7	.7	.7	.5	.4	.4	.5	.4	
.3	1.0	.6	.3	.9	.4	.4	.3	.2	.2	
.2	.4									
1080	73.5	40.9	.0	.0	.0	.0				
.0	.0	.0	.0	.0	.0	.0	.0	.0	.0	
2.7	1.5	.7	.7	.7	.5	.4	.4	.5	.4	
.3	1.0	.6	.3	.9	.4	.4	.3	.2	.2	
.2	.4									
1089	56.3	43.2	39.4	52.9	15.0	27.0				
.0	.0	.0	.0	.0	.0	.0	.0	.0	12.5	
2.0	.9	.8	.6	.5	.3	.4	.3	.3	.3	
.1	.2	.2	.1	.2	.1	.1	.1	.1	.1	
.1	.1									
1090	56.0	43.2	.0	.0	.0	.0				
.0	.0	.0	.0	.0	.0	.0	.0	.0	12.5	
2.0	.9	.8	.6	.5	.3	.4	.3	.3	.3	
.1	.2	.2	.1	.2	.1	.1	.1	.1	.1	
.1	.1									
1091	51.8	43.7	36.5	49.6	15.0	28.0				
.0	.0	.0	.0	.0	.0	.0	.0	.0	86.4	
1.9	1.4	1.0	2.0	1.8	1.4	1.2	1.2	1.0	.8	
.8	.6	.4	.4	.2	.2	.2	.1	.1	.1	
.1	.1									
1092	50.7	43.8	.0	.0	.0	.0				
.0	.0	.0	.0	.0	.0	.0	.0	.0	86.4	
1.8	1.4	1.0	2.0	1.8	1.4	1.2	1.2	1.0	.8	
.8	.6	.4	.4	.2	.2	.2	.1	.1	.1	
.1	.1									
1096	80.0	39.5	63.2	70.2	23.0	25.0				
.2	.0	.0	.0	.0	.0	.0	.0	.0	.0	
.0	.0	.0	.0	.0	.0	.0	.0	.0	.0	
.0	79.8	3.2	1.9	1.2	2.3	2.6	2.6	2.6	2.0	
2.0	2.0									
1097	80.2	39.5	.0	.0	.0	.0				
.2	.0	.0	.0	.0	.0	.0	.0	.0	.0	
.0	.0	.0	.0	.0	.0	.0	.0	.0	.0	
.0	79.8	3.2	1.9	1.2	2.3	2.6	2.6	2.6	2.0	
2.0	2.0									
1103	63.5	42.7	.0	.0	.0	.0				
.0	.0	.0	.0	.0	.0	.0	.0	.0	.0	
.0	.0	.0	.0	.0	.0	.0	58.4	25.0	1.6	
1.2	1.0	1.1	.5	.4	.6	1.2	1.2	1.9	.3	
.1	.3									
1104	62.5	42.7	42.3	56.4	13.0	28.0				
.0	.0	.0	.0	.0	.0	.0	.0	.0	.0	
.6	.0	.0	.0	.0	.0	.0	58.4	25.0	1.6	
1.2	1.0	1.1	.5	.4	.6	1.2	1.2	1.9	.3	
.1	.3									
1109	80.0	39.5	.0	.0	.0	.0				
.0	.0	.0	.0	.0	.0	.0	.0	.0	.0	
.0	.0	.0	.0	.0	.0	.0	12.1	1.9	1.9	
.9	.9	.4	.4	.4	.4	.4	.4	.4	.4	
.3	.3									
1110	79.3	39.4	62.9	69.7	12.0	23.0				
.0	.0	.0	.0	.0	.0	.0	.0	.0	.0	
.0	.0	.0	.0	.0	.0	.0	12.1	1.9	1.9	
.9	.9	.4	.4	.4	.4	.4	.4	.4	.4	
.3	.3									
1111	83.2	38.9	.0	.0	.0	.0				
.2	.1	.1	.1	.1	.1	.1	.0	.0	.0	
.0	.0	.0	.0	.0	.0	.0	3.5	1.2	1.2	
.5	.5	.5	.3	.3	.3	.3	.3	.3	.3	
.3	.4									

1118	88.1	30.8	66.3	71.w	12.0	23.0				
.0	.1	.1	.1	.1	.1	.1	.0	.0	.0	
.0	.0	.0	.0	.0	.0	.0	3.6	1.2	1.2	
.5	.5	.5	.3	.3	.3	.3	.3	.3	.3	
.3	.4									
1116	59.3	43.5	34.2	49.3	15.0	29.0				
.1	.1	.0	.0	.0	.4	.0	.0	.0	.0	
.0	.0	72.0	18.7	2.0	2.0	.7	.7	.5	.5	
.5	.3	.3	.3	.3	.3	.3	.3	.3	.4	
.5	.9									
1126	76.8	40.4	58.4	67.4	12.0	22.0				
.0	.0	.0	.0	.0	.0	.6	.0	.0	.0	
.0	.0	.0	.0	8.7	3.5	1.5	.8	.7	.5	
.5	.4	.6	.7	.7	.9	.9	.8	.7	.8	
.2	.5									
1127	77.5	40.3	.0	.0	.0	.0				
.0	.0	.0	.0	.0	.0	.0	.0	.0	.0	
.0	.0	.0	.0	8.7	3.5	1.5	.8	.7	.5	
.5	.4	.6	.7	.7	.9	.9	.8	.7	.8	
.2	.5									
1128	81.9	38.9	66.7	71.8	13.0	23.0				
.0	.0	.0	.0	.0	.0	.0	.0	.0	.0	
.0	.0	.0	.0	.0	.0	.0	.6	3.1	.9	
.7	.7	.7	.7	.7	.7	.7	.3	.2	.2	
.2	.2									
1129	81.5	38.9	.0	.0	.0	.0				
.0	.0	.0	.0	.0	.0	.0	.0	.0	.0	
.0	.0	.0	.0	.0	.0	.0	.0	3.1	.9	
.7	.7	.7	.7	.7	.7	.7	.3	.2	.2	
.2	.2									
1142	79.0	39.8	.0	.0	.0	.0				
.0	.0	.0	.0	.0	.0	.0	.0	.4	.0	
.0	.0	.0	.0	.0	.0	.0	.0	.0	.0	
.0	.0	.0	771.9	4.1	2.1	1.3	1.2	1.0	1.0	
.8	.5									
1143	77.8	39.8	60.3	69.3	13.9	26.0				
.0	.0	.0	.0	.0	.0	.0	.0	.0	.0	
.0	.0	.0	.0	.0	.0	.0	.0	.0	.0	
.0	.0	.0	771.9	4.1	2.1	1.3	1.2	1.0	1.0	
.8	.5									
1146	81.5	39.3	.0	.0	.0	.0				
.0	.0	.1	.0	.0	.0	.0	.0	.0	.0	
.0	.0	.0	.0	.0	.0	.0	.0	.0	.0	
.0	.0	.0	277.1	4.7	4.6	1.2	1.2	1.2	1.2	
1.2	1.2									
1147	79.8	39.4	61.8	69.9	13.0	25.0				
.0	.0	.1	.0	.0	.0	.0	.0	.0	.0	
.0	.0	.0	.0	.0	.0	.0	.0	.0	.0	
.0	.0	.0	277.1	4.7	4.6	1.2	1.2	1.2	1.2	
1.2	1.2									
1170	78.5	39.6	.0	.0	.0	.0				
.1	.1	.0	.0	.0	.0	.0	.0	.0	.0	
.0	.0	.0	.0	.0	.0	.0	.0	.0	.0	
88.7	100.0	4.9	1.2	.8	.9	.6	.4	.5	.4	
.4	7.1									
1171	78.5	39.9	60.6	69.0	13.0	25.0				
.1	.1	.0	.0	.0	.0	.0	.0	.0	.0	
.0	.0	.0	.0	.0	.0	.0	.0	.0	.0	
88.7	100.0	4.9	1.2	.8	.9	.6	.4	.5	.4	
.4	7.1									
1176	78.2	39.8	.0	.0	.0	.0				
.1	.0	.0	.0	.0	.0	.0	.0	.0	.0	
.0	.0	.0	.0	.0	.0	.0	.0	.0	.0	
29.1	252.2	50.6	1.4	1.3	.9	.7	.6	.6	.2	
.3	36.7									
1177	79.0	39.8	58.6	68.4	13.0	31.0				
.1	.0	.0	.0	.0	.0	.0	.0	.0	.0	
.0	.0	.0	.0	.0	.0	.0	.0	.0	.0	
29.1	252.2	50.6	1.4	1.3	.9	.7	.6	.6	.2	
.3	36.7									
1178	77.5	39.9	.0	.0	.0	.0				
.8	.2	.0	.0	.0	.0	.0	.0	.0	.0	
.0	.0	.0	.0	.0	.0	.0	19.0	15.5	2.0	
.9	.9	.5	.5	.5	.4	.4	.3	.3	.2	
.2	15.1									

1179	78.0	40.1	60.2	68.3	12.0	25.0				
.8	.2	.0	.0	.0	.0	.0	.0	.0	.0	.0
.0	.0	.0	.0	.0	.0	.0	19.0	15.5	2.0	
.9	.9	.5	.5	.5	.4	.4	.3	.3	.2	
.2	15.1									
1186	81.5	39.5	.0	.0	.0	.0				
1.3	.0	.0	.0	.0	.0	.0	.0	.0	.0	
.0	.0	.0	.0	.0	1.2	2.2	1.9	1.0	.5	
.4	.4	.3	.3	.3	.2	.2	.3	.2	.2	
.2	3.4									
1187	81.8	38.8	61.1	78.8	13.0	26.0				
1.3	.0	.0	.0	.0	.0	.0	.0	.0	.0	
.0	.0	.0	.0	.0	1.2	2.2	1.9	1.0	.5	
.4	.4	.3	.3	.3	.2	.2	.3	.2	.2	
.2	3.4									
1202	75.4	40.1	58.7	67.9	12.0	25.0				
.2	.2	.2	.2	.1	.0	.0	.0	.0	.0	
.0	.0	.0	.0	4.0	6.8	2.0	1.1	.7	.8	
.6	.4	.4	.4	.4	.3	.4	.3	.2	.3	
.2	28.5									
1203	76.7	40.0	.0	.0	.0	.0				
.2	.2	.2	.2	.1	.0	.0	.0	.0	.0	
.0	.0	.0	.0	4.0	6.8	2.0	1.1	.7	.8	
.6	.4	.4	.4	.4	.3	.4	.3	.2	.3	
.2	28.5									
1206	66.5	41.8	.0	.0	.0	.0				
.8	.6	.0	.0	.0	.0	.0	.0	.0	.0	
.0	.0	.0	.0	.6	7.5	26.4	1.0	.9	.7	
.5	.4	.5	.3	.3	.3	.3	.3	.3	.5	
.3	3.9									
1207	65.8	42.1	46.2	58.9	13.0	26.0				
.8	.6	.0	.0	.0	.0	.0	.0	.0	.0	
.0	.0	.0	.0	.0	7.5	26.4	1.0	.9	.7	
.5	.4	.5	.3	.3	.3	.3	.3	.3	.5	
.3	3.9									
1210	55.9	43.7	38.9	50.9	14.0	27.0				
.0	.0	.0	.0	.0	.1	.1	6.2	104.3	79.0	
3.3	1.5	1.9	.7	.3	.4	.3	.4	.4	.4	
.1	.2	.2	.2	.2	.1	.2	.1	.0	.0	
.1	16.8									
1211	50.5	43.4	.0	.0	.0	.0				
.0	.0	.0	.0	.0	.1	.1	6.2	104.3	79.0	
3.3	1.5	1.9	.7	.3	.4	.3	.4	.4	.4	
.1	.2	.2	.2	.2	.1	.2	.1	.0	.0	
.1	16.8									
1230	52.8	43.6	38.1	50.0	15.0	27.0				
1.1	.1	.0	.0	.0	.0	.0	.0	181.4	310.0	
3.9	.8	.6	.5	.4	.4	.3	.4	.2	.3	
.2	.2	.2	.2	.2	.1	.1	.2	.2	.2	
.2	6.4									
1231	54.7	43.3	.0	.0	.0	.0				
1.1	.1	.0	.0	.0	.0	.0	.0	181.4	310.0	
3.9	.8	.6	.5	.4	.4	.3	.4	.2	.3	
.2	.2	.2	.2	.2	.1	.1	.2	.2	.2	
.2	6.4									
1310	47.8	43.6	34.4	48.7	.0	.0				
.1	.0	.0	.0	.0	.0	.0	.0	.0	.0	
.0	.0	.0	.0	434.7	15.4	2.0	.0	.0	.8	
.5	.4	.5	.5	.3	.3	.2	.3	.2	.2	
.2	.2									
1311	48.0	43.2	34.5	49.4	.0	.0				
.1	.0	.0	.0	.0	.0	.0	.0	.0	.0	
.0	.0	.0	.0	434.7	15.4	2.0	.0	.0	.8	
.5	.4	.5	.5	.3	.3	.2	.3	.2	.2	
.2	.2									
1305	63.8	41.9	43.9	57.6	.0	.0				
.2	.0	.0	.0	.0	.0	.0	.0	.0	.0	
.0	.0	.0	.0	5.2	24.0	2.6	2.1	1.5	.7	
.8	.6	.3	.3	.3	.3	.3	.3	.3	.3	
.2	.3									
1308	64.4	41.9	44.4	57.7	.0	.0				
.2	.0	.0	.0	.0	.0	.0	.0	.0	.0	
.0	.0	.0	.0	5.2	24.0	2.6	2.1	1.5	.7	
.8	.6	.3	.3	.3	.3	.3	.3	.3	.3	
.2	.3									

```
1326   68.8    41.5    49.4    61.8      .0      .0
  13.7    5.0      .0      .0      .0      .0      .0      .0      .0      .0
    .0      .0      .5   10.4     2.4     1.1      .9      .9      .6      .4
    .5      .2      .3      .3      .3      .2      .2      .2      .2      .3
    .5      .3
1327   67.8    41.3    50.2    62.3      .0      .0
  13.7    5.0      .0      .0      .0      .0      .0      .0      .0      .0
    .0      .0      .5   10.4     2.4     1.1      .9      .9      .6      .4
    .5      .2      .3      .3      .3      .2      .2      .2      .2      .3
    .5      .3
1330   64.5    42.7    37.8    52.5      .0      .0
   2.6    1.0      .0      .0      .0      .0      .0      .0      .0      .0
    .0      .1    21.5    11.1     1.7      .9      .7      .8      .5      .6
    .4      .2      .3      .3      .2      .3      .2      .5      .4      .3
    .3      .4
1331   66.8    42.6    37.8    52.8      .0      .0
   2.6    1.0      .0      .0      .0      .0      .0      .0      .0      .0
    .0      .1    21.5    11.1     1.7      .9      .7      .8      .5      .6
    .4      .2      .3      .3      .2      .3      .2      .5      .4      .3
    .3      .4
1334   43.8    44.0    38.4    47.0      .0      .0
   3.5      .0      .0      .0      .0      .0      .0      .0      .0      .0
    .0      .0   248.5   249.7     1.4     1.0      .8      .0      .8      .9
    .3      .3      .4      .2      .2      .2      .3      .3      .2      .4
    .1      .3
1335   43.8    43.8    32.6    47.3      .0      .0
   3.5      .0      .0      .0      .0      .0      .0      .0      .0      .0
    .0      .6   242.5   249.7     1.4     1.0      .8      .8      .6      .5
    .3      .3      .4      .2      .2      .2      .3      .3      .2      .4
    .1      .3
1347   55.2    42.9    38.9    51.8      .0      .0
    .2      .0      .4      .0      .0      .0      .0      .0   30.6     3.0
   1.6      .7      .7      .7      .8      .8      .6      .2      .1      .1
    .1      .1      .1      .1      .1      .1      .1      .1      .2      .2
    .2      .4
1348   55.7    42.8    39.4    52.5      .0      .0
    .2      .0      .0      .0      .0      .0      .0      .0   30.6     3.0
   1.6      .7      .7      .7      .8      .8      .6      .2      .1      .1
    .1      .1      .1      .1      .1      .1      .1      .1      .2      .2
    .2      .4
END
```

2024-T351 SEQUENCE A

```
TEMP RANGES
10  496.5  485.0  473.0  461.5  450.0  438.0  426.0  414.0  402.5  390.5
10  370.0  367.0  355.0  343.0  331.0  319.0  307.0  295.0  283.0  270.5
10  258.5  246.0  234.0  221.0  209.0  197.0  184.0  172.0  159.0  147.0
 3  134.0  122.0  110.0
END
1005   76.7    28.4      .0      .0      .0      .0
    .0      .0      .0      .0      .0      .0      .0      .0      .0      .0
    .0      .0      .0      .0      .0      .0      .0      .0      .0      .0
    .0      .0      .0      .0      .0      .0      .0      .0      .0      .0
    .0      .0
1006   79.4    29.5    55.1    68.9    23.0    26.0
    .0      .0      .0      .0      .0      .0      .0      .0      .0      .0
    .0      .0      .0      .0      .0      .0      .0      .0      .0      .0
    .0      .0      .0      .0      .0      .0      .0      .0      .0      .0
    .0      .0
1007   79.9    29.0    55.5    69.9    22.0    28.0
    .0      .0      .0      .0      .0      .0      .0      .0      .0      .0
    .0      .0      .0      .0      .0      .0      .0      .0      .0      .0
    .0      .0      .0      .0      .0      .0      .0      .0      .0      .0
    .0      .0
1008   76.0    28.7      .0      .0      .0      .0
    .0      .0      .0      .0      .0      .0      .0      .0      .0      .0
    .0      .0      .0      .0      .0      .0      .0      .0      .0      .0
    .0      .0      .0      .0      .0      .0      .0      .0      .0      .0
    .0      .0
1013   79.1    29.4    54.2    68.0    24.0    28.0
    .0      .0      .0      .0      .0      .0      .0      .0      .0      .0
    .0      .0      .0      .0      .0      .0      .0      .0      .0      .0
    .0      .0      .0      .0      .0      .0      .0      .0      .0      .0
    .0      .0
```

1014	79.3	29.2	54.8	68.4	24.0	28.0				
.0	.0	.0	.0	.0	.0	.0	.0	.0	.0	
.0	.0	.0	.0	.0	.0	.0	.0	.0	.0	
.0	.0	.0	.0	.0	.0	.0	.0	.0	.0	
.0	.0									
1036	76.1	31.4	53.8	67.0	20.0	20.0				
.1	.1	.2	.2	.5	.4	.5	.5	.7	1.2	
2.4	6.0	.0	.0	.0	.0	.0	.0	.0	.0	
.0	.0	.0	.0	.0	.0	.0	.0	.0	.0	
.0	.0									
1037	75.0	31.3	.0	.0	.0	.0				
.1	.1	.2	.2	.5	.4	.5	.5	.7	1.2	
2.4	6.0	.0	.0	.0	.0	.0	.0	.0	.0	
.0	.0	.0	.0	.0	.0	.0	.0	.0	.0	
.0	.0									
1065	67.5	35.6	48.1	60.6	16.0	23.0				
.1	.2	.2	.2	.1	.2	.1	.3	.2	.3	
.3	.3	.5	.8	1.4	2.2	94.0	.0	.0	.0	
.0	.0	.0	.0	.0	.0	.0	.0	.0	.0	
.0	.0									
1066	66.0	35.2	.0	.0	.6	.0				
.1	.2	.2	.2	.1	.2	.1	.3	.2	.3	
.3	.3	.5	.8	1.4	2.2	94.0	.0	.0	.0	
.0	.0	.0	.0	.0	.0	.0	.0	.0	.0	
.0	.0									
1069	69.4	32.5	50.5	64.2	11.0	19.0				
.1	.3	.4	.4	.6	.6	1.2	52.0	50.8	.0	
.0	.0	.0	.0	.0	.0	.0	.0	.0	.0	
.0	.0	.0	.0	.0	.0	.0	.0	.0	.0	
.0	.0									
1070	69.0	31.8	.0	.0	.0	.0				
.1	.3	.4	.4	.6	.6	1.2	52.0	50.8	.0	
.0	.0	.0	.0	.0	.0	.0	.0	.0	.0	
.0	.0	.0	.0	.0	.0	.0	.0	.0	.0	
.0	.0									
1073	77.1	29.6	55.2	68.6	22.0	28.0				
.6	.4	1.4	2.6	99.0	.0	.0	.0	.0	.0	
.0	.0	.0	.0	.0	.0	.0	.0	.0	.0	
.0	.0	.0	.0	.0	.0	.0	.0	.0	.0	
.0	.0									
1074	76.5	29.7	.0	.0	.0	.0				
.6	.4	1.4	2.6	99.0	.0	.0	.0	.0	.0	
.0	.0	.0	.0	.0	.0	.0	.0	.0	.0	
.0	.0	.0	.0	.0	.0	.0	.0	.0	.0	
.0	.0									
1101	68.0	36.5	.0	.0	.0	.0				
.2	.2	.2	.2	.2	.2	.2	.2	.4	.4	
.4	.4	.6	.6	1.2	2.9	104.5	.0	.0	.0	
.0	.0	.0	.0	.0	.0	.0	.0	.0	.0	
.0	.0									
1102	65.0	36.9	47.8	58.6	16.0	22.0				
.2	.2	.2	.2	.2	.2	.2	.2	.4	.4	
.4	.4	.6	.6	1.2	2.9	104.5	.0	.0	.0	
.0	.0	.0	.0	.0	.0	.0	.0	.0	.0	
.0	.0									
1134	71.8	32.6	51.6	65.2	19.0	23.0				
.3	.3	.3	.3	.5	.5	.5	.5	1.0	1.0	
2.6	8.9	3.8	.0	.0	.0	.0	.0	.0	.0	
.0	.0	.0	.0	.0	.0	.0	.0	.0	.0	
.0	.1									
1135	71.5	32.6	.0	.0	.0	.0				
.3	.3	.3	.3	.5	.5	.5	.5	1.0	1.0	
2.6	8.9	3.8	.0	.0	.0	.0	.0	.0	.0	
.0	.0	.0	.0	.0	.0	.0	.0	.0	.0	
.0	.1									
1156	81.7	33.1	.0	.0	.0	.0				
.2	.2	.2	.2	.2	.2	.2	.2	.2	.2	
.2	.2	.2	.4	.4	.4	.4	.6	.6	1.2	
1.9	4.6	727.0	.3	.3	.3	.3	.3	.3	.3	
.3	.3									
1157	81.5	32.8	60.5	73.2	21.0	25.0				
.2	.2	.2	.2	.2	.2	.2	.2	.2	.2	
.2	.2	.2	.4	.4	.4	.4	.6	.6	1.2	
1.9	4.6	727.0	.3	.3	.3	.3	.3	.3	.3	
.3	.3									

1158	75.7	35.3	.0	.0	.0	.0				
.7	.6	.2	.0	.1	.1	.2	.2	.2	.4	
.3	.3	.3	.6	.5	.8	.9	1.1	1.6	9.9	
315.9	68.2	.2	.0	.0	.0	.0	.0	.0	.0	
.0	.1									
1161	76.8	35.2	59.4	65.8	16.0	23.0				
.7	.6	.2	.0	.1	.1	.2	.2	.2	.4	
.3	.3	.3	.5	.5	.8	.9	1.1	1.6	9.9	
315.9	62.2	.2	.0	.0	.0	.0	.0	.0	.0	
.0	.1									
1162	80.5	72.2	.0	.0	.0	.0				
.1	.1	.1	.2	.2	.1	.1	.2	.4	.3	
.2	.3	.3	.4	.4	.3	.7	.7	1.0	1.5	
2.0	5.0	337.9	.1	.1	.1	.1	.1	.1	.1	
.1	.1									
1165	81.0	31.9	59.3	72.5	19.0	19.0				
.1	.1	.1	.2	.2	.1	.1	.2	.4	.3	
.2	.3	.3	.4	.4	.3	.7	.7	1.0	1.5	
2.0	5.0	337.9	.1	.1	.1	.1	.1	.1	.1	
.1	.1									
1168	78.5	33.8	.0	.0	.0	.0				
2.0	.6	.1	.1	.3	.2	.2	.2	.2	.2	
.2	.3	.3	.3	.3	.6	.5	.8	1.8	5.7	
132.3	56.3	.0	.0	.0	.0	.0	.0	.0	.0	
.0	.1									
1169	78.8	33.5	61.5	70.0	18.0	21.0				
2.0	.6	.1	.1	.3	.2	.2	.2	.2	.2	
.2	.3	.3	.3	.3	.6	.5	.8	1.8	5.7	
132.3	56.3	.0	.0	.0	.0	.0	.0	.0	.0	
.0	.1									
1184	73.2	33.1	.0	.0	.0	.0				
.3	.3	.3	.3	.3	.3	.3	.3	.3	.4	
.5	.5	.8	1.0	2.6	25.2	8.3	.1	.0	.0	
.0	.0	.0	.0	.0	.0	.0	.0	.0	.0	
.0	.0									
1185	71.3	33.1	51.3	64.8	11.0	16.0				
.3	.3	.3	.3	.3	.3	.3	.3	.3	.4	
.5	.5	.8	1.0	2.6	25.2	8.3	.1	.0	.0	
.0	.0	.0	.0	.0	.0	.0	.0	.0	.0	
.0	.0									
1192	73.9	32.8	52.5	66.0	10.0	15.0				
.1	.1	.1	.1	.2	.1	.2	.3	.2	.2	
.7	.7	1.0	1.4	12.6	2.1	.3	.1	.0	.0	
.0	.0	.0	.0	.0	.0	.0	.0	.0	.0	
.0	.0									
1193	73.2	32.3	.0	.0	.0	.0				
.1	.1	.1	.1	.2	.1	.2	.3	.2	.2	
.7	.7	1.0	1.4	12.6	2.1	.3	.1	.0	.0	
.0	.0	.0	.0	.0	.0	.0	.0	.0	.0	
.0	.0									
1196	66.0	35.1	47.1	60.3	17.0	23.0				
1.5	.9	.3	.3	.3	.2	.4	.5	.6	.6	
.9	1.0	1.3	28.6	5.2	.8	.8	.1	.0	.0	
.0	.0	.0	.0	.0	.0	.0	.0	.0	.0	
.0	.1									
1197	65.0	34.9	.0	.0	.0	.0				
1.5	.9	.3	.3	.3	.2	.4	.5	.6	.6	
.9	1.0	1.3	28.6	5.2	.8	.8	.1	.0	.0	
.0	.9	.0	.0	.0	.0	.0	.0	.0	.0	
.0	.1									
1200	75.8	30.9	53.9	67.7	20.0	25.0				
1.0	.6	.3	.2	.2	.2	.3	.3	.3	.3	
.6	.8	1.3	3.2	1.4	1.1	1.1	.1	.0	.0	
.0	.0	.0	.0	.0	.0	.0	.0	.0	.0	
.0	.1									
1201	75.7	31.0	.0	.0	.0	.0				
1.0	.6	.3	.2	.2	.2	.3	.3	.3	.3	
.6	.8	1.3	3.2	1.4	1.1	1.1	.1	.0	.0	
.0	.0	.0	.0	.0	.0	.0	.0	.0	.0	
.0	.1									

1216	66.1	33.3	47.4	61.5	14.0	17.0			
.3	.5	.6	1.3	2.6	3.2	6.4	18.5	92.3	77.8
.0	.0	.0	.0	.0	.0	.0	.0	.0	.0
.0	.0	.0	.0	.0	.0	.0	.0	.0	.1
.1	.1								
1217	67.2	33.3	.0	.0	.0	.0			
.3	.5	.6	1.3	2.6	3.2	6.4	18.5	92.3	77.8
.0	.0	.0	.0	.0	.0	.0	.0	.0	.0
.0	.0	.0	.0	.0	.0	.0	.0	.0	.1
.1	.1								
1226	59.5	35.3	43.2	56.3	10.0	15.0			
1.2	.6	.5	.3	.6	.5	1.2	6.0	443.1	48.3
.1	.1	.1	.1	.0	.0	.0	.0	.0	.0
.0	.0	.0	.0	.0	.0	.0	.0	.0	.0
.0	.1								
1227	64.2	34.2	.0	.0	.0	.0			
1.2	.6	.5	.3	.6	.5	1.2	6.0	443.1	48.3
.1	.1	.1	.1	.0	.0	.0	.0	.0	.0
.0	.0	.0	.0	.0	.0	.0	.0	.0	.0
.0	.1								
1301	36.8	41.3	39.4	44.1	.0	.0			
3.5	2.9	.1	.1	.6	.1	.1	.3	.3	.7
.5	.4	.4	.4	1.2	4.2	490.2	20.1	1.6	.6
.1	.0	.0	.0	.0	.0	.0	.0	.0	.0
.1	.1								
1304	37.8	41.6	39.9	44.2	.0	.0			
3.5	2.9	.1	.1	.6	.1	.1	.3	.3	.7
.5	.4	.4	.4	1.2	4.2	490.2	20.1	1.6	.6
.1	.0	.0	.0	.0	.0	.0	.0	.0	.0
.1	.1								
1314	68.8	33.5	52.1	62.2	.0	.0			
1.0	1.1	1.0	1.0	.6	.3	.3	.3	.4	1.1
2.1	8.8	6.5	.3	.2	.1	.0	.0	.0	.0
.0	.0	.0	.0	.0	.0	.0	.0	.0	.1
.1	.1								
1315	68.7	33.4	51.6	62.3	.0	.0			
1.0	1.1	1.0	1.0	.6	.3	.3	.3	.4	1.1
2.1	8.8	6.5	.3	.2	.1	.0	.0	.0	.0
.0	.0	.0	.0	.0	.0	.0	.0	.0	.1
.1	.1								
1318	49.3	37.6	39.7	51.0	.0	.0			
1.5	1.0	.3	.3	.3	.4	.4	.5	.6	.7
1.1	2.2	35.8	47.5	12.7	.0	.0	.0	.0	.0
.0	.0	.0	.0	.0	.0	.0	.0	.0	.0
.0	.1								
1321	50.0	37.5	39.4	50.9	.0	.0			
1.5	1.0	.3	.3	.3	.4	.4	.5	.6	.7
1.1	2.2	35.3	47.5	12.7	.0	.0	.0	.0	.0
.0	.0	.0	.0	.0	.0	.0	.0	.0	.0
.0	.1								
1322	38.4	40.3	36.5	43.8	.0	.0			
1.7	.4	.1	.1	.3	.4	.4	.4	.5	.6
.9	2.2	346.5	148.5	.1	.1	.0	.0	.0	.0
.0	.0	.0	.0	.0	.0	.0	.0	.0	.0
.0	.1								

```
1325   36.6    40.3    37.1    43.9      .0      .0
   1.7      .4      .1      .1      .3      .4      .4      .4      .5      .6
    .9     8.2   348.5   148.5      .1      .1      .0      .0      .0      .0
    .0      .0      .0      .0      .0      .0      .0      .0      .0      .0
    .0      .1
1339   77.8    29.6    57.9    69.0      .0      .0
   1.2      .3      .5      .5      .6      .7     1.4     6.5    10.5      .1
    .0      .0      .1      .1      .0      .0      .0      .0      .0      .0
    .0      .0      .0      .0      .0      .0      .0      .0      .0      .0
    .0      .1
1340   78.1    29.6    57.7    68.7      .0      .0
   1.2      .3      .5      .5      .6      .7     1.4     6.5    10.5      .1
    .0      .0      .1      .1      .0      .0      .0      .0      .0      .0
    .0      .0      .0      .0      .0      .0      .0      .0      .0      .0
    .0      .1
1342   72.0    31.6    51.3    64.4      .0      .0
   2.2      .3      .3      .4      .5      .7     1.2    43.4    53.2      .1
    .0      .0      .0      .0      .0      .0      .0      .0      .0      .0
    .0      .0      .0      .0      .0      .0      .0      .0      .0      .0
    .0      .1
1345   70.1    31.9    50.6    64.2      .0      .0
   2.2      .3      .3      .4      .5      .7     1.2    43.4    53.2      .1
    .0      .0      .0      .0      .0      .0      .0      .0      .0      .0
    .0      .0      .0      .0      .0      .0      .0      .0      .0      .0
    .0      .1
END
```

2024-T351 SEQUENCE B

```
TEMP RANGES
10   496.5   485.0   473.0   461.5   450.0   438.0   426.0   414.0   402.5   390.5
10   379.0   367.0   355.0   343.0   331.0   319.0   307.0   295.0   283.0   270.5
10   258.5   246.0   234.0   221.5   209.0   197.0   184.0   172.0   159.0   147.0
 3   134.0   122.0   110.0
END
1005   76.7    28.4      .0      .0      .0      .0
    .0      .0      .0      .0      .0      .0      .0      .0      .0      .0
    .0      .0      .0      .0      .0      .0      .0      .0      .0      .0
    .0      .0      .0      .0      .0      .0      .0      .0      .0      .0
    .0      .0
1006   79.4    29.5    55.1    68.9    23.0    26.0
    .0      .0      .0      .0      .0      .0      .0      .0      .0      .0
    .0      .0      .0      .0      .0      .0      .0      .0      .0      .0
    .0      .0      .0      .0      .0      .0      .0      .0      .0      .0
    .0      .0
1007   79.9    29.0    55.5    69.9    22.0    28.0
    .0      .0      .0      .0      .0      .0      .0      .0      .0      .0
    .0      .0      .0      .0      .0      .0      .0      .0      .0      .0
    .0      .0      .0      .0      .0      .0      .0      .0      .0      .0
    .0      .0
1008   76.0    28.7      .0      .0      .0      .0
    .0      .0      .0      .0      .0      .0      .0      .0      .0      .0
    .0      .0      .0      .0      .0      .0      .0      .0      .0      .0
    .0      .0      .0      .0      .0      .0      .0      .0      .0      .0
    .0      .0
1013   79.1    29.4    54.2    68.0    24.0    28.0
    .0      .0      .0      .0      .0      .0      .0      .0      .0      .0
    .0      .0      .0      .0      .0      .0      .0      .0      .0      .0
    .0      .0      .0      .0      .0      .0      .0      .0      .0      .0
    .0      .0
1014   79.3    29.2    54.8    68.4    24.0    28.0
    .0      .0      .0      .0      .0      .0      .0      .0      .0      .0
    .0      .0      .0      .0      .0      .0      .0      .0      .0      .0
    .0      .0      .0      .0      .0      .0      .0      .0      .0      .0
    .0      .0
1077   69.8    34.3    48.3    62.6    19.0    20.0
    .0      .0      .0      .0      .0    94.9     2.7     1.2      .8      .6
    .6      .5      .4      .4      .3      .3      .4      .4      .3      .3
    .5      .7      .6      .5      .5      .5      .2      .5      .2      .2
    .2      .2
```

1078	79.0	34.4	.0	.0	.0	.0			
.0	.0	.0	.0	.0	94.9	2.7	1.2	.8	.6
.6	.5	.4	.4	.3	.3	.4	.4	.3	.3
.5	.7	.6	.5	.5	.5	.2	.5	.2	.2
.2	.2								
1081	76.3	31.9	55.2	67.3	19.0	24.0			
.0	.0	.0	.0	.0	.0	.0	.0	.0	.0
2.7	1.5	.7	.7	.7	.5	.4	.4	.5	.4
.3	1.0	.6	.3	.9	.4	.4	.3	.2	.2
.2	.4								
1082	76.0	31.7	.0	.0	.0	.0			
.0	.0	.0	.0	.0	.0	.0	.0	.0	.0
2.7	1.5	.7	.7	.7	.5	.4	.4	.5	.4
.3	1.0	.6	.3	.9	.4	.4	.3	.2	.2
.2	.4								
1087	84.9	36.4	47.7	59.3	9.0	12.0			
.0	.0	.0	.0	.0	.0	.0	.0		12.5
2.0	.9	.8	.6	.5	.3	.4	.3		.3
.1	.2	.2	.1	.2	.1	.1	.1	.1	.1
.1	.1								
1088	65.0	36.2	.0	.0	.0	.0			
.0	.0	.0	.0	.0	.0	.0	.0	.0	12.5
2.0	.9	.8	.6	.5	.3	.4	.3	.3	.3
.1	.2	.2	.1	.2	.1	.1	.1	.1	.1
.1	.1								
1093	59.5	37.7	43.4	56.1	10.0	8.0			
.0	.0	.0	.0	.0	.0	.0	.0	.0	86.4
1.8	1.4	1.0	2.0	1.8	1.4	1.2	1.2	1.0	.8
.8	.6	.4	.4	.2	.2	.2	.1	.1	.1
.1	.1								
1094	56.3	37.6	.0	.0	.6	.0			
.0	.0	.0	.0	.0	.0	.0	.0	.0	86.4
1.8	1.4	1.0	2.0	1.8	1.4	1.2	1.2	1.0	.8
.8	.6	.4	.4	.2	.2	.2	.1	.1	.1
.1	.1								
1095	77.5	31.1	.0	.0	.0	.0			
.2	.0	.0	.0	.0	.0	.0	.0	.0	.0
.0	.0	.0	.0	.0	.0	.0	.0	.0	.0
.0	79.8	3.2	1.9	1.2	2.3	2.6	2.6	2.6	2.0
2.0	2.0								
1098	77.8	30.7	55.2	70.2	23.0	27.0			
.2	.0	.0	.0	.6	.0	.0	.0	.0	.0
.0	.0	.0	.0	.0	.0	.0	.0	.0	.0
.0	79.8	3.2	1.9	1.2	2.3	2.6	2.6	2.6	2.0
2.0	2.0								
1105	70.2	36.3	.0	.0	.0	.0			
.0	.0	.0	.0	.0	.0	.0	.0	.0	.0
.0	.0	.0	.0	.0	.0	.0	58.4	25.0	1.6
1.2	1.0	1.1	.5	.4	.6	1.2	1.2	1.9	.3
.1	.3								
1106	69.0	36.4	53.1	62.2	16.0	20.0			
.0	.0	.0	.0	.0	.0	.0	.0	.0	.0
.0	.0	.0	.0	.0	.0	.0	58.4	25.0	1.6
1.2	1.0	1.1	.5	.4	.6	1.2	1.2	1.9	.3
.1	.3								
1107	80.0	30.0	.0	.0	.0	.0			
.0	.0	.0	.0	.0	.0	.0	.0	.0	.0
.0	.0	.0	.0	.0	.0	.0	12.1	1.9	1.9
.9	.9	.4	.4	.4	.4	.4	.4	.4	.4
.3	.3								
1108	77.8	29.9	57.0	69.7	21.0	23.0			
.0	.0	.0	.0	.0	.0	.0	.0	.0	.0
.0	.0	.0	.0	.0	.0	.0	12.1	1.9	1.9
.9	.9	.4	.4	.4	.4	.4	.4	.4	.4
.3	.3								
1113	77.7	29.6	.0	.0	.0	.0			
.2	.1	.1	.1	.1	.1	.1	.0	.0	.0
.0	.0	.0	.0	.0	.0	.0	3.5	1.2	1.2
.5	.5	.5	.3	.3	.3	.3	.3	.3	.3
.3	.4								
1114	79.0	29.3	59.0	70.2	21.0	22.0			
.2	.1	.1	.1	.1	.1	.1	.0	.0	.0
.0	.0	.0	.0	.0	.0	.0	3.5	1.2	1.2
.6	.6	.6	.3	.3	.3	.3	.3	.3	.3
.3	.4								

1115	54.7	38.8	.0	.0	.0	.0			
.1	.1	.0	.0	.0	.0	.0	.0	.0	.0
.0	.0	72.0	18.7	2.0	2.0	.7	.7	.6	.6
.6	.3	.3	.3	.3	.3	.3	.3	.3	.4
.5	.9								
1118	54.6	39.2	44.7	52.8	14.0	23.0			
.1	.1	.0	.0	.0	.0	.0	.0	.0	.0
.0	.0	72.0	18.7	2.0	2.0	.7	.7	.6	.5
.6	.3	.3	.3	.3	.3	.3	.3	.3	.4
.5	.9								
1124	77.8	31.0	56.4	68.6	21.0	26.0			
.0	.0	.0	.0	.0	.0	.0	.0	.0	.0
.0	.0	.0	.0	8.7	3.5	1.5	.8	.7	.5
.5	.4	.6	.7	.7	.9	.9	.8	.7	.8
.2	.5								
1125	77.5	30.7	.0	.0	.0	.0			
.0	.0	.0	.0	.0	.0	.0	.0	.0	.0
.0	.0	.0	.0	8.7	3.5	1.5	.8	.7	.5
.5	.4	.6	.7	.7	.9	.9	.8	.7	.8
.2	.5								
1130	78.0	29.7	54.2	68.9	15.0	17.0			
.0	.0	.0	.0	.0	.0	.0	.0	.0	.0
.0	.0	.0	.0	.0	.0	.0	.0	3.1	.9
.7	.7	.7	.7	.7	.7	.7	.3	.2	.2
.2	.2								
1131	78.0	30.1	.0	.0	.0	.0			
.0	.0	.0	.0	.0	.0	.0	.0	.0	.0
.0	.0	.0	.0	.0	.0	.0	.0	3.1	.9
.7	.7	.7	.7	.7	.7	.7	.3	.2	.2
.2	.2								
1144	80.0	31.0	58.9	72.9	24.0	25.0			
.0	.0	.0	.0	.0	.0	.0	.0	.0	.0
.0	.0	.0	.0	.0	.0	.0	.0	.0	.0
.0	.0	.0	771.9	4.1	2.1	1.3	1.2	1.0	1.0
.8	.5								
1145	80.5	31.5	.0	.0	.0	.0			
.0	.0	.0	.0	.0	.0	.0	.0	.0	.0
.0	.0	.0	.0	.0	.0	.0	.0	.0	.0
.0	.0	.0	771.9	4.1	2.1	1.3	1.2	1.0	1.0
.8	.5								
1148	78.0	30.8	.0	.0	.0	.0			
.0	.0	.1	.0	.0	.0	.0	.0	.0	.0
.0	.0	.0	.0	.0	.0	.0	.0	.0	.0
.0	.0	.0	277.1	4.7	4.6	1.2	1.2	1.2	1.2
1.2	1.2								
1149	83.4	30.2	65.0	73.1	22.0	25.0			
.0	.0	.1	.0	.0	.0	.0	.0	.0	.0
.0	.0	.0	.0	.0	.0	.0	.0	.0	.0
.0	.0	.0	277.1	4.7	4.6	1.2	1.2	1.2	1.2
1.2	1.2								
1172	82.5	31.6	.0	.0	.0	.0			
.1	.1	.0	.0	.0	.0	.0	.0	.0	.0
.0	.0	.0	.0	.0	.0	.0	.0	.0	.0
88.7	100.0	4.9	1.2	.6	.9	.6	.4	.5	.4
.4	7.1								
1173	81.3	31.5	62.1	72.6	20.0	24.0			
.1	.1	.0	.0	.0	.0	.0	.0	.0	.0
.0	.0	.0	.0	.0	.0	.0	.0	.0	.0
88.7	100.0	4.9	1.2	.6	.9	.6	.4	.5	.4
.4	7.1								
1174	83.0	32.7	.0	.0	.0	.0			
.1	.0	.0	.0	.0	.0	.0	.0	.0	.0
.0	.0	.0	.0	.0	.0	.0	.0	.0	.0
29.1	262.2	50.6	1.4	1.3	.9	.7	.6	.6	.2
.3	36.7								
1175	82.8	32.2	64.2	73.2	19.6	24.0			
.1	.0	.0	.0	.0	.0	.0	.0	.0	.0
.0	.0	.0	.0	.0	.0	.0	.0	.0	.0
29.1	262.2	50.6	1.4	1.3	.9	.7	.6	.6	.2
.3	36.7								
1180	79.7	30.9	.0	.0	.0	.0			
.8	.2	.0	.0	.0	.0	.0	.0	.0	.0
.0	.0	.0	.0	.0	.0	.0	19.0	15.5	2.0
.0	.9	.5	.5	.5	.4	.4	.3	.3	.2
.2	15.1								

1181	80.3	30.8	58.1	69.3	21.0	24.0				
.8	.2	.0	.0	.0	.0	.0	.0	.0	.0	.0
.0	.0	.0	.0	.0	.0	.0	19.0	15.5	2.0	
.9	.9	.5	.5	.5	.4	.4	.3	.3	.2	
.2	15.1									
1188	78.7	29.5	.0	.0	.0	.0				
1.3	.0	.0	.0	.0	.0	.0	.0	.0	.0	
.0	.0	.0	.0	.0	1.2	2.2	1.9	1.0	.5	
.4	.4	.3	.3	.3	.2	.2	.3	.2	.2	
.2	3.4									
1189	76.8	29.4	58.0	71.8	22.0	27.0				
1.3	.0	.0	.0	.0	.0	.6	.0	.0	.0	
.0	.0	.0	.0	.0	1.2	2.2	1.9	1.0	.5	
.4	.4	.3	.3	.3	.2	.2	.3	.2	.2	
.2	3.4									
1204	77.5	31.5	57.1	68.9	20.0	26.0				
.2	.2	.2	.2	.1	.0	.0	.0	.0	.0	
.0	.0	.0	.0	4.0	6.8	2.0	1.1	.7	.8	
.6	.4	.4	.4	.4	.3	.4	.3	.2	.3	
.2	28.5									
1205	76.7	31.0	.0	.0	.0	.0				
.2	.2	.2	.2	.1	.0	.0	.0	.0	.0	
.0	.0	.0	.0	4.0	6.8	2.0	1.1	.7	.8	
.6	.4	.4	.4	.4	.3	.4	.3	.2	.3	
.2	28.5									
1208	72.3	35.5	54.5	63.9	15.0	22.0				
.8	.6	.0	.0	.0	.0	.0	.0	.0	.0	
.0	.0	.0	.0	.0	7.5	26.4	1.0	.9	.7	
.5	.4	.5	.3	.3	.3	.3	.3	.3	.5	
.3	3.9									
1209	71.5	34.7	.0	.0	.0	.0				
.8	.6	.0	.0	.0	.0	.0	.0	.0	.0	
.0	.0	.0	.0	.0	7.5	26.4	1.0	.9	.7	
.5	.4	.5	.3	.3	.3	.3	.3	.3	.5	
.3	3.9									
1212	59.0	37.9	42.2	55.8	11.0	15.0				
.0	.0	.0	.0	.0	.1	.1	6.2	104.3	79.0	
3.3	1.5	1.9	.7	.3	.4	.3	.4	.4	.4	
.1	.2	.2	.2	.2	.1	.2	.1	.0	.0	
.1	16.8									
1213	57.2	37.8	.0	.0	.0	.0				
.0	.0	.0	.0	.0	.1	.1	6.2	104.3	79.0	
3.3	1.5	1.9	.7	.3	.4	.3	.4	.4	.4	
.1	.2	.2	.2	.2	.1	.2	.1	.0	.0	
.1	16.8									
1232	57.3	38.3	41.9	54.1	15.0	20.0				
1.1	.1	.0	.0	.0	.0	.0	.0	181.4	310.0	
3.9	.8	.6	.5	.4	.4	.3	.4	.2	.3	
.2	.2	.2	.2	.2	.1	.1	.2	.2	.2	
.2	6.4									
1233	53.7	38.0	.0	.0	.0	.0				
1.1	.1	.0	.0	.0	.0	.0	.0	181.4	310.0	
3.9	.8	.6	.5	.4	.4	.3	.4	.2	.3	
.2	.2	.2	.2	.2	.1	.1	.2	.2	.2	
.2	6.4									
1312	54.7	39.8	51.5	53.6	.0	.0				
.1	.0	.0	.0	.0	.0	.0	.0	.0	.0	
.0	.0	.0	.0	434.7	15.4	2.0	.0	.0	.8	
.5	.4	.5	.5	.3	.3	.2	.3	.2	.2	
.2	.2									
1313	55.8	39.7	49.7	53.2	.0	.0				
.1	.0	.0	.0	.0	.0	.0	.0	.0	.0	
.0	.0	.0	.0	434.7	15.4	2.0	.0	.0	.8	
.5	.4	.5	.5	.3	.3	.2	.3	.2	.2	
.2	.2									
1306	68.4	35.5	56.3	61.2	.0	.0				
.2	.0	.0	.0	.0	.0	.0	.0	.0	.0	
.0	.0	.0	.0	5.2	24.0	2.6	2.1	1.5	.7	
.8	.6	.3	.3	.3	.3	.3	.3	.3	.3	
.2	.3									
1307	68.2	35.4	55.8	61.3	.0	.0				
.2	.0	.0	.0	.0	.0	.0	.0	.0	.0	
.0	.0	.0	.0	5.2	24.0	2.6	2.1	1.5	.7	
.8	.6	.3	.3	.3	.3	.3	.3	.3	.3	
.2	.3									

```
 1388   71.7   33.5   54.1   64.2     .0     .0
   13.7    5.0     .0     .0     .0     .0     .0     .0     .0     .0
      .0     .0     .5   10.4    2.4    1.1     .9     .9     .6     .4
      .5     .2     .3     .3     .3     .2     .2     .2     .2     .3
      .5     .3
 1389   73.0   33.6   56.0   65.0     .0     .0
   13.7    5.0     .0     .0     .0     .0     .0     .0     .0     .0
      .0     .0     .5   10.4    2.4    1.1     .9     .9     .6     .4
      .5     .2     .3     .3     .3     .2     .2     .2     .2     .3
      .5     .3
 1332   61.3   37.4   52.8   57.0     .0     .0
    2.6    1.0     .0     .0     .0     .0     .0     .0     .0     .0
      .0     .1   21.5   11.1    1.7     .9     .7     .8     .5     .6
      .4     .2     .3     .3     .2     .3     .2     .5     .4     .3
      .3     .4
 1333   61.0   37.5   51.5   57.3     .0     .0
    2.6    1.0     .0     .0     .0     .0     .0     .0     .0     .0
      .0     .1   21.5   11.1    1.7     .9     .7     .8     .5     .6
      .4     .2     .3     .3     .2     .3     .2     .5     .4     .3
      .3     .4
 1336   53.4   39.5   48.6   52.2     .0     .0
    3.5     .0     .0     .0     .0     .0     .0     .0     .0     .0
      .0     .0  248.5  249.7    1.4    1.0     .8     .8     .6     .5
      .3     .3     .4     .2     .2     .2     .3     .3     .2     .4
      .1     .3
 1337   54.0   39.3   49.2   52.5     .0     .0
    3.5     .0     .0     .0     .0     .0     .0     .0     .0     .0
      .0     .0  248.5  249.7    1.4    1.0     .8     .8     .6     .5
      .3     .3     .4     .2     .2     .2     .3     .3     .2     .4
      .1     .3
 1346   61.0     .0     .0     .0     .0     .0
      .2     .0     .0     .0     .0     .0     .0     .0     .0   30.6    3.0
     1.6     .7     .7     .7     .8     .8     .6     .2     .1     .1
      .1     .1     .1     .1     .1     .1     .1     .1     .2     .2
      .2     .4
 1349   63.4     .0   47.3   58.6     .0     .0
      .2     .0     .0     .0     .0     .0     .0     .0     .0   30.6    3.0
     1.6     .7     .7     .7     .8     .8     .6     .2     .1     .1
      .1     .1     .1     .1     .1     .1     .1     .1     .2     .2
      .2     .4
END
```

TABLE V

C-Curve Parameters For Aluminum Alloy 2024, K_5 For All Cases is Taken Equal to 32,000 cal/mol.

Temper	Sequence	Property	σ_m	σ_o	K_2, ns	K_3 Cal/Mol	K_4 Kelvins	Est. Std. Dev.
T851	A	U.T.S. ksi	71.2	38.5	14.9	125	750	2.0
	A	Y.S. ksi	66.6	27.8	12.1	125	750	2.4
	A	HRB	82.5	22.0	23.1	125	750	2.8
	A	%IACS	38.7	44.5	11.3	125	750	0.55
T851	B	U.T.S. ksi	71.2	47.0	25.0	45	750	2.6
	B	Y.S. ksi	66.6	34.0	17.2	45	750	2.7
	B	HRB	82.5	43.7	32.6	45	750	3.0
	B	%IACS	38.7	44.0	18.2	45	750	0.49
T351	A	U.T.S. ksi	68.5	43.0	18.1	138	760	1.6
	A	Y.S. ksi	55.4	37.5	12.8	138	760	1.8
	A	HRB	77.4	34.4	23.8	138	760	3.1
	A	%IACS	29.2	40.5	11.4	138	760	1.1
T851	B	U.T.S. ksi	68.5	53.6	12.2	156	800	1.6
	B	Y.S. ksi	55.4	43.0	21.0	156	800	3.2
	B	HRB	77.4	55.5	13.9	156	800	2.2
	B	%IACS	29.2	38.7	5.2	156	800	1.0

TABLE VI

Additional Specimens Not Shown in Figure 66 Studied in the TEM
(Specimen Numbers Refer to Table IV)

Specimen Number	"Pre-aging" Treatment	Final Temper Treatment
1001	None (direct quench)	T4
1008	None (direct quench)	T351
1009	None (direct quench)	T851
1040	Sequence A 350°C for 20s	T851
1042	Sequence A 350°C for 109s	T851

TABLE VII

Average Hardness Values of 3 Percent Stretched and Unstretched Specimens After Aging

Aging Temperature (°C)	HARDNESS (HRB)			
	After 6 Hours, Stretched	After 6 Hours Unstretched	After 16 Hours Unstretched	After 30 Hours Unstretched
21	77	75	-	-
35	78	76	-	-
50	79	77	-	-
150	80	74	76	79
170	-	77	79	80
180	-	80	82	77
190	84	79	-	71

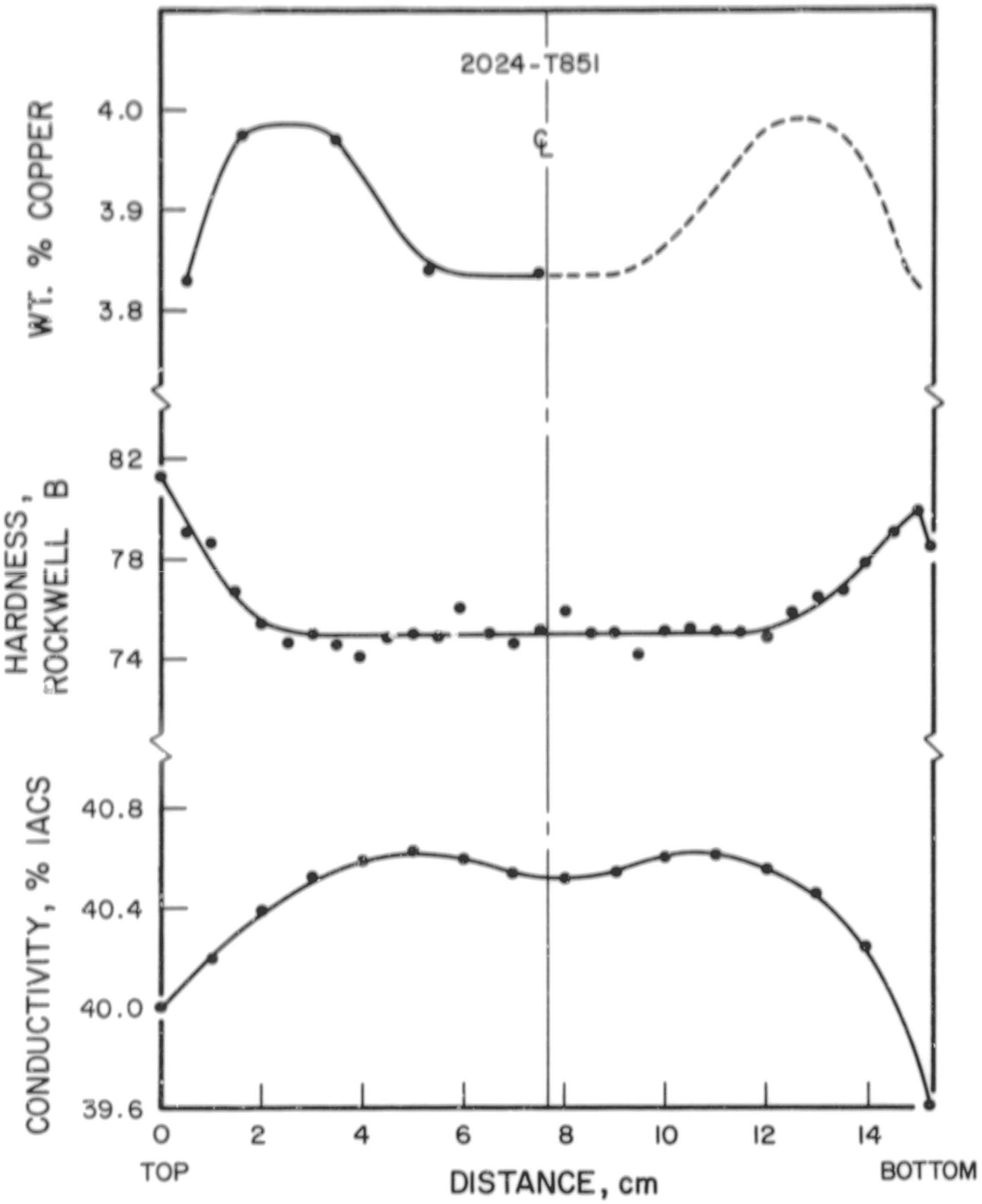

Figure 1. Measured average composition (wt%Cu), hardness (HRB), and eddy-current conductivity (%IACS) distance across the thickness of a 15.24 cm thick plate of the 2024-T851 aluminum alloy.

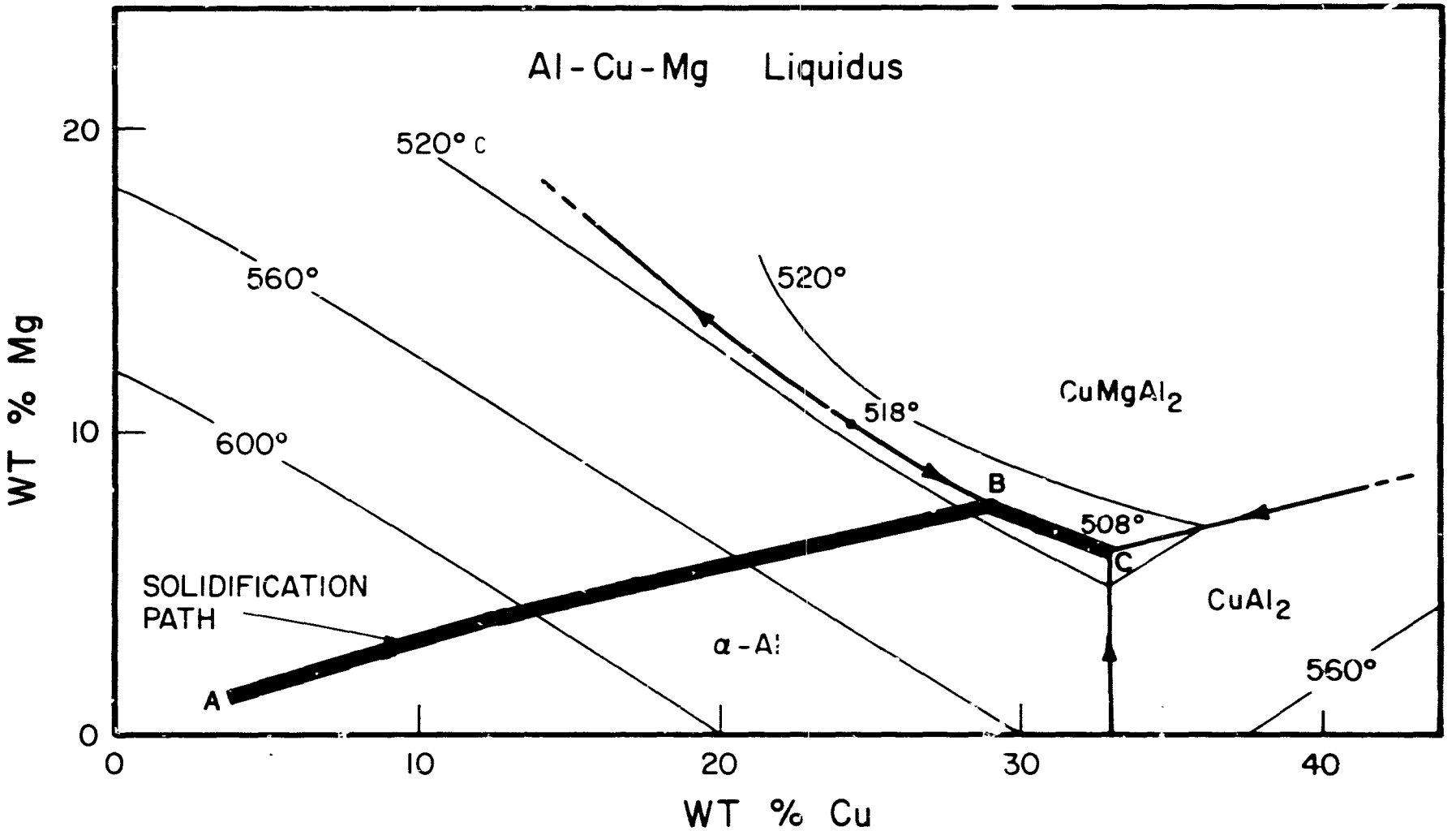

Figure 2. Calculated solidification "path" (AB) shown on the liquidus surface of the aluminum rich corner of the Al-Cu-Mg system. The second phase to form is $CuMgAl_2$ by way of the monovariant eutectic $L \rightarrow \alpha\text{-Al}+CuMgAl_2$ along BC and solidification is completed at the ternary eutectic $L \rightarrow \alpha\text{-Al}+CuMgAl_2+CuAl_2$ at point C.

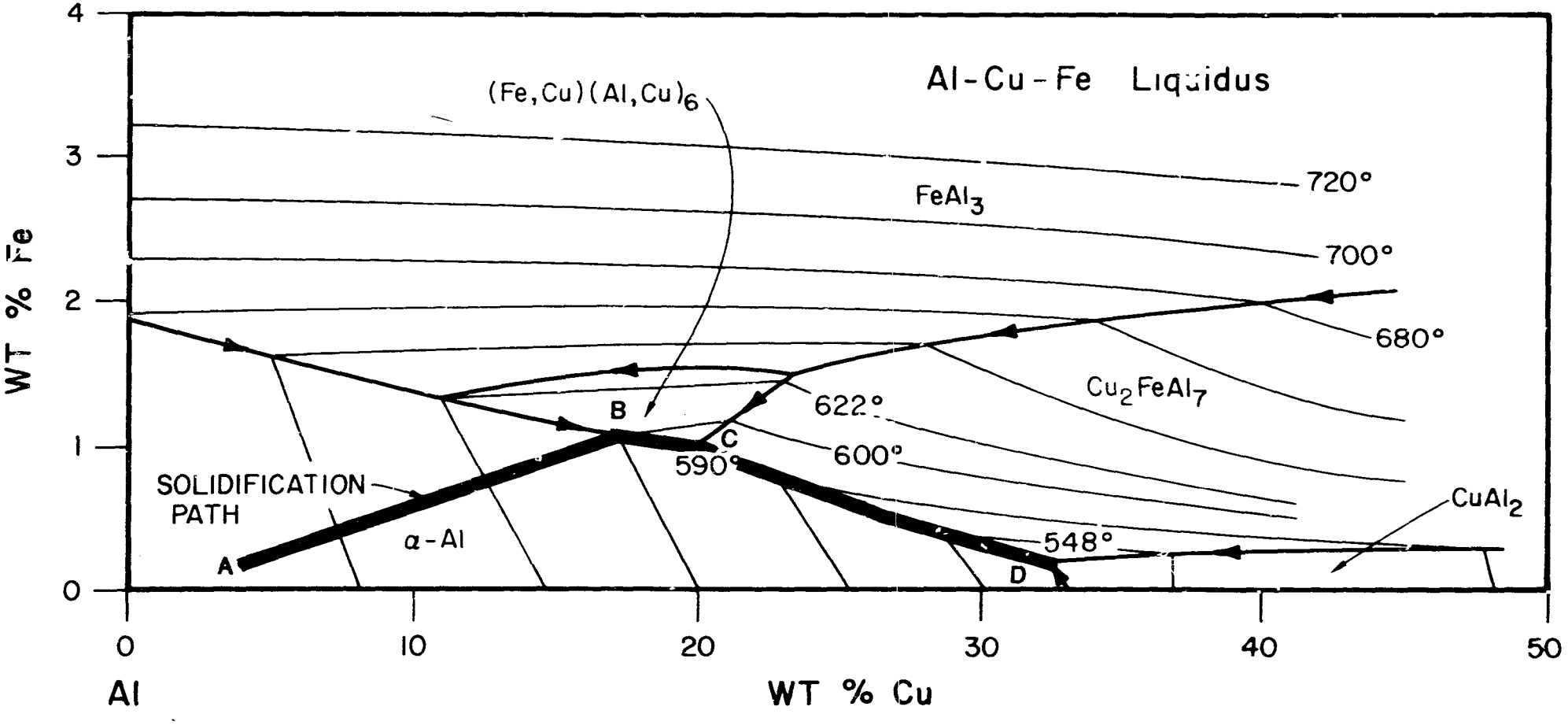

Figure 3. Calculated solidification "path" AB shown on the liquidus surface of the aluminum rich corner of the Al-Cu-Fe system. The second phase to form is $(Fe,Cu)(Al,Cu)_6$ along BC followed by Cu_2FeAl_7 along CD. Solidification is completed at point D by the ternary eutectic $L \rightarrow \alpha\text{-Al}+Cu_2FeAl_7+CuAl_2$.

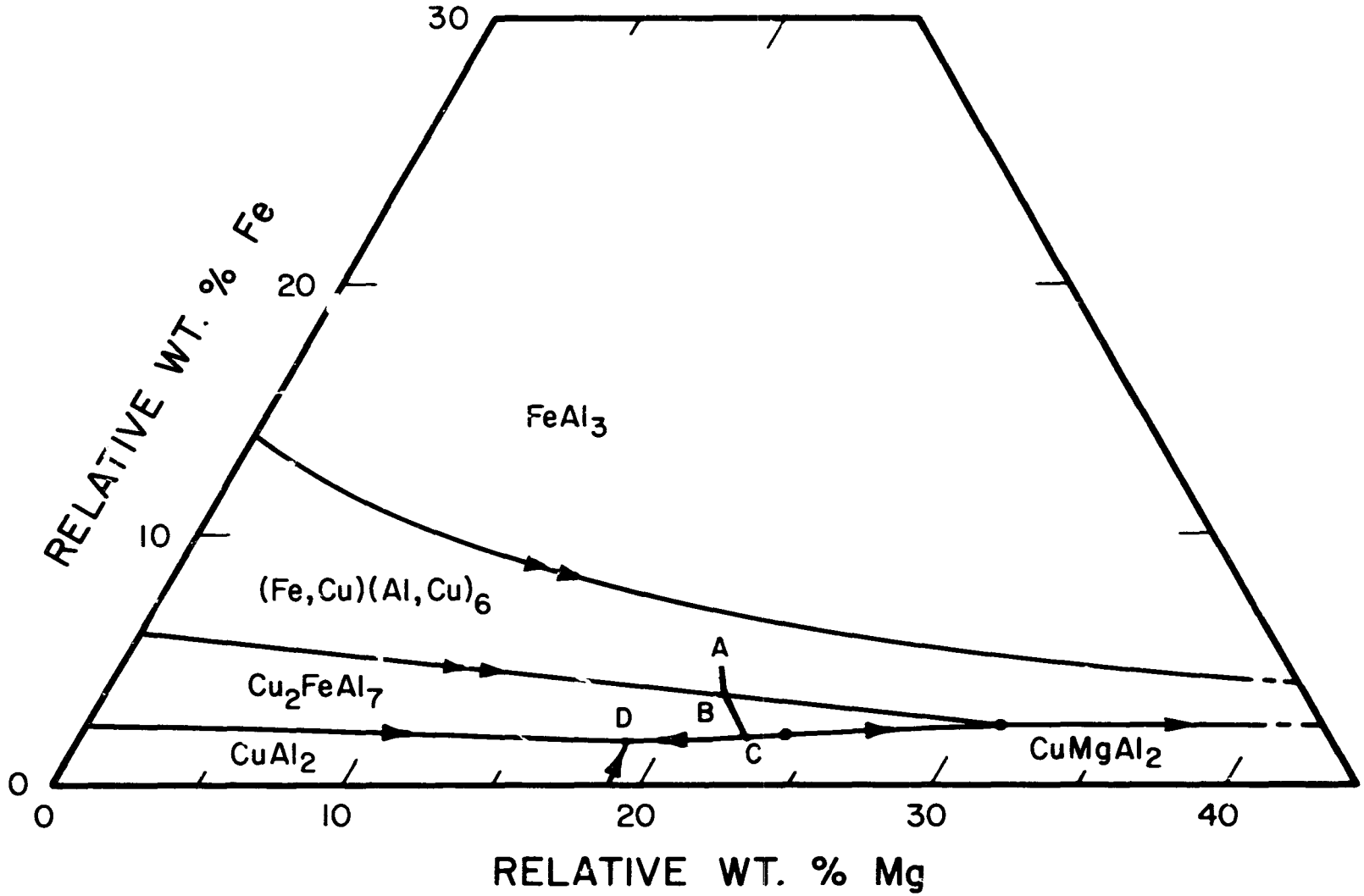

Figure 4. Aluminum rich alloys in the Al-Cu-Mg-Fe system showing relative percentages of Fe vs. Mg with the remainder copper (4). Regions represent solidification of α-Al in addition to the phase noted. After the formation of primary α-Al, the solidification continues along AB in the region for $(Fe,Cu)(Al,Cu)_6$ where $L \rightarrow \alpha\text{-Al}+(Fe,Cu)(Al,Cu)_6$. At point B, the ternary peritectic reaction $L + (Fe,Cu)(Al,Cu)_6 \rightarrow \alpha\text{-Al}+Cu_2FeAl_7$ occurs thermodynamically but is kinetically difficult. From B to C with region for Cu_2FeAl_7, solidification continues with $L \rightarrow \alpha\text{-Al}+Cu_7FeAl_7$. Along CD solidification involves $L \rightarrow \alpha\text{-Al}+Cu_2FeAl_7+CuMgAl_2$ and finally solidification is completed at D by the quaternary eutectic $L \rightarrow \alpha\text{-Al}+Cu_7FeAl_7+CuMgAl_2+CuAl_2$.

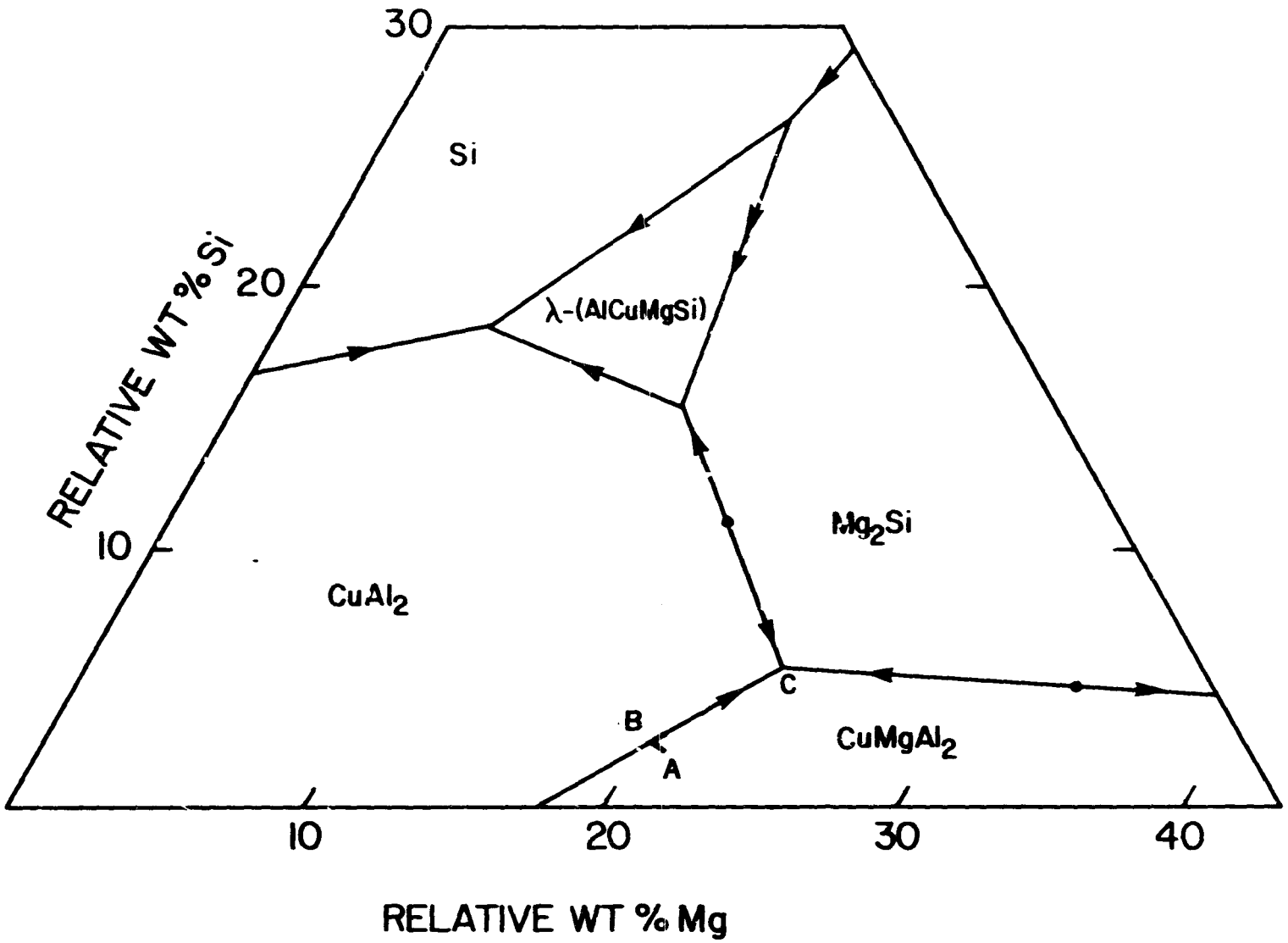

Figure 5. Aluminum rich alloys of the Al-Cu-Mg-Si systems showing relative percentages of Si vs. Mg with the remainder Cu (4). Regions represent solidification of α-Al in addition to the phase noted. After solidification of primary α-Al, the solidification "path" AB lies in the region for $L \rightarrow \alpha\text{-Al}+CuMgAl_2$.

Subsequently, the "path" BC moves along the tenary eutectic for $L \rightarrow \alpha\text{-Al}+CuMgAl_2+CuAl_2$. Solidification is completed at point C by the quarternary eutectic $L \rightarrow \alpha\text{-Al}+CuMgAl_2+CuAl_2+Mg_2Si$.

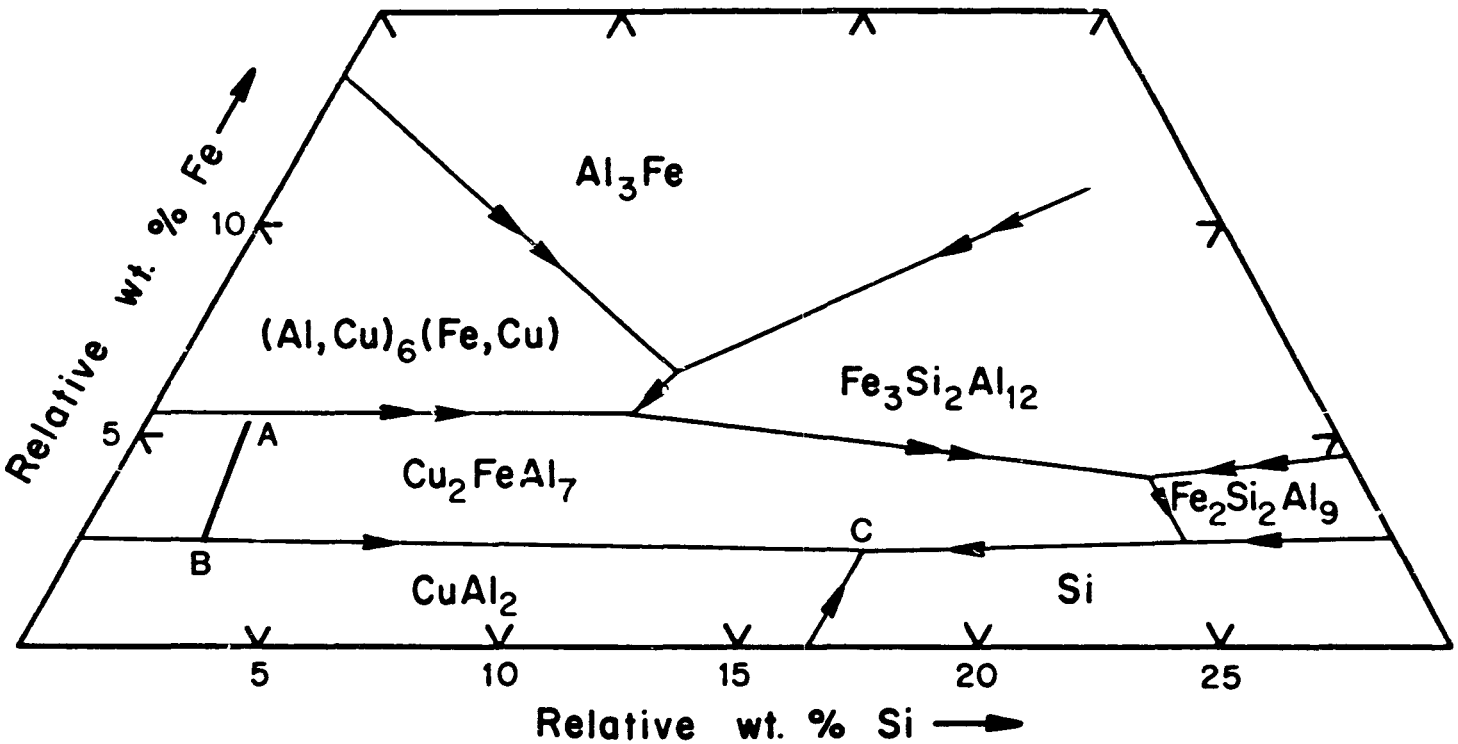

Figure 6. Aluminum rich alloys of the Al-Cu-Fe-Si system showing relative percentage of Fe vs. Si with the remainder copper (4). Regions represent solidification of α-Al in addition to the phase noted. After solidification of primary α-Al the solidification "path" (AB) lies in the region for Cu_2FeAl_7 where $L \rightarrow \alpha\text{-Al}+Cu_2FeAl_7$. Solidification continues from B toward C along the ternary eutectic line $L \rightarrow \alpha\text{-Al}+Cu_2FeAl_7+CuAl_2$. Solidification may reach point C where $L \rightarrow \alpha\text{-Al}+Cu_2FeAl_7+CuAl_2+Si$.

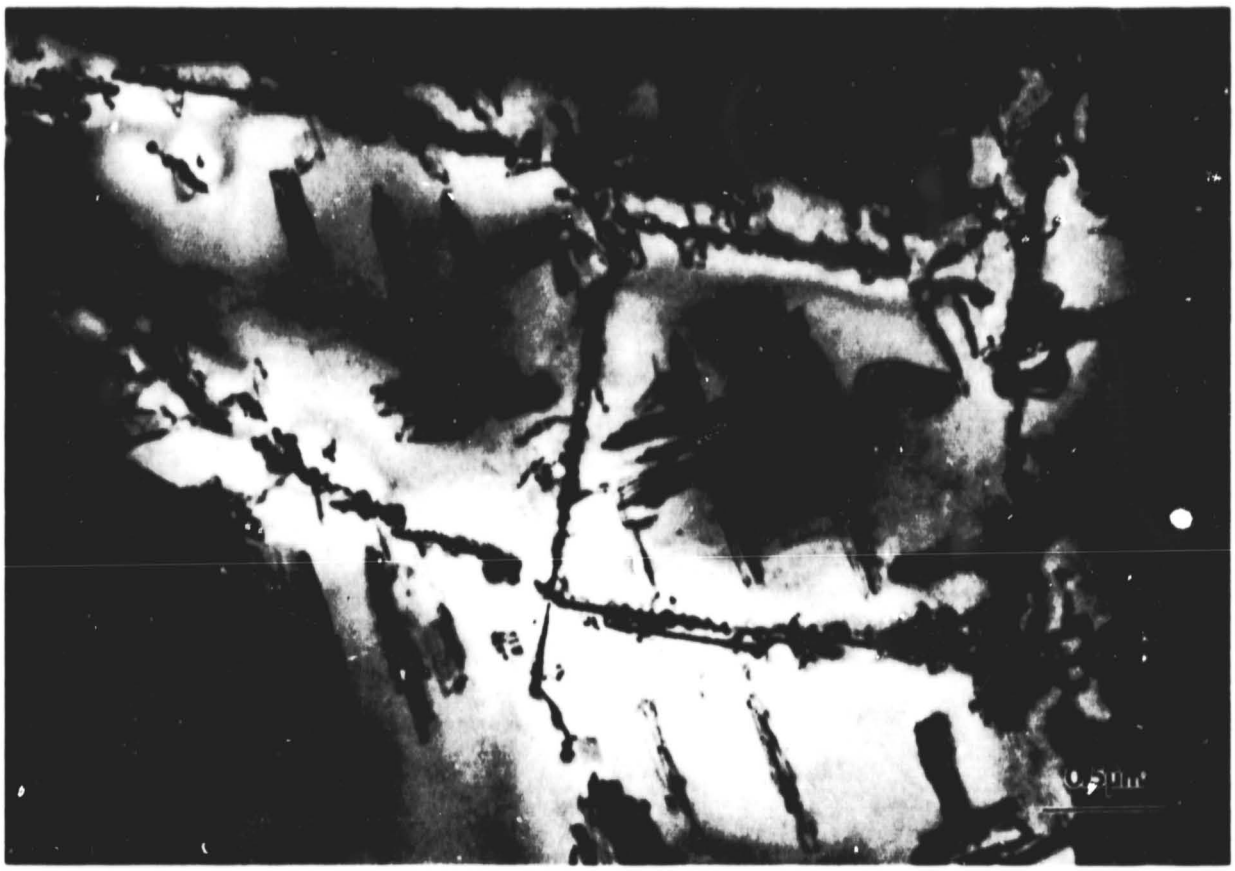

Figure 7. S' precipitates within borders of α-Al dendrites in the laboratory cast ingot.

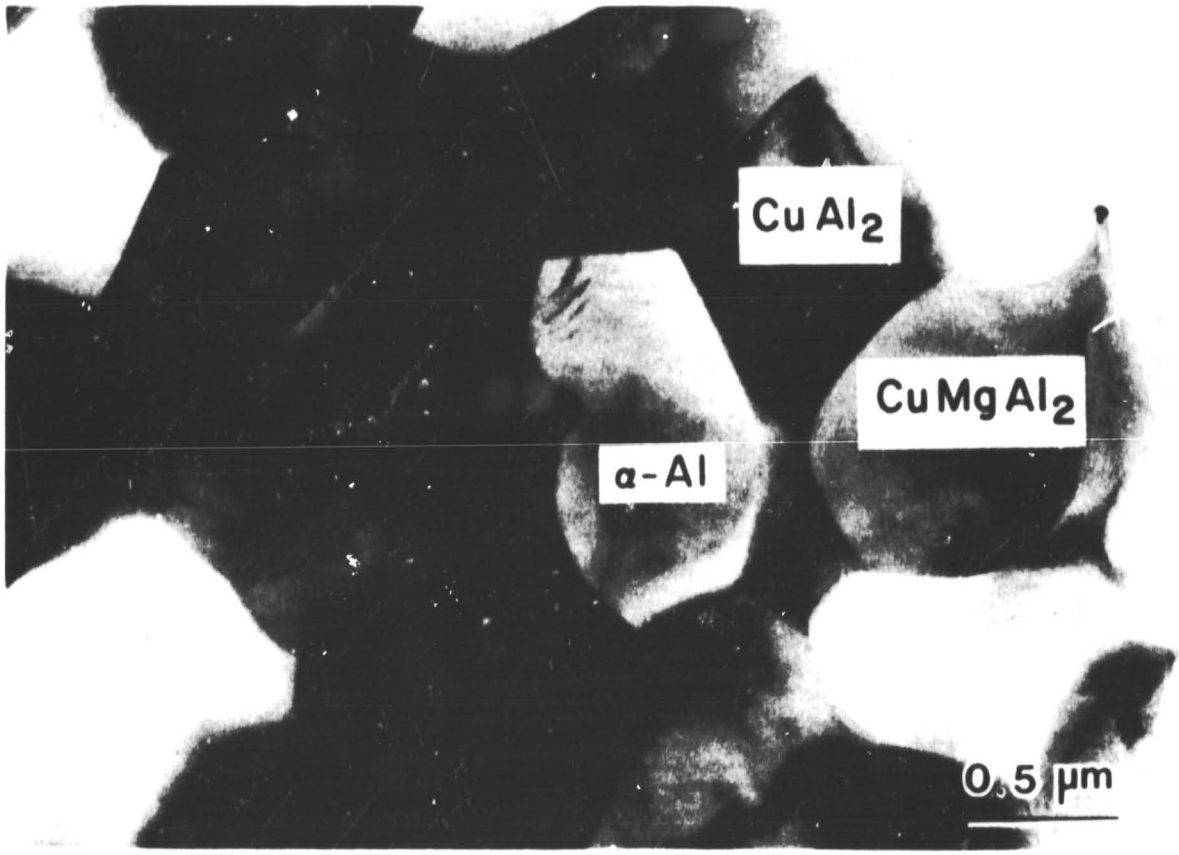

Figure 8. Interdendritic structure in laboratory cast ingot. The phases α-Al, θ-$CuAl_2$ and S-$CuMgAl_2$ are identified.

Figure 9. Cu_2FeAl_7 interdendritic phase identified by electron diffraction and EDS in the laboratory cast ingot.

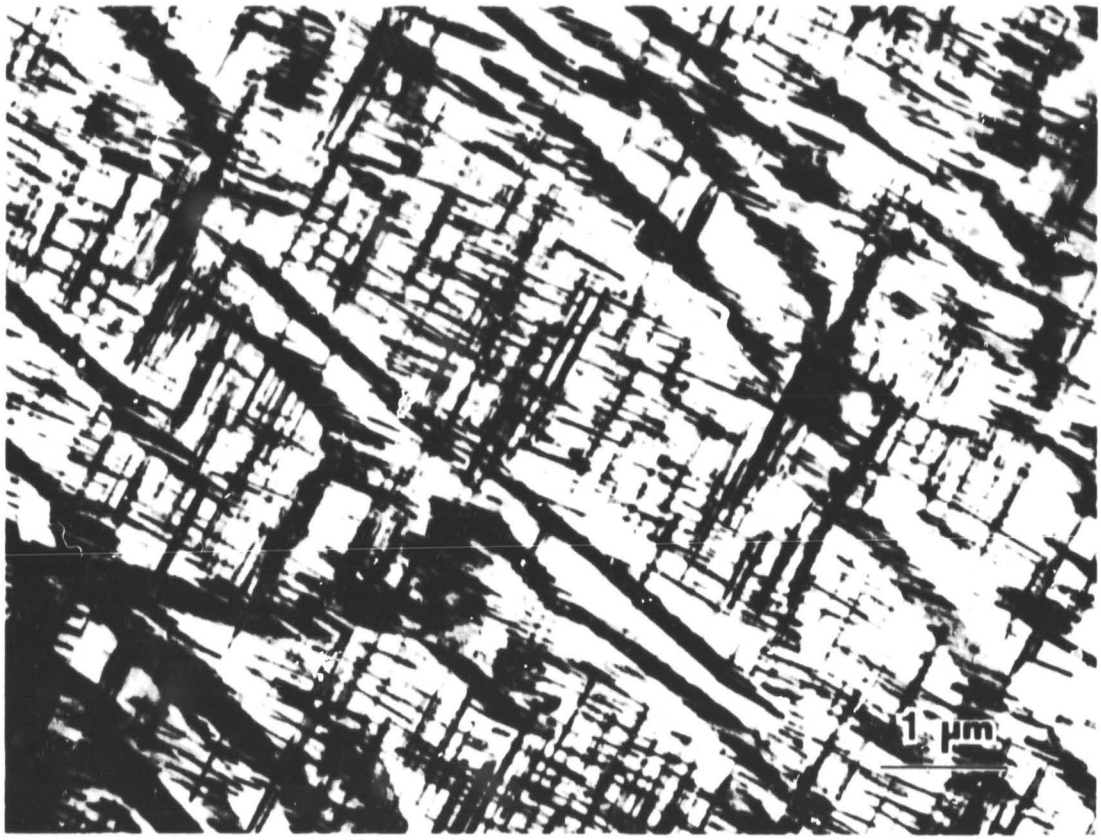

Figure 10. S' precipitates within the α-Al dendrites in the DC cast ingot.

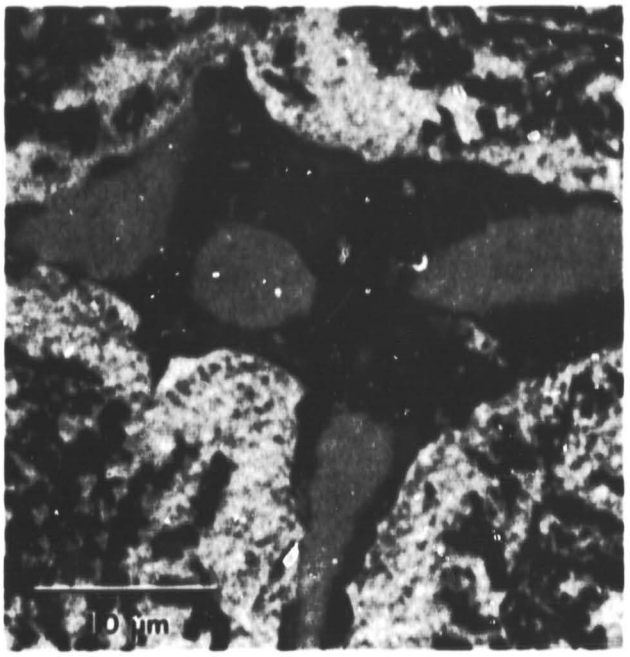

a

b

Figure 11. Typical views of the interdendritic region of the DC cast ingot. (a) Optical view. The dark gray blade is Cu_2FeAl_7; the large rounded light gray phase is α-Al(Fe,M)Si and the fine eutectic like structure consists of α-Al-$CuMgAi_2$+$CuAl_2$. (b) SEM view shows the Cu_2FeAl_7 phase.

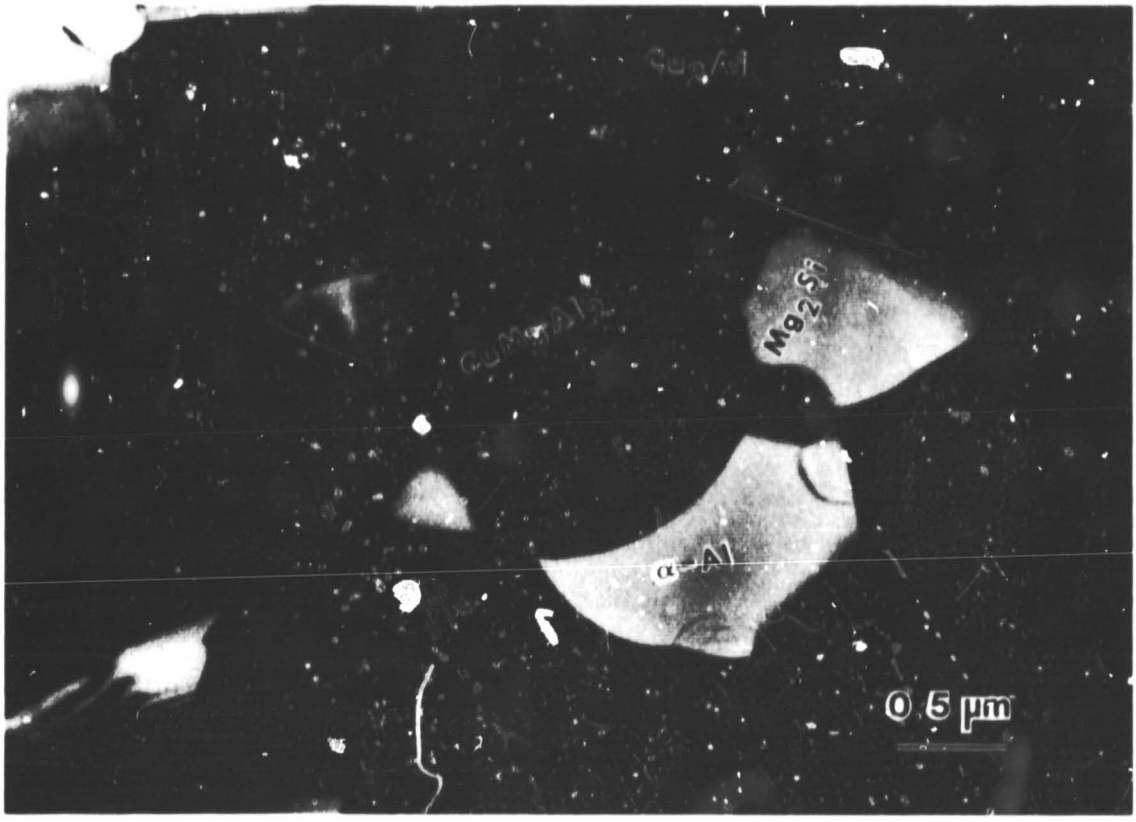

Figure 12. Interdendritic eutectic structure in the DC cast ingot. Four phases are identified; α-Al, θ-$CuAl_2$, S-$CuMgAl_2$ and Mg_2Si.

B

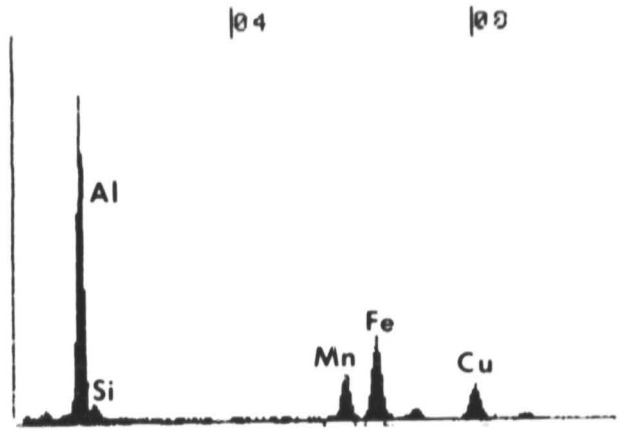

Figure 13. (a) α-Al(Fe,M)Si phase in the indendritic region of the DC cast ingot. (b) X-ray spectrum of α-Al(Fe,M)Si polyhedrally shaped particle in Figure 13(a).

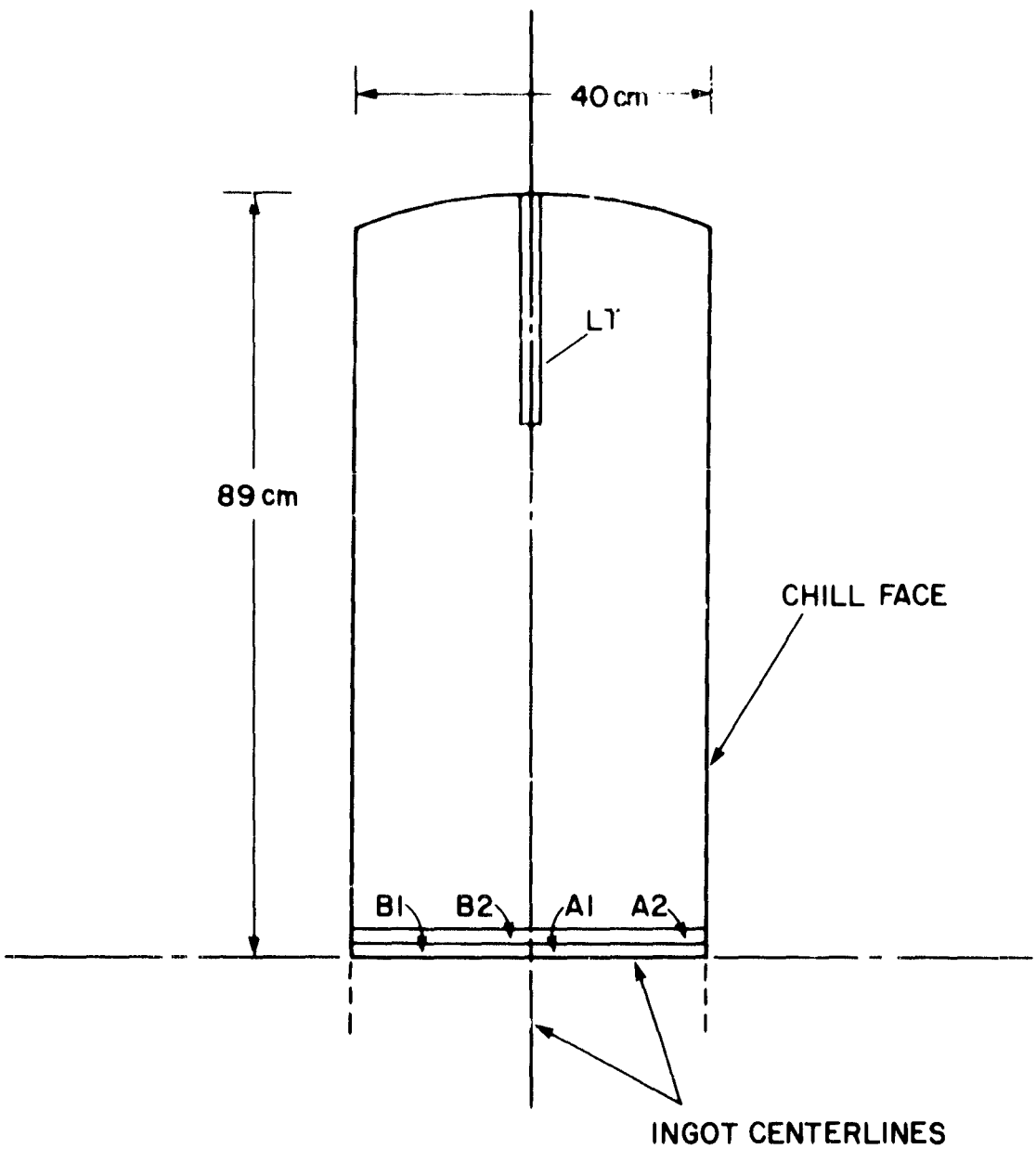

Figure 14. Location of various macrosegregation profiles taken from the transverse section of the DC cast ingot.

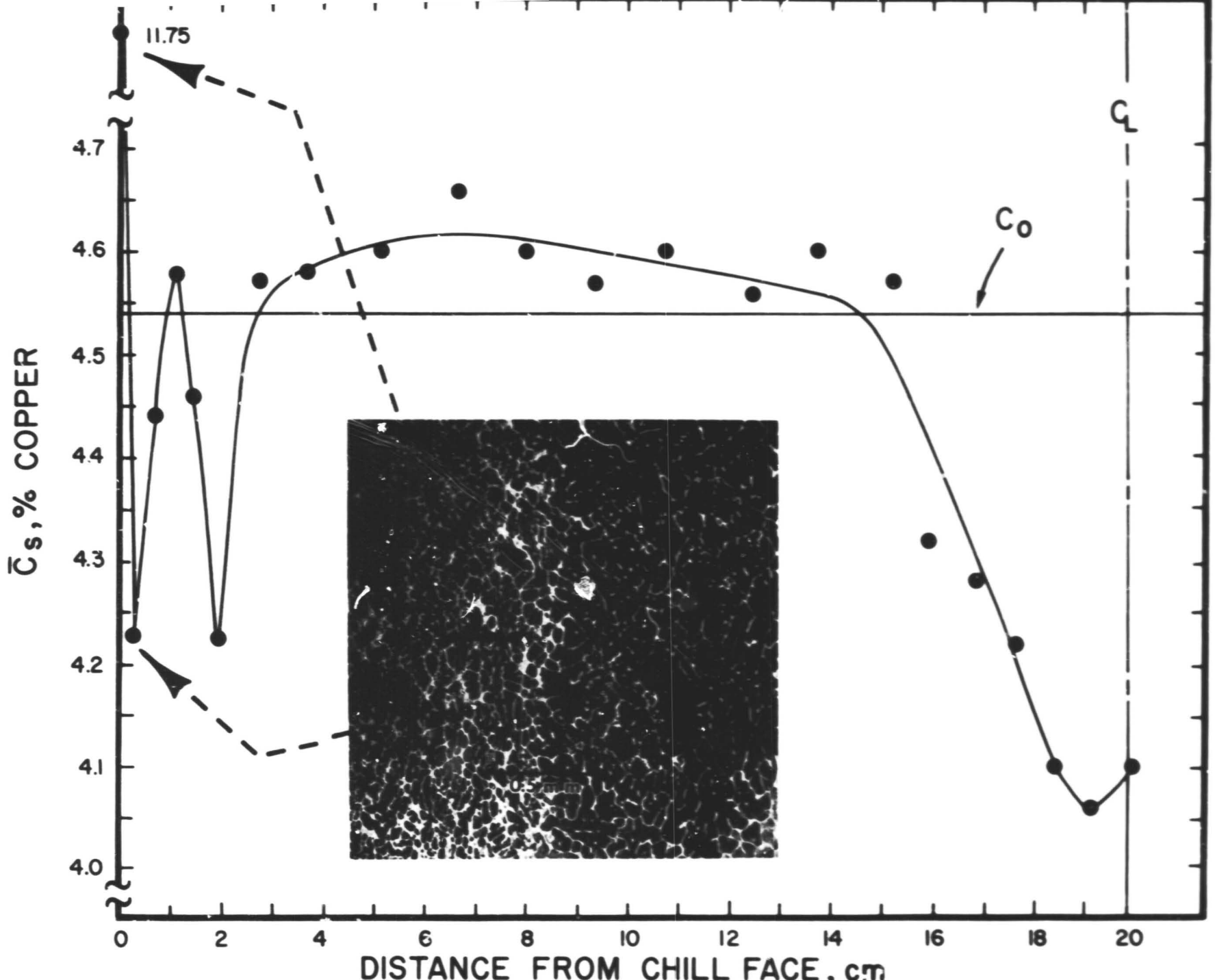

Figure 15. Macrosegregation profile, average copper content versus distance from the chill face in the short transverse direction (position B1 in Figure 14) of the semi-continuous DC cast ingot of 2024 aluminum alloy. The insert shows the drastic change in volume fraction eutectic which occurs near the chill face.

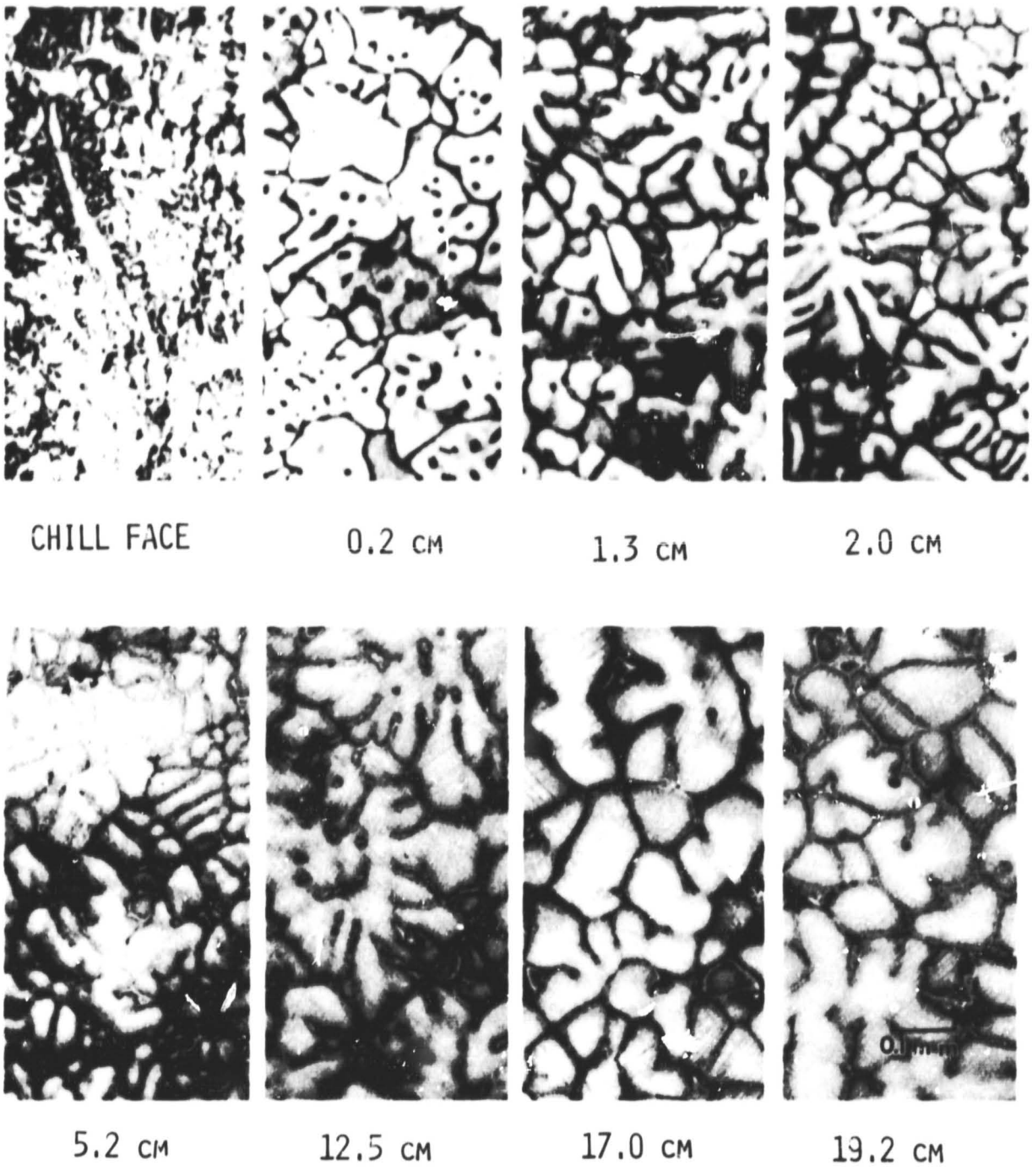

Figure 16. Optical micrographs showing microstructure of the DC cast 2024 aluminum alloy ingot at various distances (in cm) from the chill face. Keller's etch.

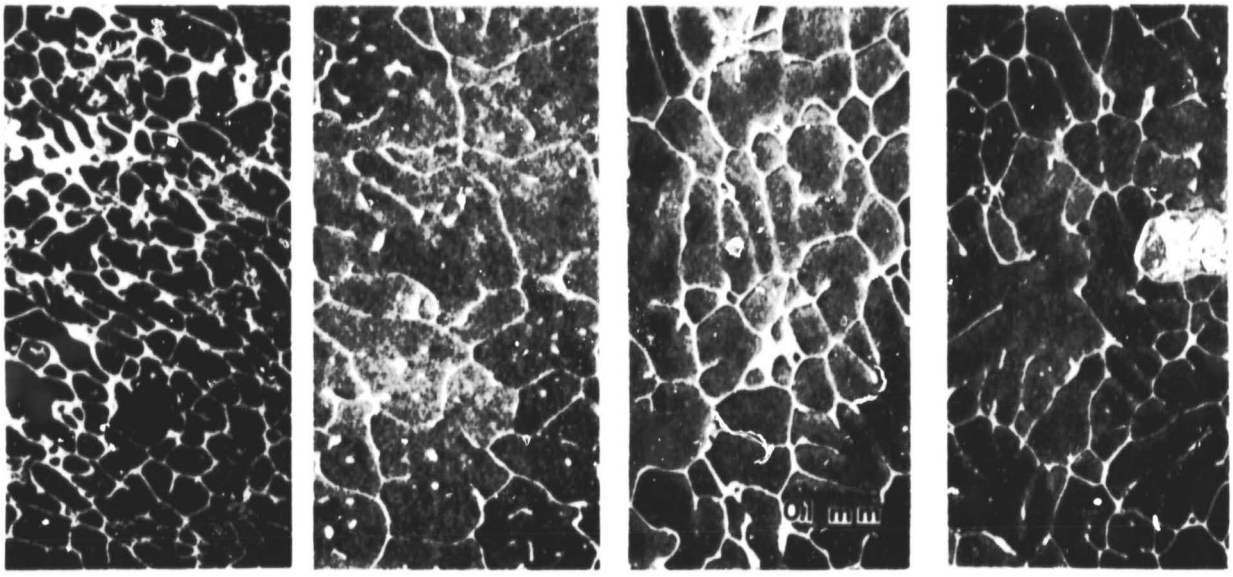

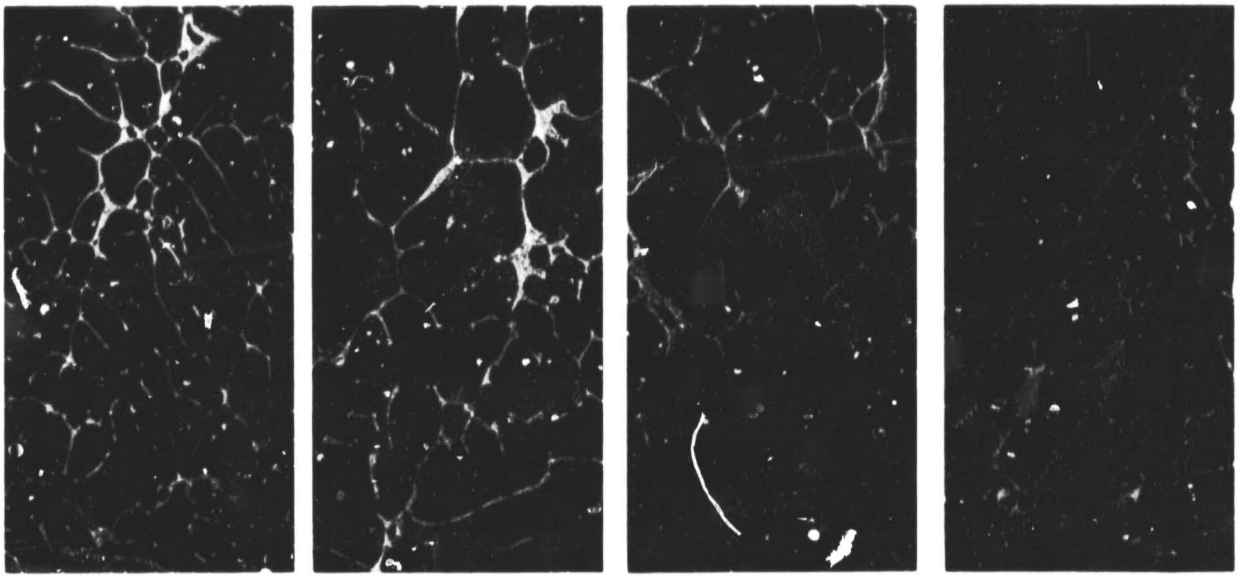

Figure 17. SEM micrographs corresponding to Figure 16.

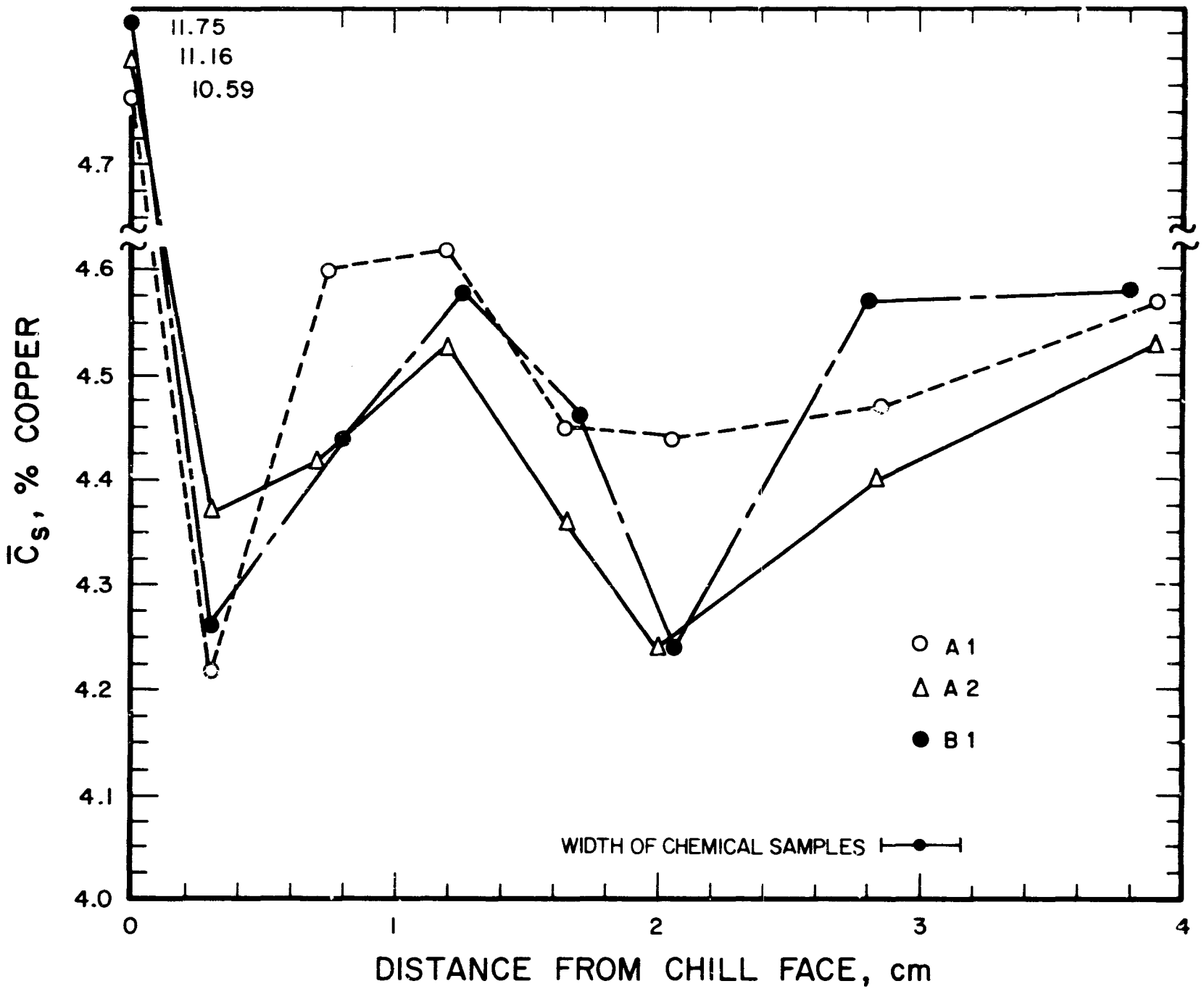

Figure 18. Macrosegregation profile, average copper content versus distance from the chill face in the short transverse direction (at three different positions A1, A2 and B1 in Figure 14) in the semi-continuou DC cast ingot of 2024 aluminum alloy.

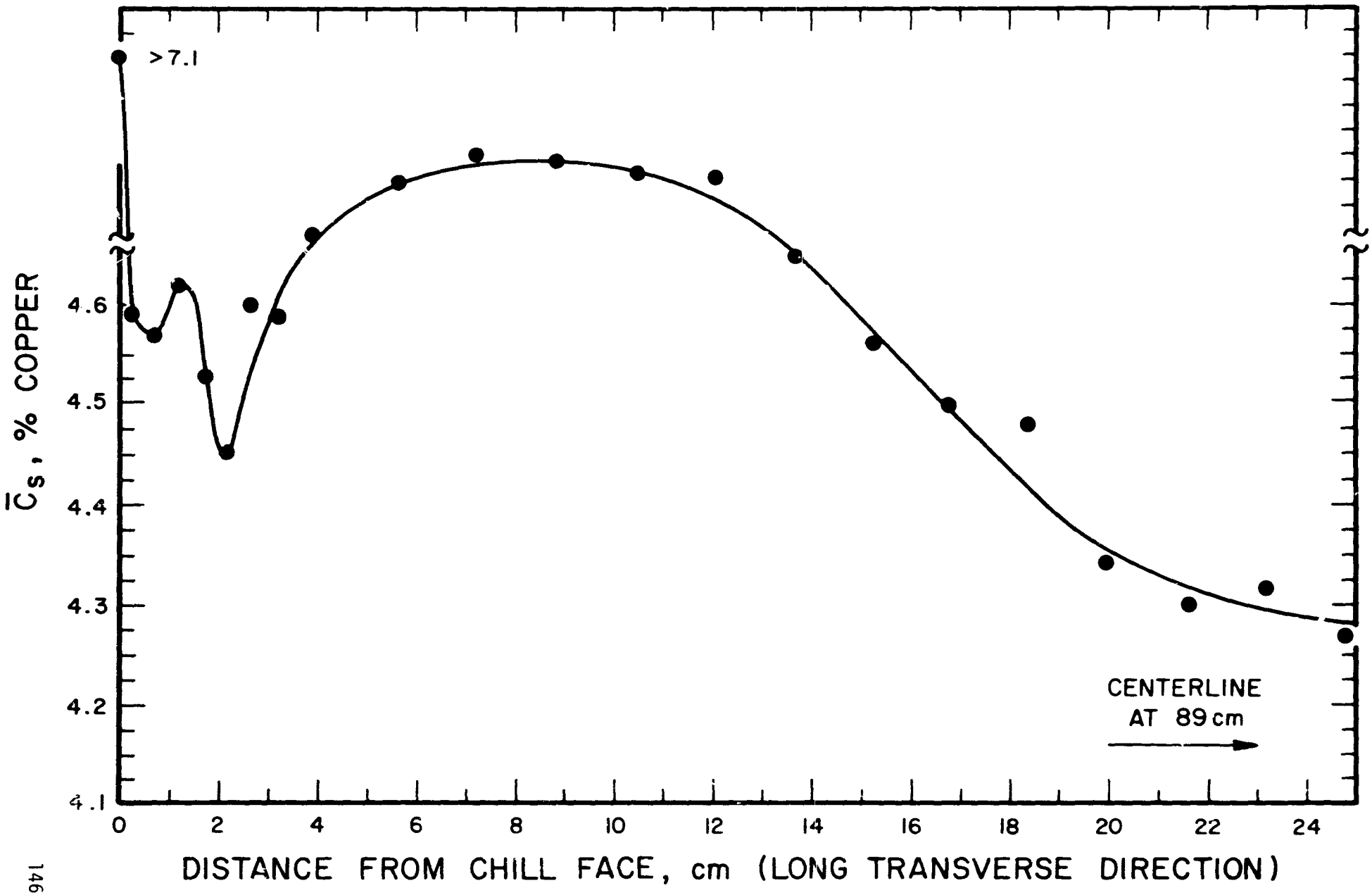

Figure 19. Macrosegregation profile, average copper content versus distance from the chill face in the long transverse direction (position LT in Figure 14) in the semi-continuous DC cast ingot of 2024 aluminum alloy.

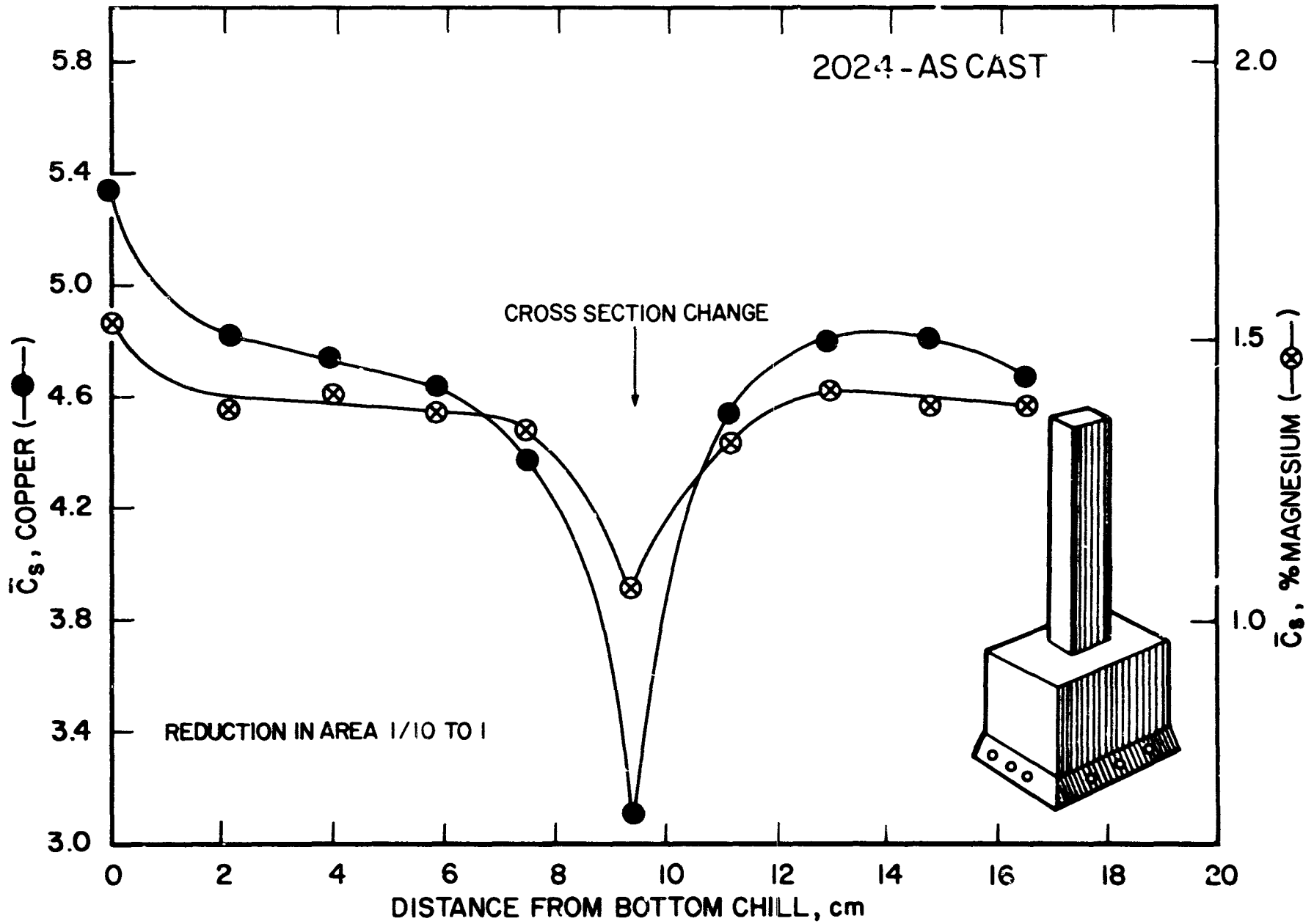

Figure 20. Macrosegregation profile, average copper and magnesium content versus distance from the bottom chill, in a unidirectionally solidified reduced cross section laboratory ingot of 2024 aluminum alloy.

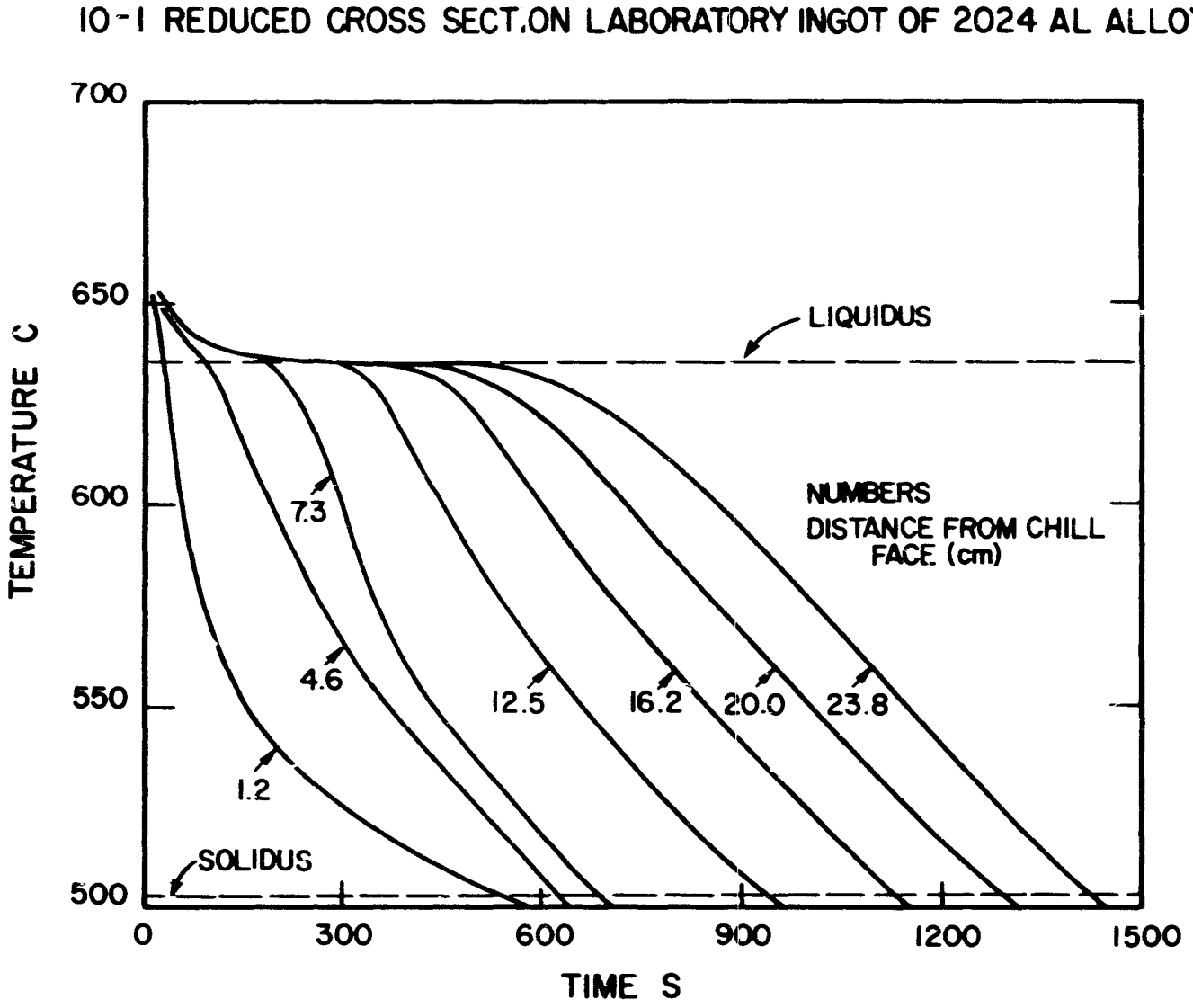

Figure 21. Measured temperature-time curves during solidification of 10 to 1 reduced cross-section ingot of 2024 aluminum alloy obtained from thermocouples located at different distances from the bottom water-cooled chill.

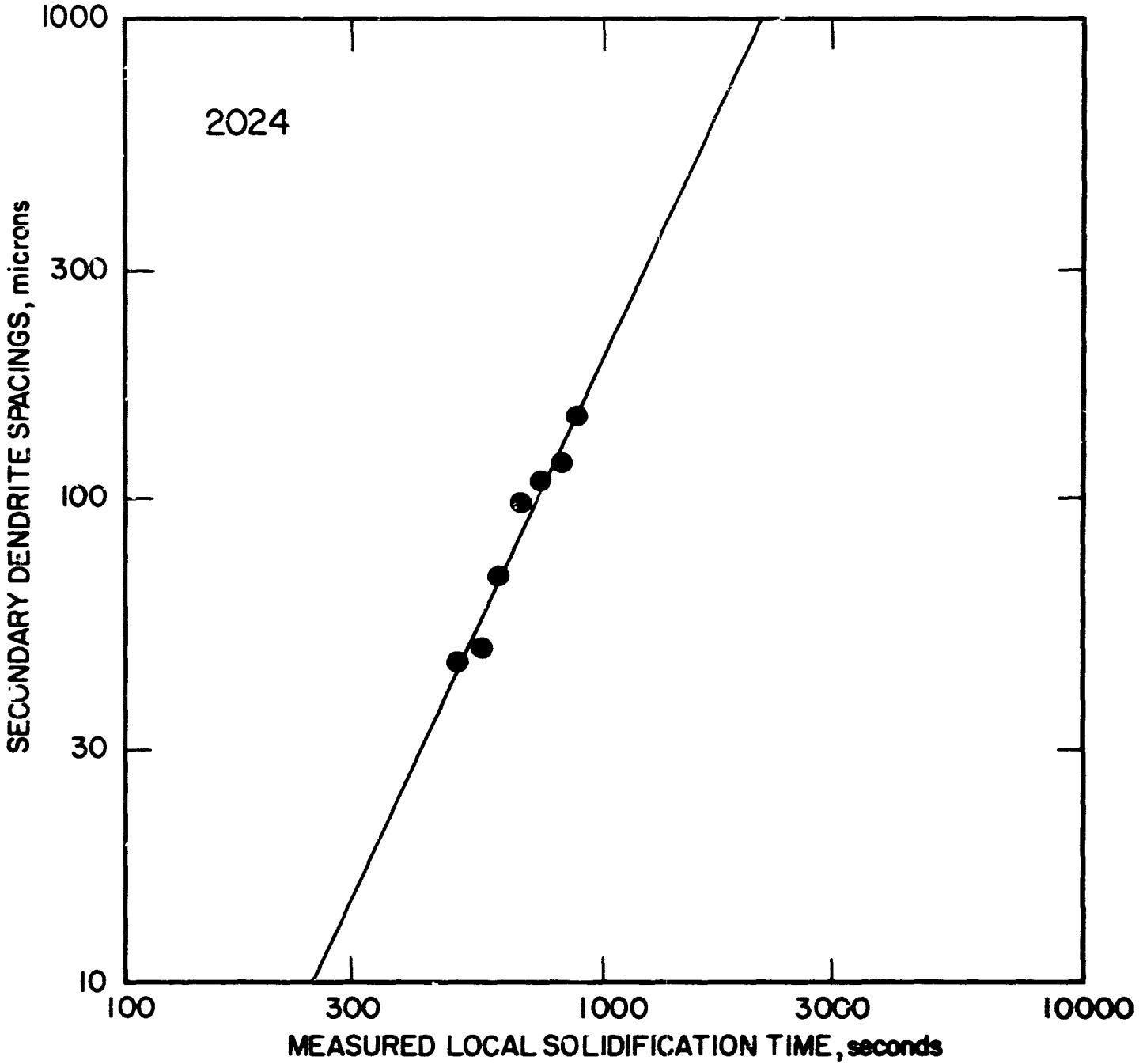

Figure 22. Measured secondary dendrite arm spacings versus local solidification time in unidirectionally solidified ingot of 2024 aluminum alloy.

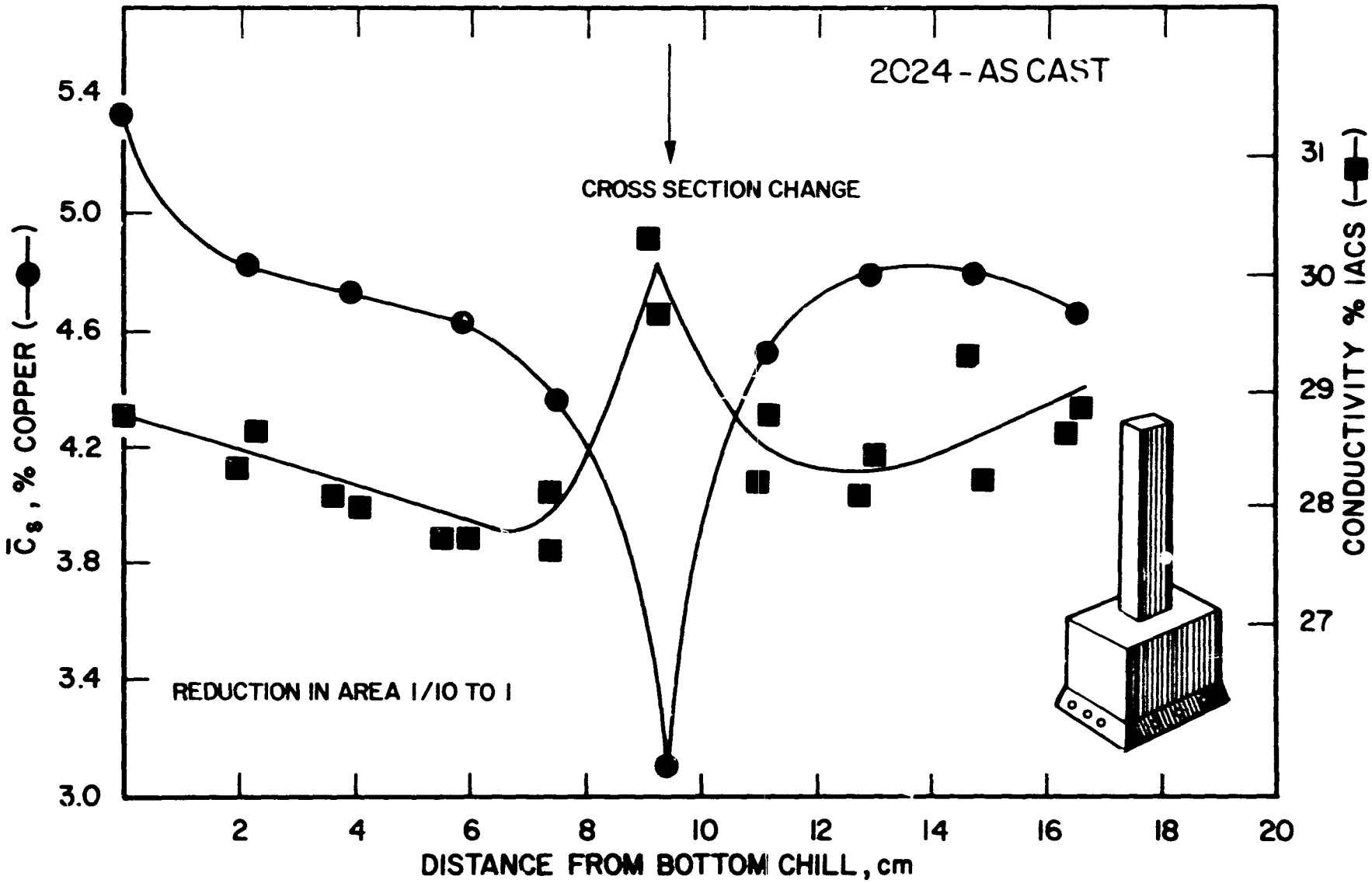

Figure 23. Average copper content and electrical conductivity versus distance from the bottom chill, in the as-cast unidirectionally solidified reduced cross-section laboratory ingot of 2024 aluminum alloy.

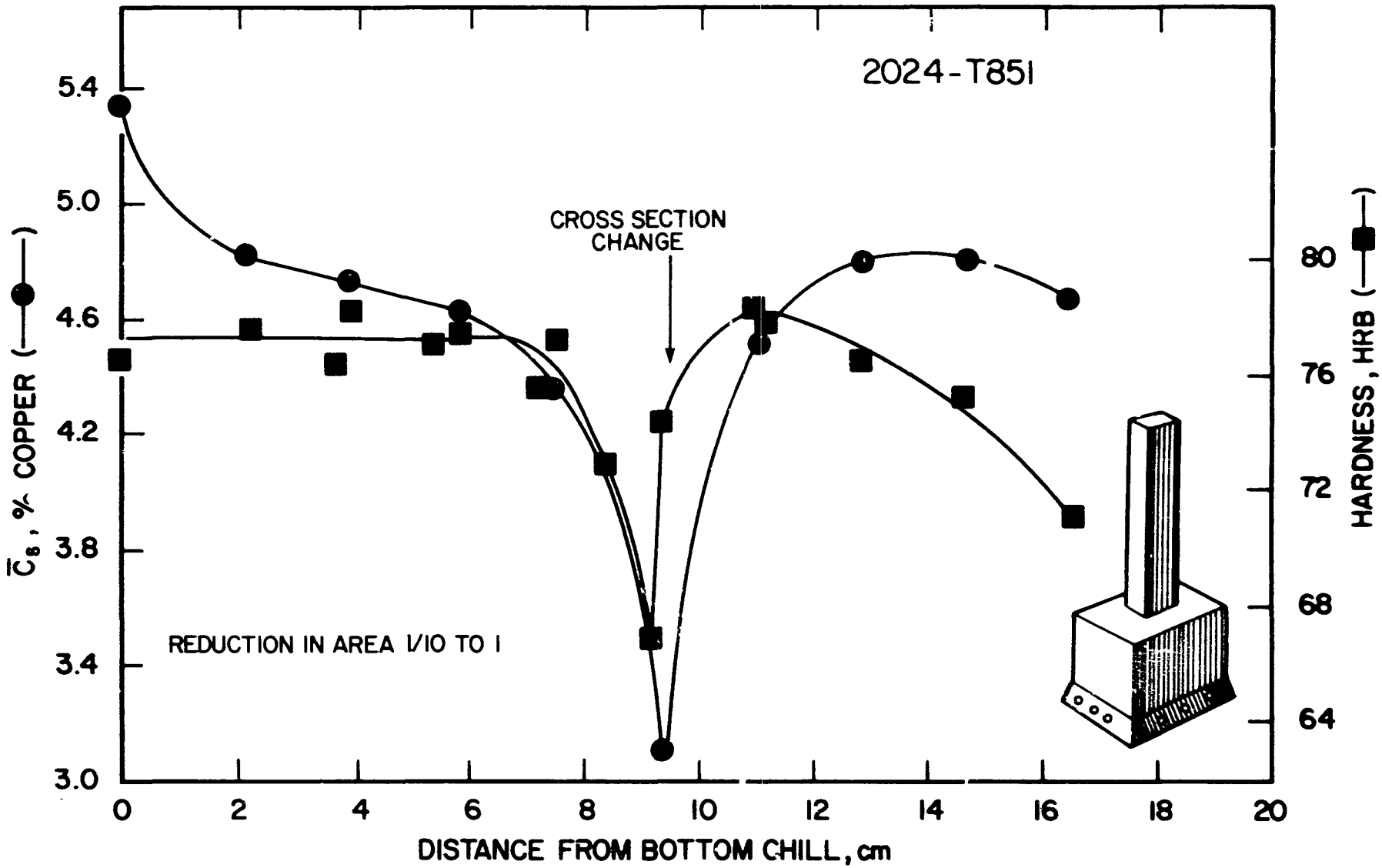

Figure 24. Hardness after thermomechanical treatment to the T851 condition and copper content versus distance from the bottom chill in the unidirectionally cast reduced cross-section laboratory ingot.

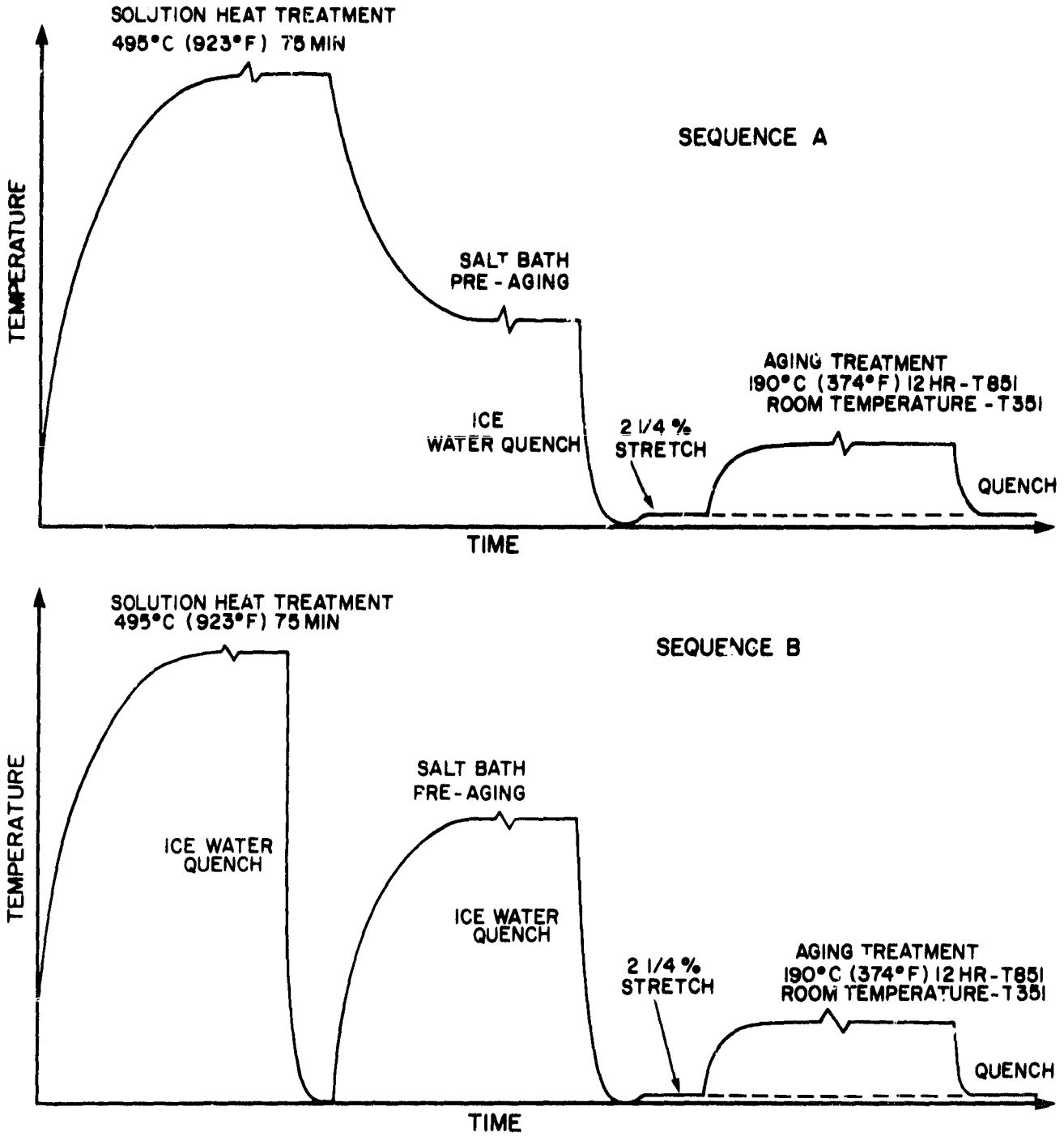

Figure 25. Schematic representation of the thermomechanical treatment sequences given the 2024-T851 and 2024-T351 aluminum alloys.

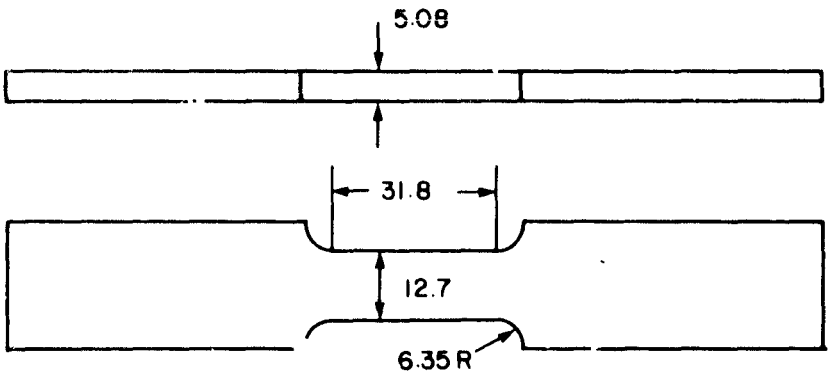

Figure 26. Schematic of tensile test specimen. Dimensions are in mm.

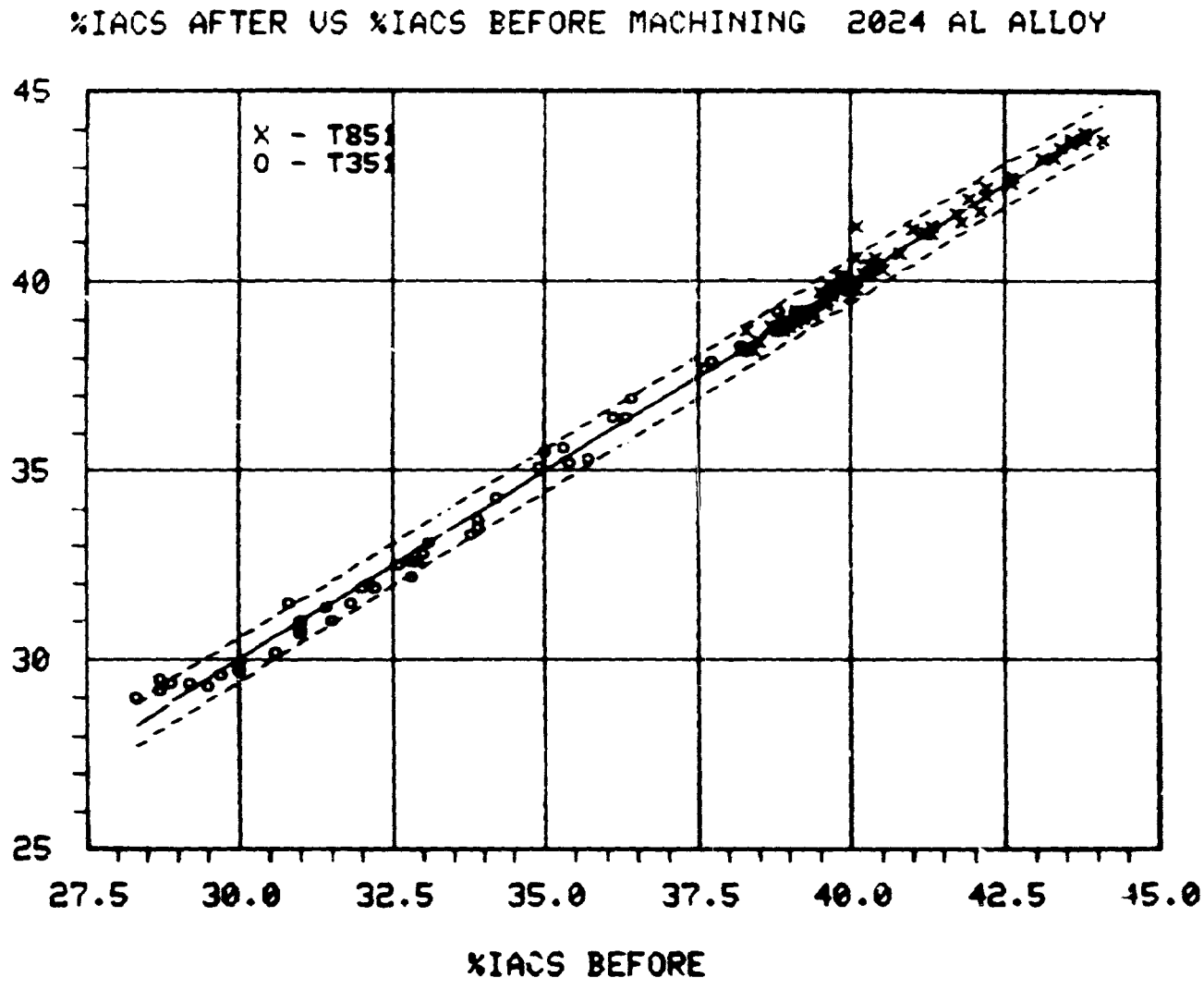

Figure 27. Conductivity after machining approximately 0.5 mm from each surface of the thermomechanically processed 2024-T851 and 2024-T351 samples vs. the conductivity measured before the machining operation. The solid line is a linear least squares fit and the dashed lines represent the scatter band (approximately 95% confidence level).

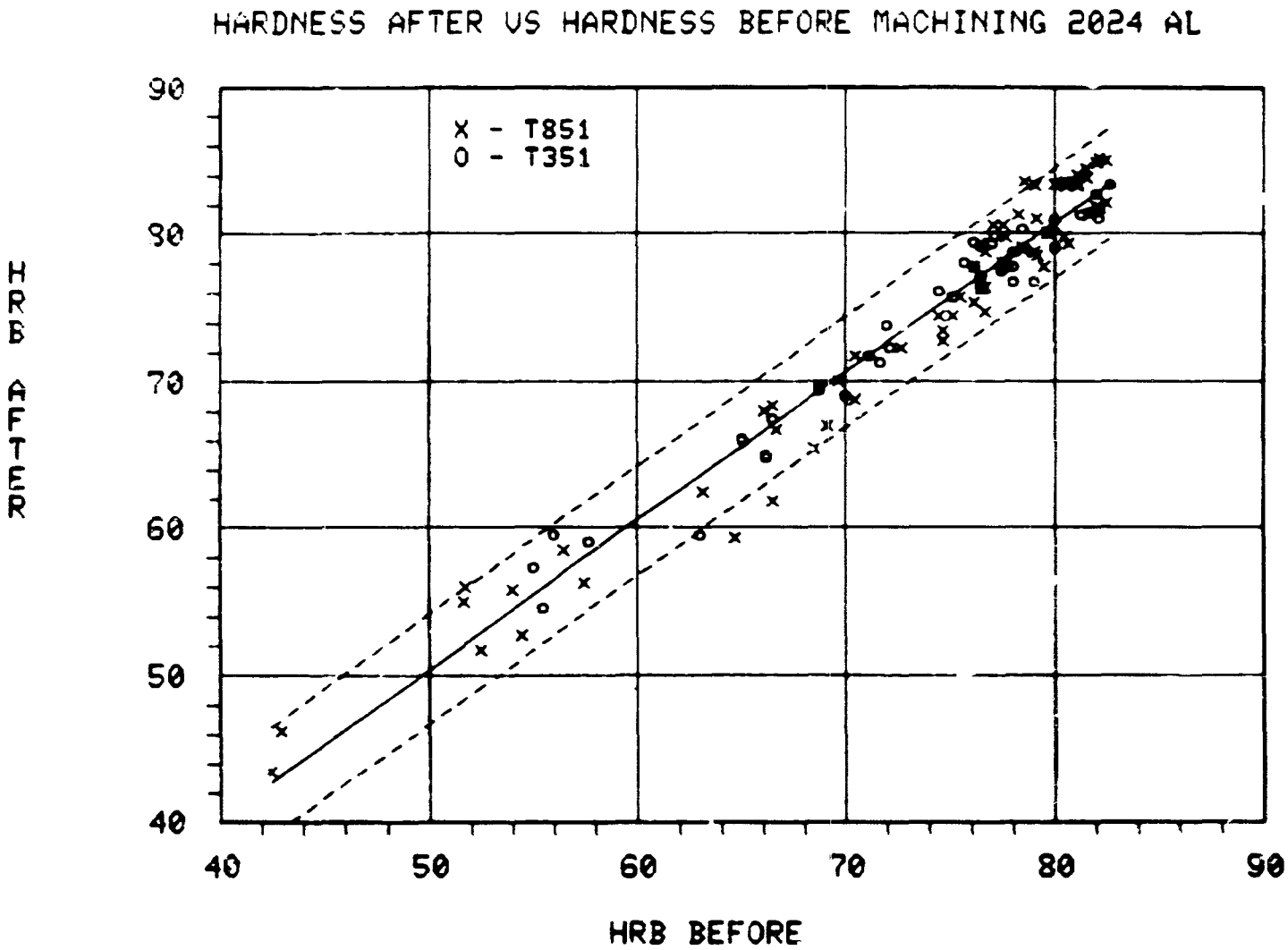

Figure 28. Rockwell B hardness measured after machining approximately 0.5 mm from each surface of the thermomechanically processed 2024-T851 and 2024-T351 samples vs. the hardness measured before the machining operation. The solid line is a linear least squares fit and the dashed lines represent the scatter band (approximately 95% confidence level).

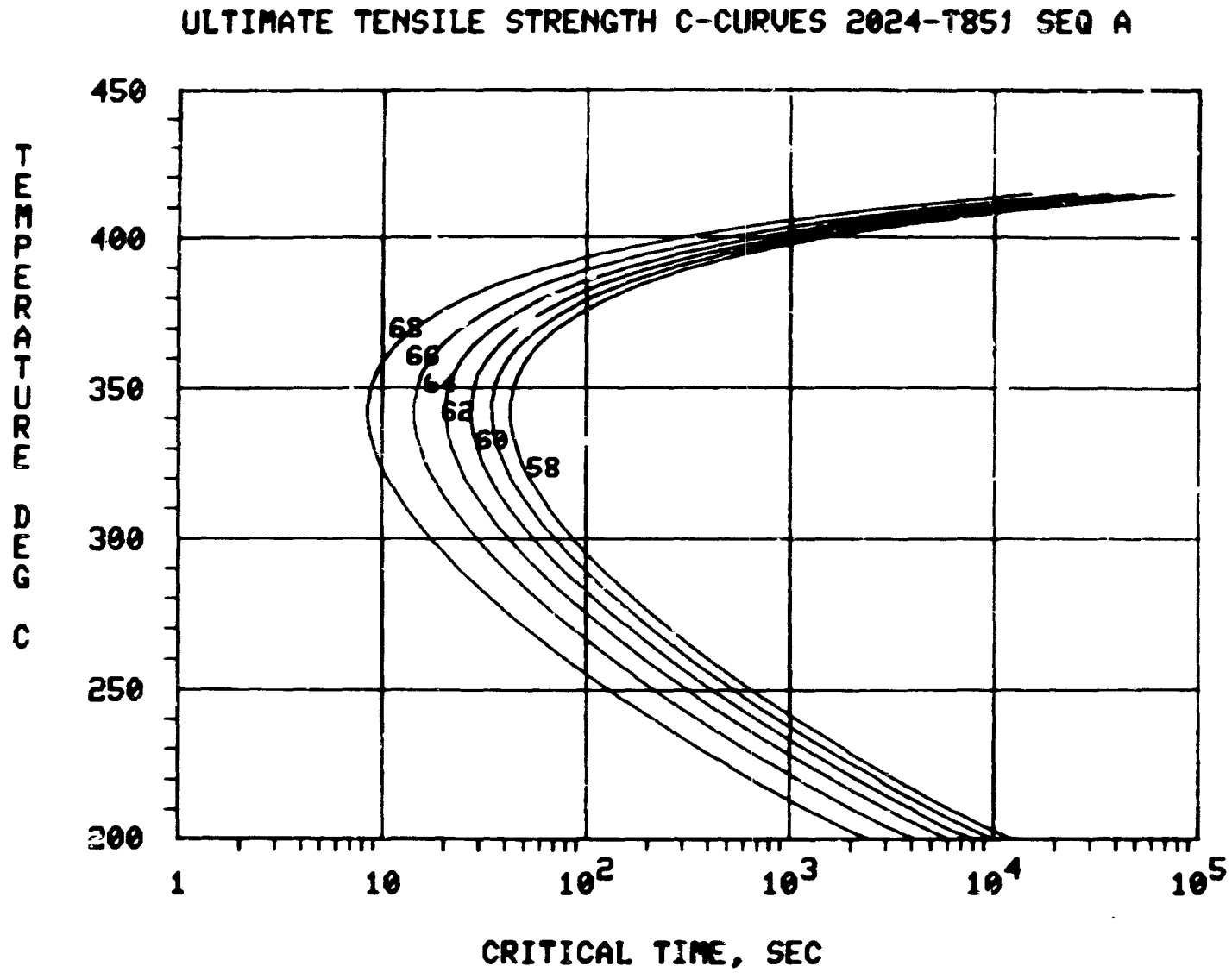

Figure 29. (a) Ultimate tensile strength C-curves for 2024-T851 sequence A alloys. The curves give the critical times for obtaining the indicated tensile strength for an isothermal sequence A type "pre-aging" heat treatment and a subsequent aging to the T851 temper.

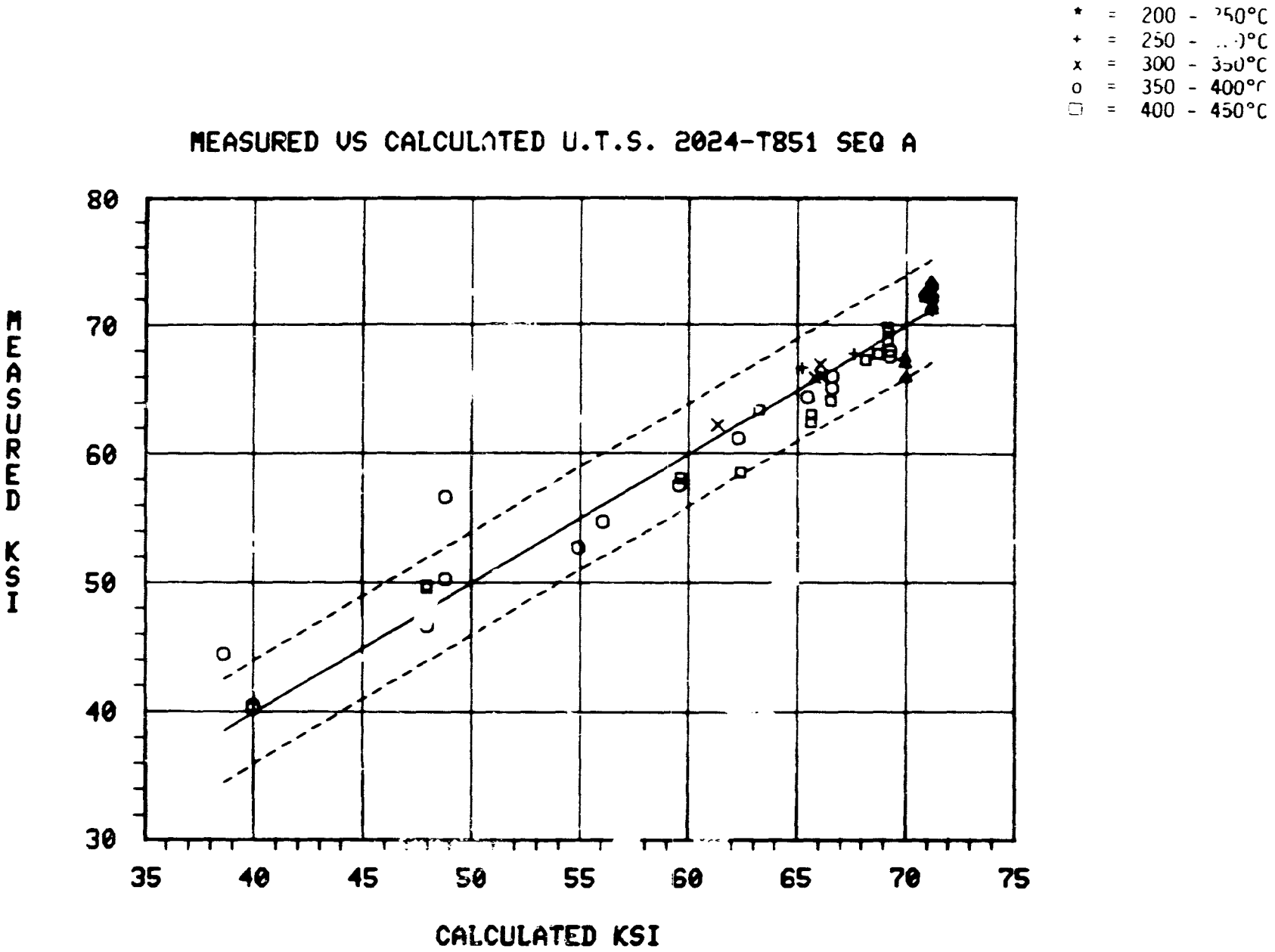

Figure 29. (b) Measured values of the ultimate tensile strength plotted against the values calculated using the C-curve for 2024-T851 sequence A. The solid line is a line of unit slope and the dashed line is the scatter band (approximately 95 percent confidence level). The symbols indicate the average temperature during the "pre-aging" treatment: asterisk - direct quench, plus sign - 200 to 250°C, x - 250 to 300°C, circle - 300 to 350°C, square - 350 to 400°C, triangle - 400 to 450°C.

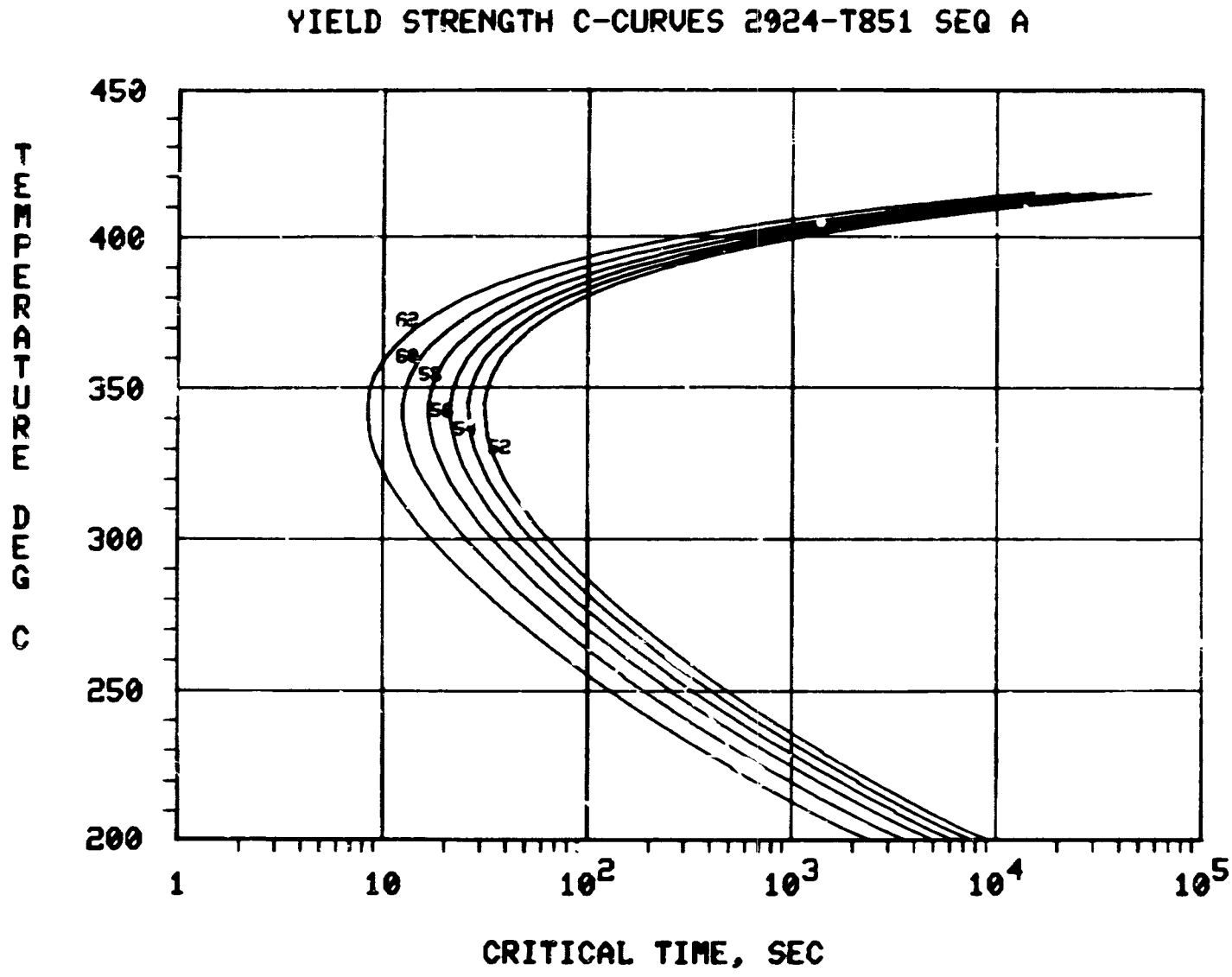

Figure 30. (a) Yield strength (0.2 percent offset) C-curves for 2024-T851 sequence A alloys. The curves give the critical times for obtaining the indicated yield strength for an isothermal sequence A type "pre-aging" heat treatment and a subsequent aging to the T851 temper.

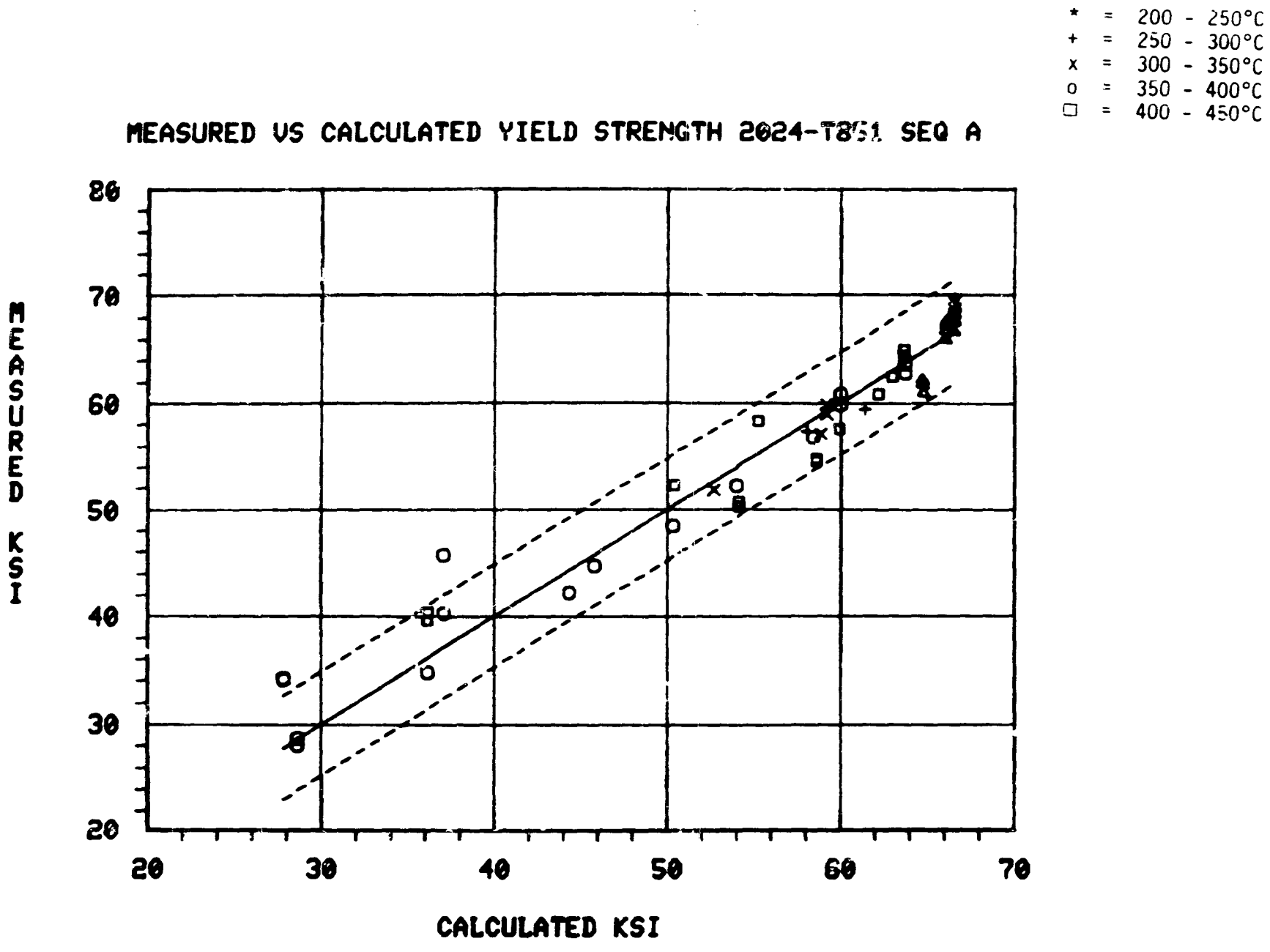

Figure 30. (b) Measured values of the yield strength plotted versus values calculated using the yield strength C-curve for 2024-T851 sequence A. The solid line is a line of unit slope and the dashed lines are the scatter band (approximately 95 percent confidence level).

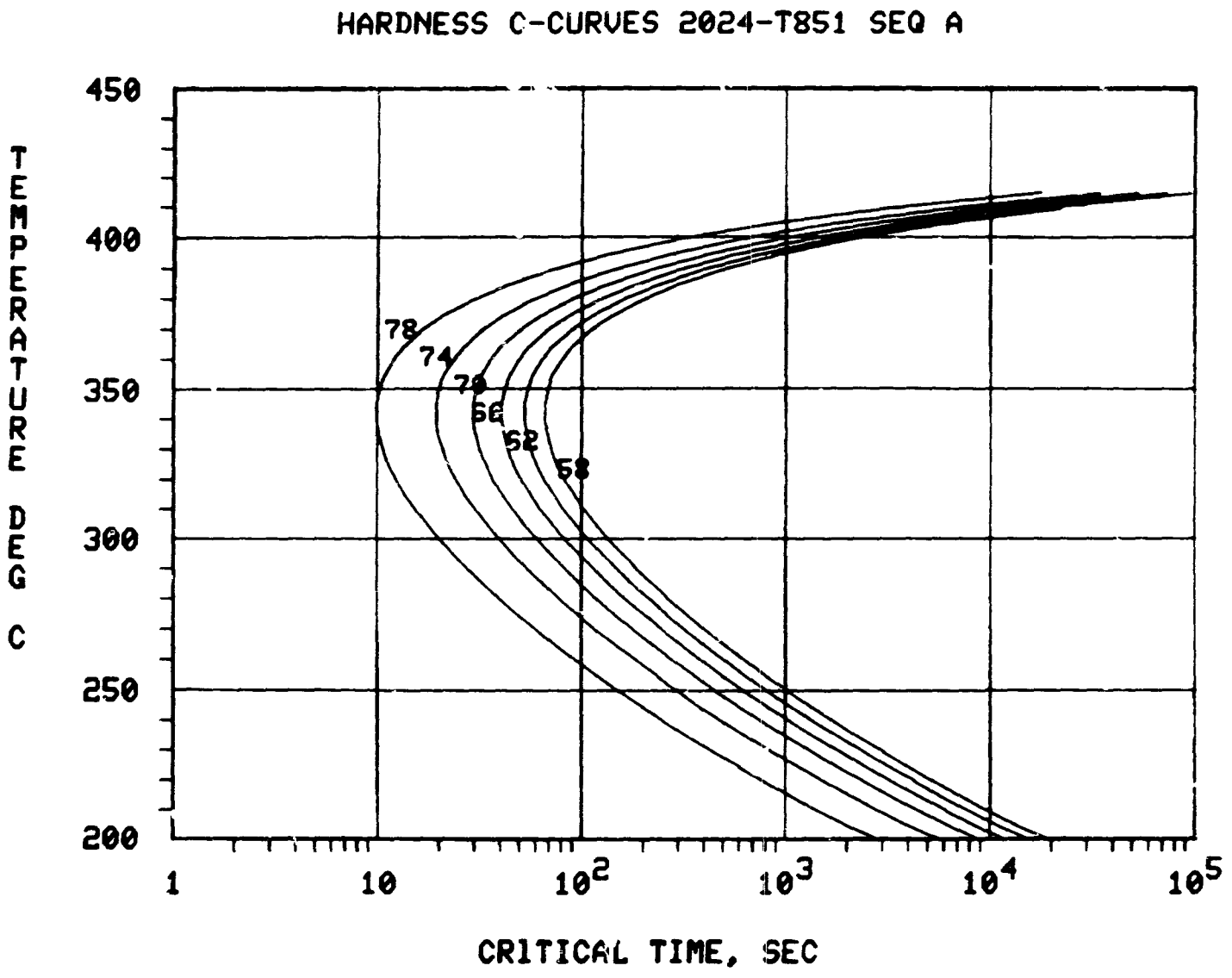

Figure 31. (a) Hardness C-curves for 2024-T851 sequence A alloys. The curves give the critical times for obtaining the indicated Rockwell B hardness for an isothermal sequence A type "pre-aging" heat treatment and a subsequent aging to the T851 temper.

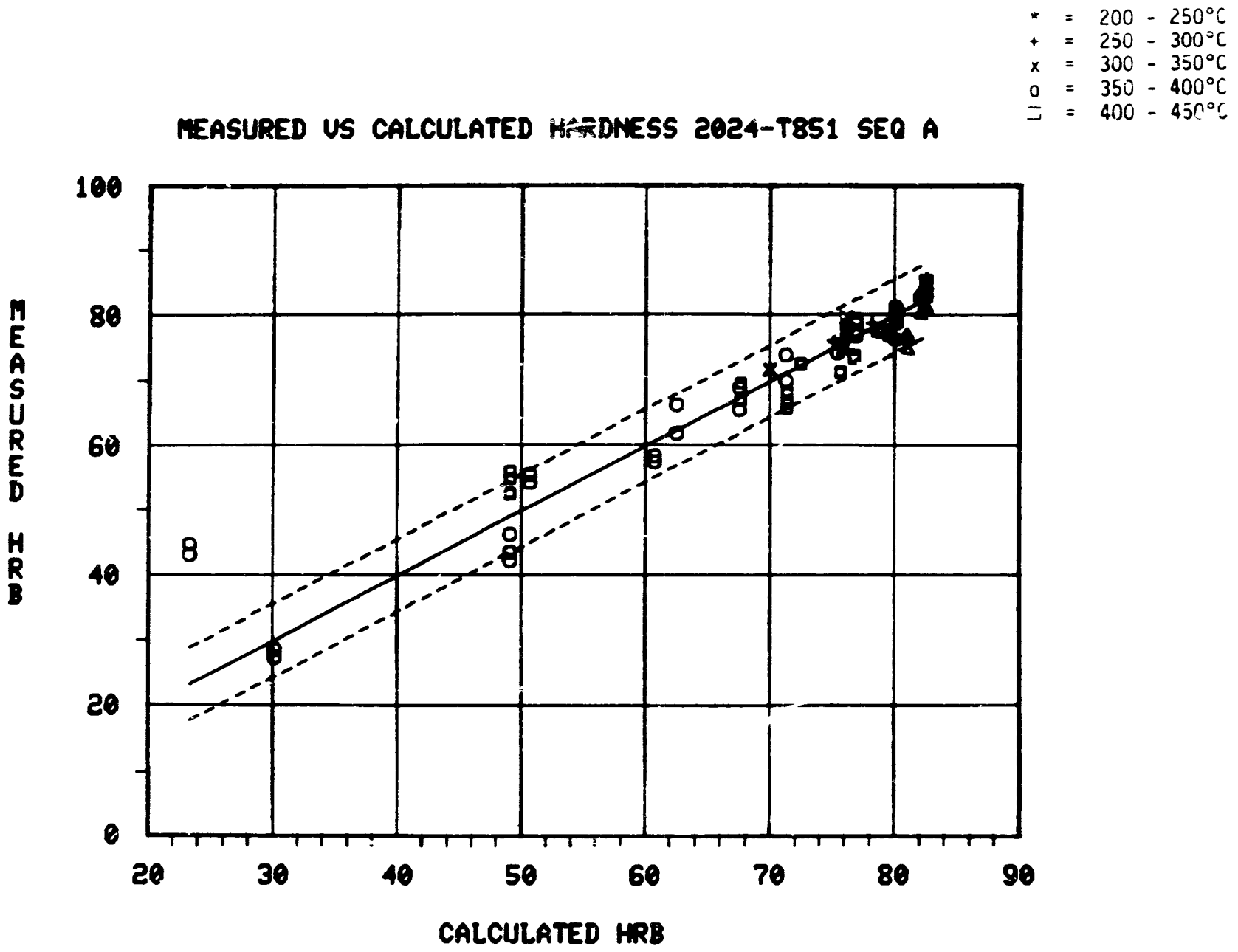

Figure 31. (b) Measured values of the Rockwell B hardness plotted vs. values calculated using the hardness C-curve for 2024-T851 sequence A. The solid line is a line of unit slope and the dashed lines are the scatter band (approximately 95 percent confidence level).

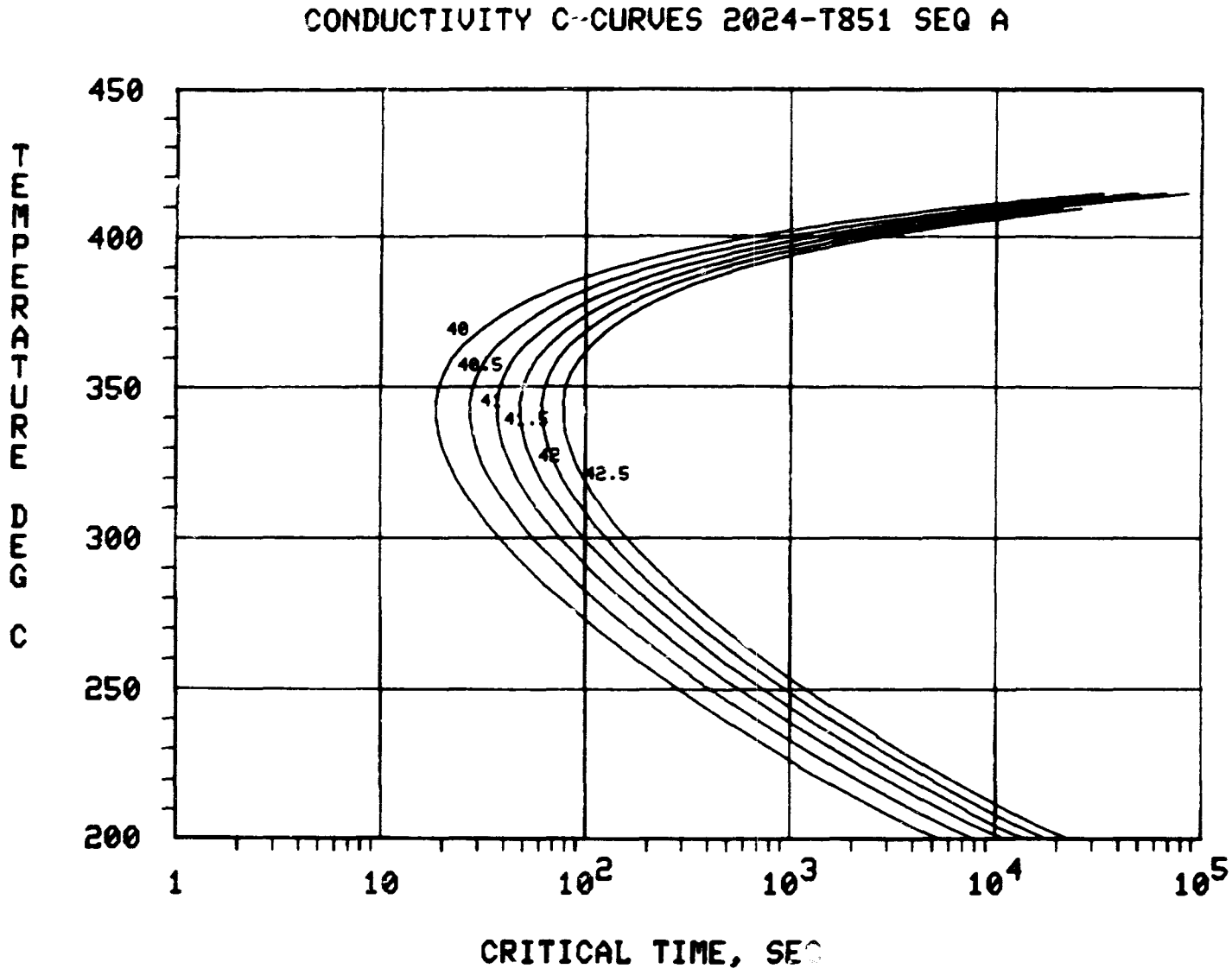

Figure 32. (a) Conductivity C-curves for 2024-T851 sequence A alloys. The curves give the critical times for obtaining the indicated conductivity for an isothermal sequence A type "pre-aging" heat treatment and a subsequent aging to the T851 temper.

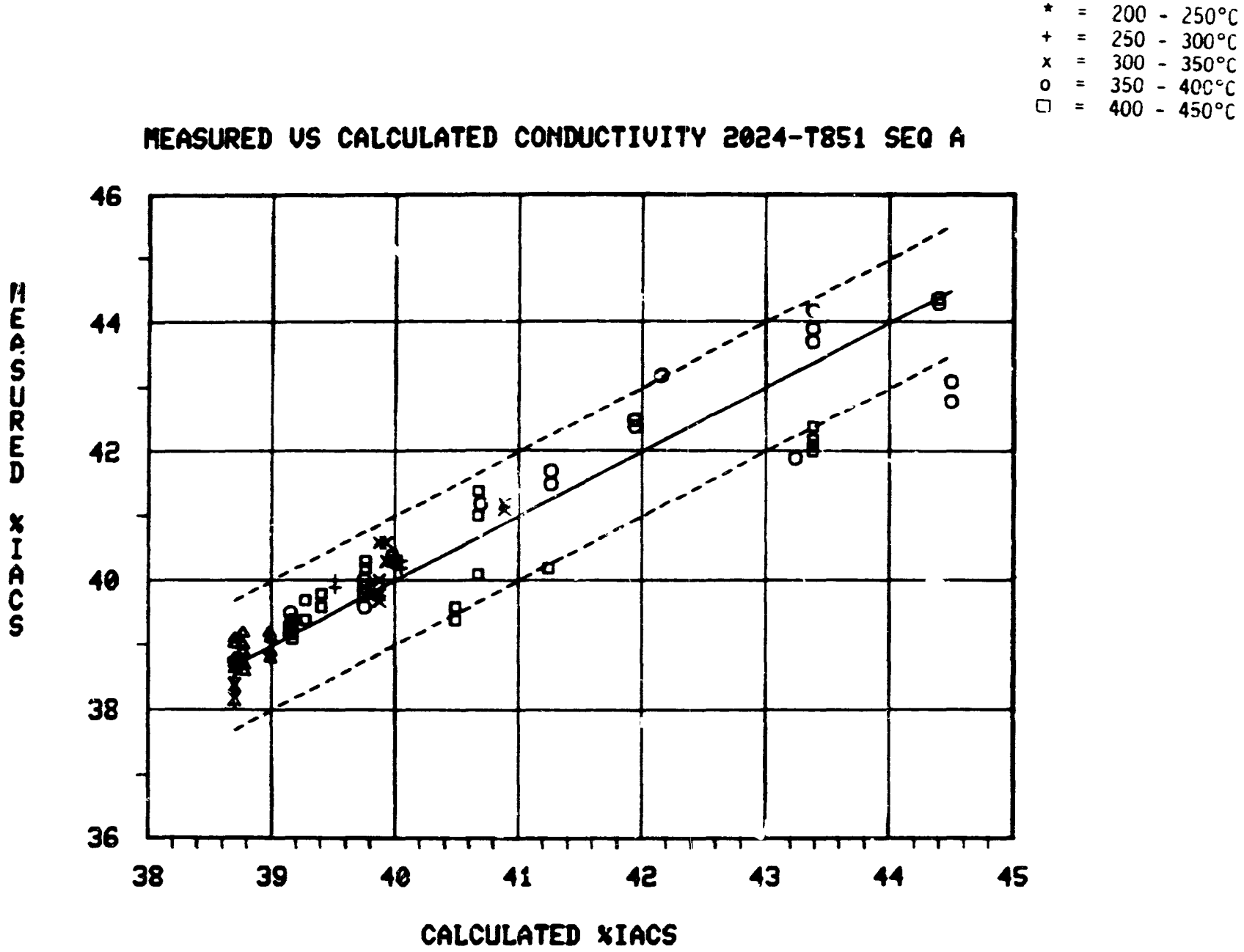

Figure 32. (b) Measured values of the conductivity plotted vs. values calculated using the 2024-T851 sequence A conductivity C-curve. The solid line is a line of unit slope and the dashed lines are the scatter band (approximately 95 percent confidence level).

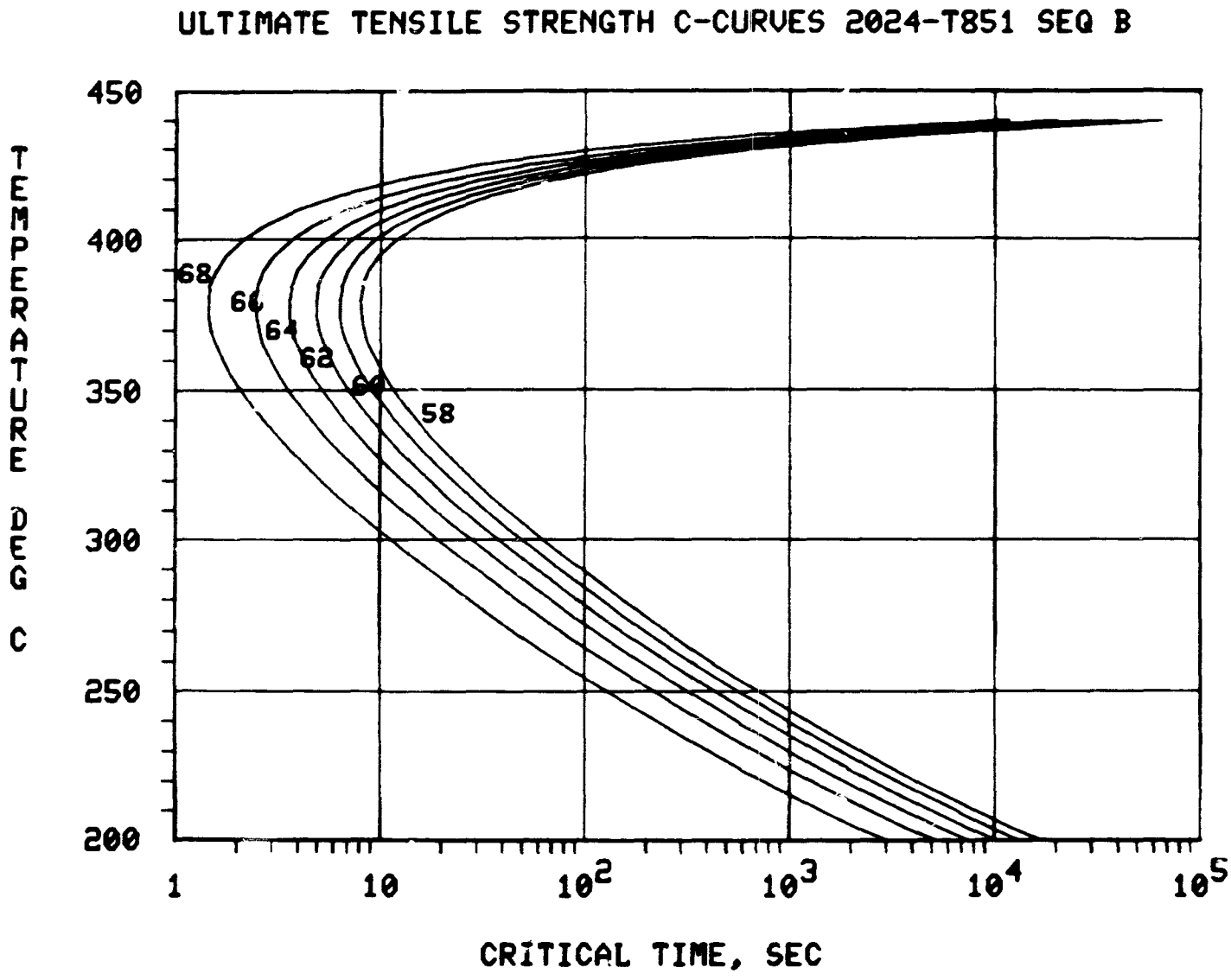

Figure 33. (a) Ultimate tensile strength C-curves for 2024-T851 sequence B alloys. The curves give the critical times for obtaining the indicated tensile strength for an isothermal sequence B type "pre-aging" heat treatment and a subsequent aging to the T851 temper.

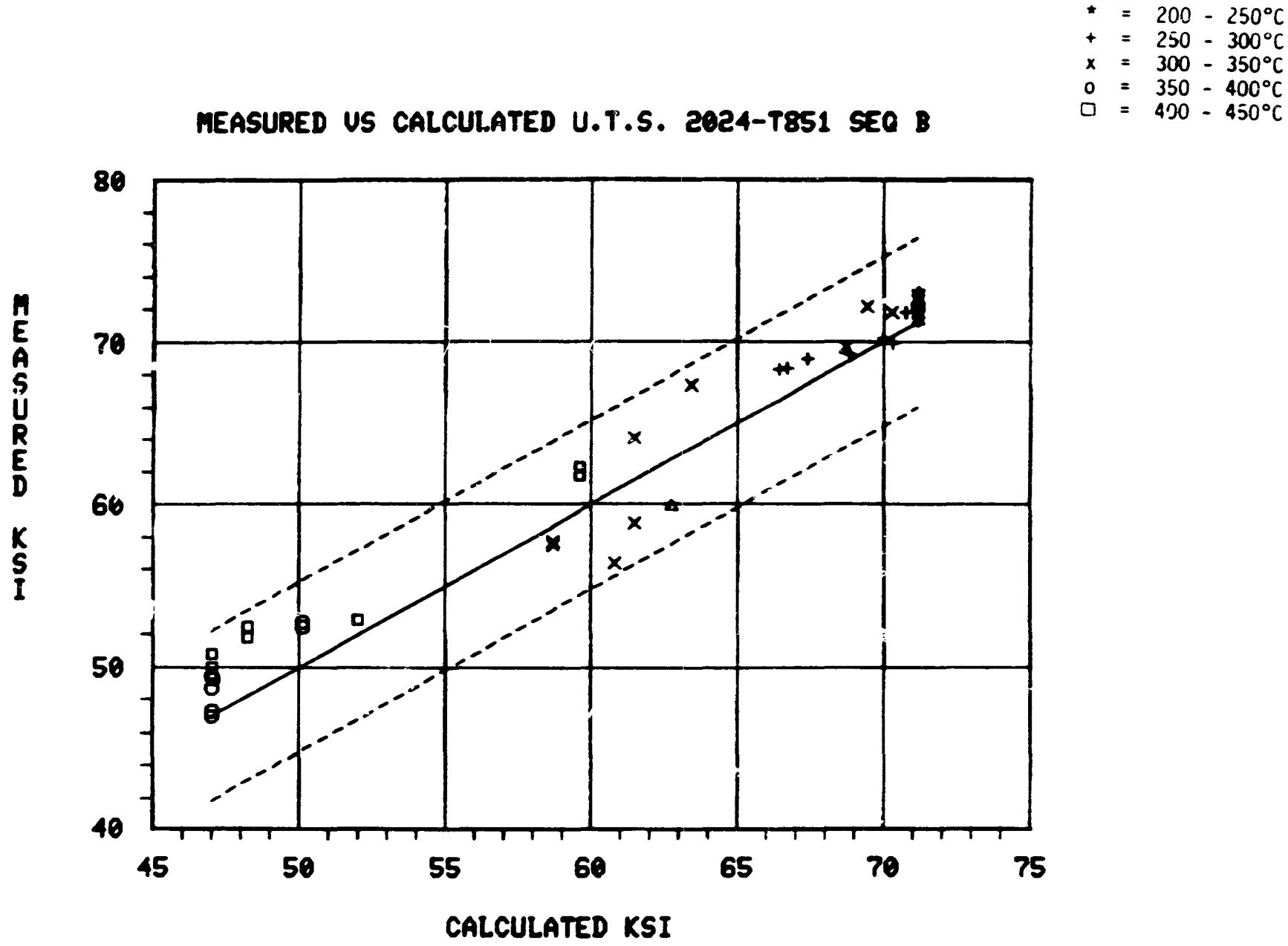

Figure 33. (b) Measured values of the ultimate tensile strength plotted against the values calculated using the C-curve for 2024-T851 sequence B. The solid line is a line of unit slope and the dashed line is the scatter band (approximately 95 percent confidence level).

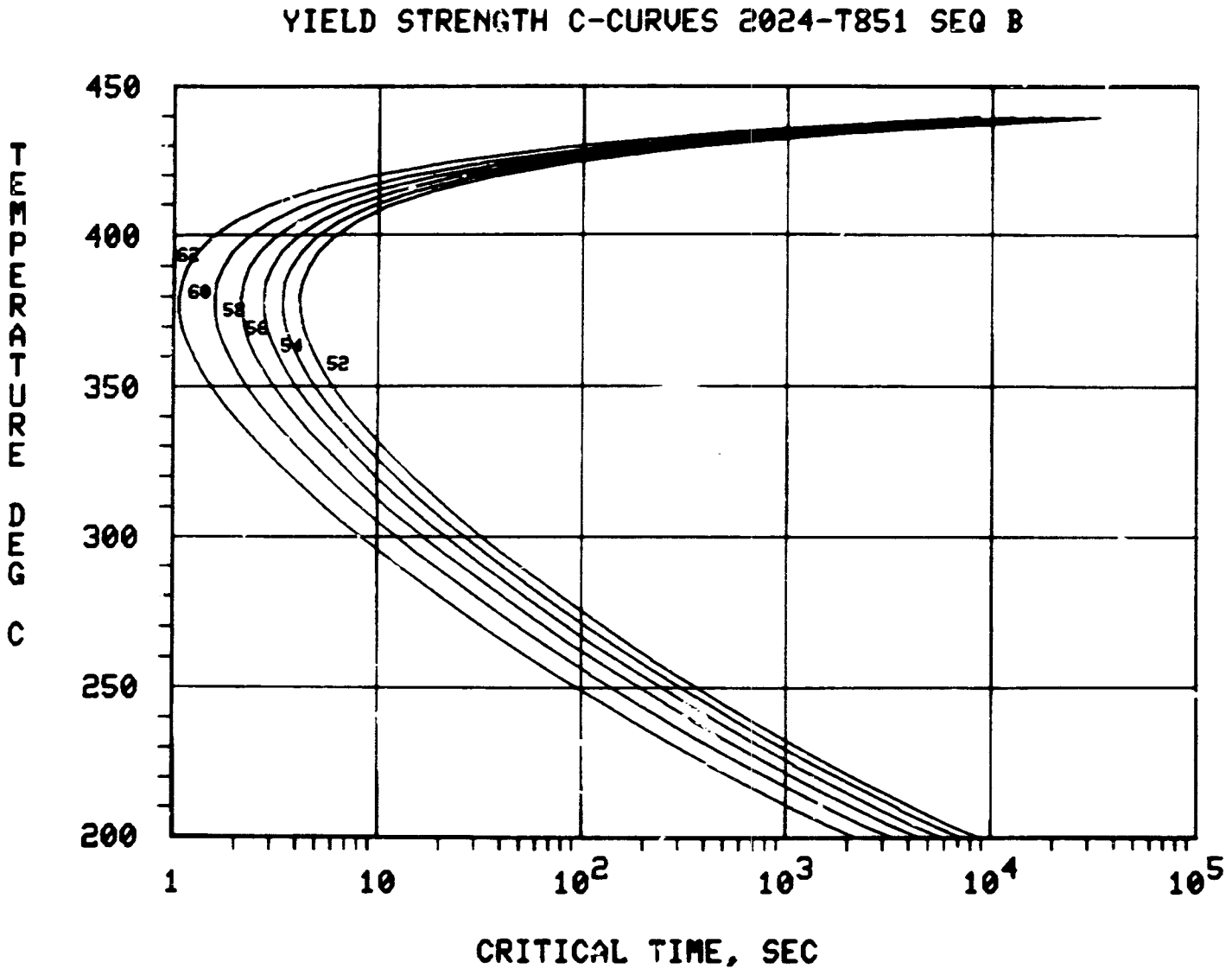

Figure 34. (a) Yield strength (0.2 percent offset) C-curves for 2024-T851 sequence B alloys. The curves give the critical times for obtaining the indicated yield strength for an isothermal sequence B type "pre-aging" heat treatment and a subsequent aging to the T851 temper.

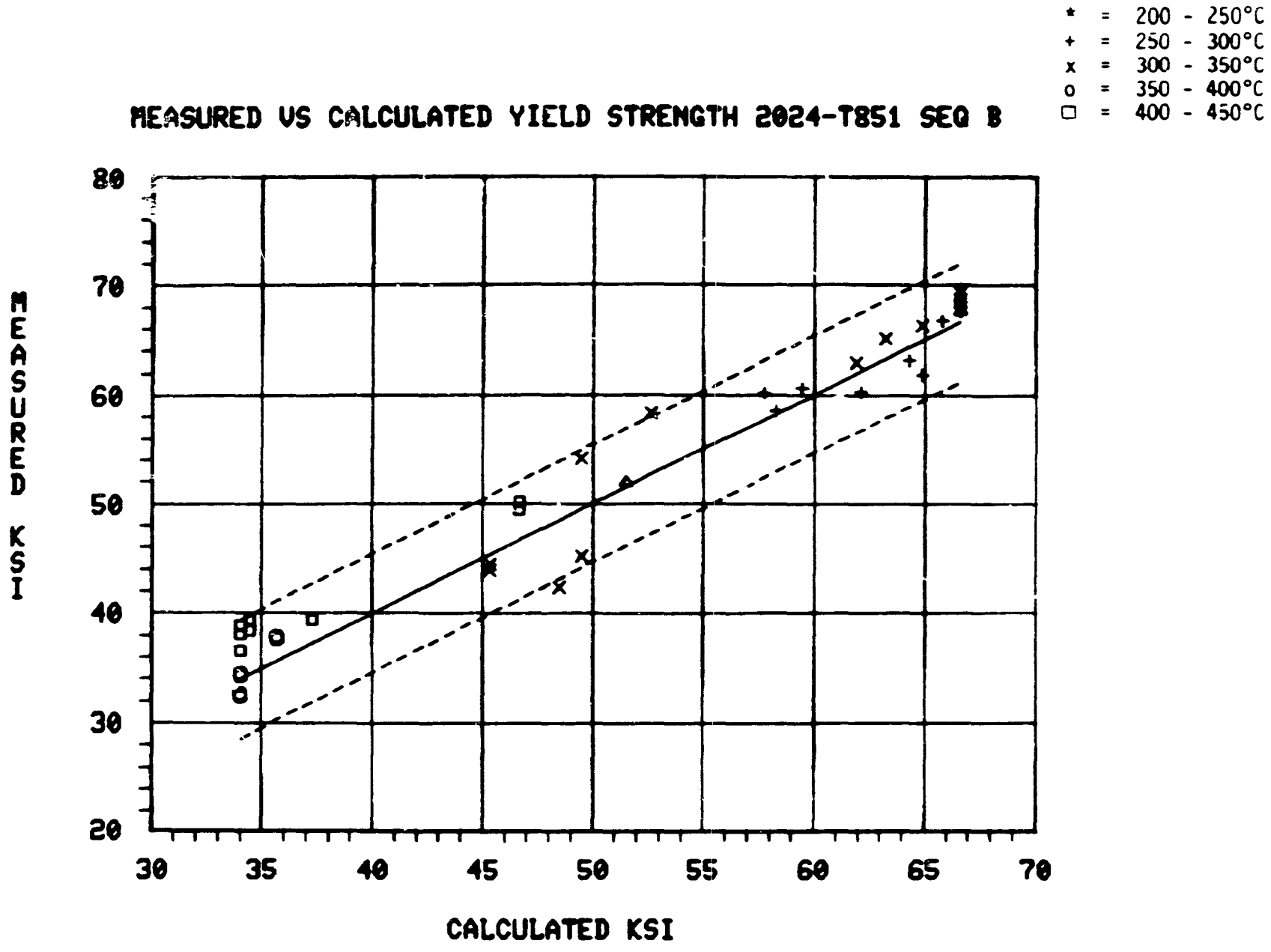

Figure 34. (b) Measured values of the yield strength plotted vs. values calculated using the yield strength C-curve for 2024-T851 sequence B. The solid line is a line of unit slope and the dashed lines are the scatter band (approximately 95 percent confidence level).

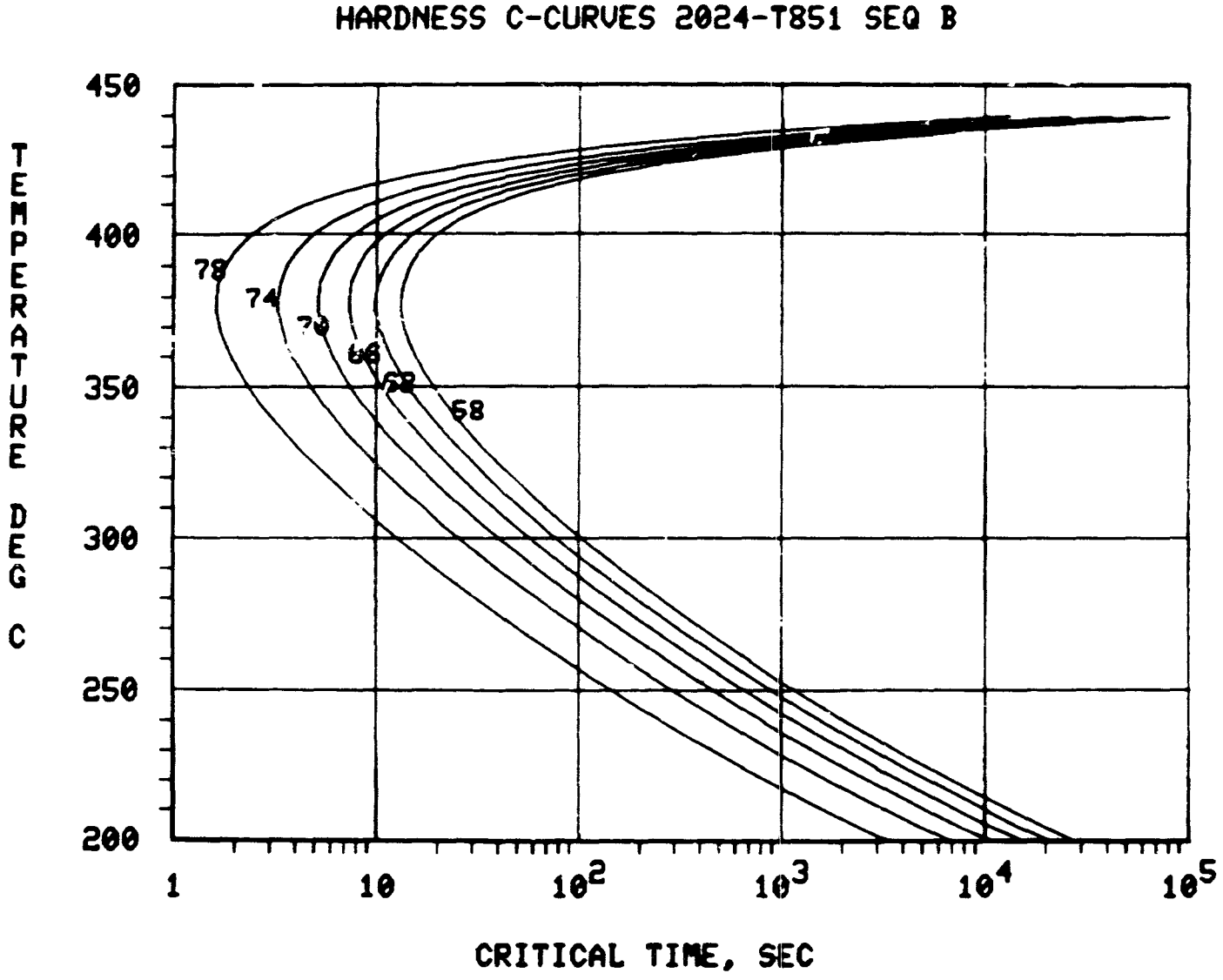

Figure 35. (a) Hardness C-curves for 2024-T851 sequence B alloys. The curves give the critical times for obtaining the indicated Rockwell B hardness for an isothermal sequence B type "pre-aging" heat treatment and a subsequent aging to the T851 temper.

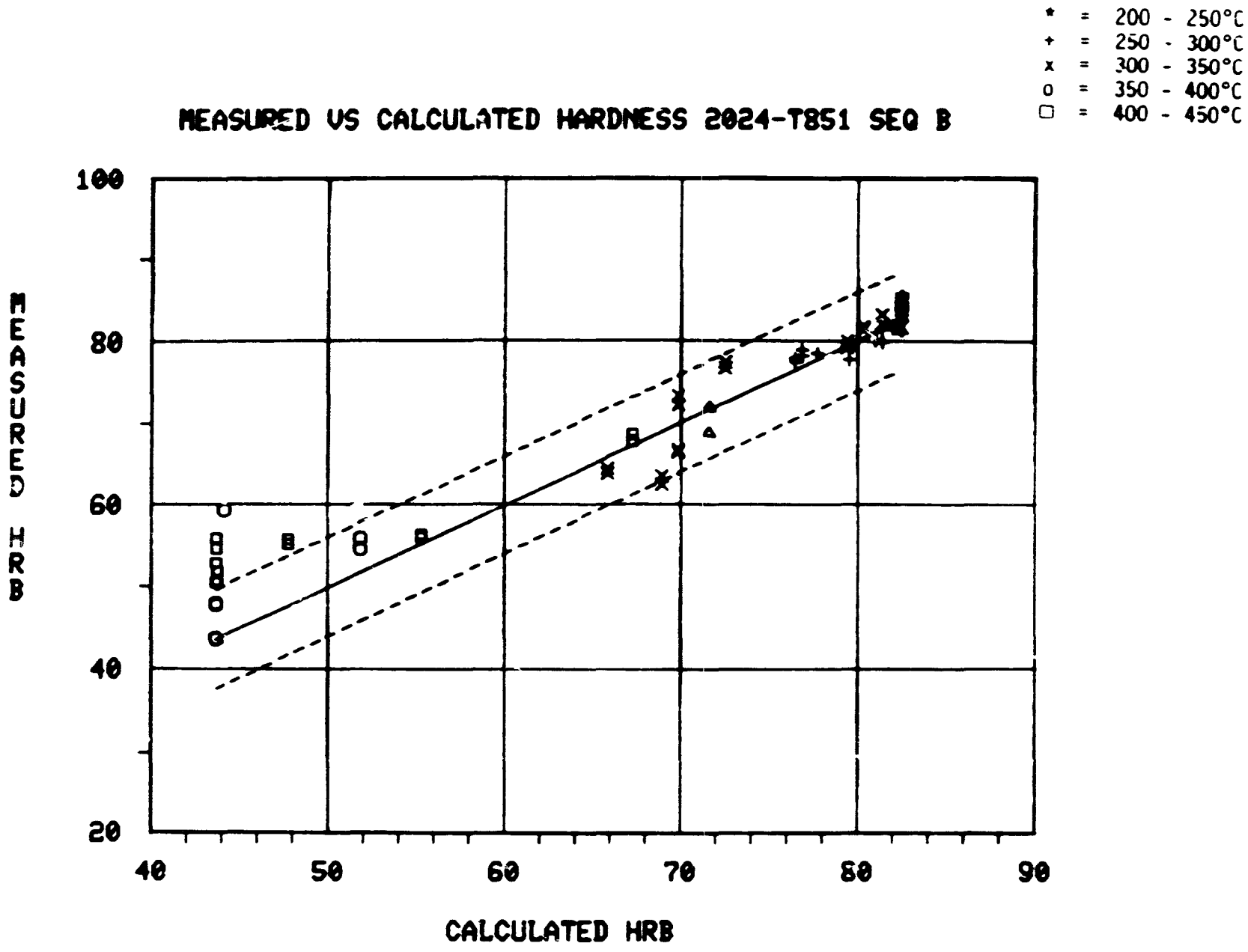

Figure 35. (b) Measured values of the Rockwell B hardness plotted vs. values calculated using the hardness C-curve for 2024-T851 sequence B. The solid line is a line of unit slope and the dashed lines are the scatter band (approximately 95 percent confidence level).

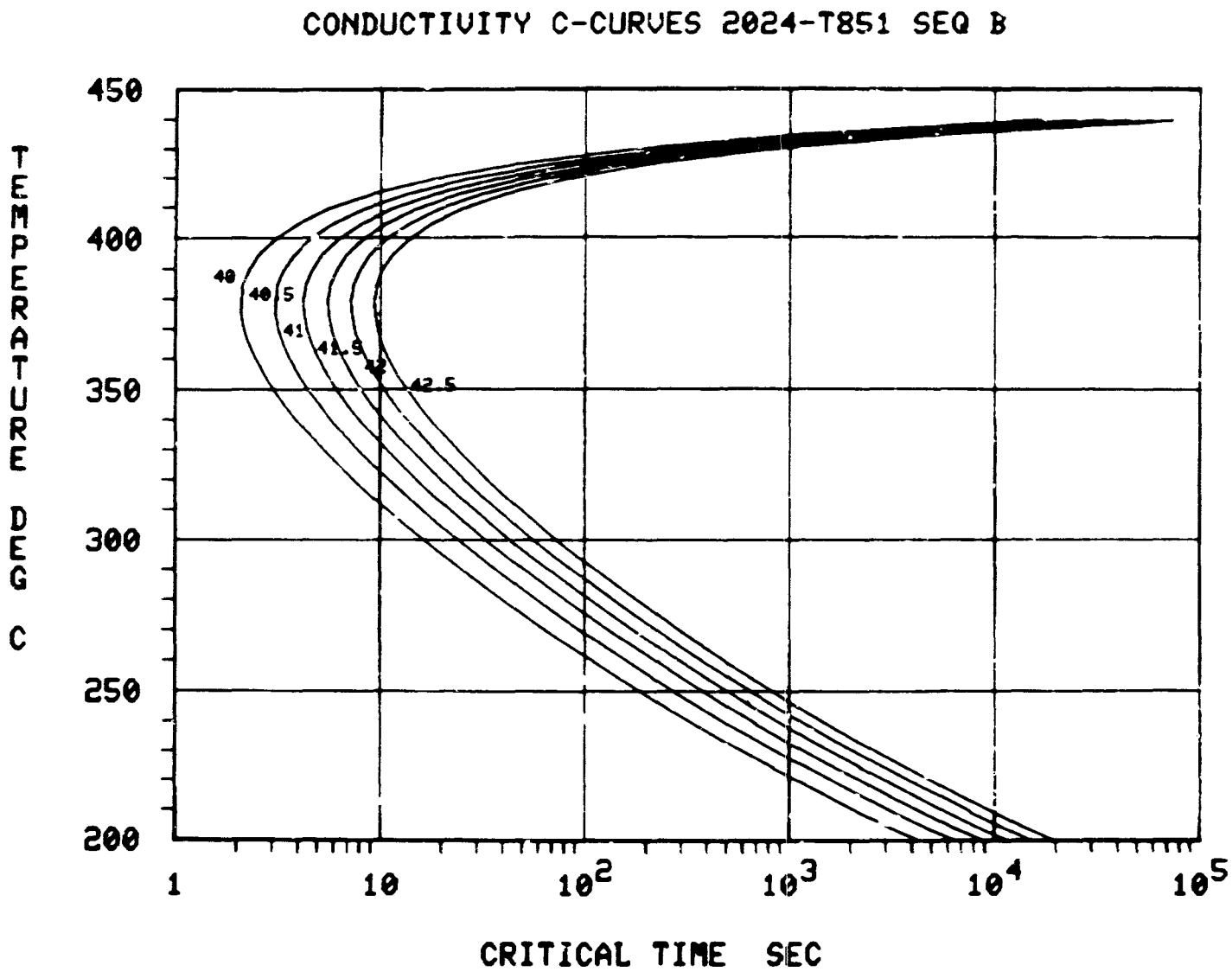

Figure 36. (a) Conductivity C-curves for 2024-T851 sequence B alloys. The curves give the critical times for obtaining the indicated conductivity for an isothermal sequence B type "pre-aging" heat treatment and a subsequent aging to the T851 temper.

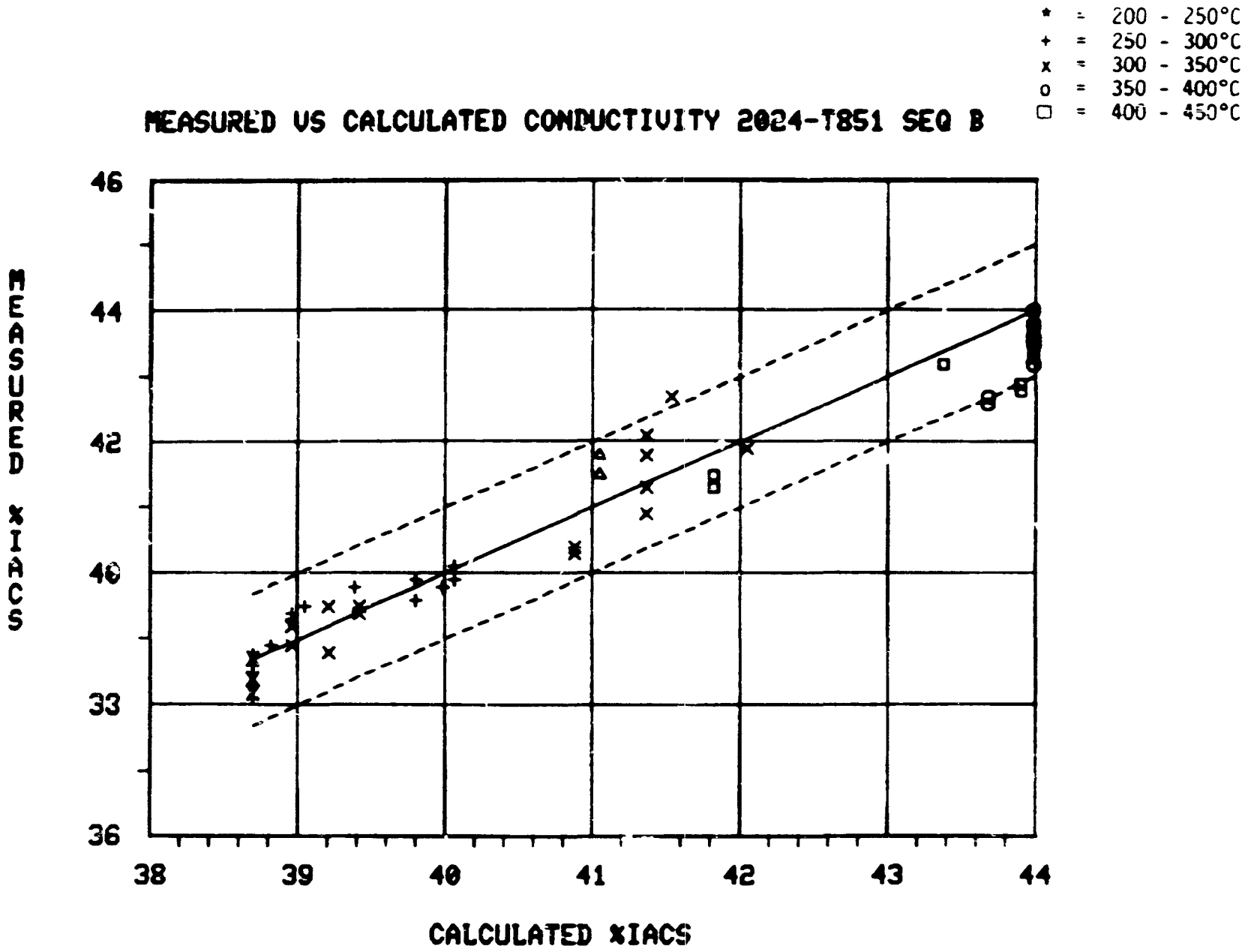

Figure 36. (b) Measured values of the conductivity plotted vs. values calc[illegible] using the 2024-T851 sequence B conductivity C-curve. The solid [illegible] a line of unit slope and the dashed lines are the scatter band (approximately 95 percent confidence level).

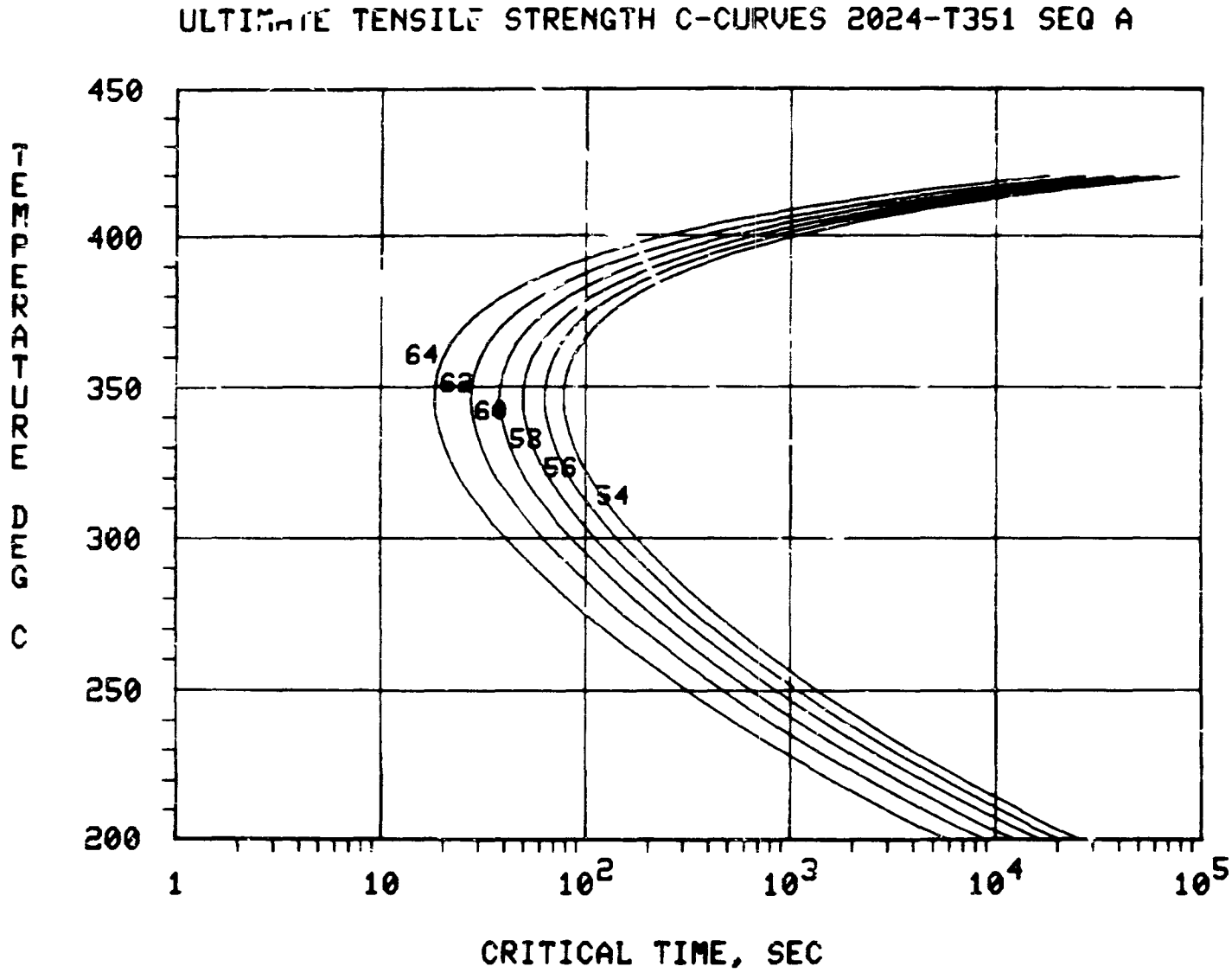

Figure 37. (a) Ultimate tensile strength C-curves for 2024-T351 equence A alloys. The curves give the critical times for obtaining the indicated tensile strength for an isothermal sequence A type "pre-aging" heat treatment and a subsequent aging to the T351 temper.

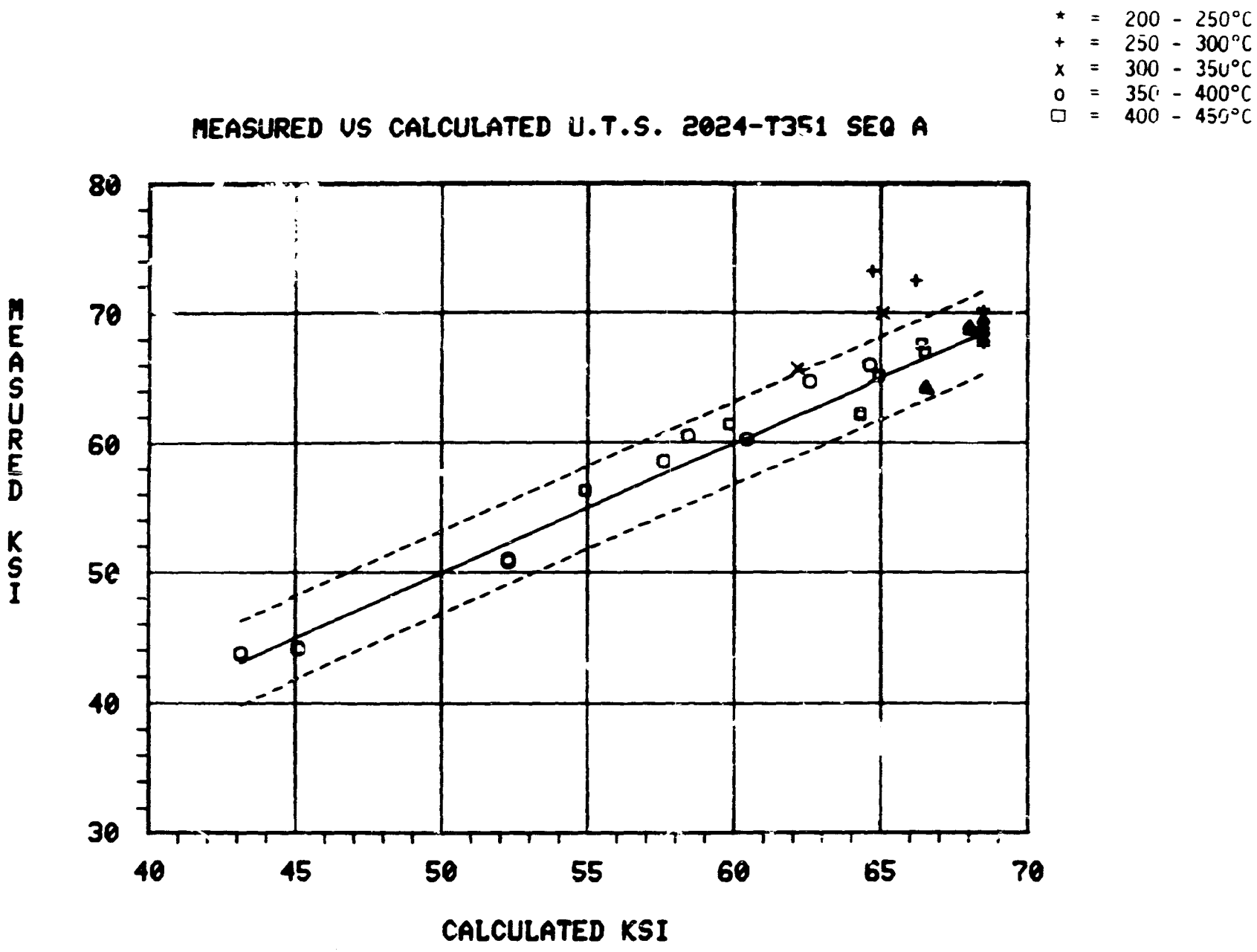

Figure 37. (b) Measured values of the ultimate tensile strength plotted against the values calculated using the C-curve for 2024-T351 sequence A. The solid line is a line of unit slope and the dashed line is the scatter band (approximately 95 percent confidence level).

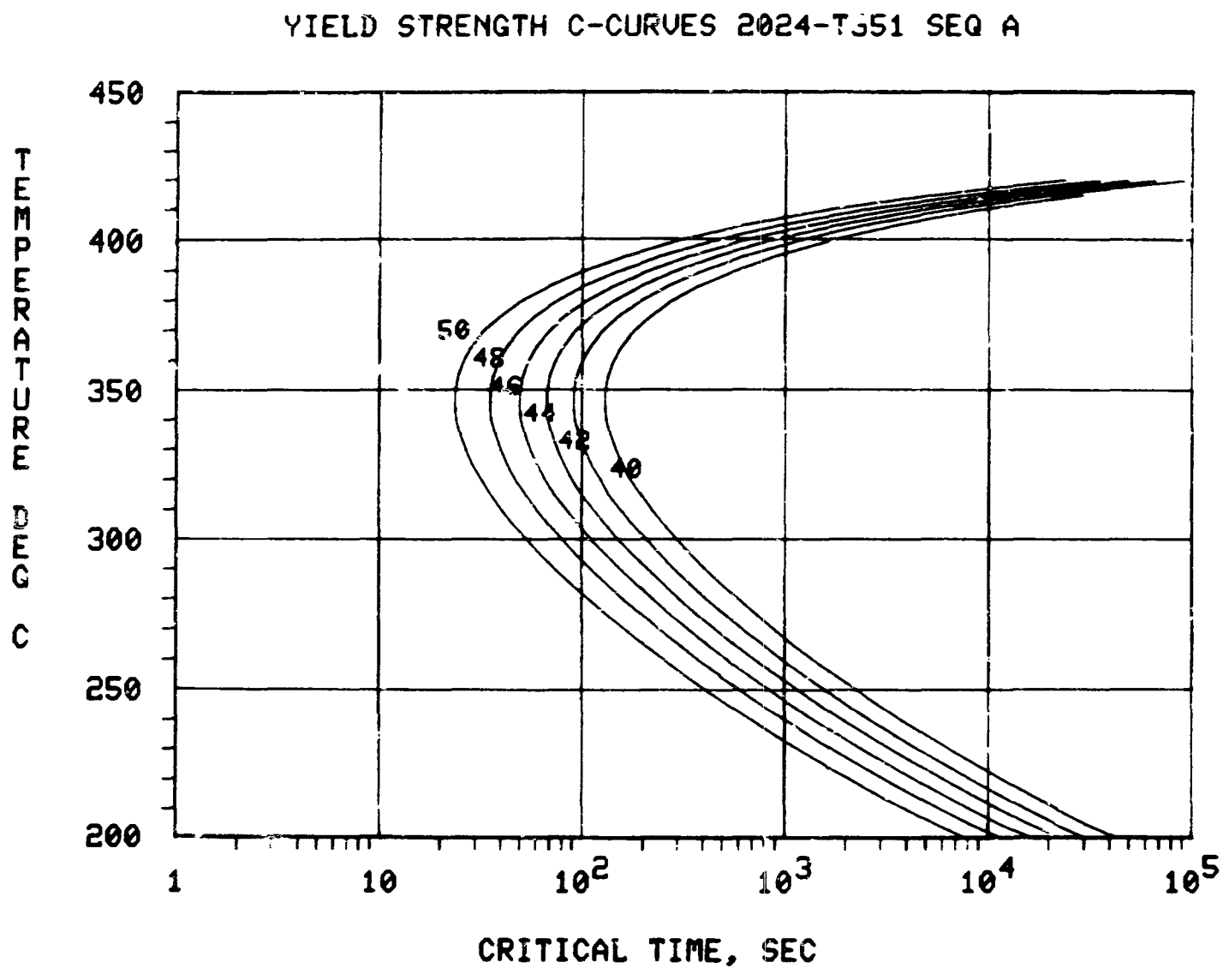

Figure 30. (a) Yield strength (0.2 percent offset) C-curves for 2024-T351 sequence A alloys. The curves give the critical times for obtaining the indicated yield strength for an isothermal sequence A type "pre-aging" heat treatment and a subsequent aging to the T351 temper.

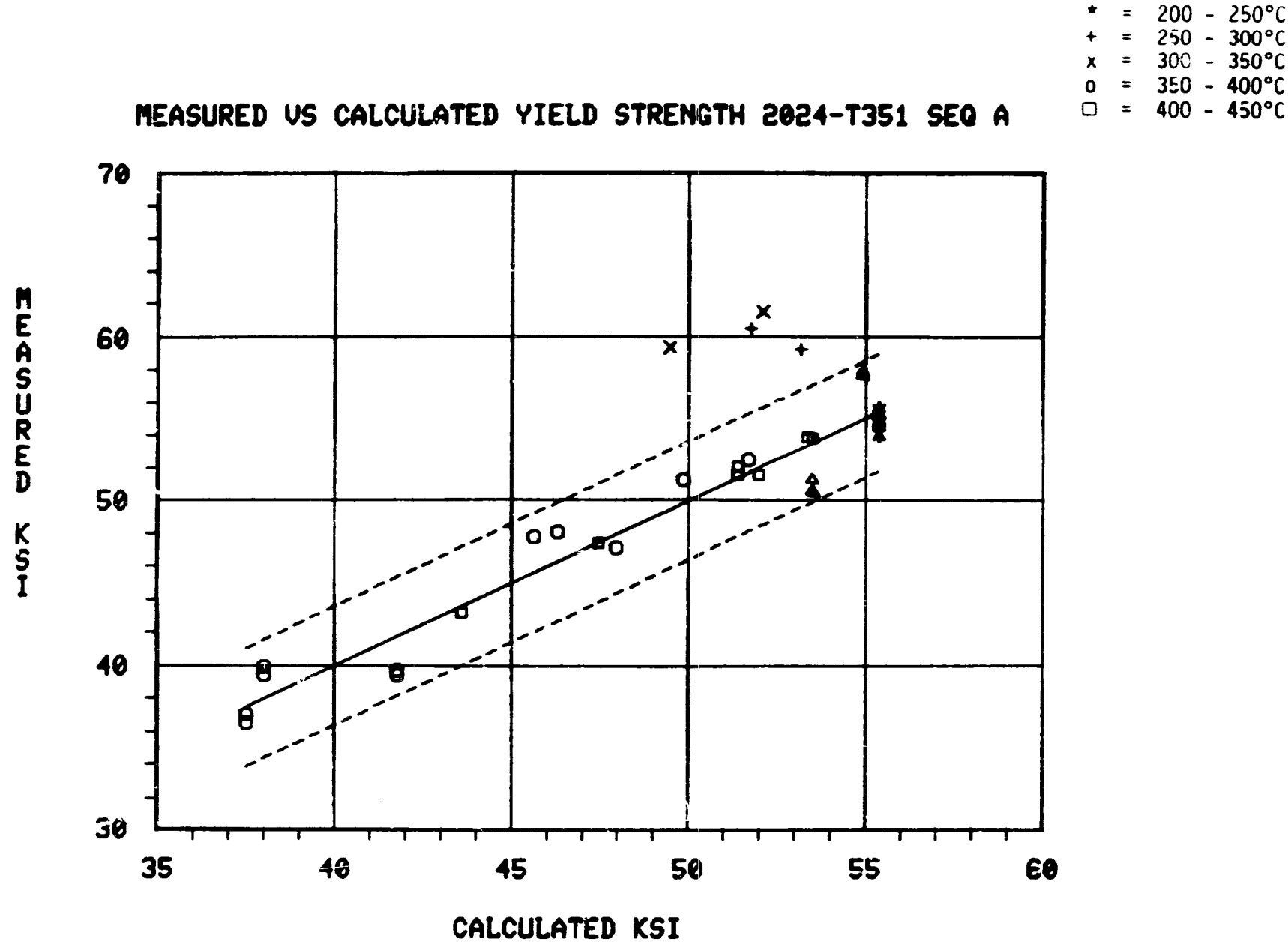

Figure 38. (b) Measured values of the yield strength plotted vs. values calculated using the yield strength C-curve for 2024-T351 sequence A. The solid line is a line of unit slope and the dashed lines are the scatter band (approximately 95 percent confidence level).

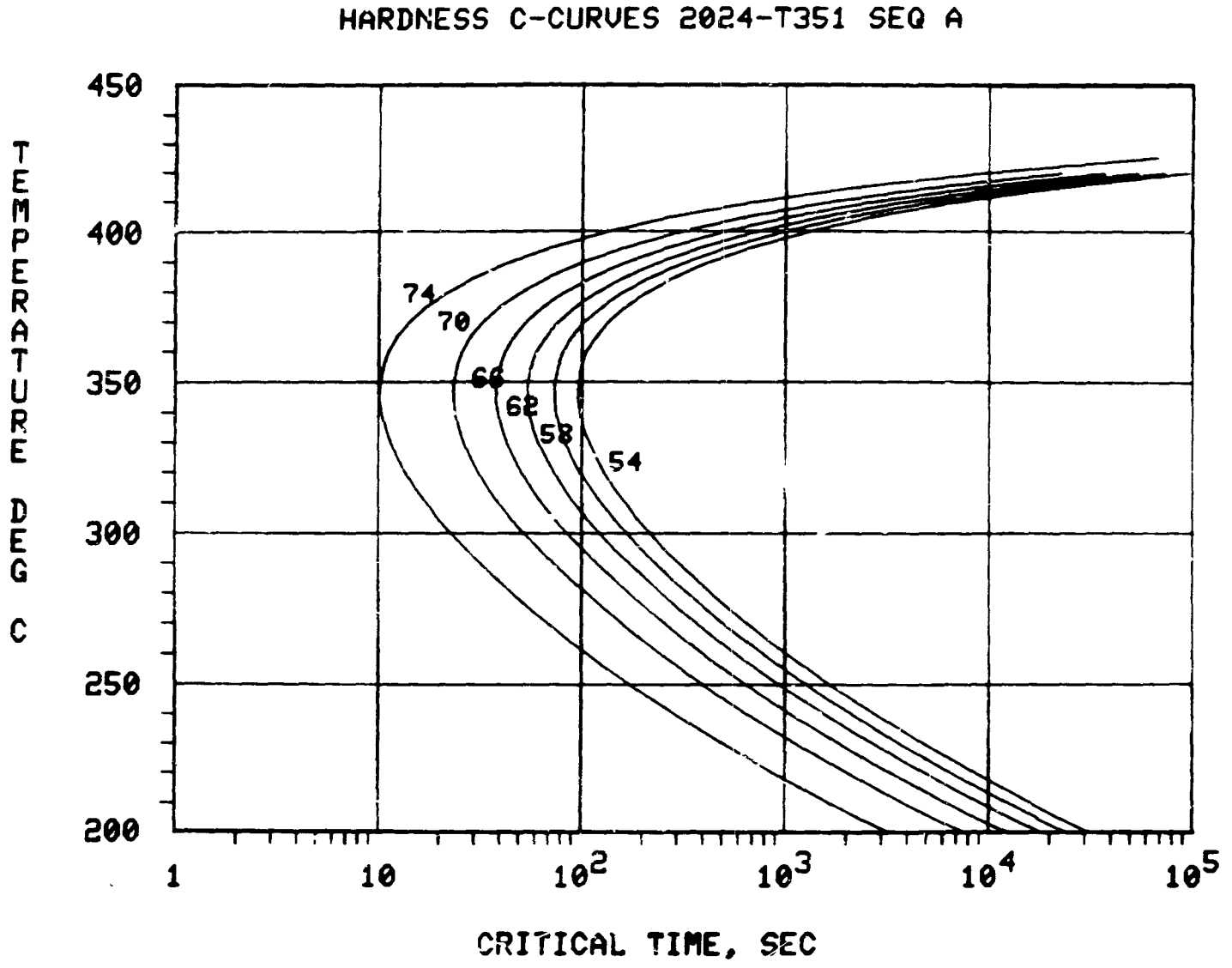

Figure 39. (a) Hardness C-curves for 2024-T351 sequence A alloys. The curves give the critical times for obtaining the indicated Rockwell B hardness for an isothermal sequence A type "pre-aging" heat treatment and a subsequent aging to the T351 temper.

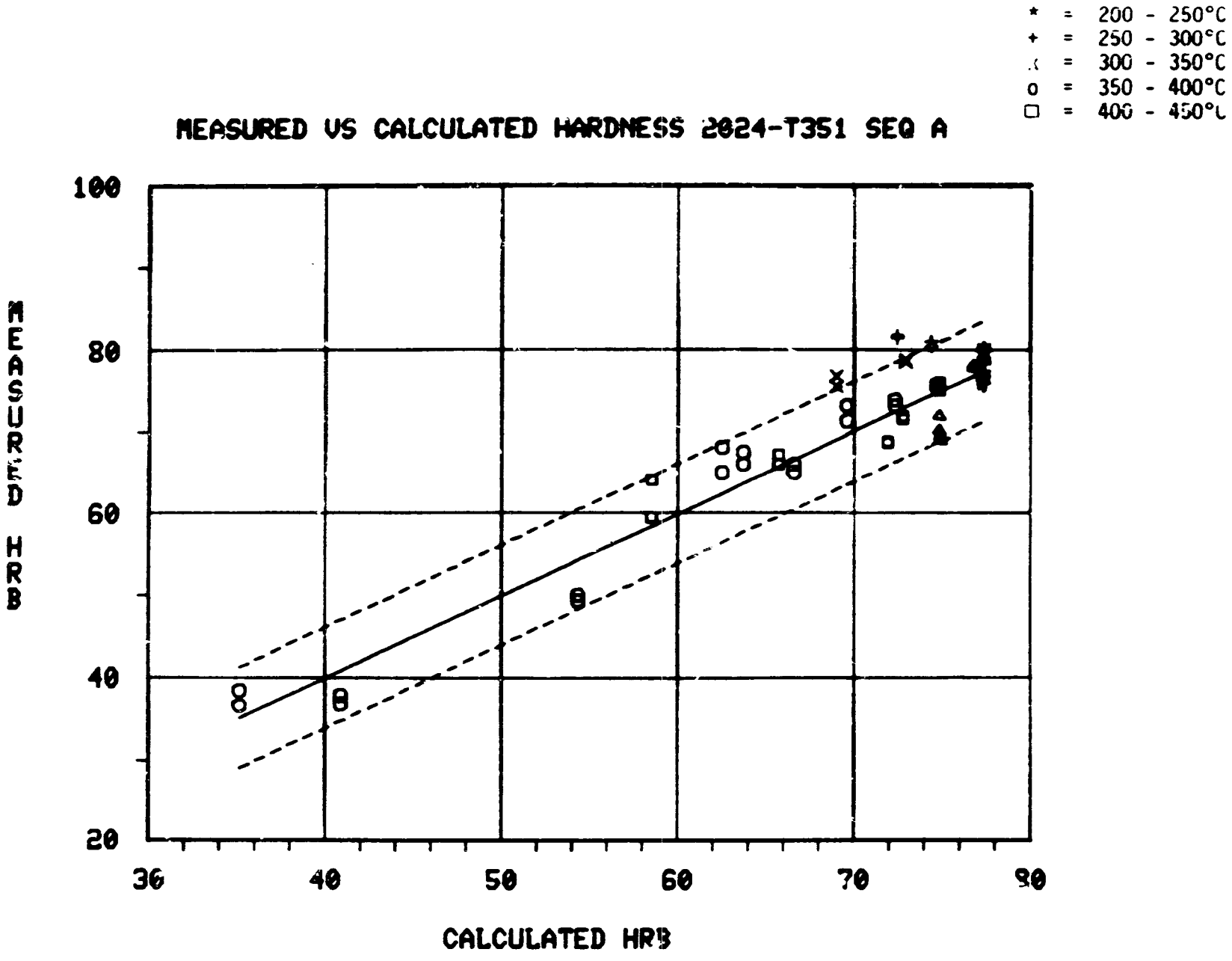

Figure 39. (b) Measured values of the Rockwell B hardness plotted vs. values calculated using the hardness C-curve for 2024-T351 sequence A. The solid line is a line of unit slope and the dashed lines are the scatter band (approximately 95 percent confidence level).

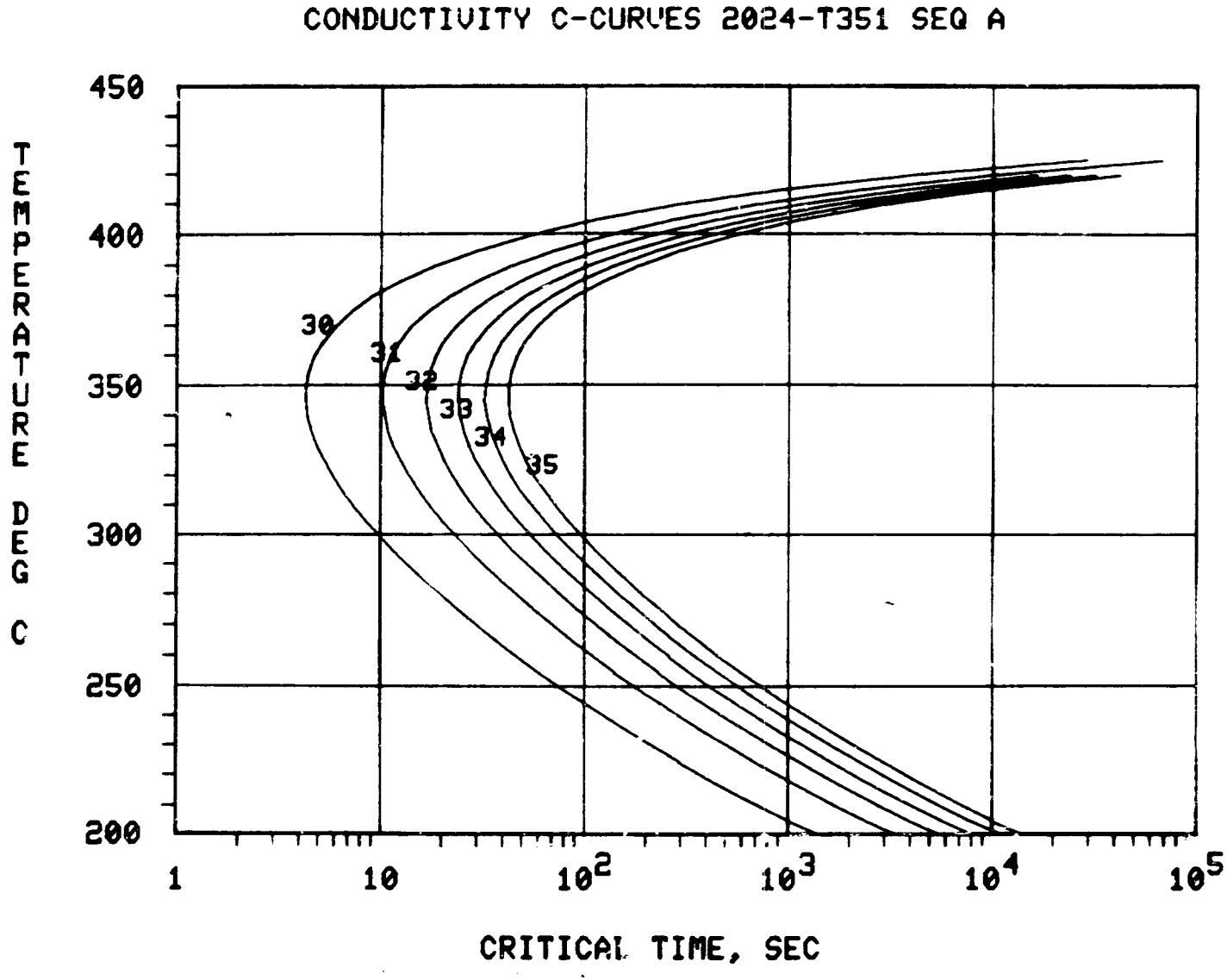

Figure 40. (a) Conductivity C-curves for 2024-T351 sequence A alloys. The curves give the critical times for obtaining the indicated conductivity for an isothermal sequence A type "pre-aging" heat treatment and a subsequent aging to the T351 temper.

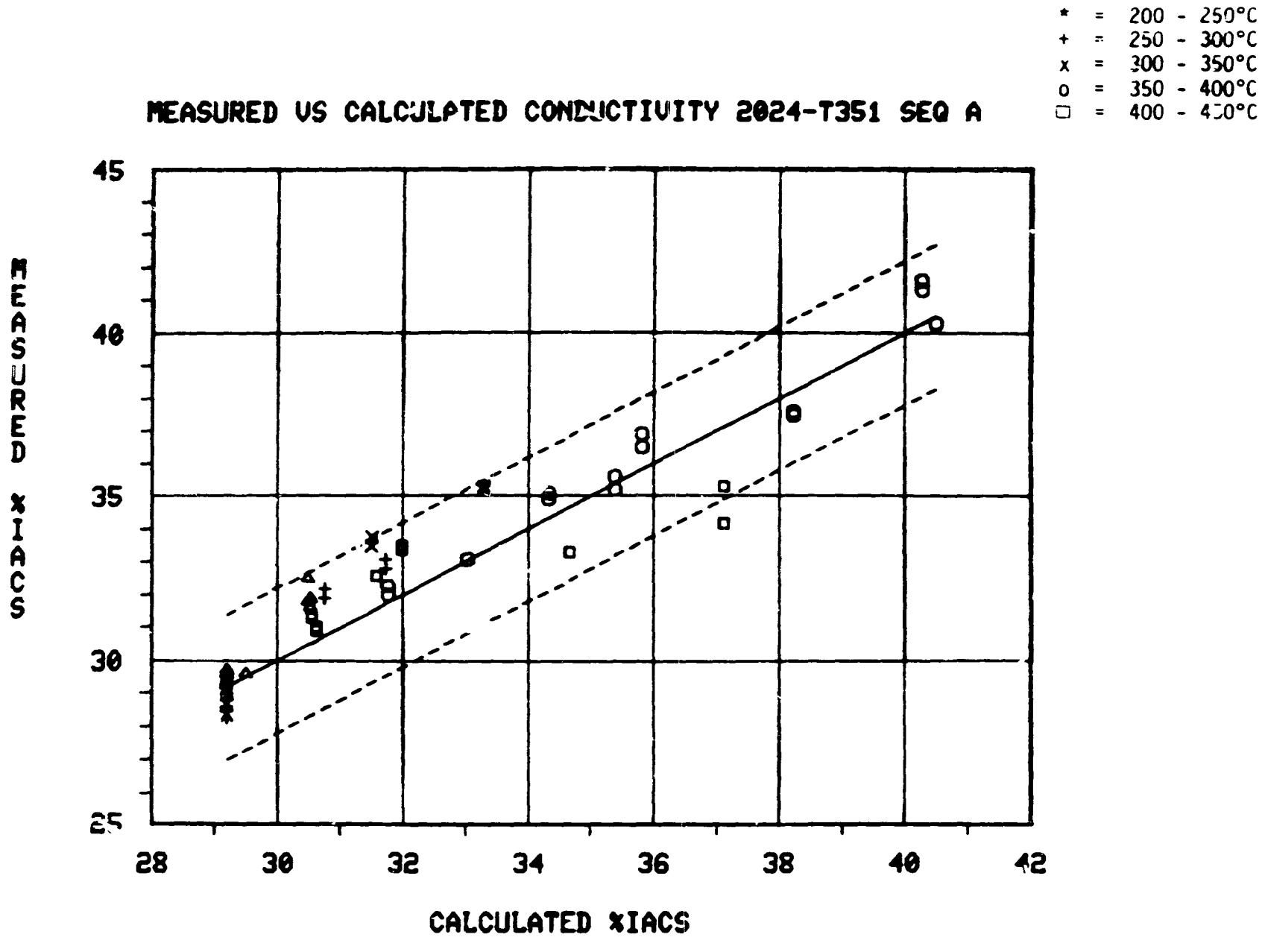

Figure 40. (b) Measured values of the conductivity plotted versus values calculated using the 2024-T351 sequence A conductivity C-curve. The solid line is a line of unit slope and the dashed lines are the scatter band (approximately 95 percent confidence level).

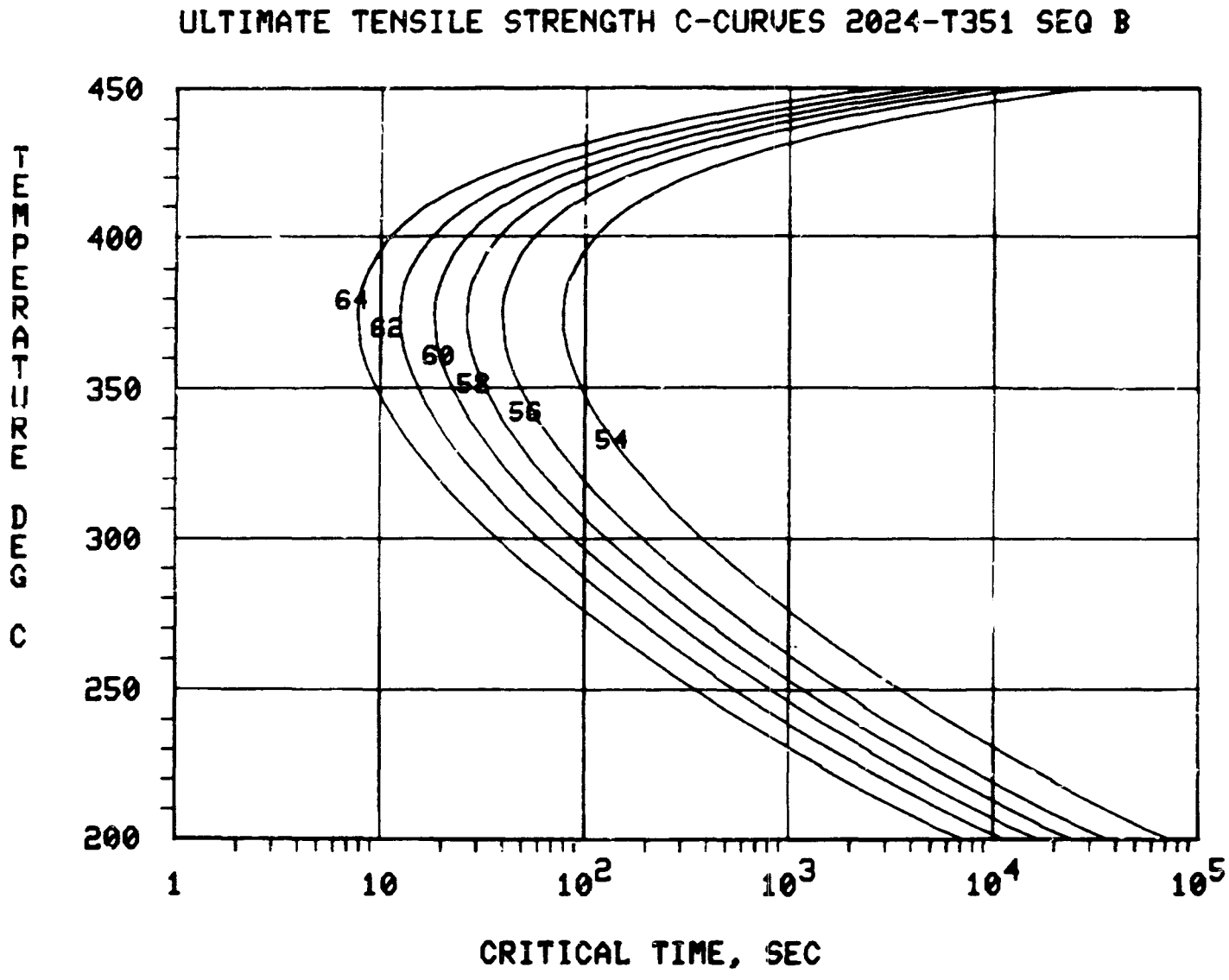

Figure 41. (a) Ultimate tensile strength C-curves for 2024-T351 sequence B alloys. The curves give the critical times for obtaining the indicated tensile strength for an isothermal sequence B type "pre-aging" heat treatment and a subsequent aging to the T351 temper.

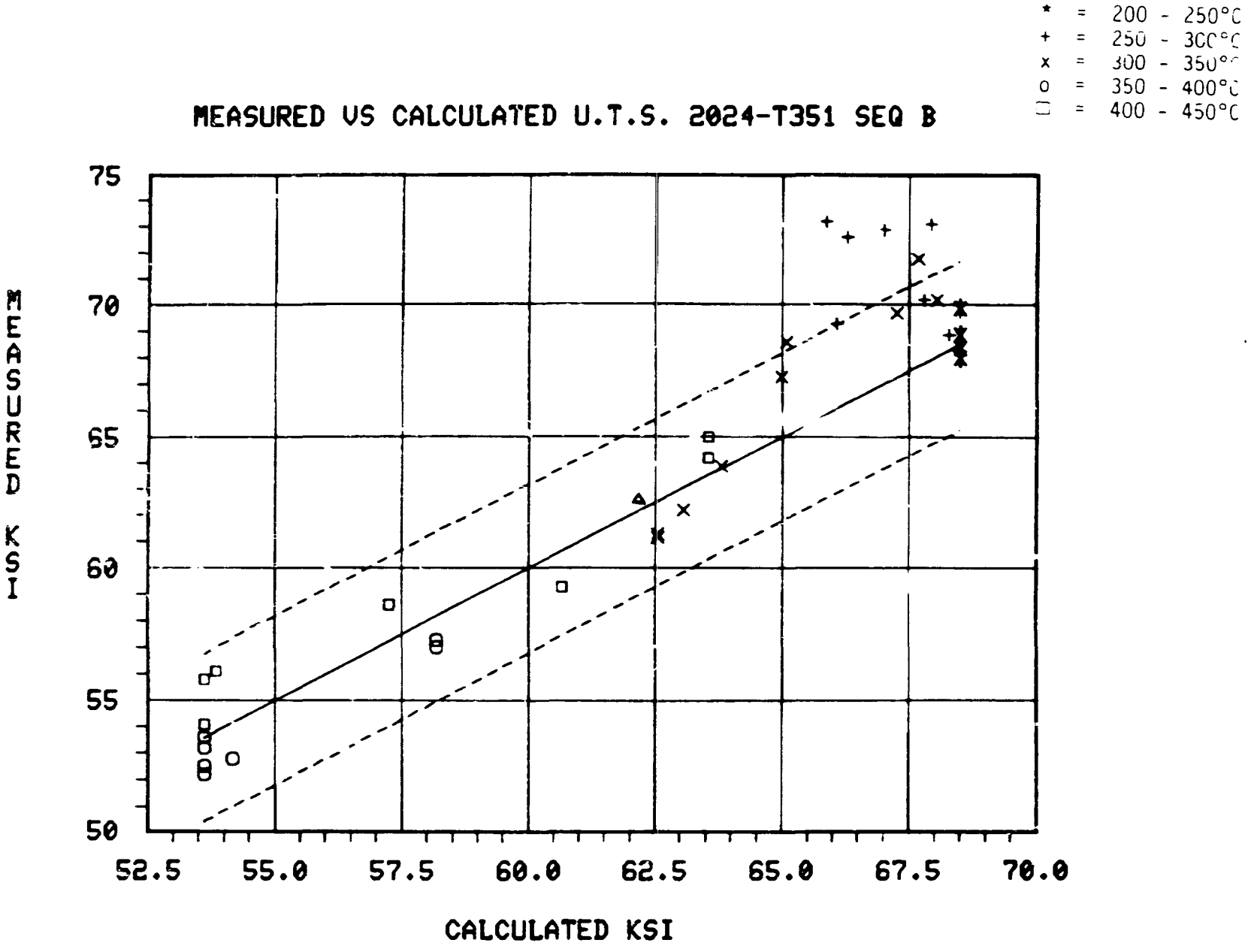

Figure 41. (b) Measured values of the ultimate tensile strength plotted against the values calculated using the C-curve for 2024-T351 sequence B. The solid line is a line of unit slop and the dashed line is the scatter band (approximately 95 percent confidence level).

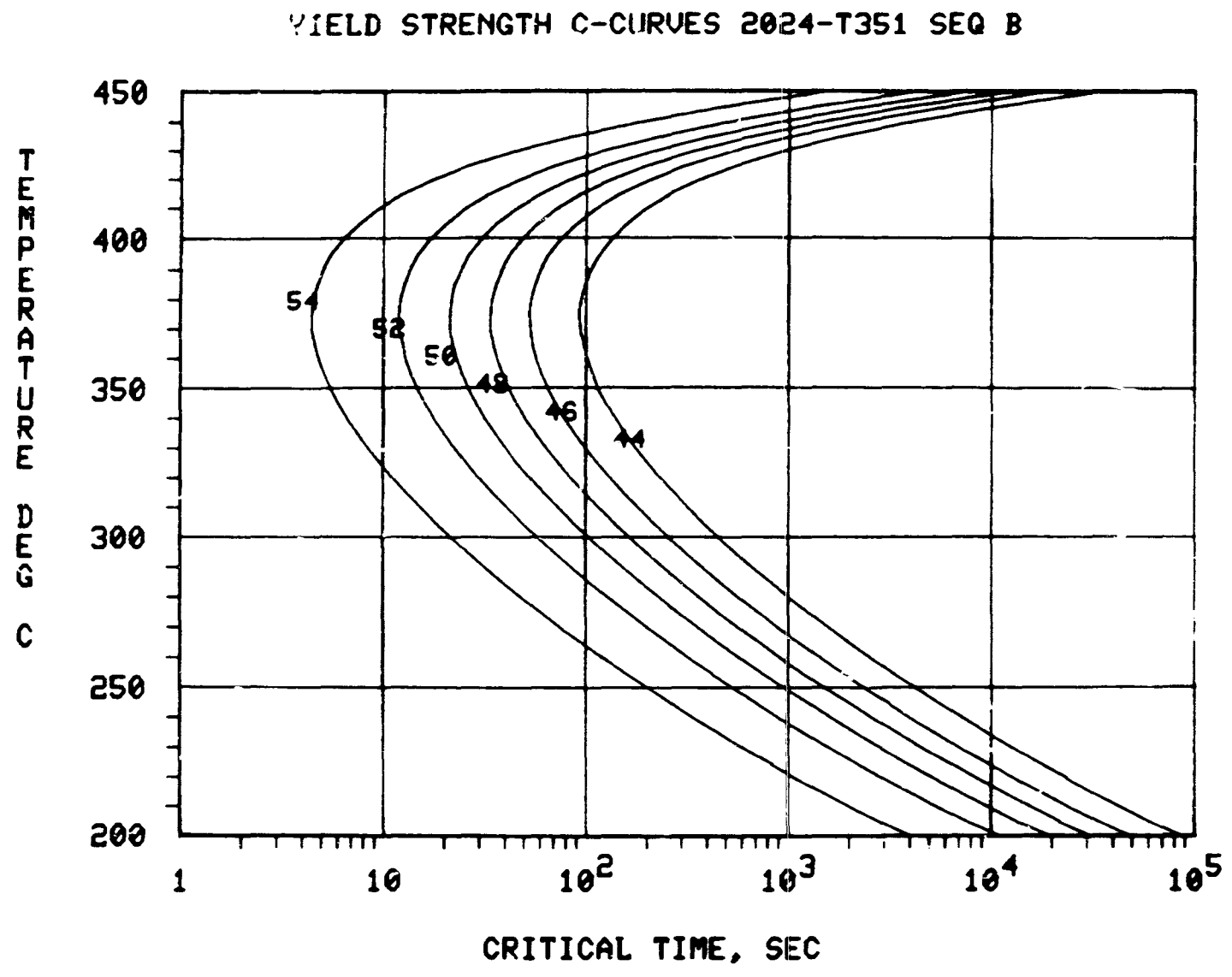

Figure 42. (a) Yield strength (0.2 percent offset) C-curves for 2024-T351 sequence B alloys. The curves give the critical times for obtaining the indicated yield strength for an isothermal sequence B type "pre-aging" heat treatment and a subsequent aging to the T351 temper.

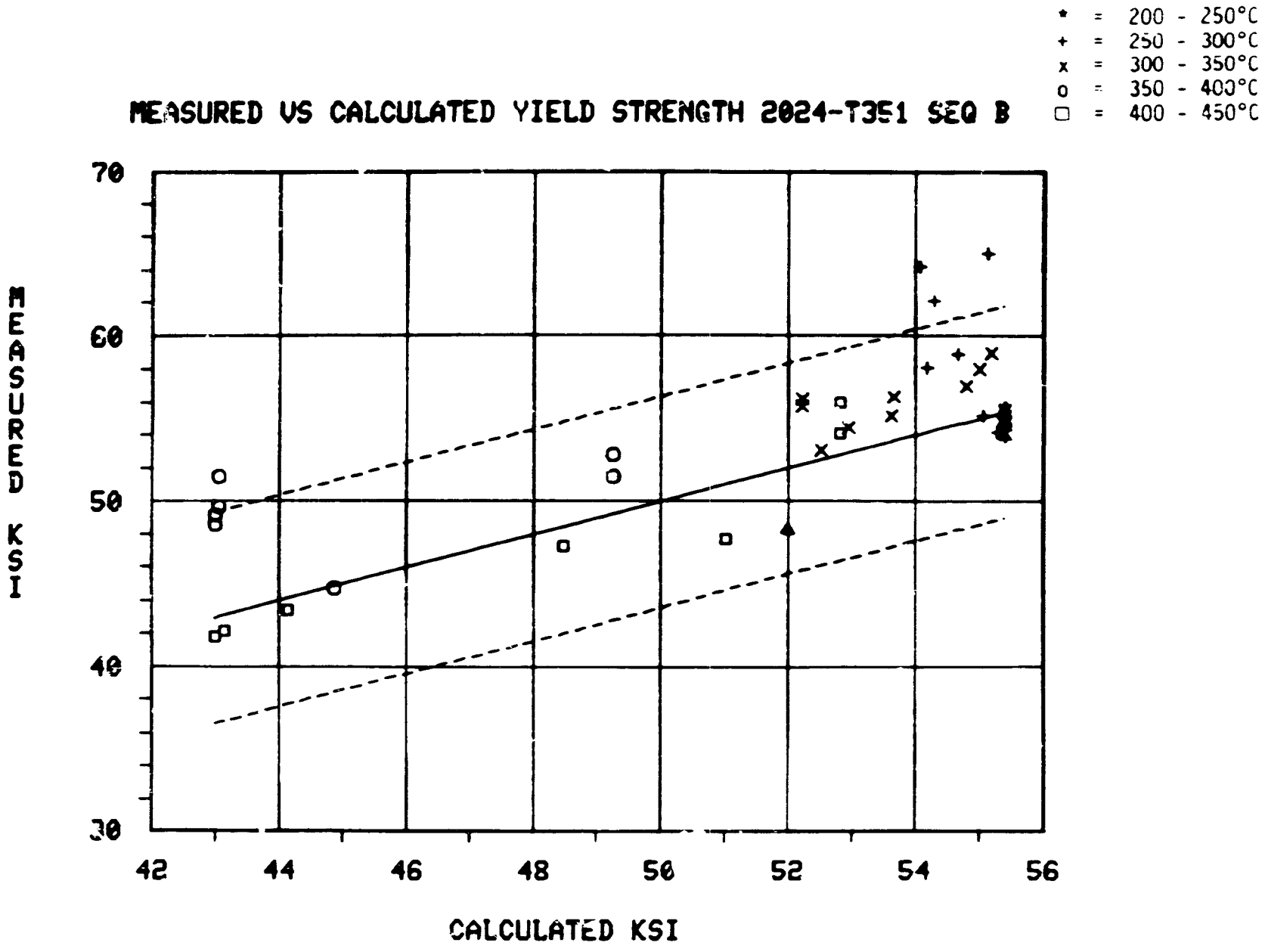

Figure 42. (b) Measured values of the yield strength plotted versus values calculated using the yield strength C-curve for 2024-T351 sequence B. The solid line is a line of unit slope and the dashed lines are the scatter band (approximately 95 percent confidence level).

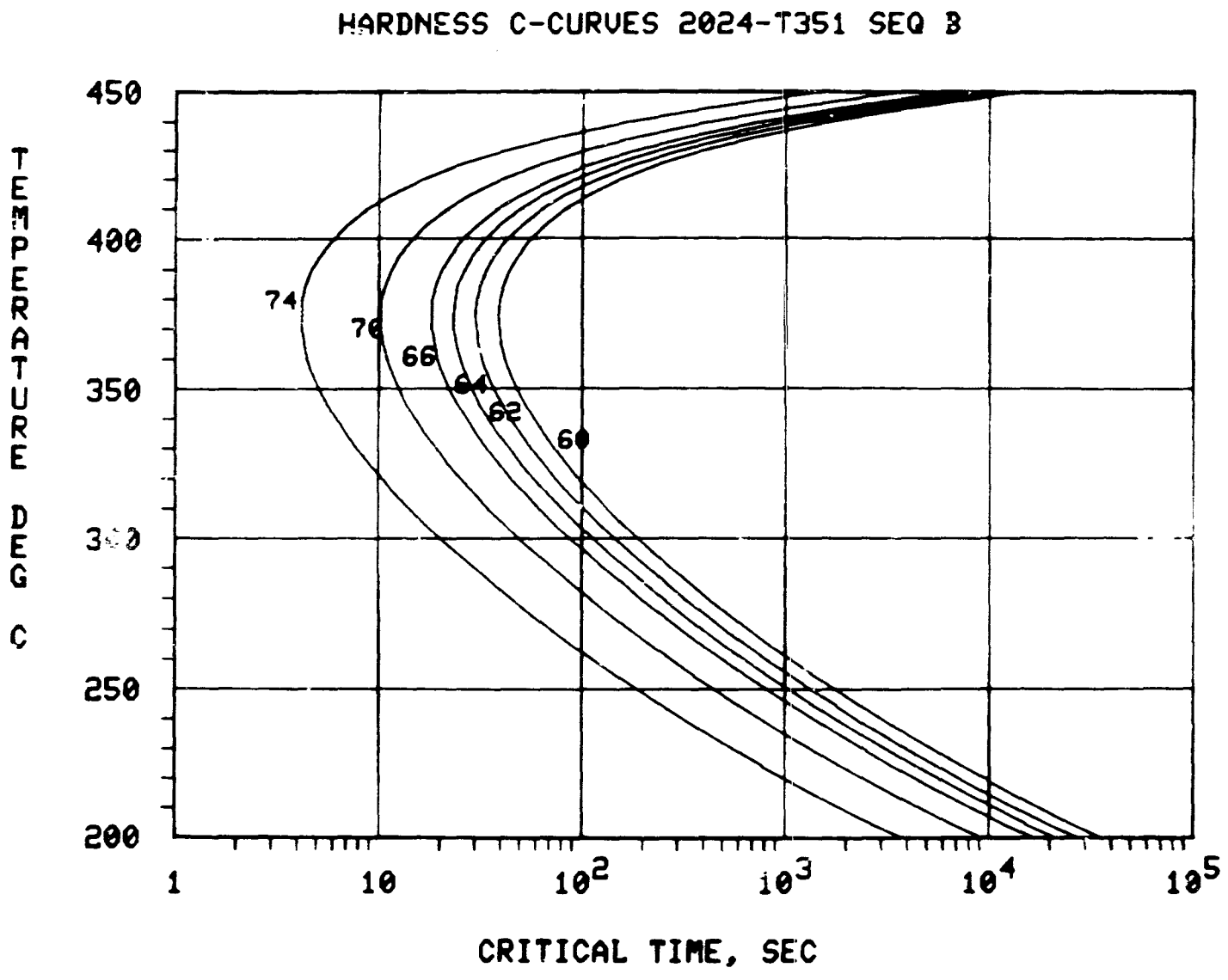

Figure 43. (a) Hardness C-curves for 2024-T351 sequence B alloys. The curves give the critical times for obtaining the indicated Rockwell B hardness for an isothermal sequence B type "pre-aging" heat treatment and a subsequent aging to the T351 temper.

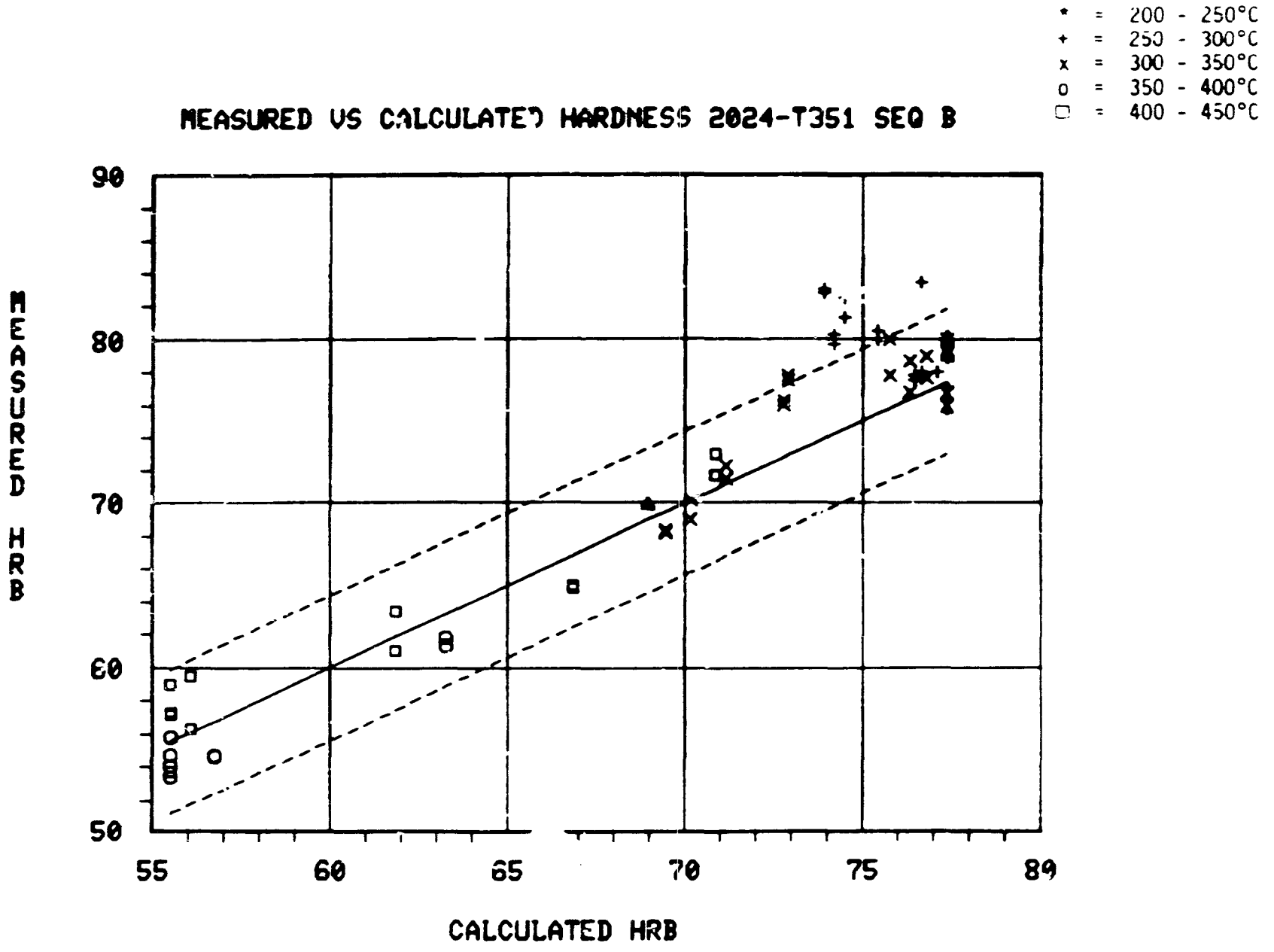

Figure 43. (b) Measured values of the Rockwell B hardness plotted vs. values calculated using the hardness C-curve for 2024-T351 sequence B. The solid line is a line of unit slope and the dashed lines are the scatter band (approximately 95 percent confidence level).

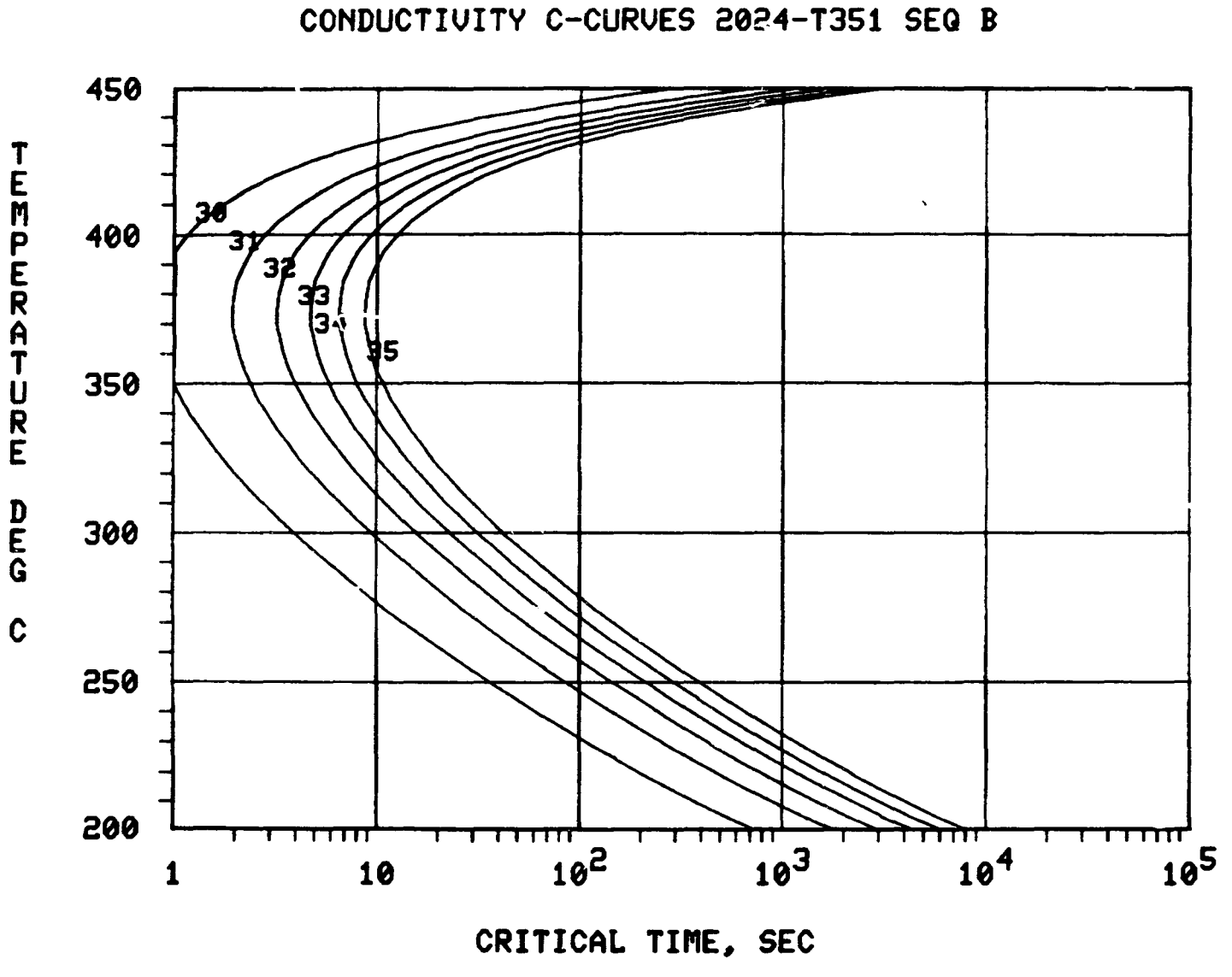

Figure 44. (a) Conductivity C-curves for 2024-T351 sequence B alloys. The curves give the critical times for obtaining the indicated conductivity for an isothermal sequence B type "pre-aging" heat treatment and a subsequent aging to the T351 temper.

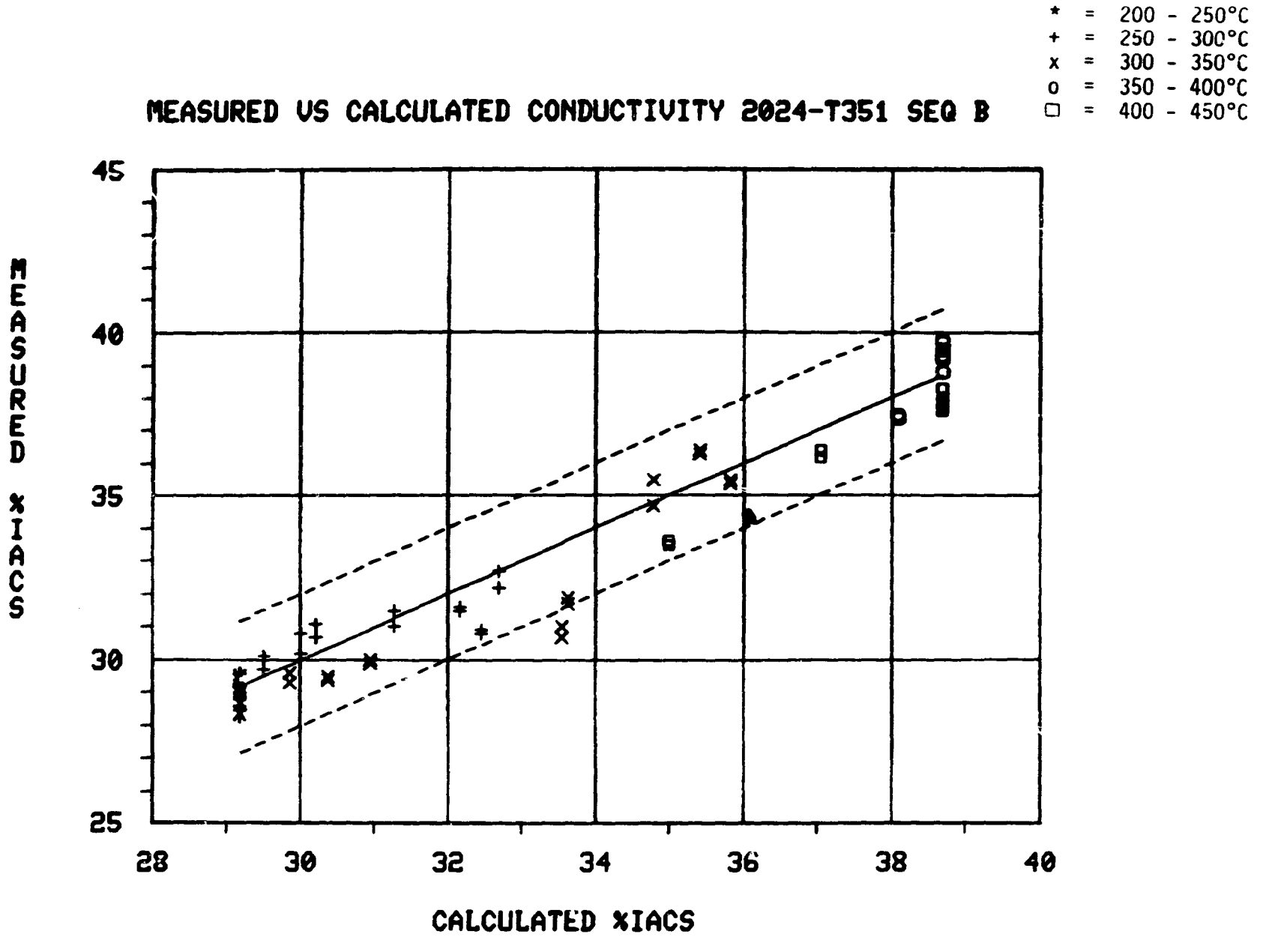

Figure 44. (b) Measured values of the conductivity plotted vs. values calculated using the 2024-T351 sequence B conductivity C-curve. The solid line is a line of unit slope and the dashed lines are the scatter band (approximately 95 percent confidence level).

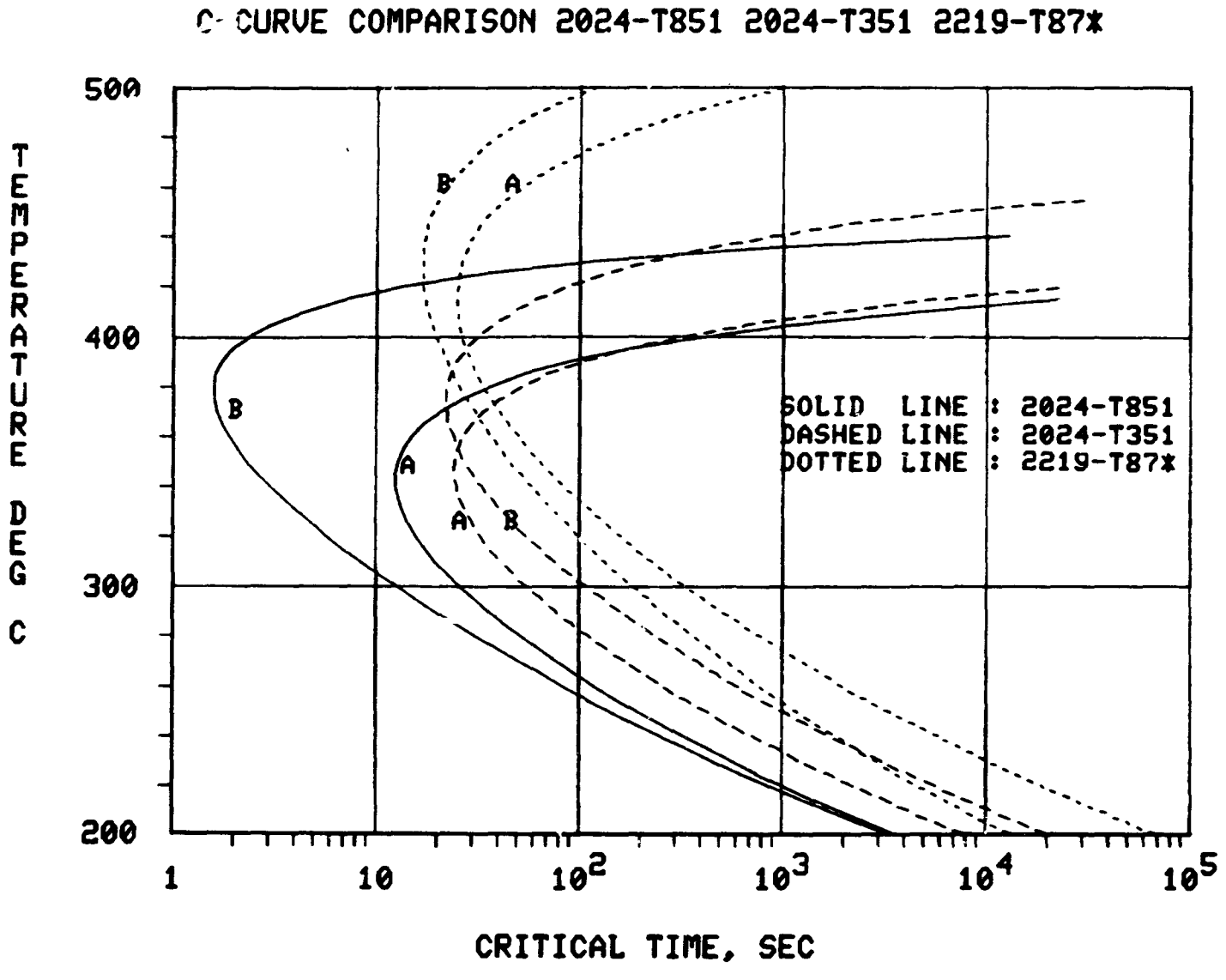

Figure 45. Comparison of yield strength (0.2 percent offset) C-curves for sequence A and sequence B "pre-aging" treatments of 2024-T851, 2024-T351, and 2219-T87* aluminum alloys. The corresponding yield strength values are 90 percent of the yield strength obtained from a direct quench (60 ksi for 2024-T851, 50 ksi for 2024-T351, and 50 ksi for 2219-T87*). The 2219-T87* data is from Reference (1).

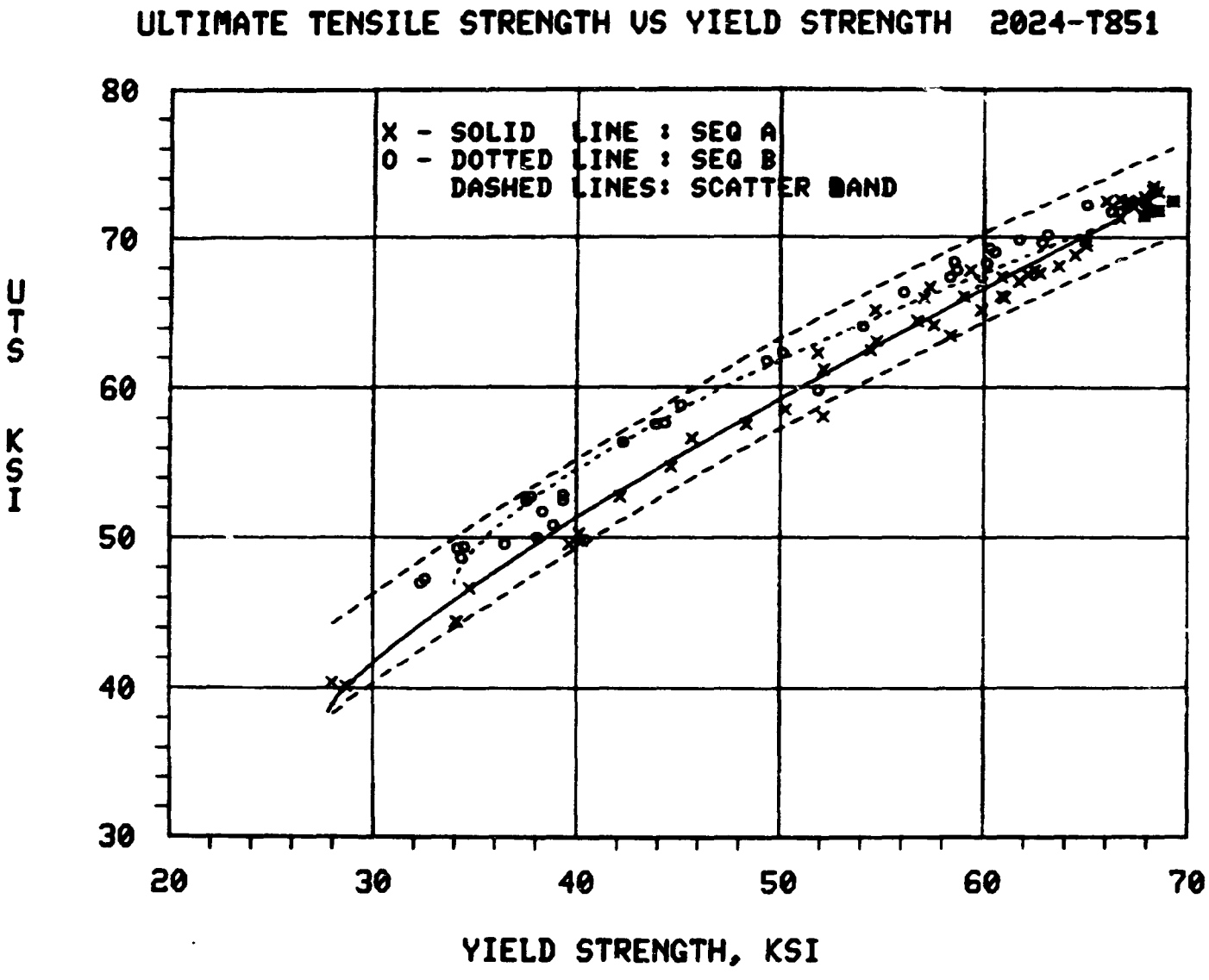

Figure 46. Comparison of ultimate tensile strength vs. yield strength for 2024-T851 with the correlations predicted by the C-curves. The dashed lines are the scatter band (~95% confidence level) obtained from a least squares quadratic fit to the data. The solid and dotted lines were calculated from the C-curves.

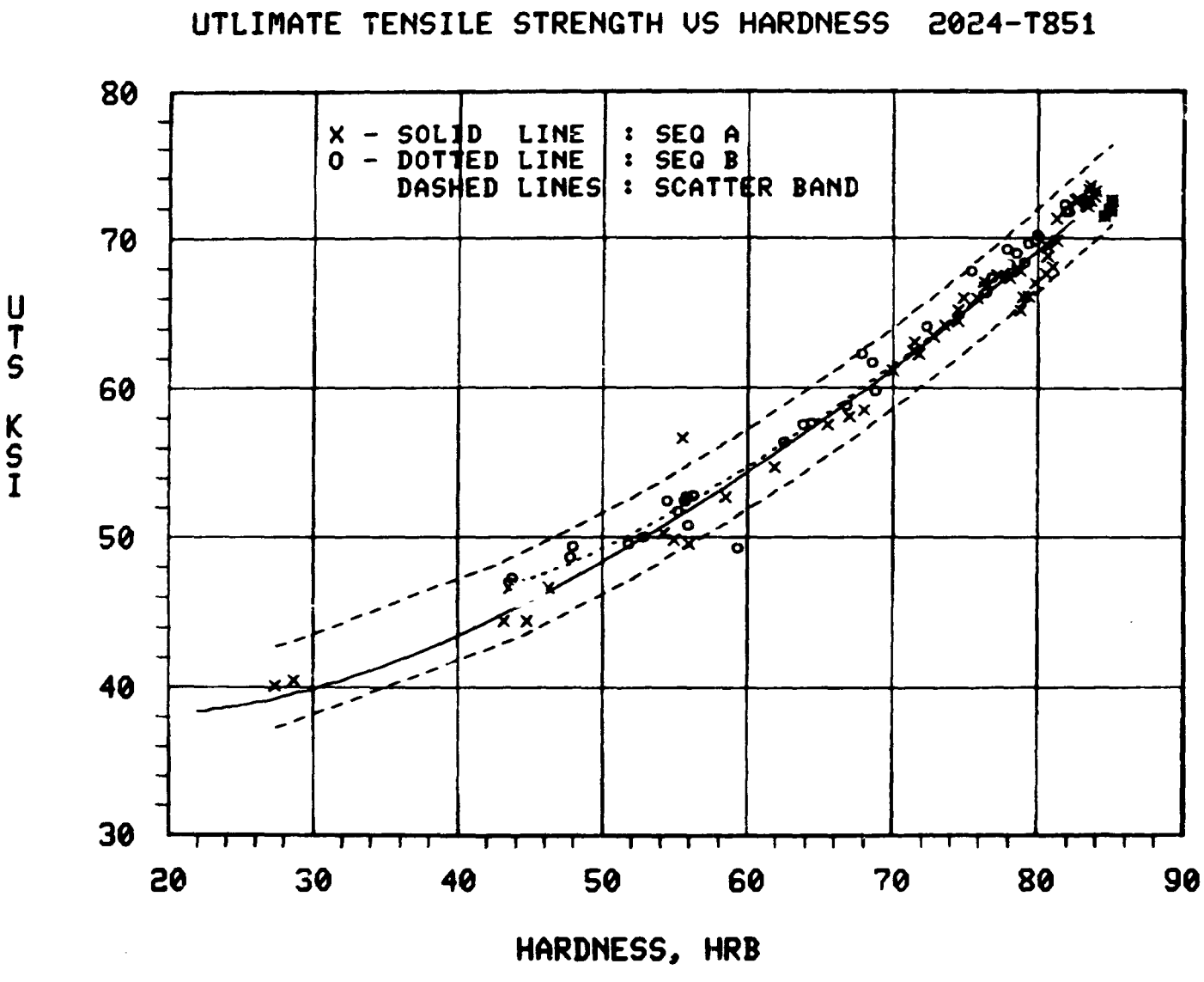

Figure 47. Comparison of ultimate tensile strength vs. hardness data for 2024-T851 with the correlations predicted by the C-curves. The dashed lines are the scatter band (~95% confidence level) obtained from the least squares quadratic fit to the data. The solid and dotted lines were calculated from the C-curves.

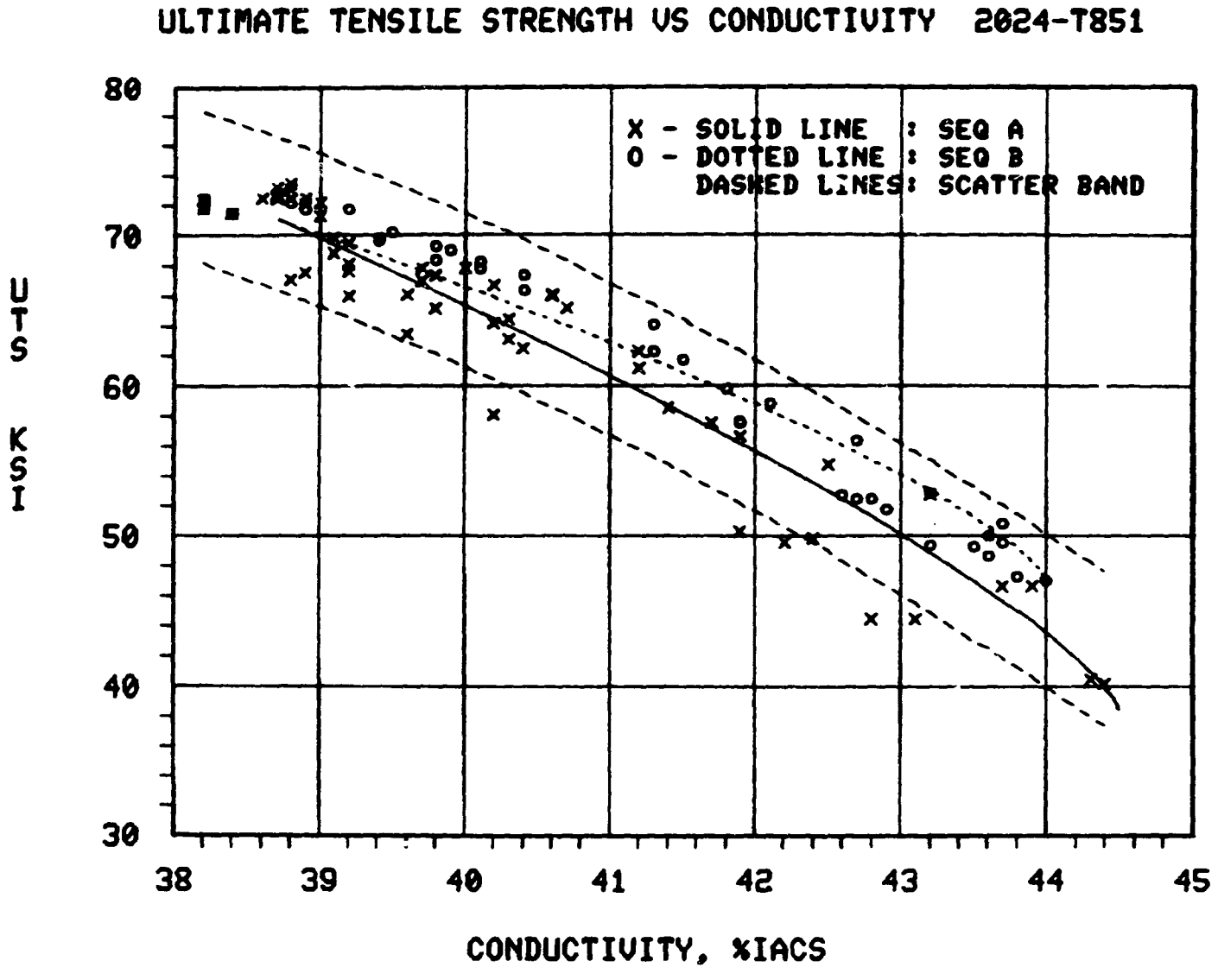

Figure 48. Comparison of ultimate tensile strength vs. conductivity data for 2024-T851 with the correlations predicted by the C-curves. The dashed lines are the scatter band (~95% confidence level) obtained from a least squares quadratic fit to the data. The solid and dotted lines were calculated from the C-curves.

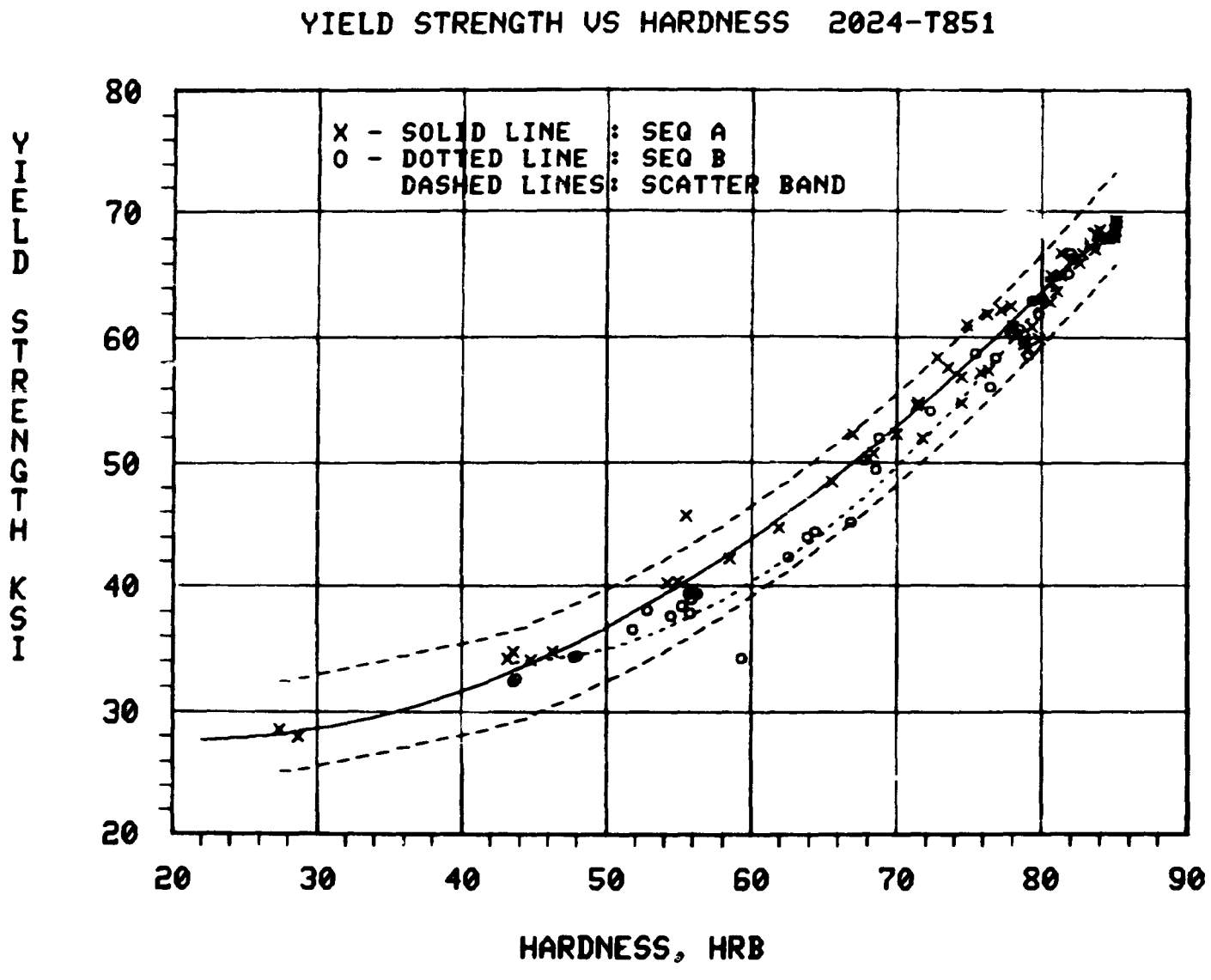

Figure 49. Comparison of yield strength vs. hardness data for 2024-T851 with the correlations predicted by the C-curves. The dashed lines are the scatter band (~95% confidence level) obtained from a least squares quadratic fit to the data. The solid and dotted lines were calculated from the C-curves.

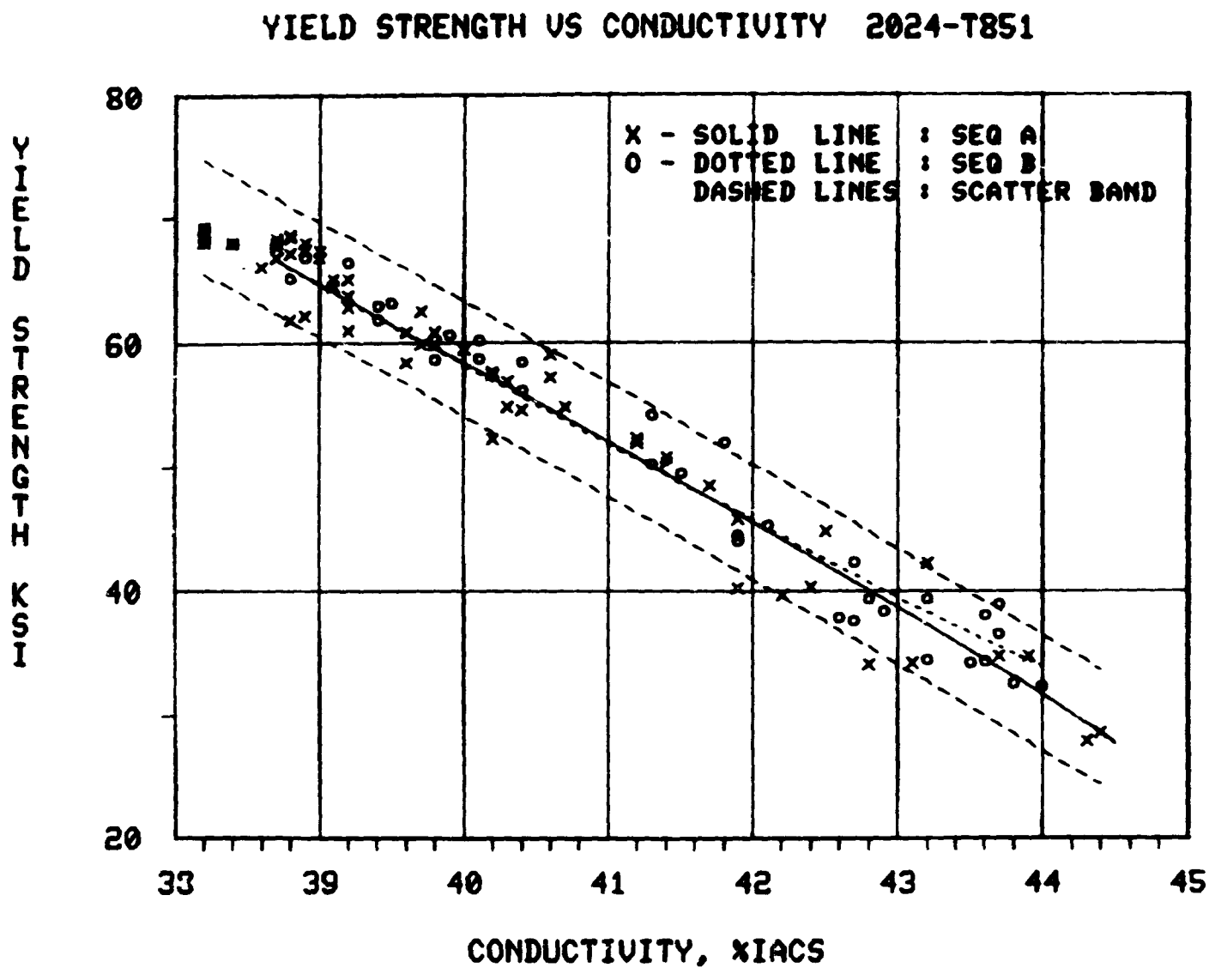

Figure 50. Comparison of yield strength vs. conductivity data for 2024-T851 with correlations predicted by the C-curves. The dashed lines are the scatter band (∿95% confidence level) obtained from a least squares quadratic fit to the data. The solid and dotted lines were calculated from the C-curves.

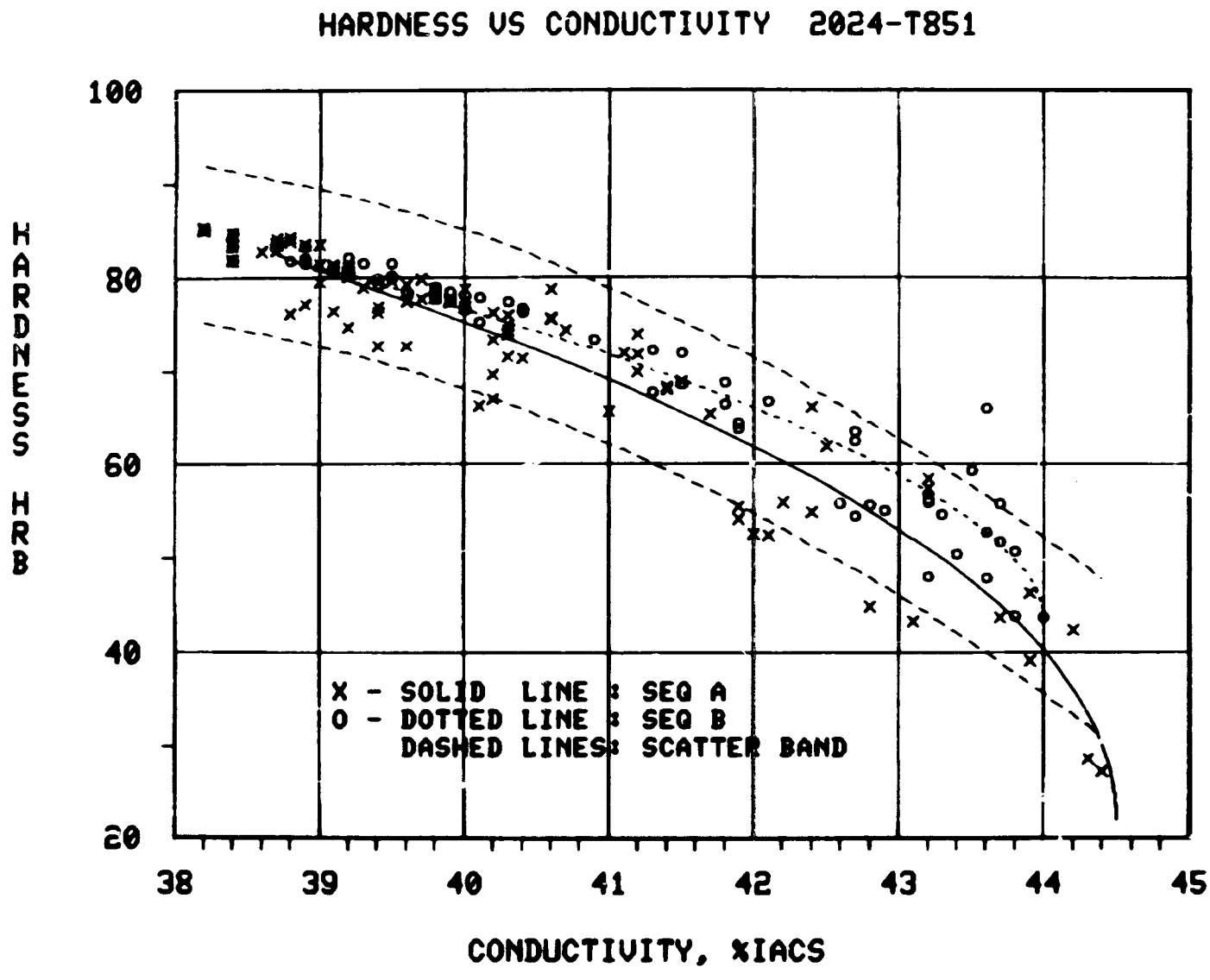

Figure 51. Comparison of hardness vs. conductivity data for 2024-T851 with the correlations predicted by the C-curves. The dashed lines are the scatter band (~95% confidence level) obtained from a least squares quadratic fit to the data. The solid and dotted lines were calculated from the C-curves.

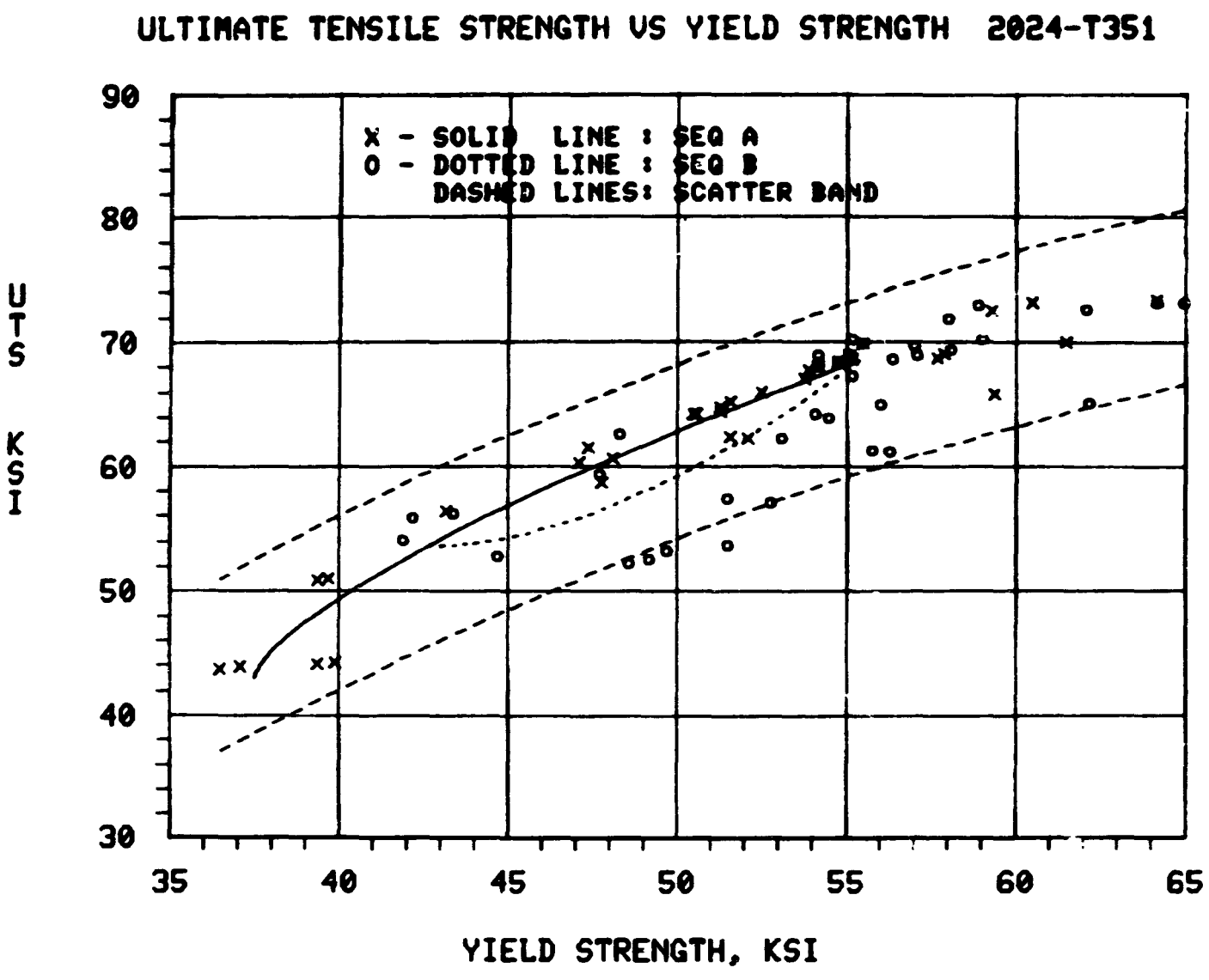

Figure 52. Comparison of ultimate tensile strength vs. yield strength for 2024-T351 with the correlations predicted by the C-curves. The dashed lines are the scatter band (~95% confidence level) obtained from a least squares quadratic fit to the data. The solid and dotted lines were calculated from the C-curves.

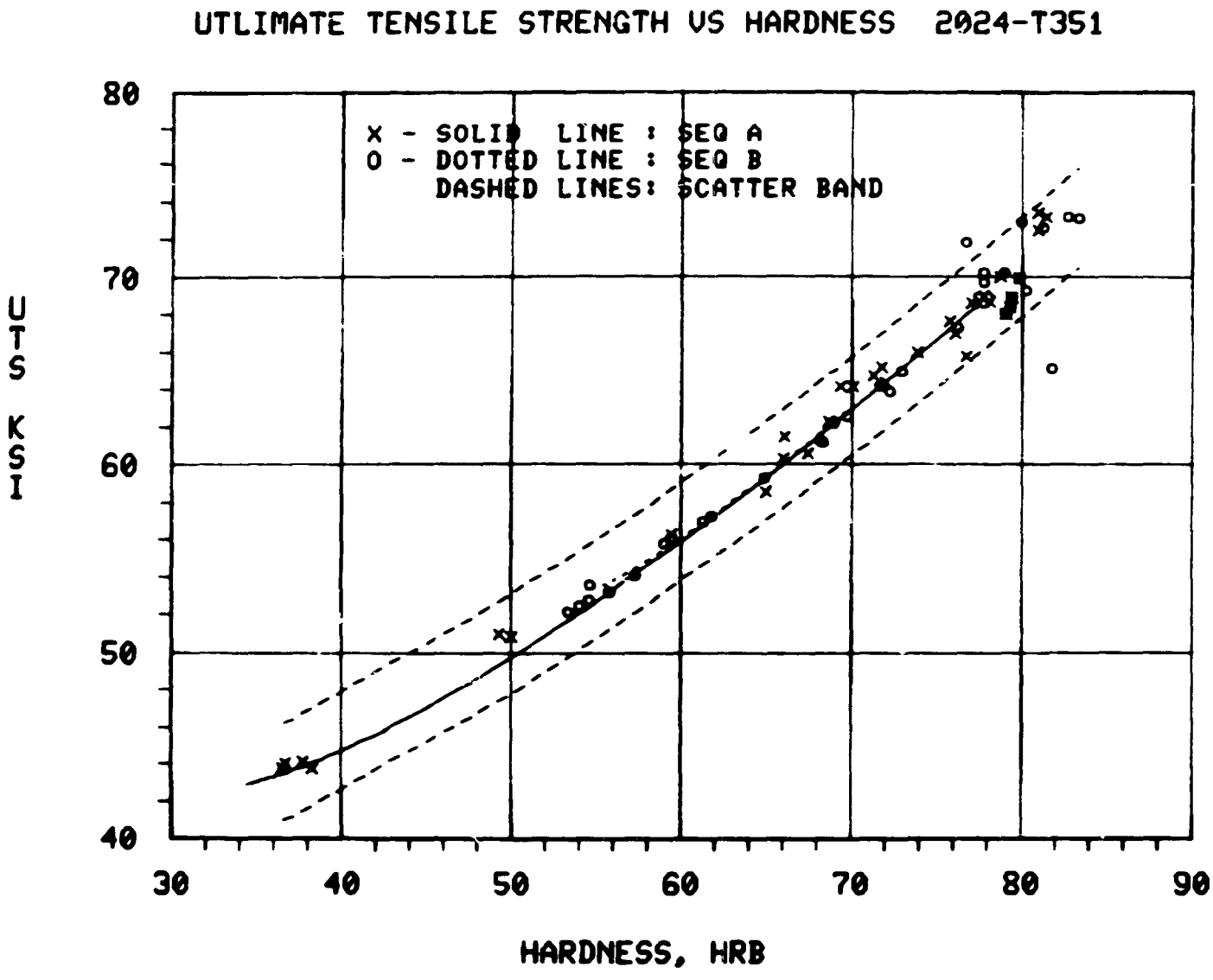

Figure 53. Comparison of ultimate tensile strength vs. hardness data for 2024-T351 with the correlations predicted by the C-curves. The dashed lines are the scatter band (~95% confidence level) obtained from a least squares quadratic fit to the data. The solid and dotted lines were calculated from the C-curves.

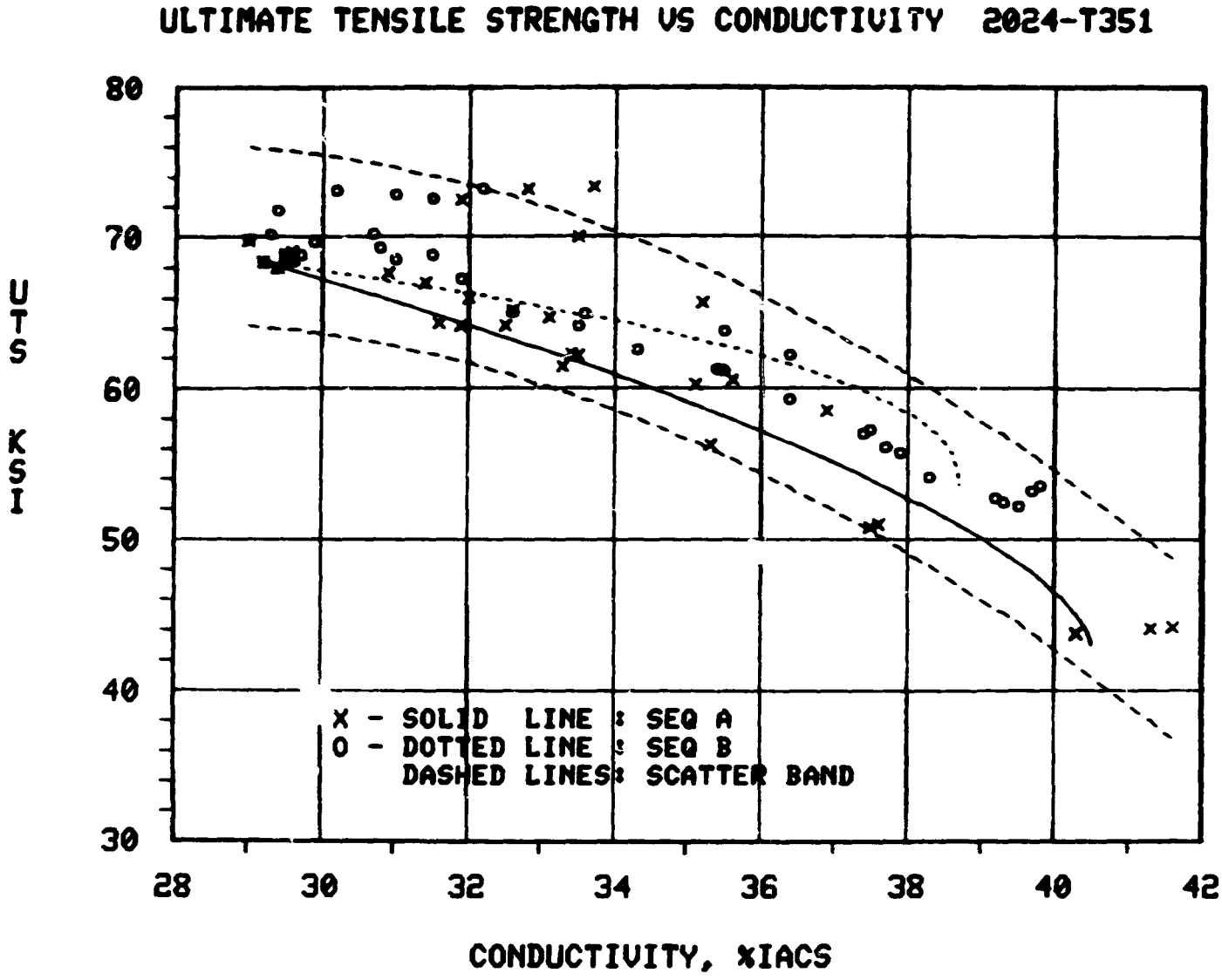

Figure 54. Comparison of ultimate tensile strength vs. conductivity data for 2024-T351 the correlation predicted by the C-curves. The dashed lines are the scatter band (~95% confidence level) obtained from a least squares quadratic fit to the data. The solid and dotted lines were calculated from the C-curves.

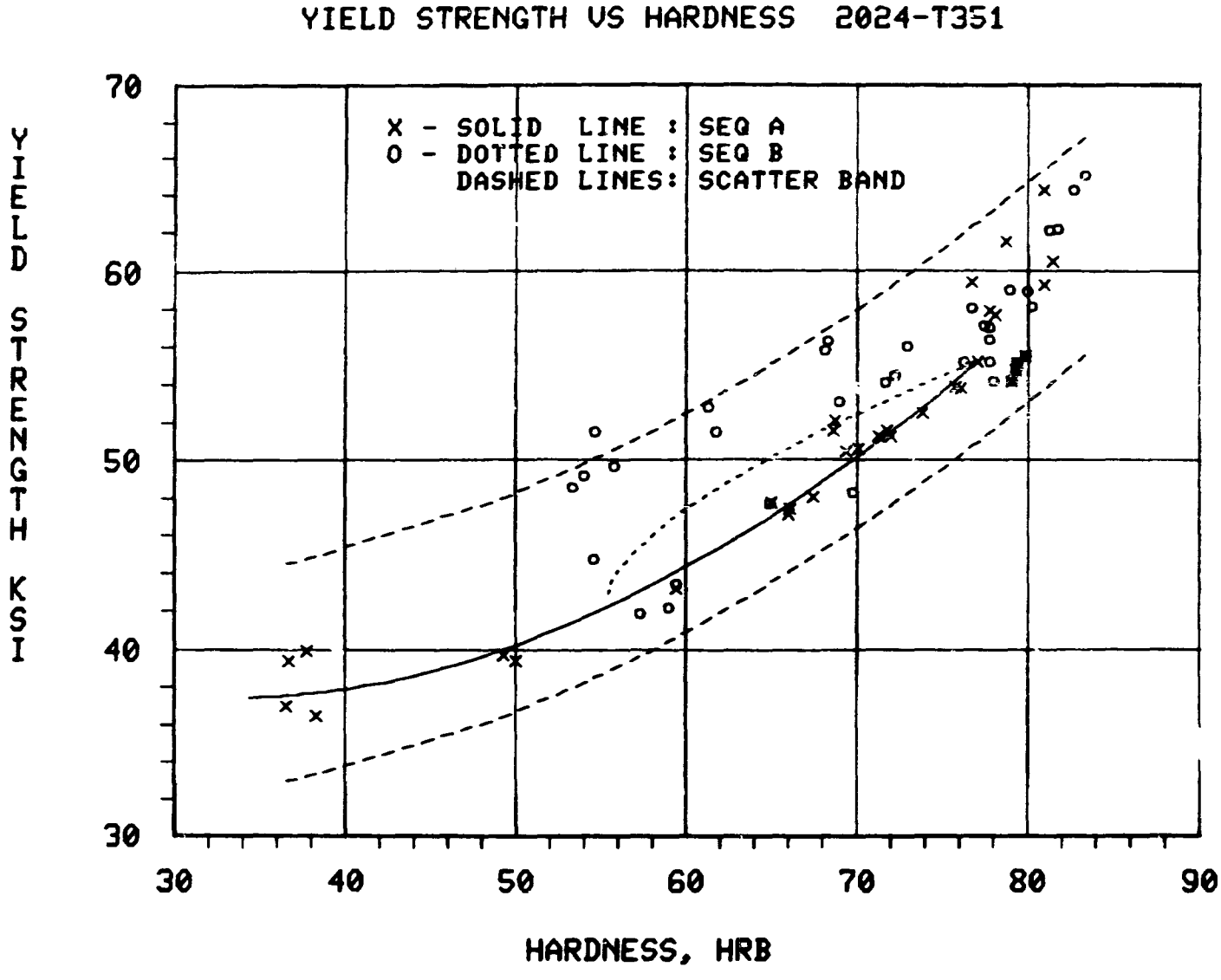

Figure 55. Comparison of yield strength vs. hardness data for 2024-T351 with the correlations predicted by the C-curves. The dashed lines are the scatter band (~95% confidence level) obtained from a least squares quadratic fit to the data. The solid and dotted lines were calculated from the C-curves.

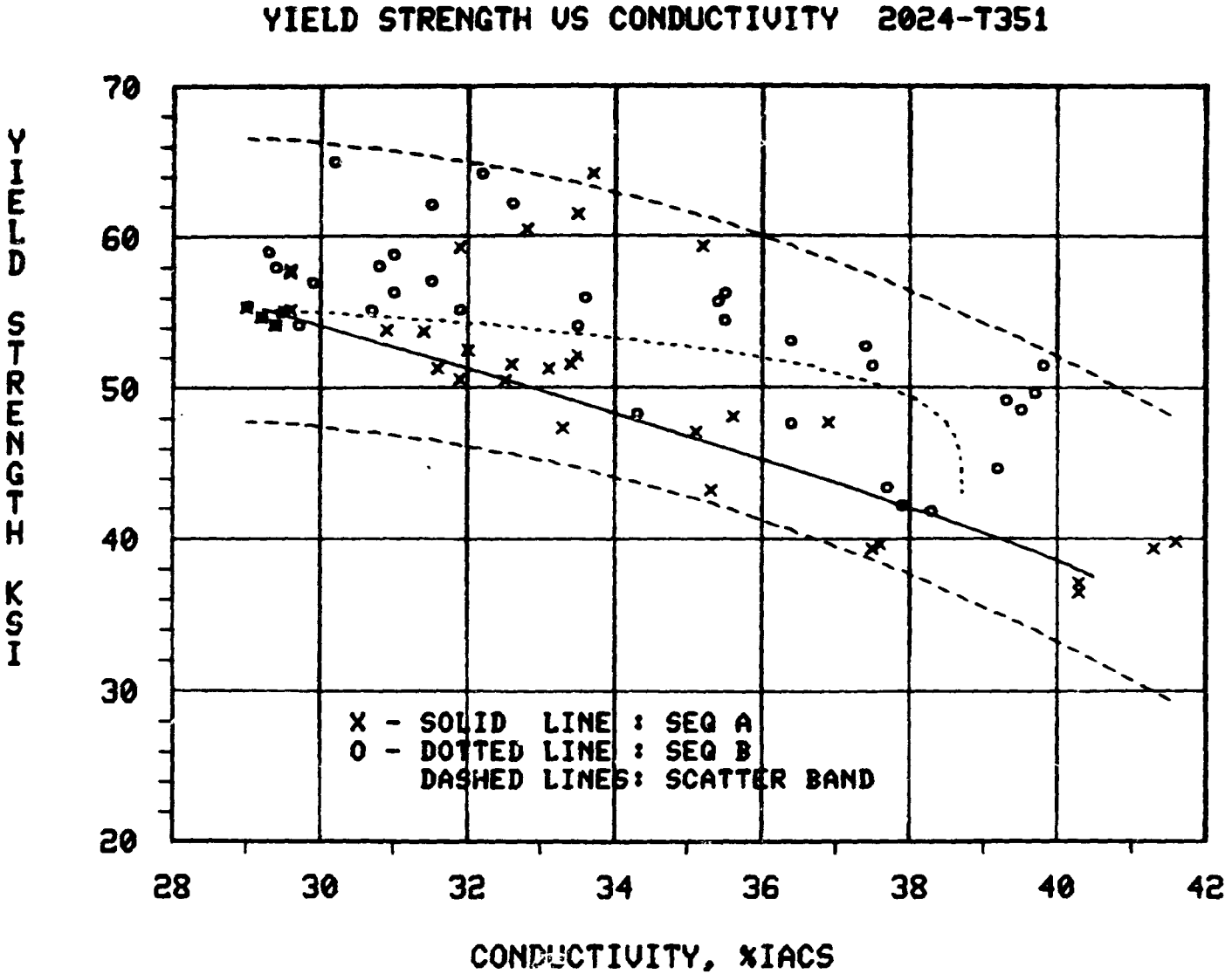

Figure 56. Comparison of yield strength vs. conductivity data for 2024-T351 with correlations predicted by the C-curves. The dashed lines are the scatter band (~95% confidence level) obtained from a least squares quadratic fit to the data. The solid and dotted lines were calculated from the C-curves.

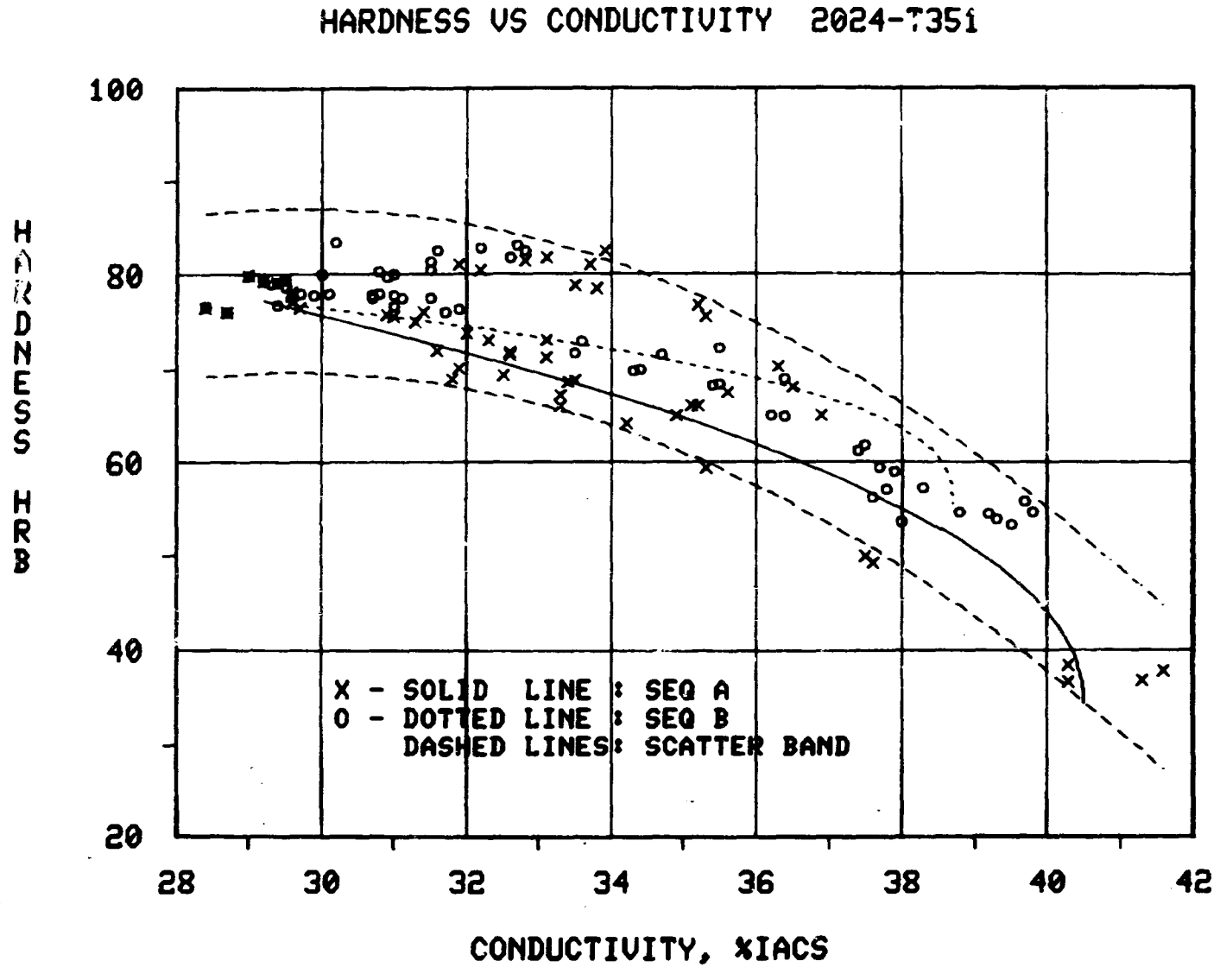

Figure 57. Comparison of hardness vs. conductivity data for 2024-T351 with the correlations predicted by the C-curves. The dashed lines are the scatter band (~95% confidence level) obtained from a least squares quadratic fit to the data. The solid and dotted lines were calculated from the C-curves.

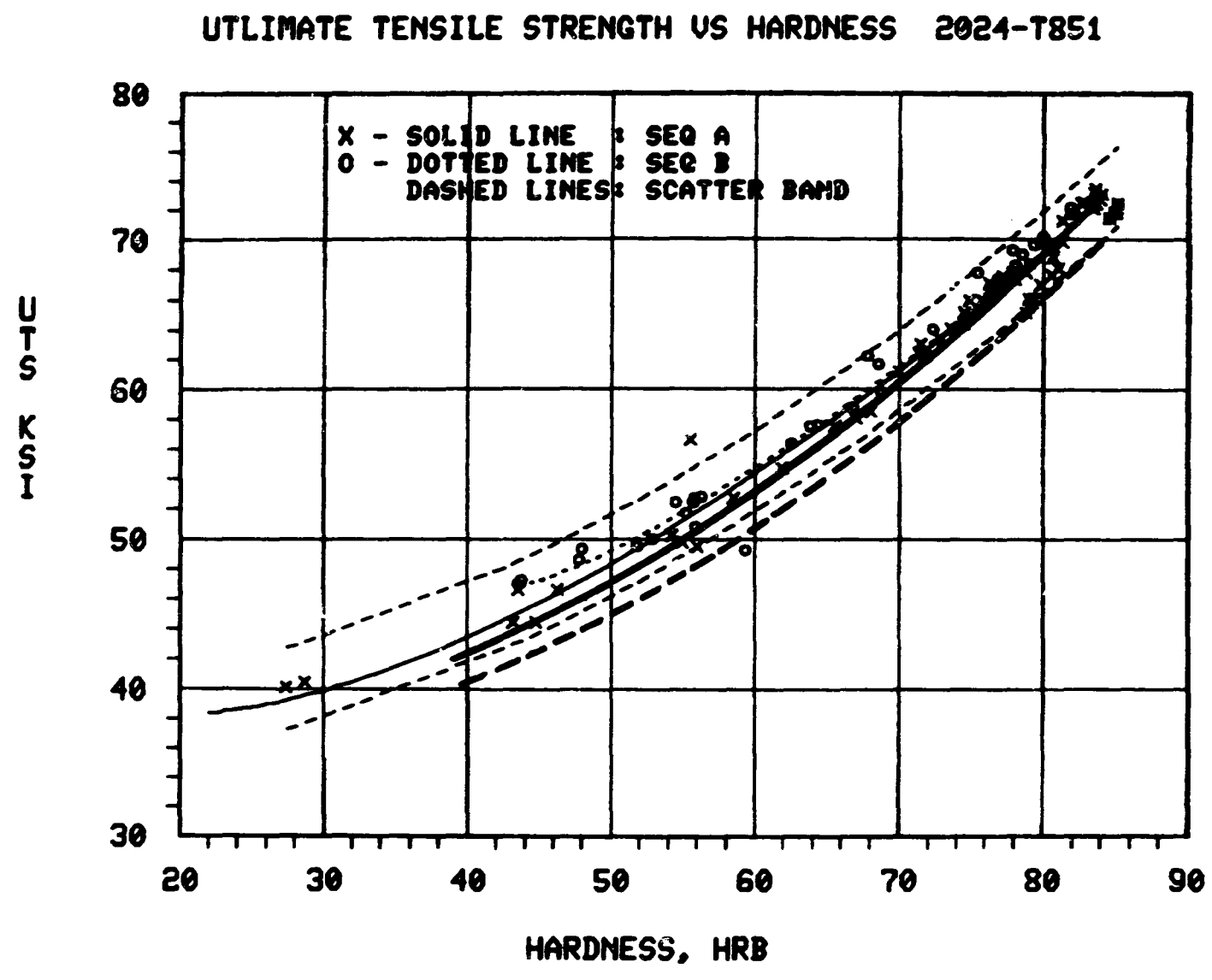

Figure 58. Comparison of the ultimate tensile strength vs. hardness data generated for 2024-T851 in this report with the data from soft 2124-T851 reported by Petrak and Gunderson (heavy solid and dashed lines, representing a least squares mean and the lower 90 percent confidence level, respectively, from Ref. 12).

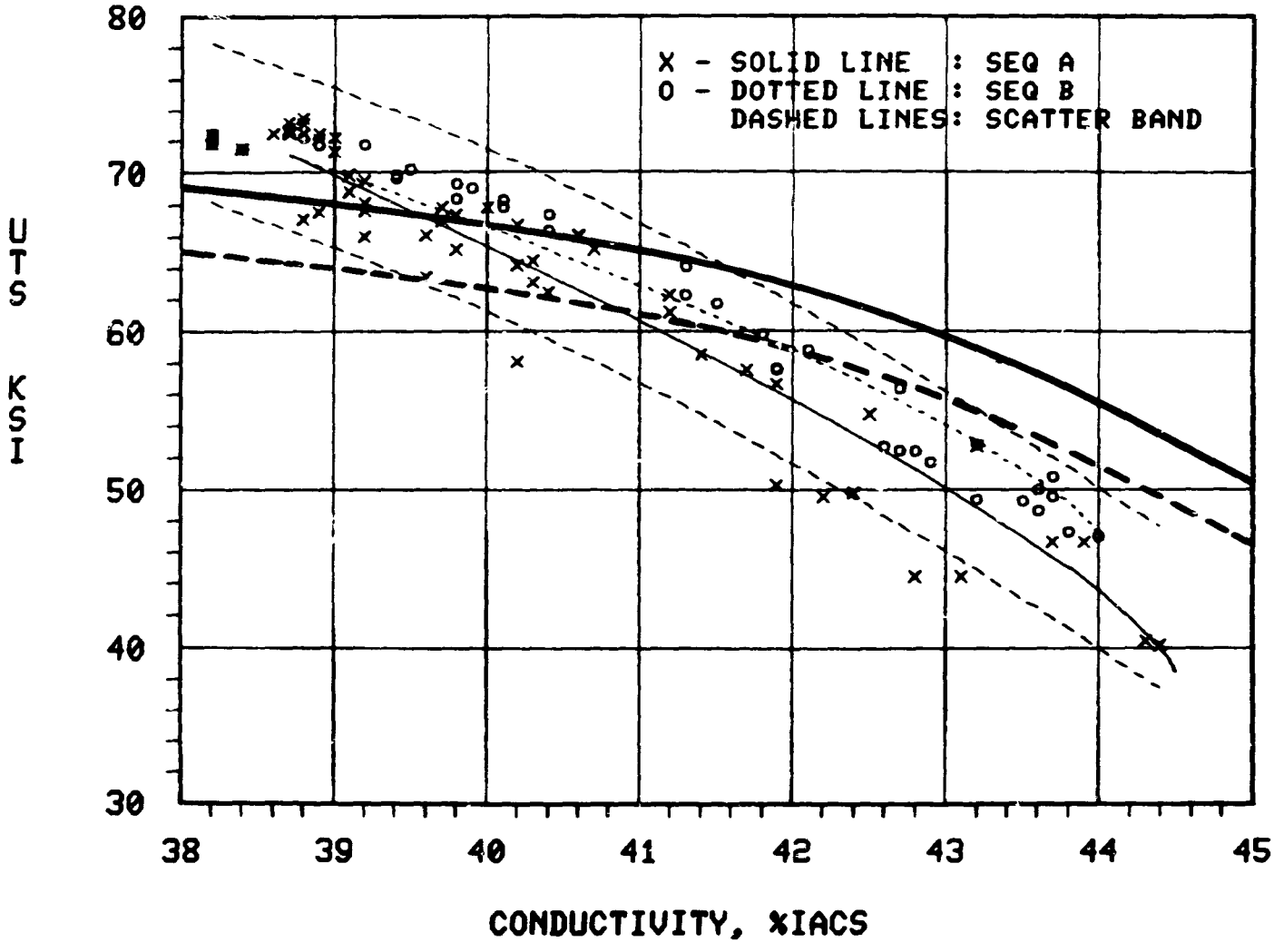

Figure 59. Comparison of the ultimate tensile strength vs. conductivity data generated for 2024-T851 in this report with the data from soft 2124-T851 reported by Petrak and Gunderson (heavy solid and dashed lines, representing a least squares mean and the lower 90 percent confidence level, respectively, from Ref. 12).

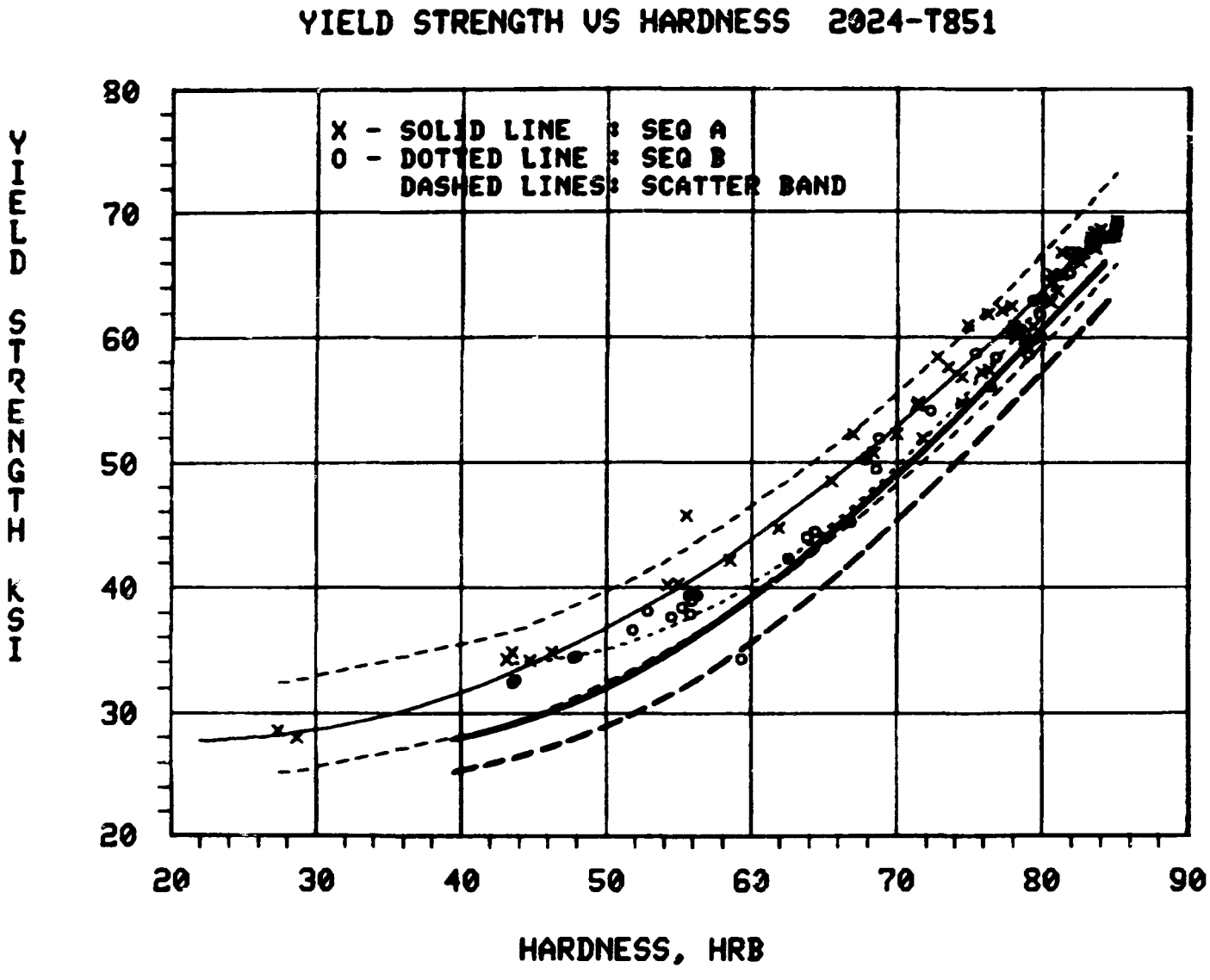

Figure 60. Comparison of the yield strength (0.2% offset) vs. hardness data generated for 2024-T851 in this report with the data from soft 2124-T851 reported by Petrak and Gunderson (heavy solid and dashed lines, representing a least squares mean and the lower 90 percent confidence level, respectively, from Ref. 12).

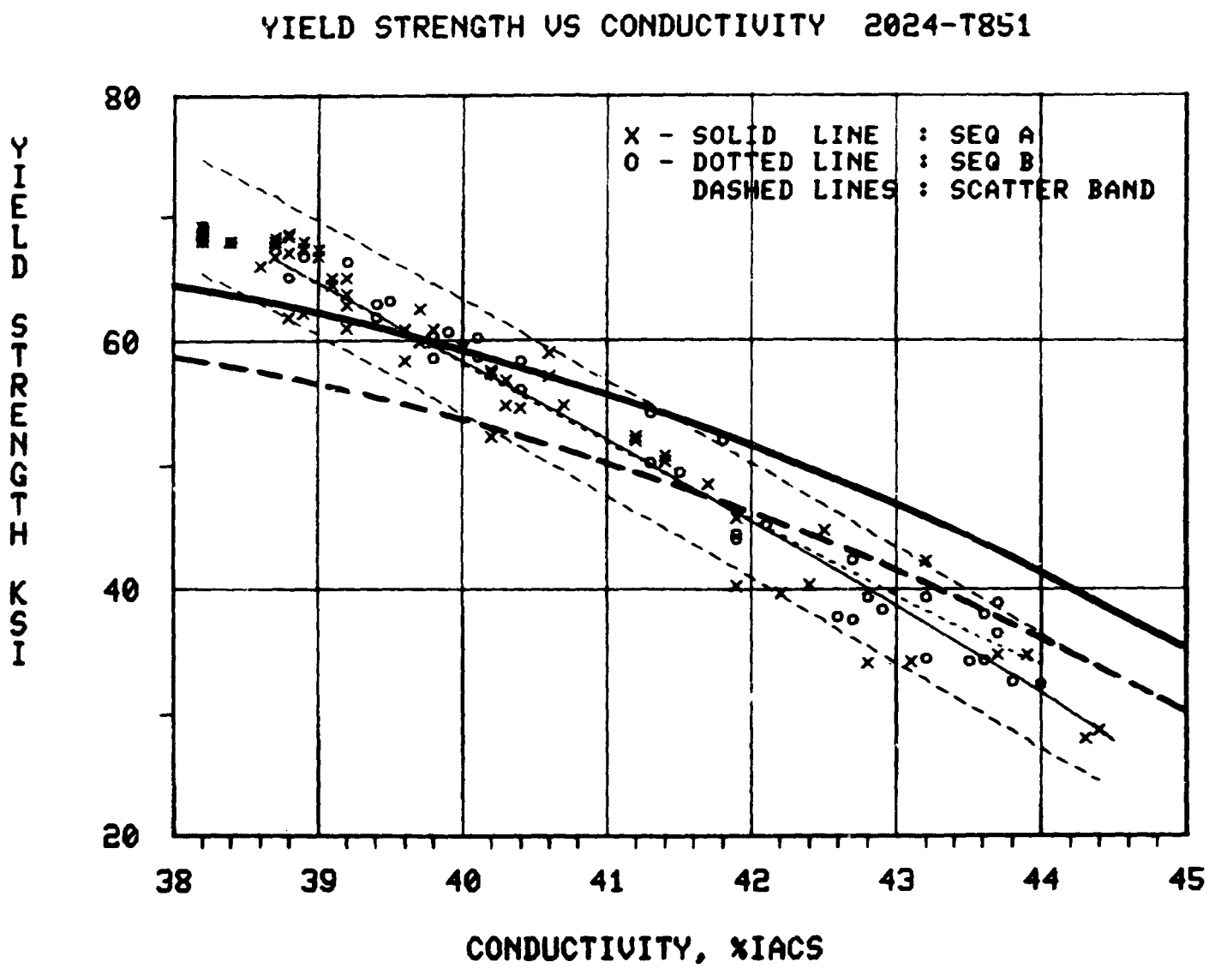

Figure 61. Comparison of the yield strength (0.2% offset) vs. conductivity data generated with the data from soft 2124-T851 reported by Petrak and Gunderson (heavy solid and dashed lines, representing a least squares mean and the lower 90% confidence level, respectively, from Ref. 12).

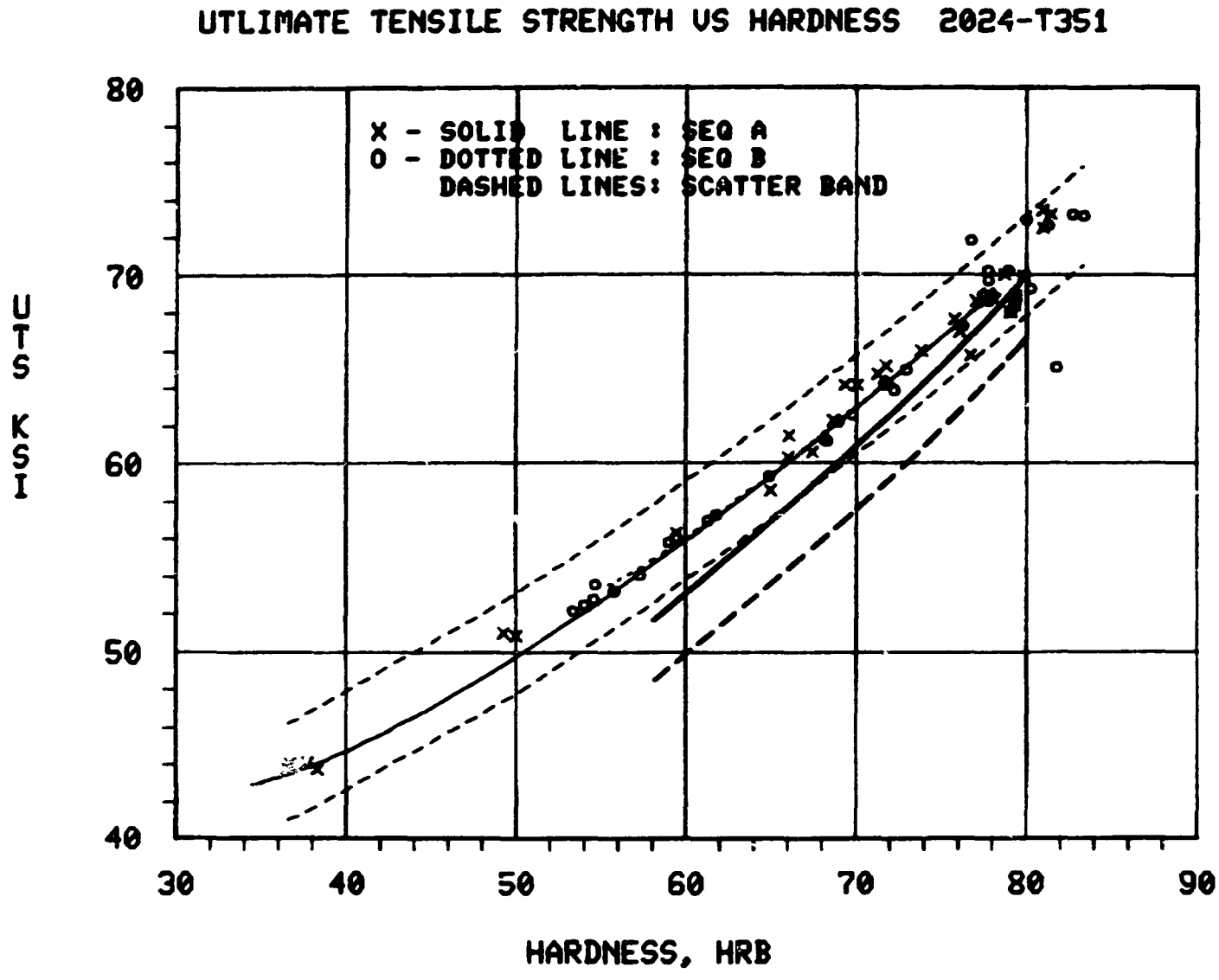

Figure 62. Comparison of the ultimate tensile strength vs. hardness data generated for 2024-T351 in this report with data from soft 2024-T351 as reported by Petrak and Gunderson (heavy solid and dasned lines, representing a least squares mean and the lower 90 percent confidence level, respectively, from Ref. 12).

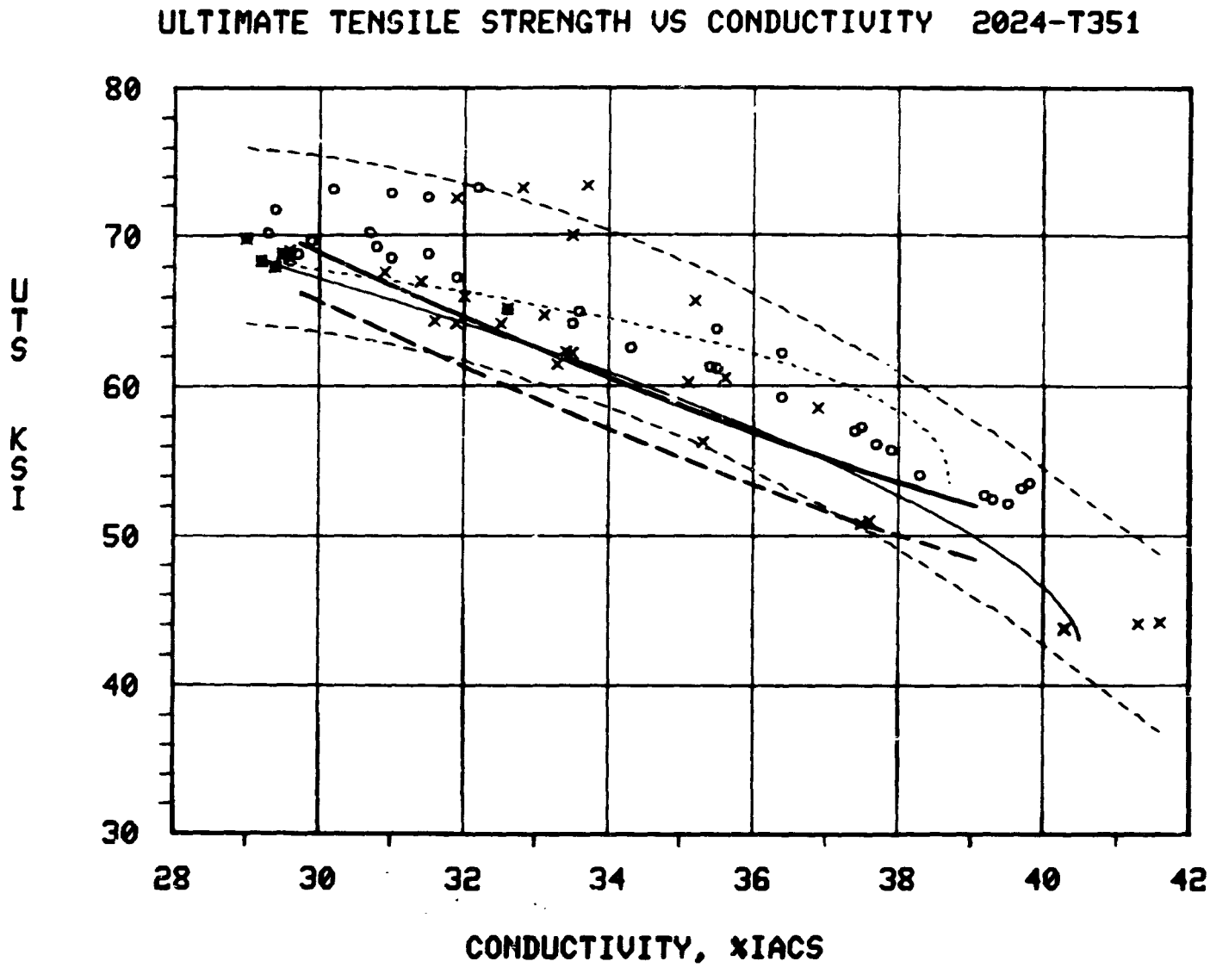

Figure 63. Comparison of the ultimate tensile strength vs. conductivity data generated for 2024-T351 in this report with data from soft 2024-T351 as reported by Petrak and Gunderson (heavy solid and dashed lines, representing a least squares mean and the lower 90 percent confidence level, respectively, from Ref. 12).

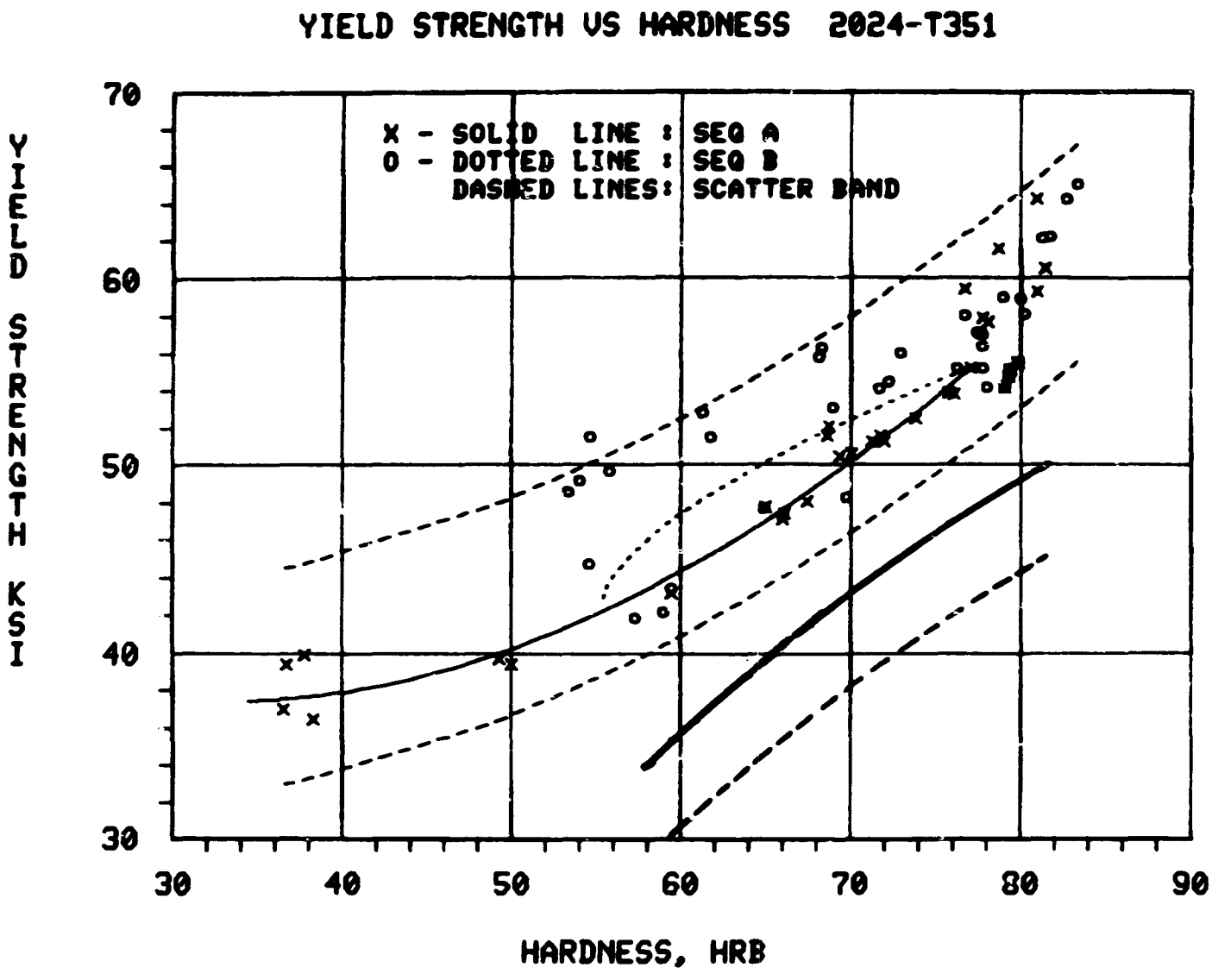

Figure 64. Comparison of yield strength (0.2% offset) vs. hardness data generated for 2024-T351 in this report with data from soft 2024-T351 as reported by Petrak and Gunderson (heavy solid and dashed lines, representing a least squares mean and the lower 90 percent confidence level, respectively, from Ref. 12).

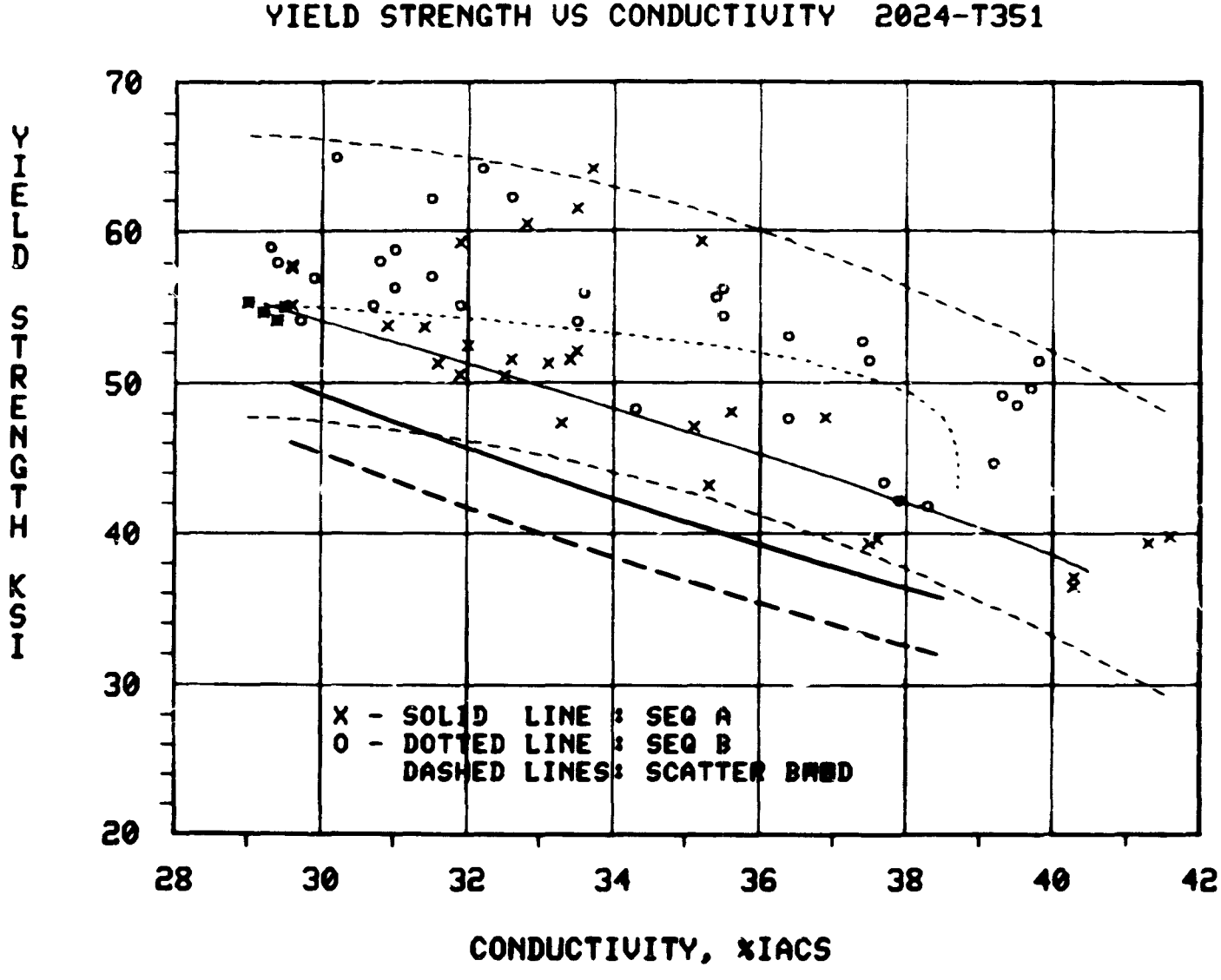

Figure 65. Comparison of yield strength (0.2% offset) vs. conductivity data generated for 2024-T351 in this report with data from soft 2024-T351 as reported by Petrak and Gunderson (heavy solid and dashed lines, representing a least squares mean and the lower 90 percent confidence level, respectively, from Ref. 12).

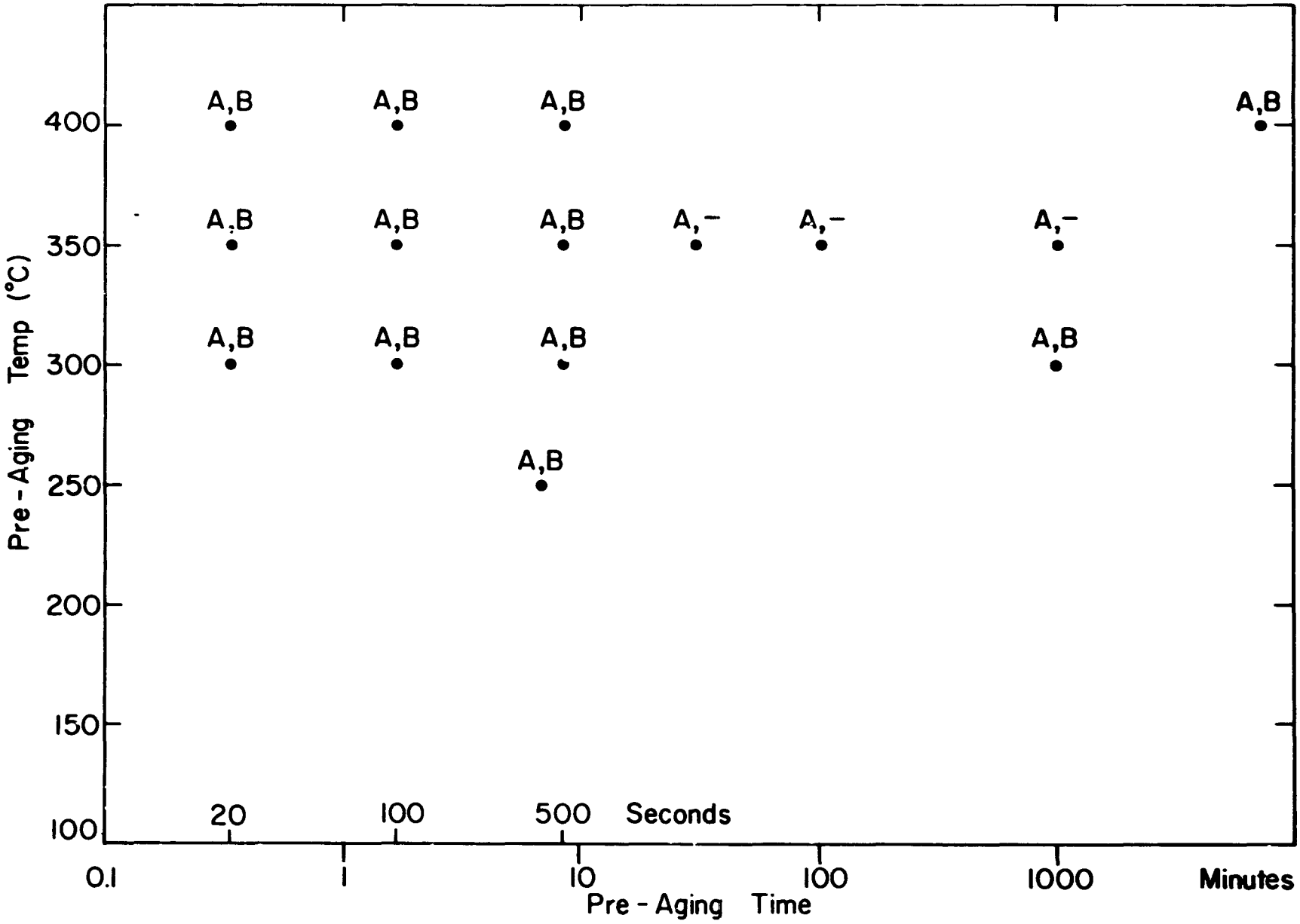

Figure 66. 0.635 cm thick plate "pre-aged" specimens examined by means of TEM. A and B refer to the "pre-aging" sequence treatment.

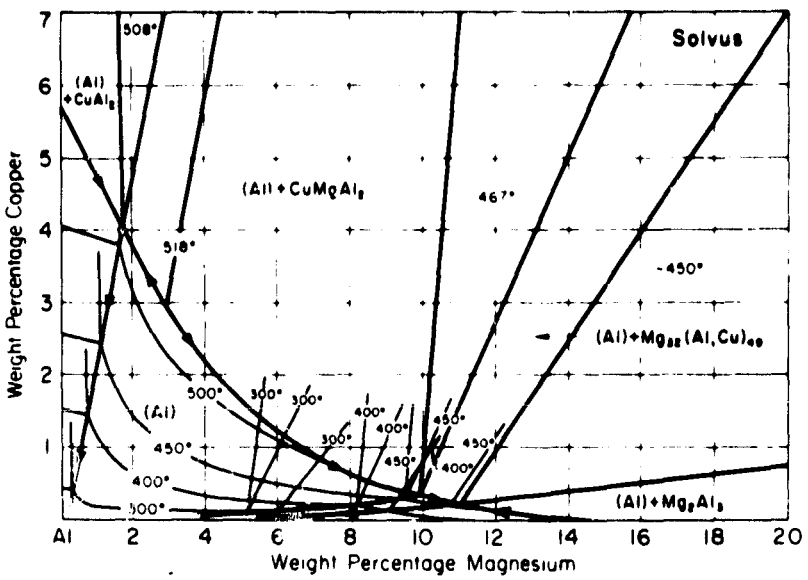

Figure 67. Phase diagram of Al-Cu-Mg system showing the aluminum rich solvus surface (40).

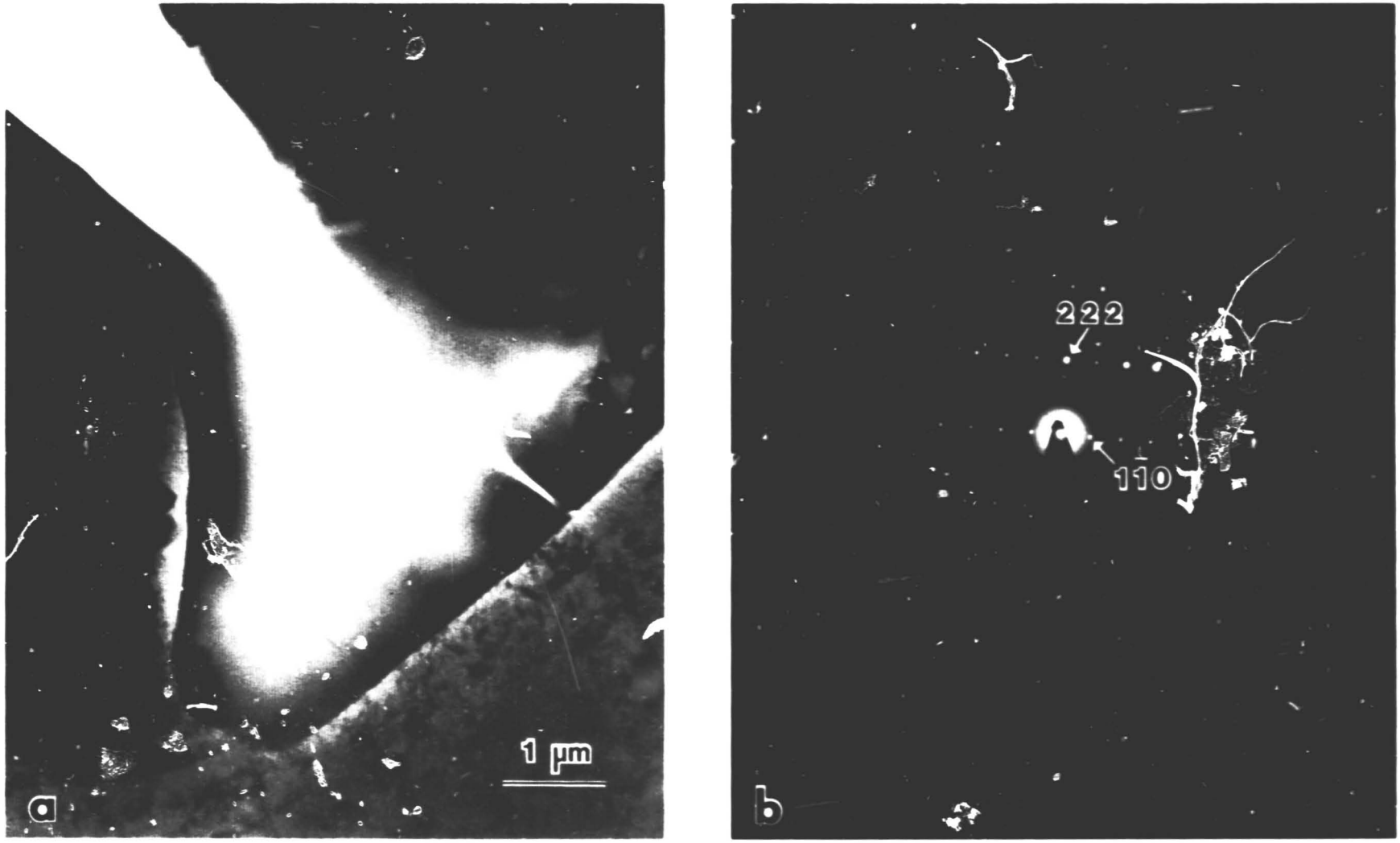

Figure 68. (a) α-Al(Fe,M)Si phase in the 0.635 cm thick plate.
(b) Electron diffraction pattern from (a). [11$\bar{2}$] zone.

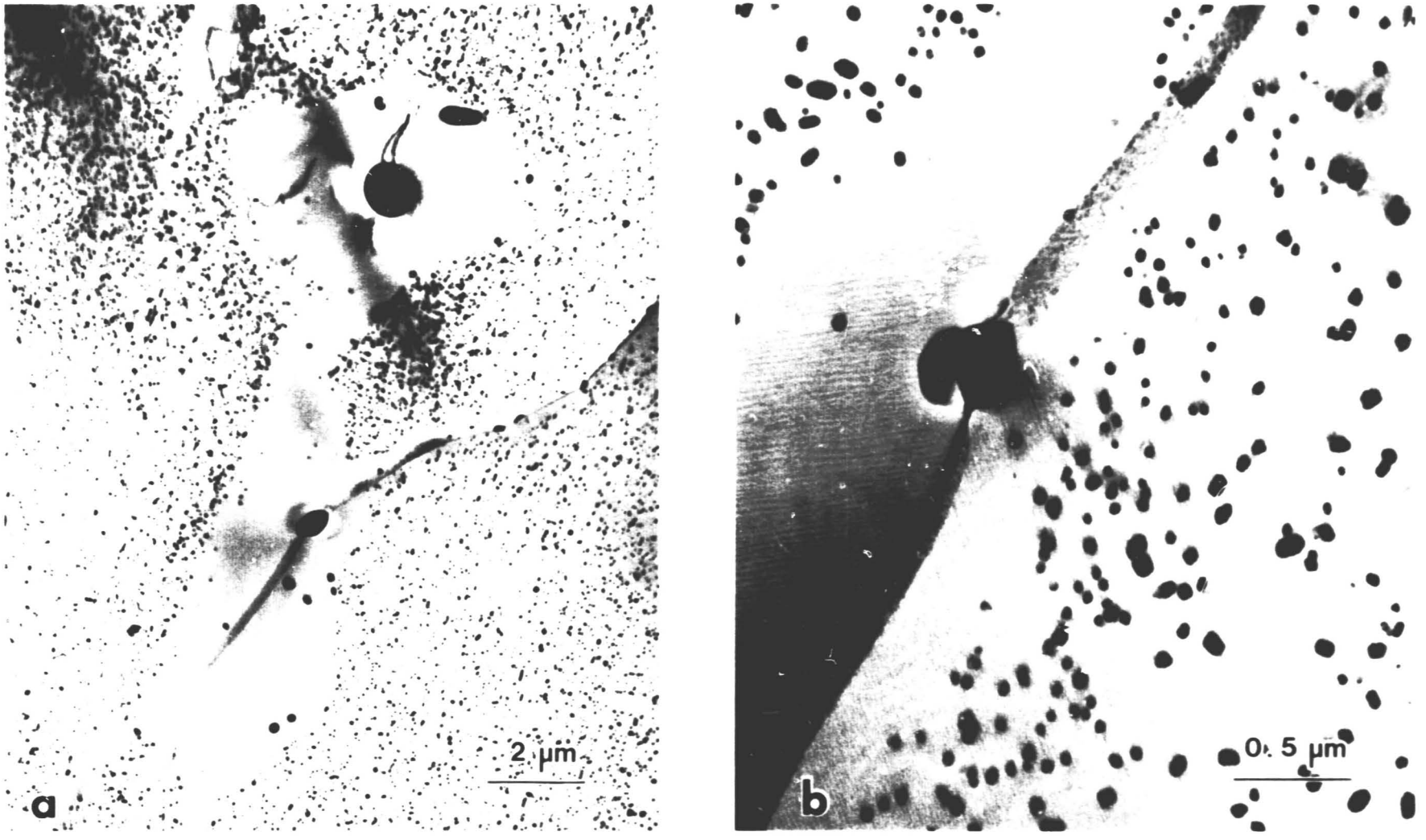

Figure 69. Dispersoid particles in directly quenched specimen (T4 condition). (a) Note regions free of dispersoid particles in vicinity of larger constituent particles. (b) Also note very small precipitates present at grain boundaries.

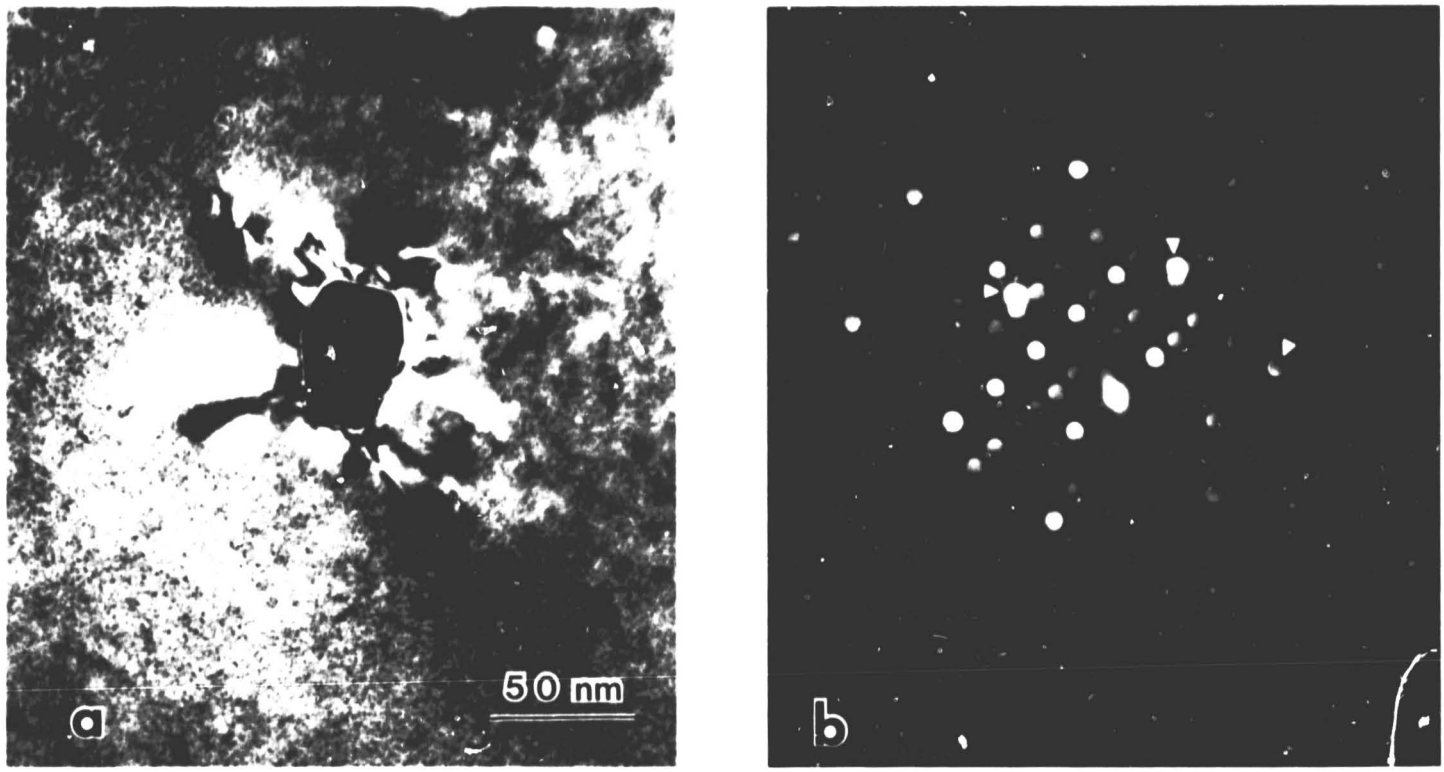

Figure 70. (a) $Cu_2Mn_3Al_{20}$ dispersoid particle.
(b) Microdiffraction pattern from (a). Dispersoid particle zone is [020]; α-Al matrix zone is [110]. Matrix spots identified by arrows.

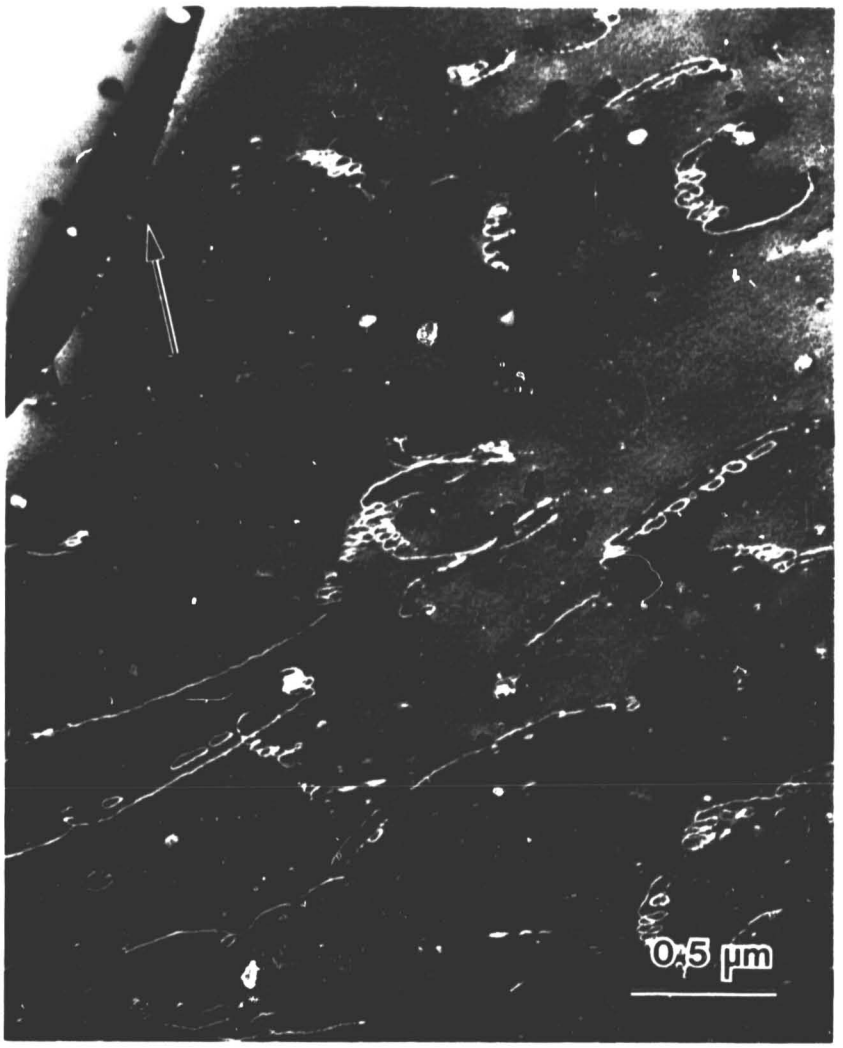

Figure 71. Helical dislocations in directly quenched specimen (T4 condition). All disiocations visible have same Burgers vector, 1/2[110]. Projection of Burgers vector is parallel to [200]. Weak beam dark field image, $\vec{g}/3\vec{g}$, $\vec{g}$ = 200.

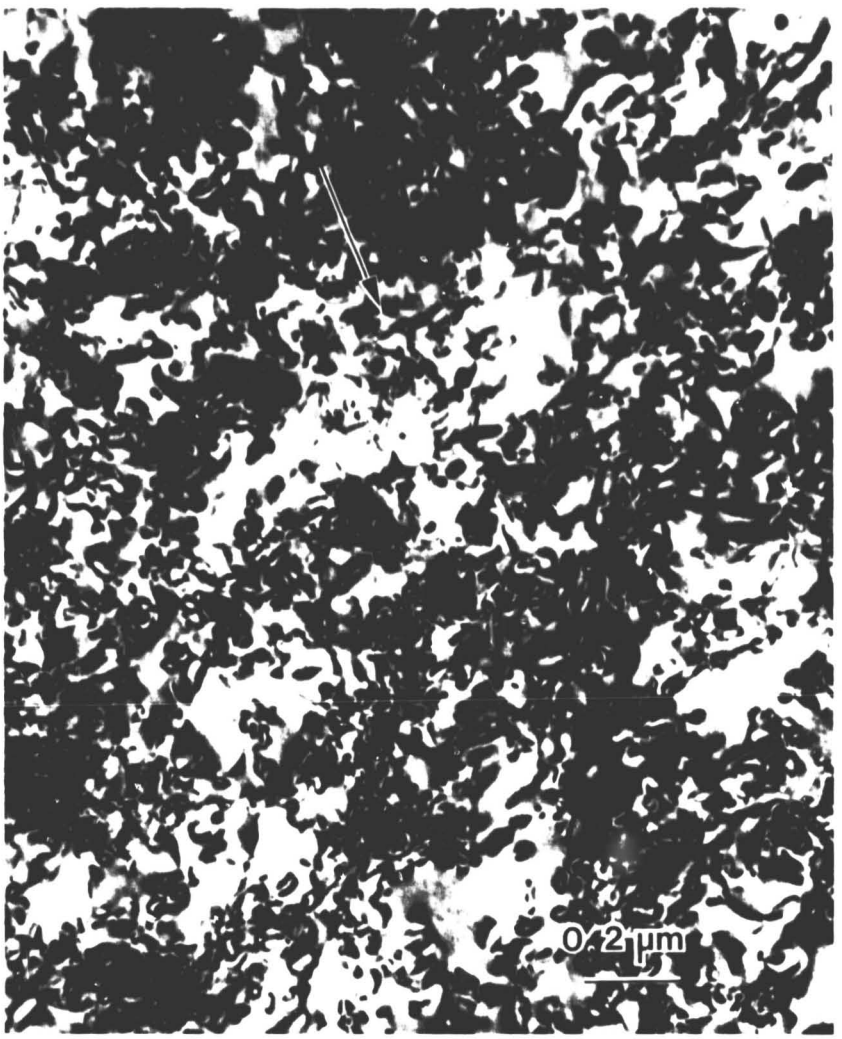

Figure 72. Structure after processing to T351 condition. Direct quench.

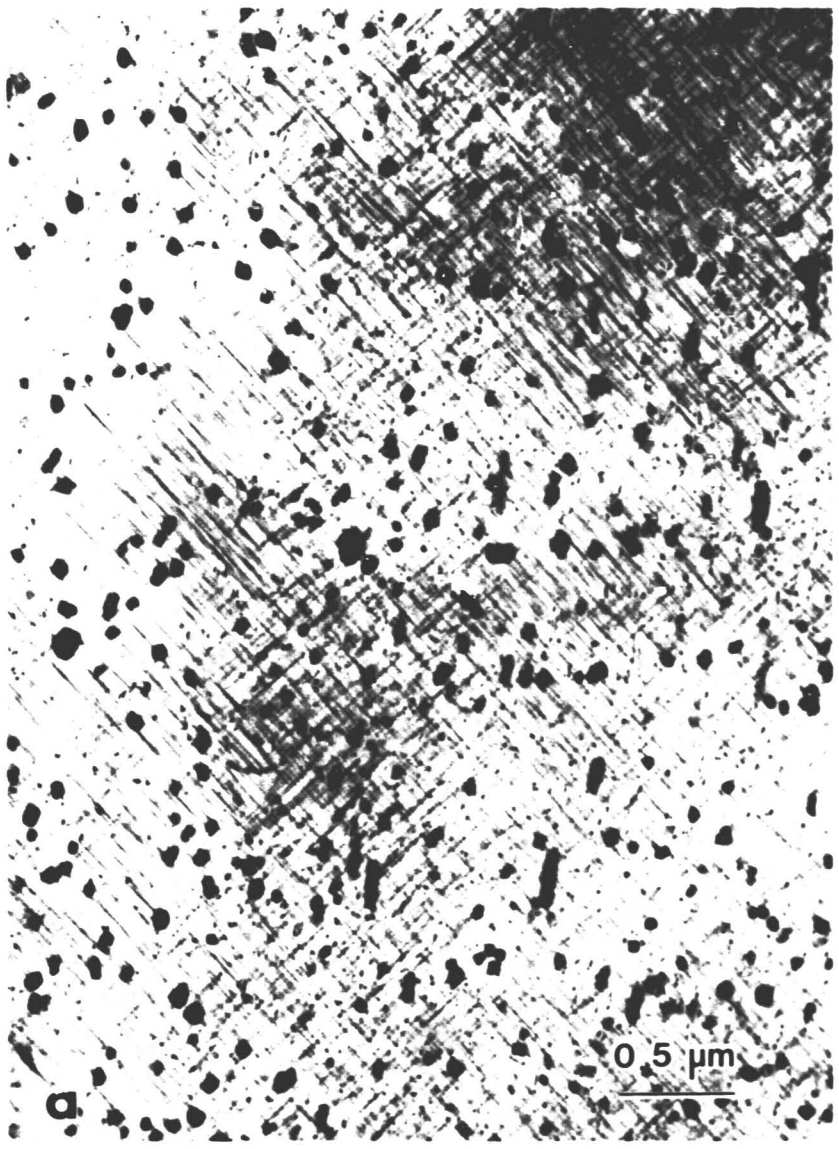

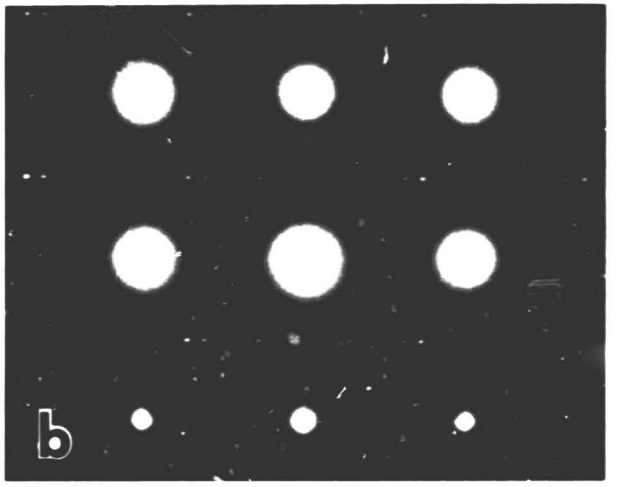

Figure 73. (a) Structure after processing to T851 condition. Direct quench.
(b) Electron diffraction pattern $[001]_{\alpha}$ zone.
(c) Indexed pattern corresponding to (b). Reflections from eight S phase variants are present. Spots not shown arise from double diffraction.

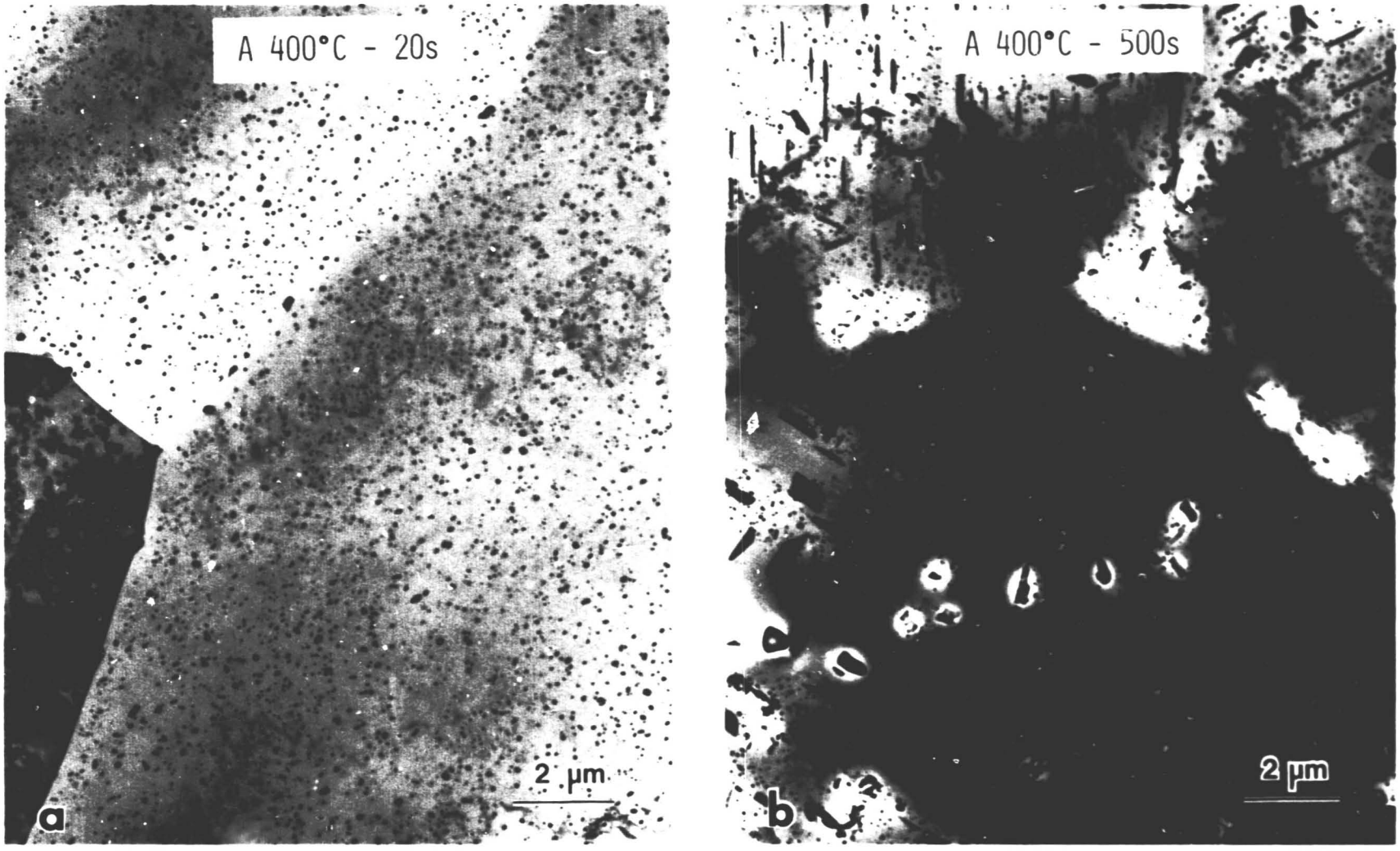

Figure 74. (a-f) Microstructures of specimens given sequence A "pre-aging" treatments (low magnification). Region of light contrast around precipitate helps identify it as the S phase. Light contrast is a result of preferential thinning during foil preparation.

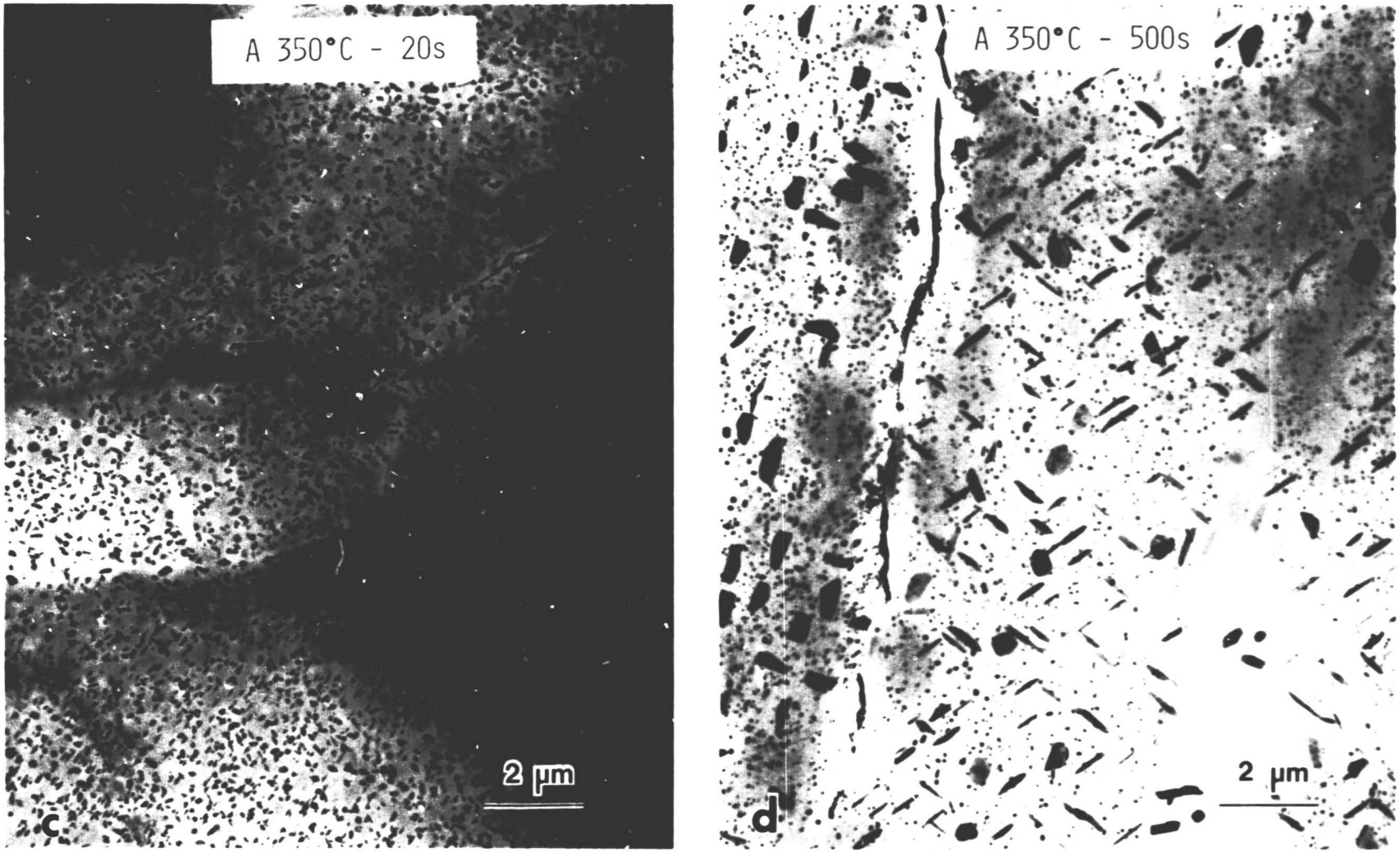

(Figure 74. Continued)

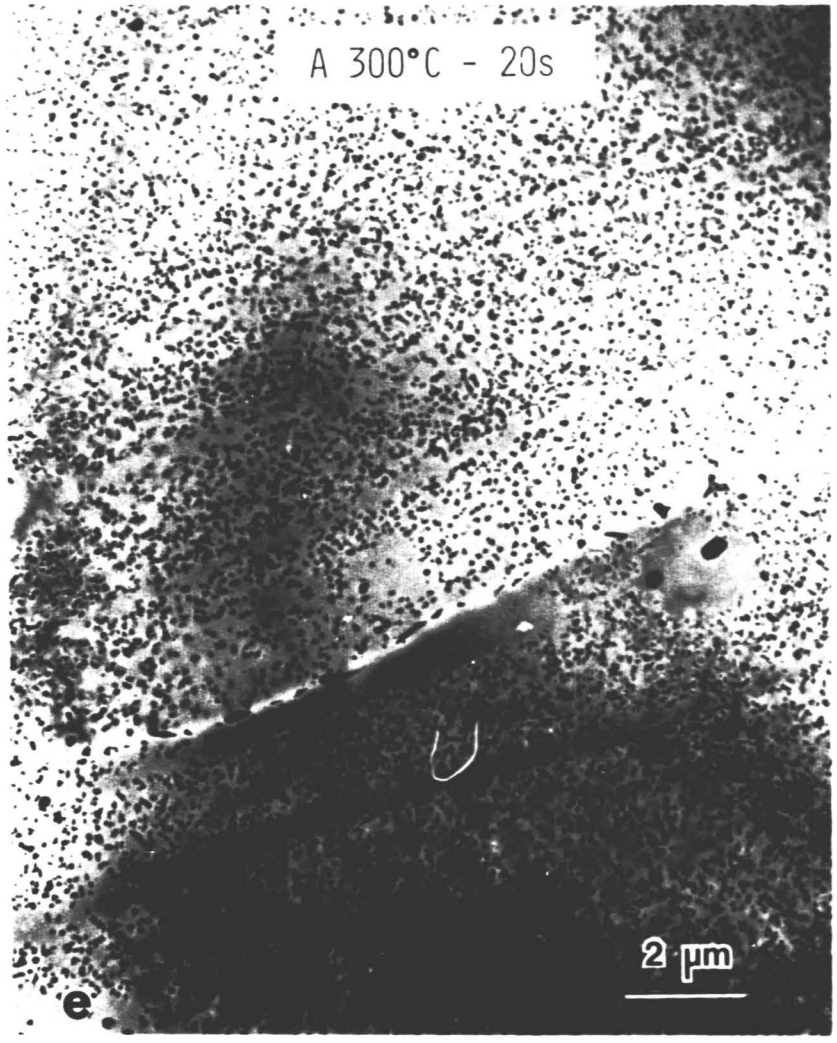

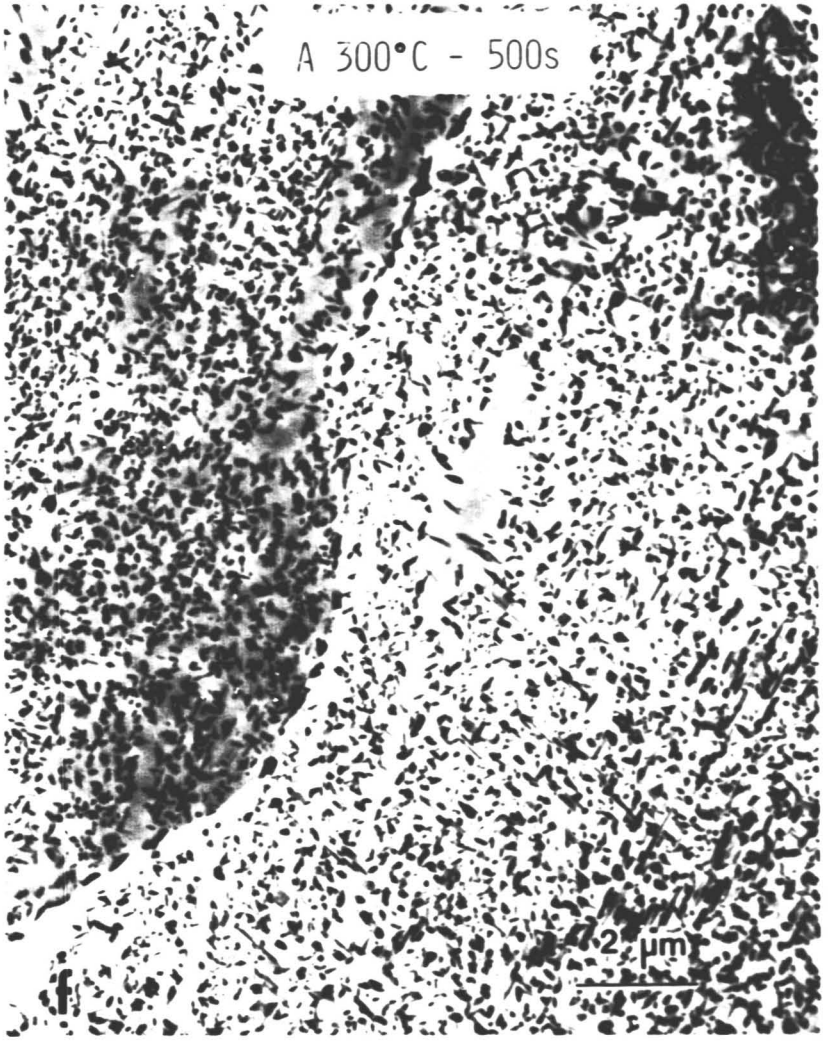

(Figure 74. Continued)

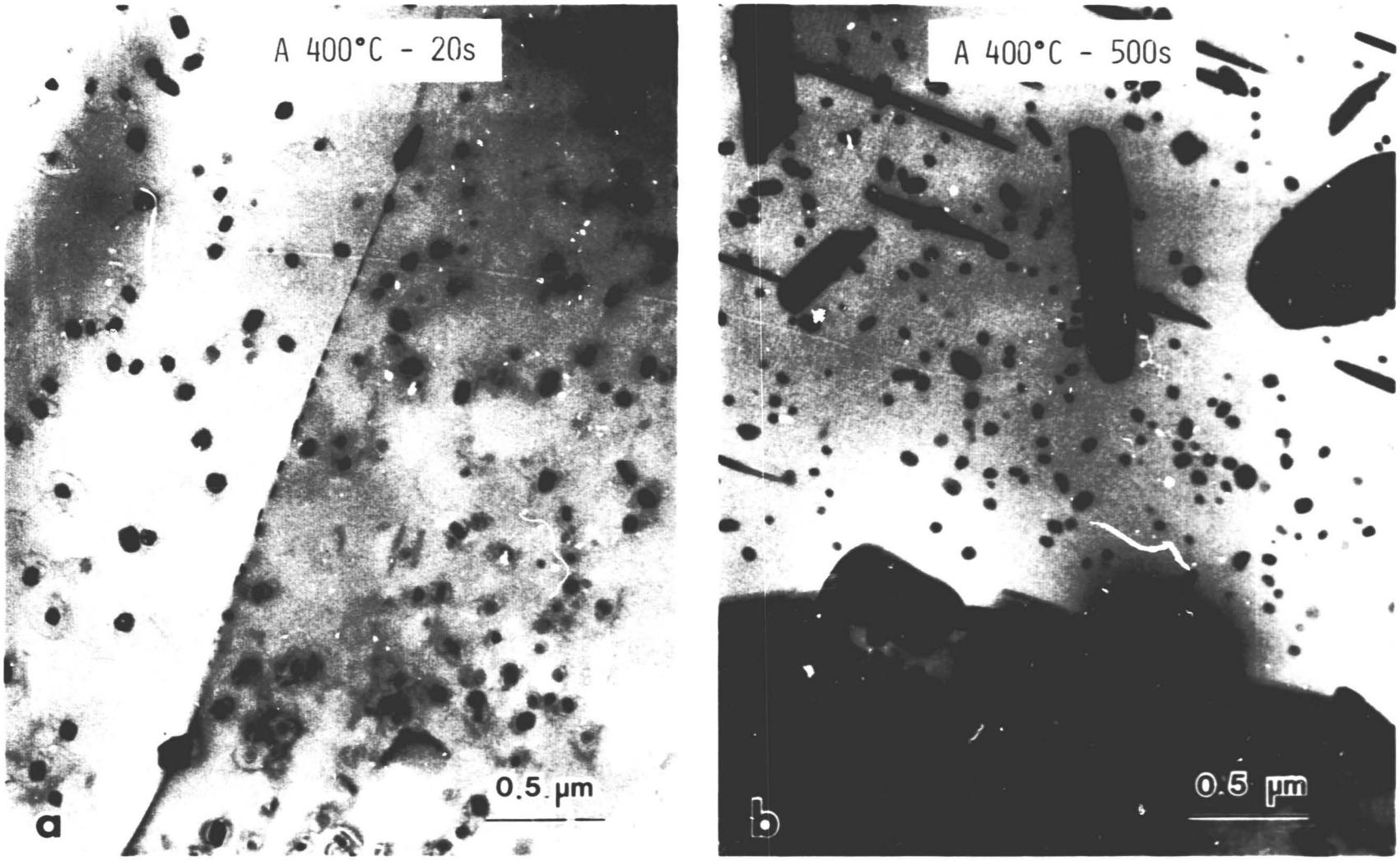

Figure 75. (a-f) Same as Figure 74 but at higher magnification.

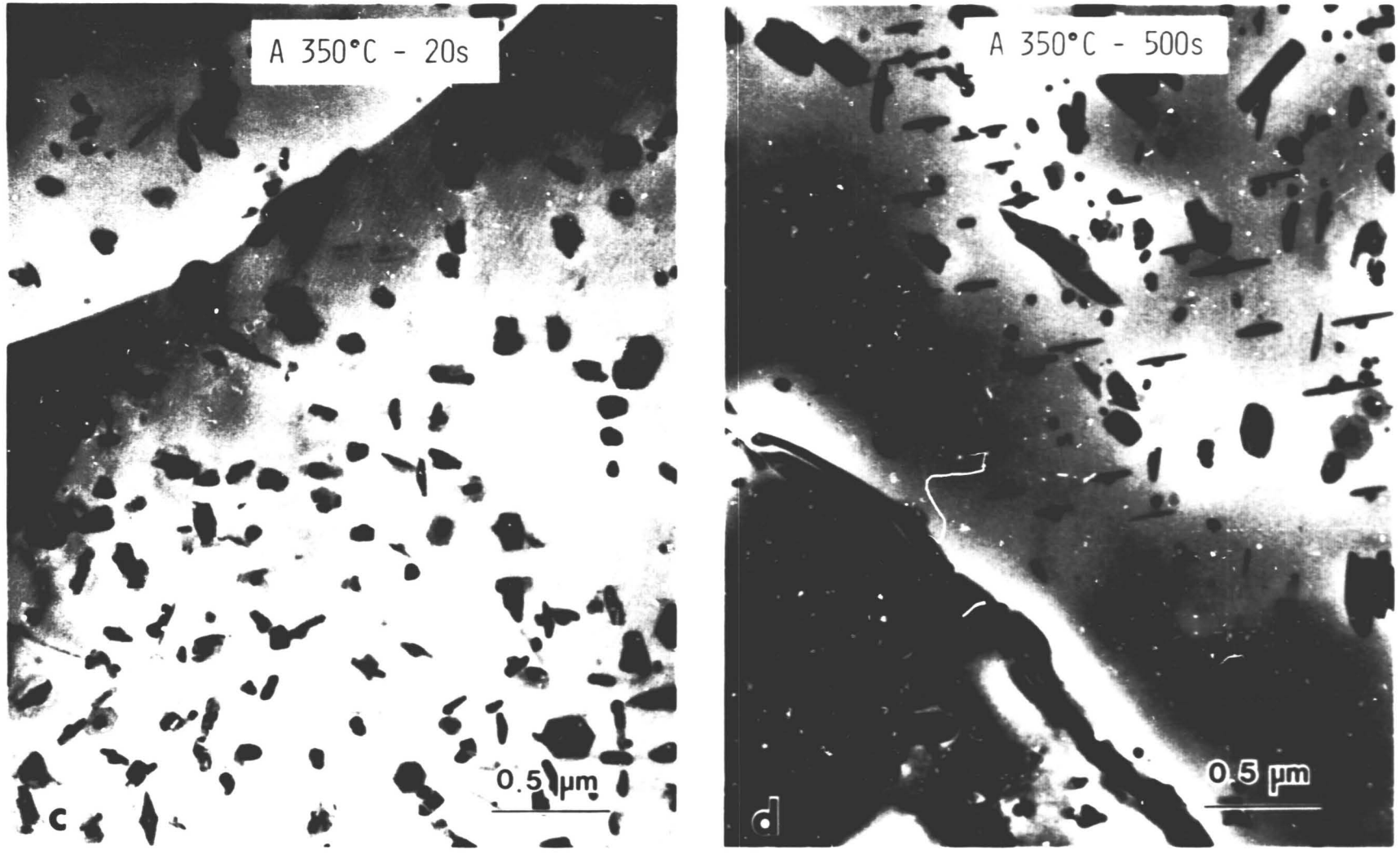

(Figure 75. Continued)

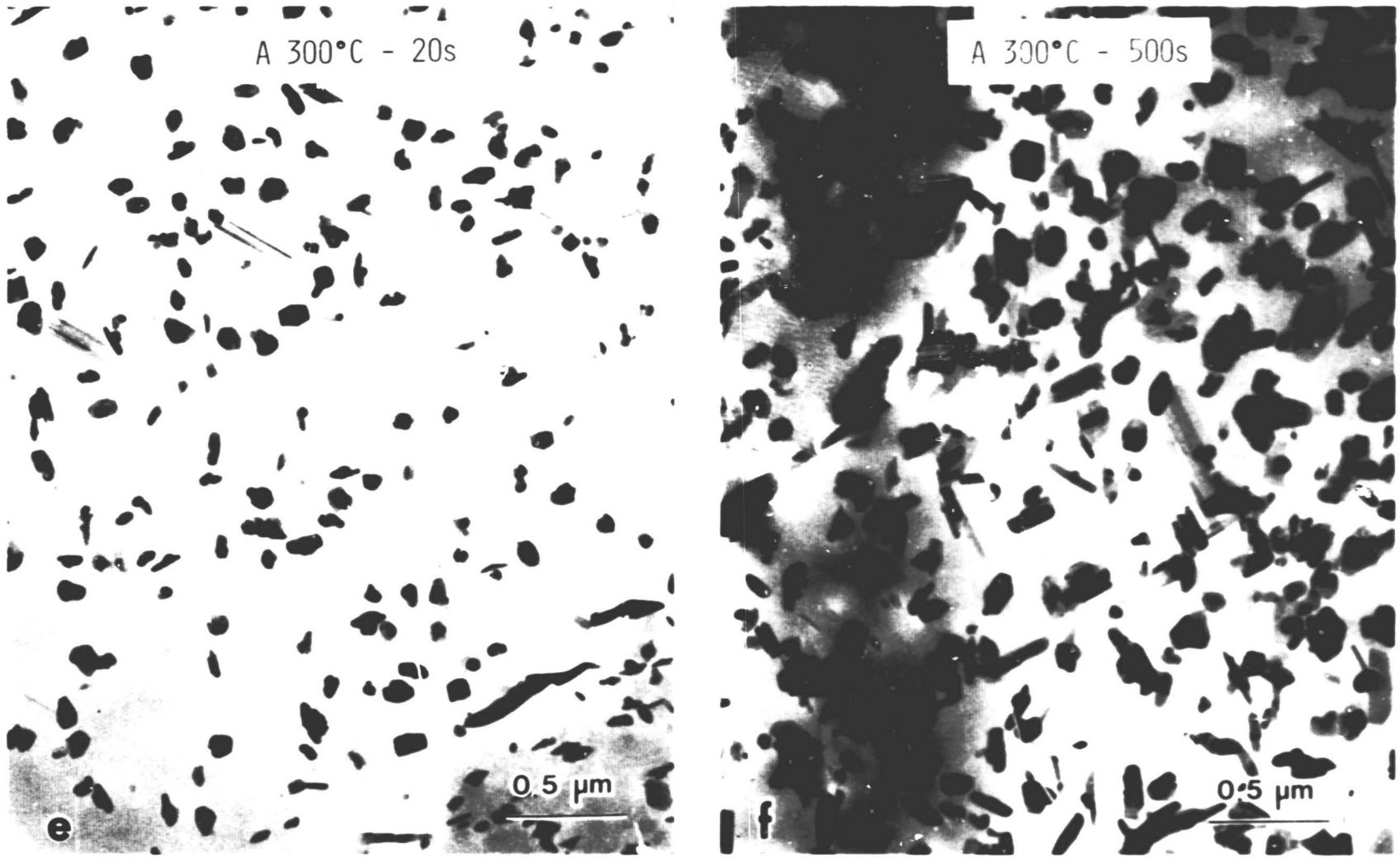

(Figure 75. Continued)

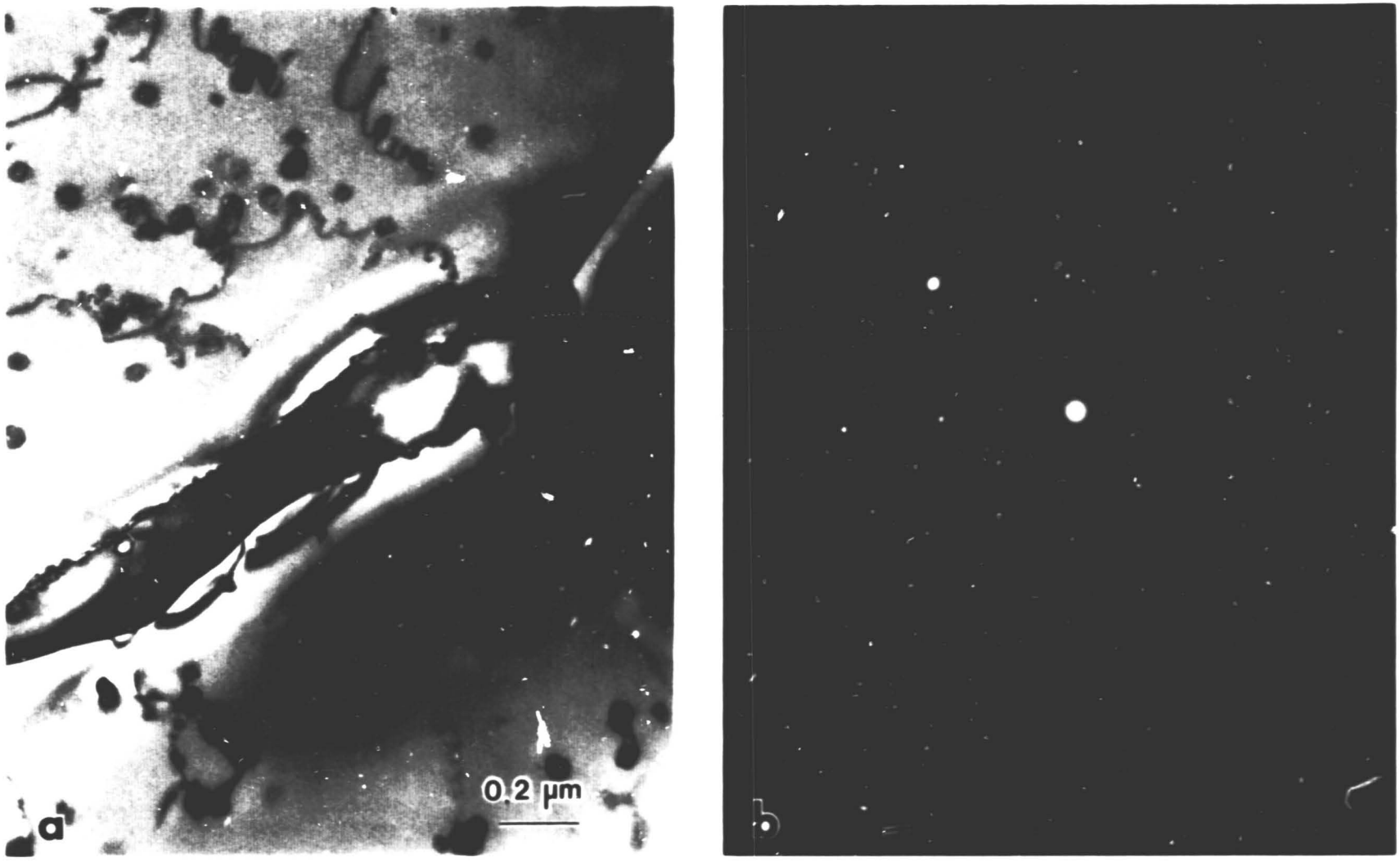

Figure 76. (a) S phase precipitate at grain boundary in specimen after sequence A "pre-aging" treatment at 400°C for 500s.
(b) Electron diffraction pattern from (a). Orientation relationship with one grain obeys $[001]_S, \| [001]_\alpha$; $[010]_S, \| [021]_\alpha$; $[001]_S, \| [01\bar{2}]_\alpha$. Precipitate and matrix zones are both [100].

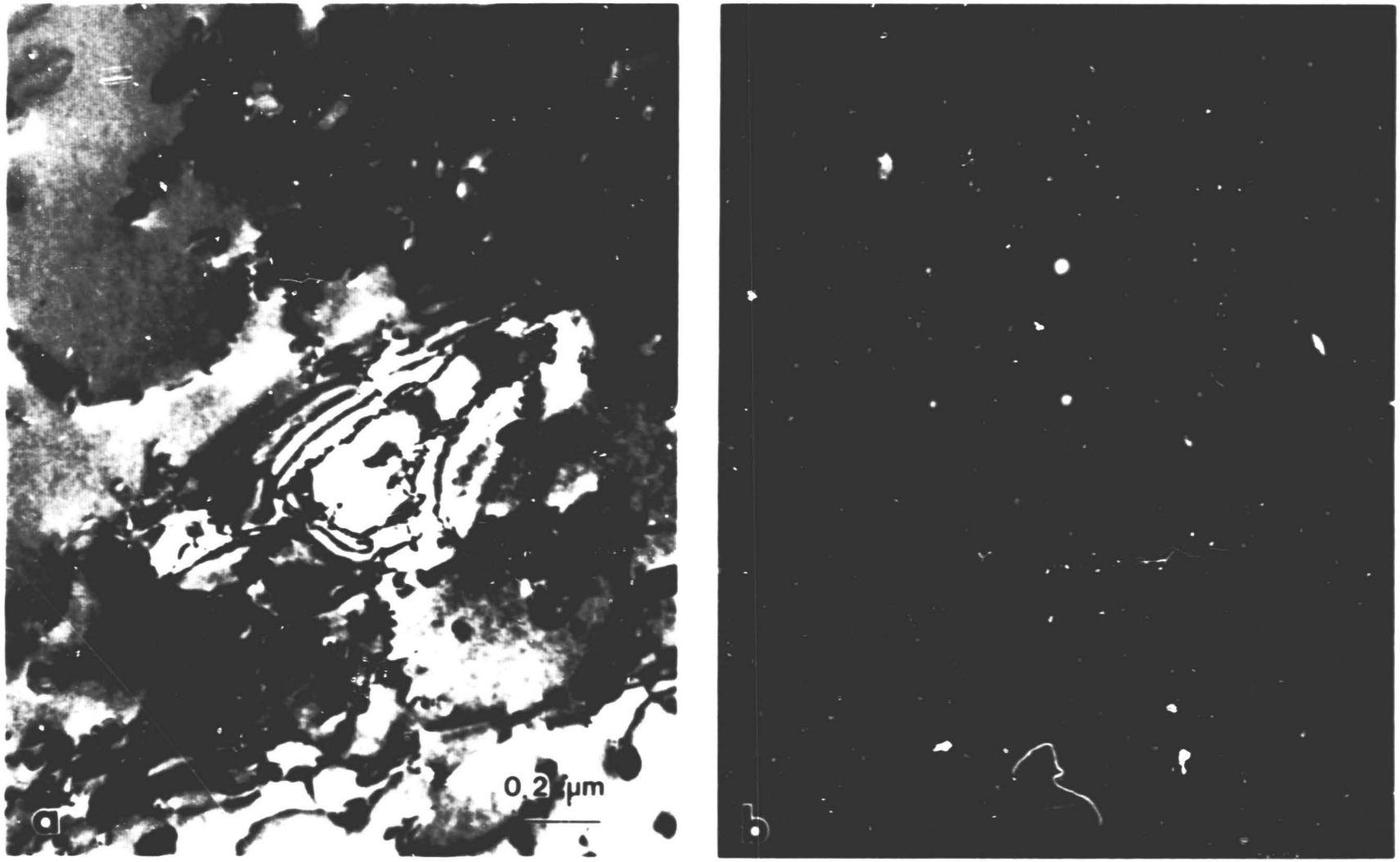

Figure 77. (a) S phase precipitate within grain. Same specimen as Figure 76. (b) Electron diffraction pattern from (a). Orientation relationship is $[100]_S \parallel [100]_\alpha$; $[010]_S \parallel [021]_\alpha$; $[001]_S \parallel [01\bar{2}]_\alpha$. Precipitate and matrix zones are [100].

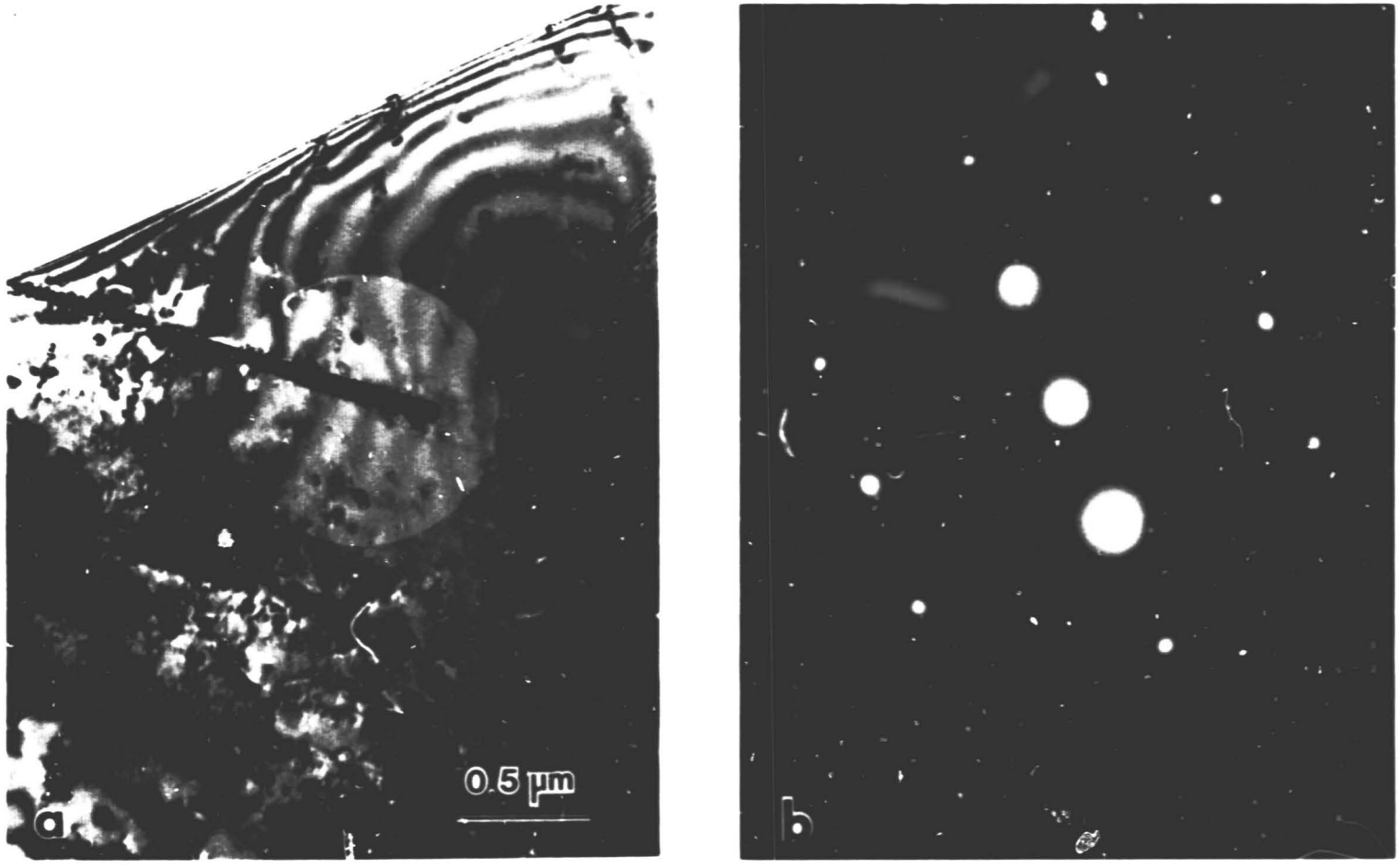

Figure 78. (a) θ phase precipitate. Sequence A "pre-aged" 400°C for 500s. (b) Electron diffraction pattern from (a). Matrix zone is [211] and θ zone is [001].

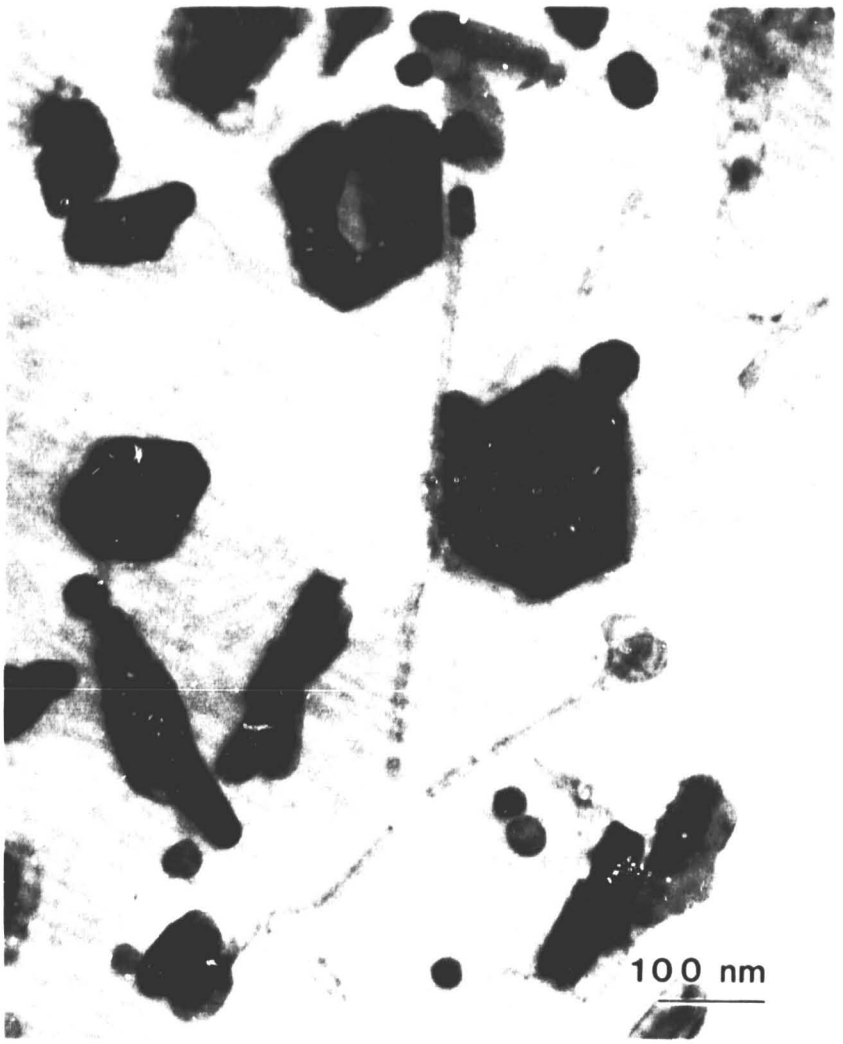

Figure 79. θ-phase precipitate with dispersoid particle at center. Precipitate lies on $[111]_\alpha$ plane which is parallel to plane of figure. Sequence A "pre-aged" at 350°C for 20s.

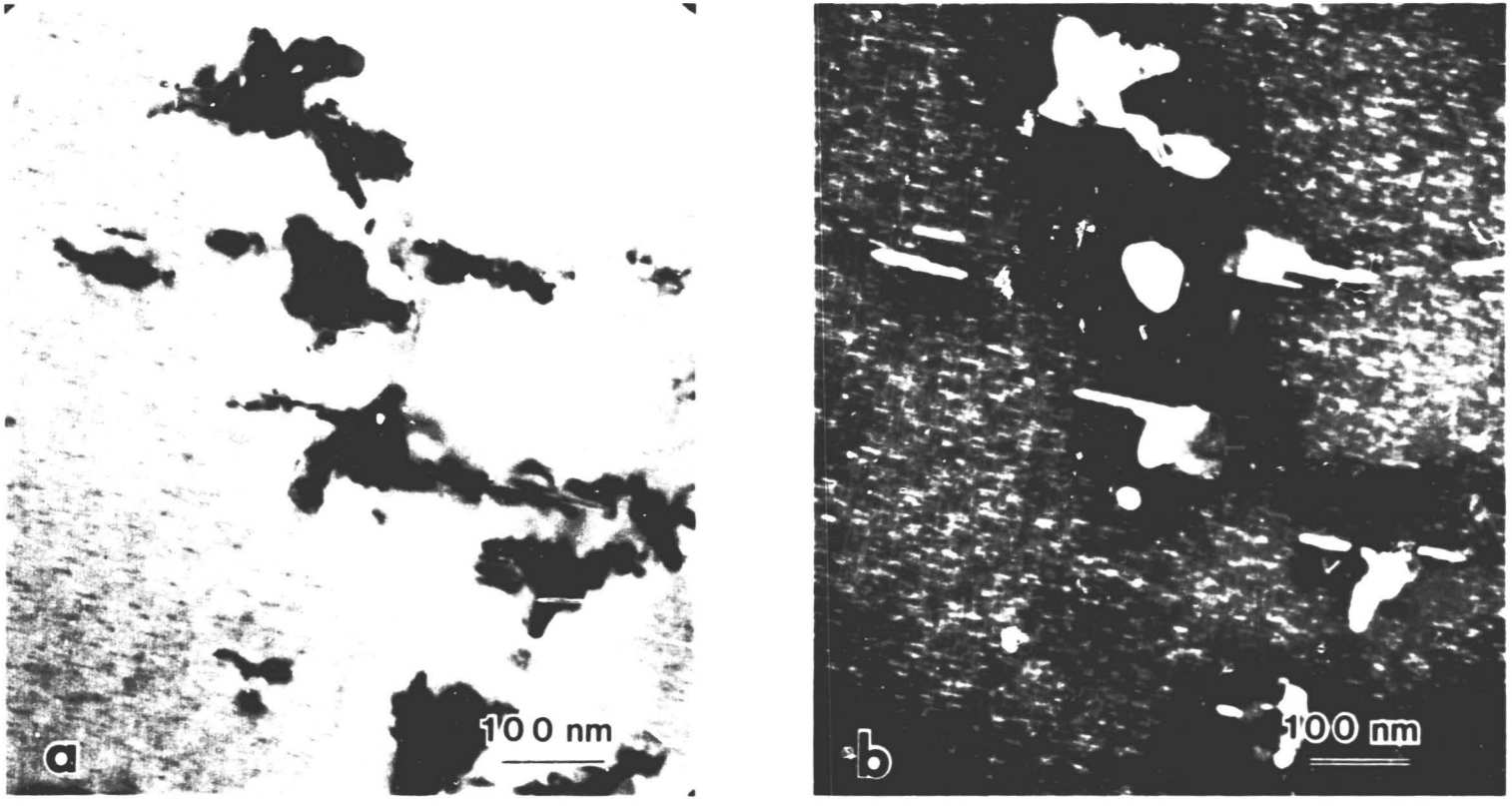

Figure 80. Bright field (a) and Dark field (b) micrographs showing θ and S' precipitates at dispersoid particles and homogeneously distributed S' precipitates in matrix Note that regions surrounding dispersoid particle-precipitate clusters are free of homogeneously distributed S'. Sequence A "pre-aged" 250°C for 400s.

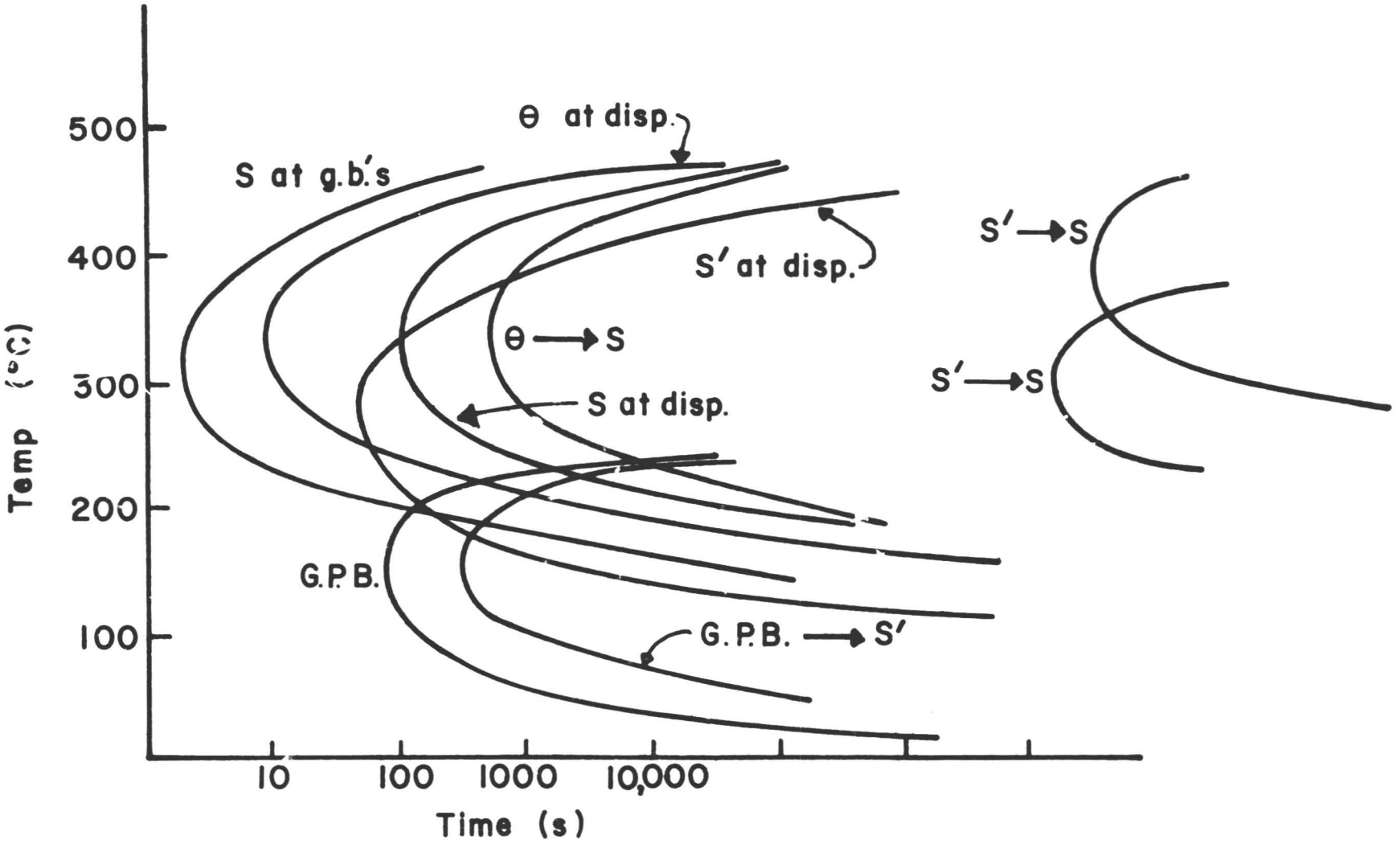

Figure 81. Schematic representation of nucleation curves for sequence A "pre-aging" treatment.

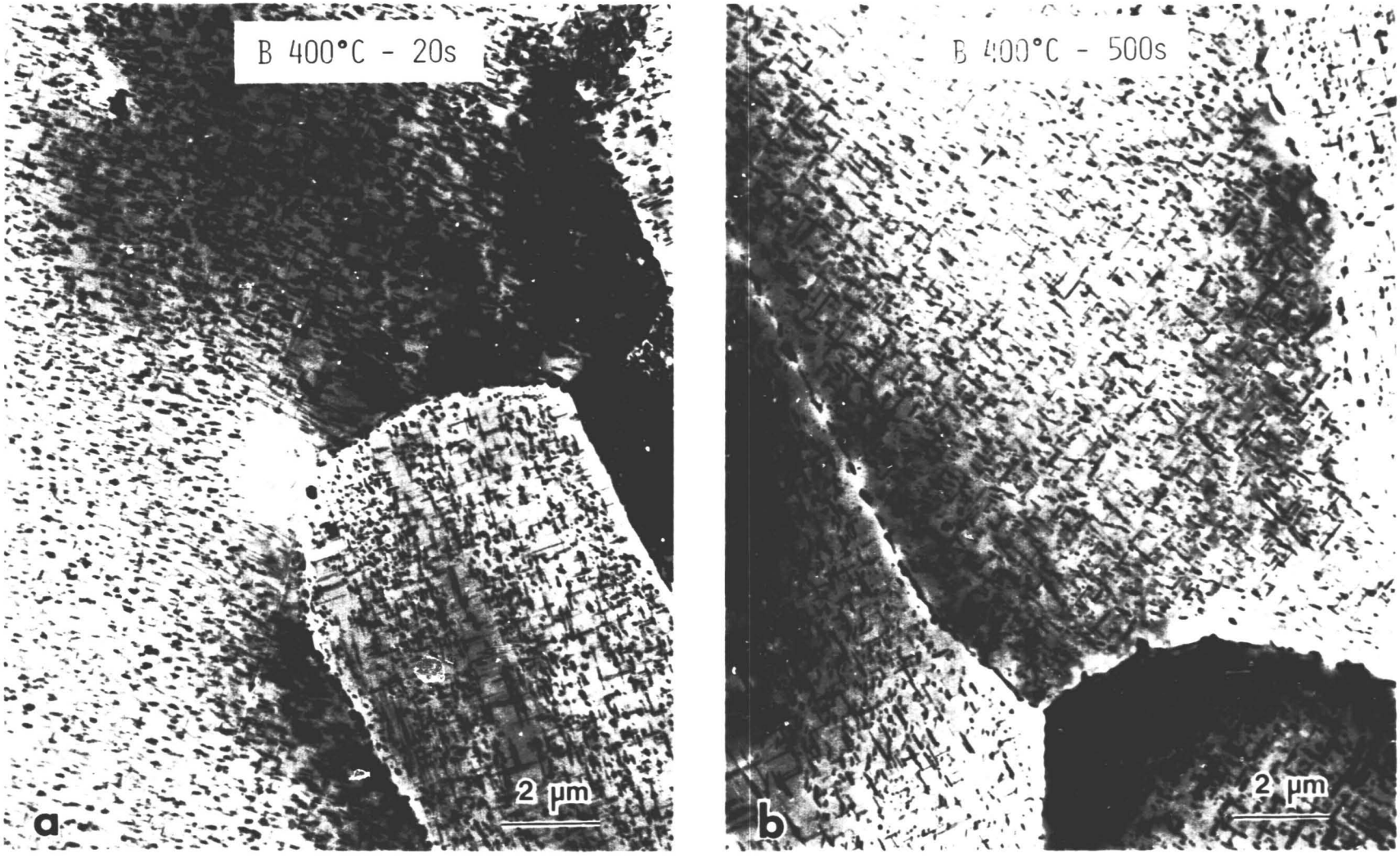

Figure 82. (a-f) Microstructures of specimens given sequence B "pre-aging" treatments (low magnification).

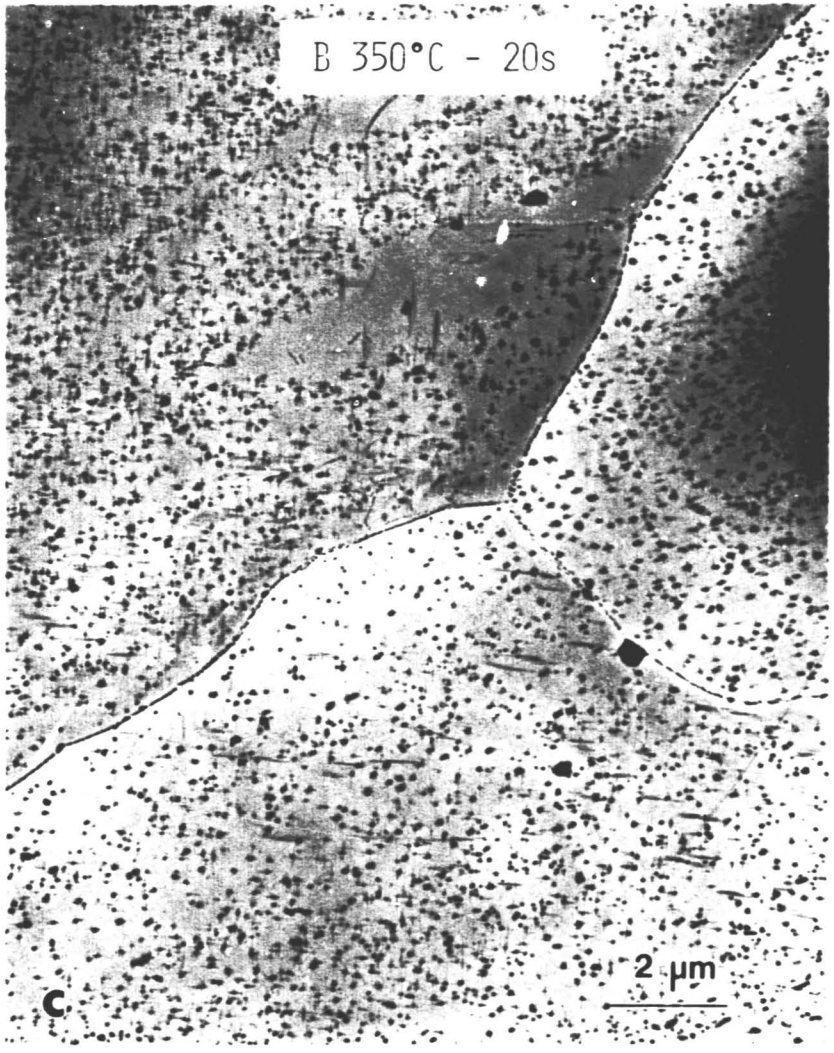

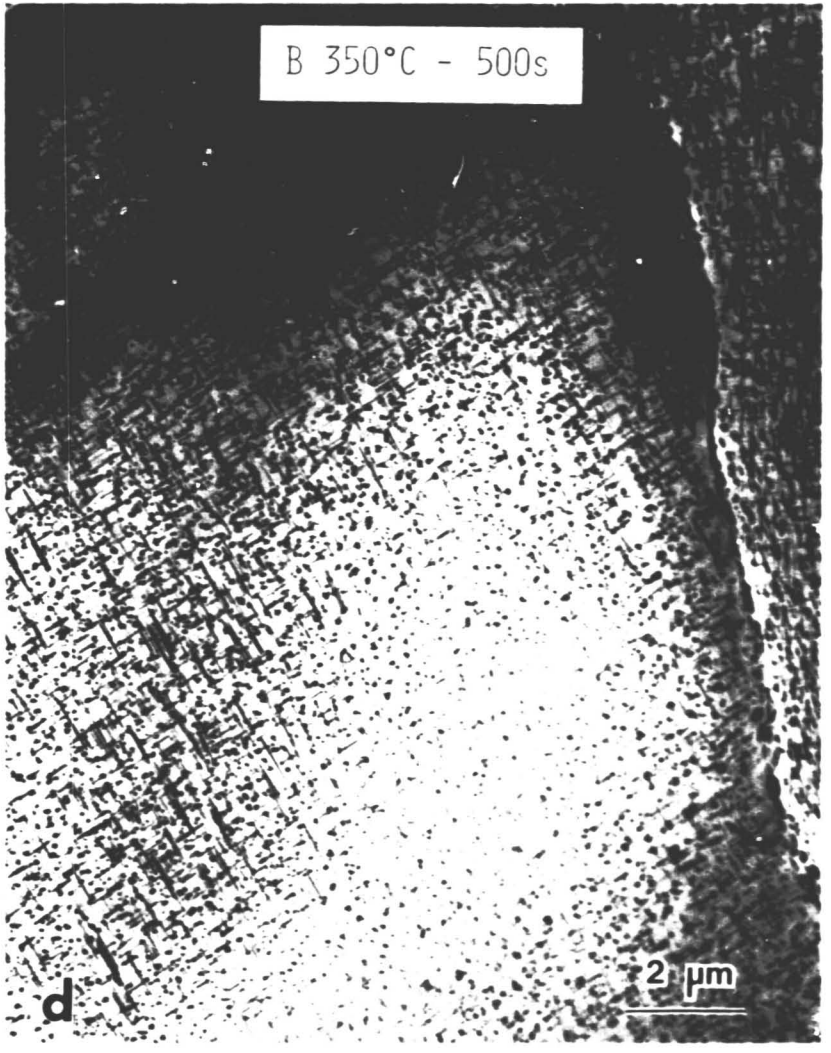

(Figure 82. Continued)

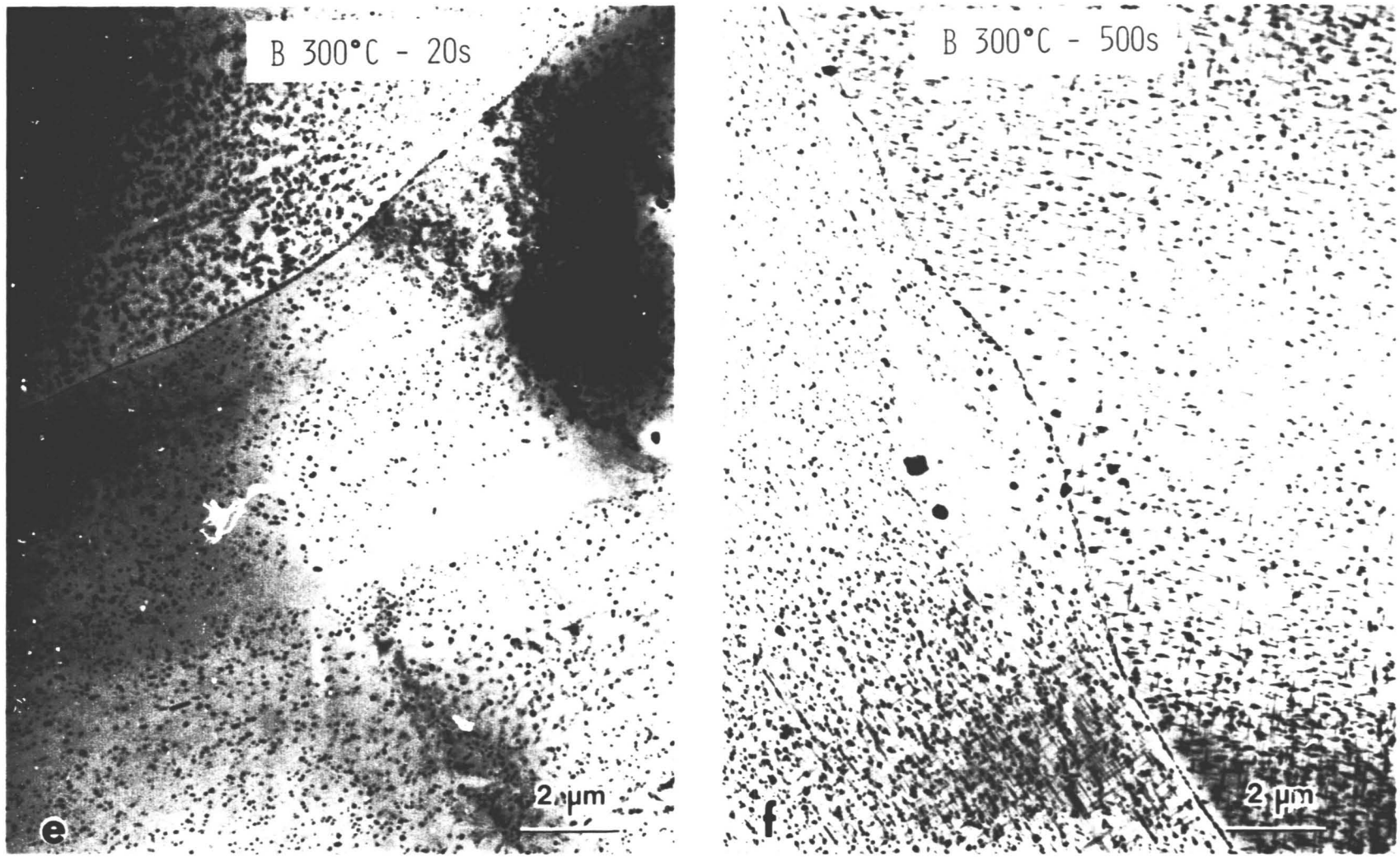

(Figure 82. Continued)

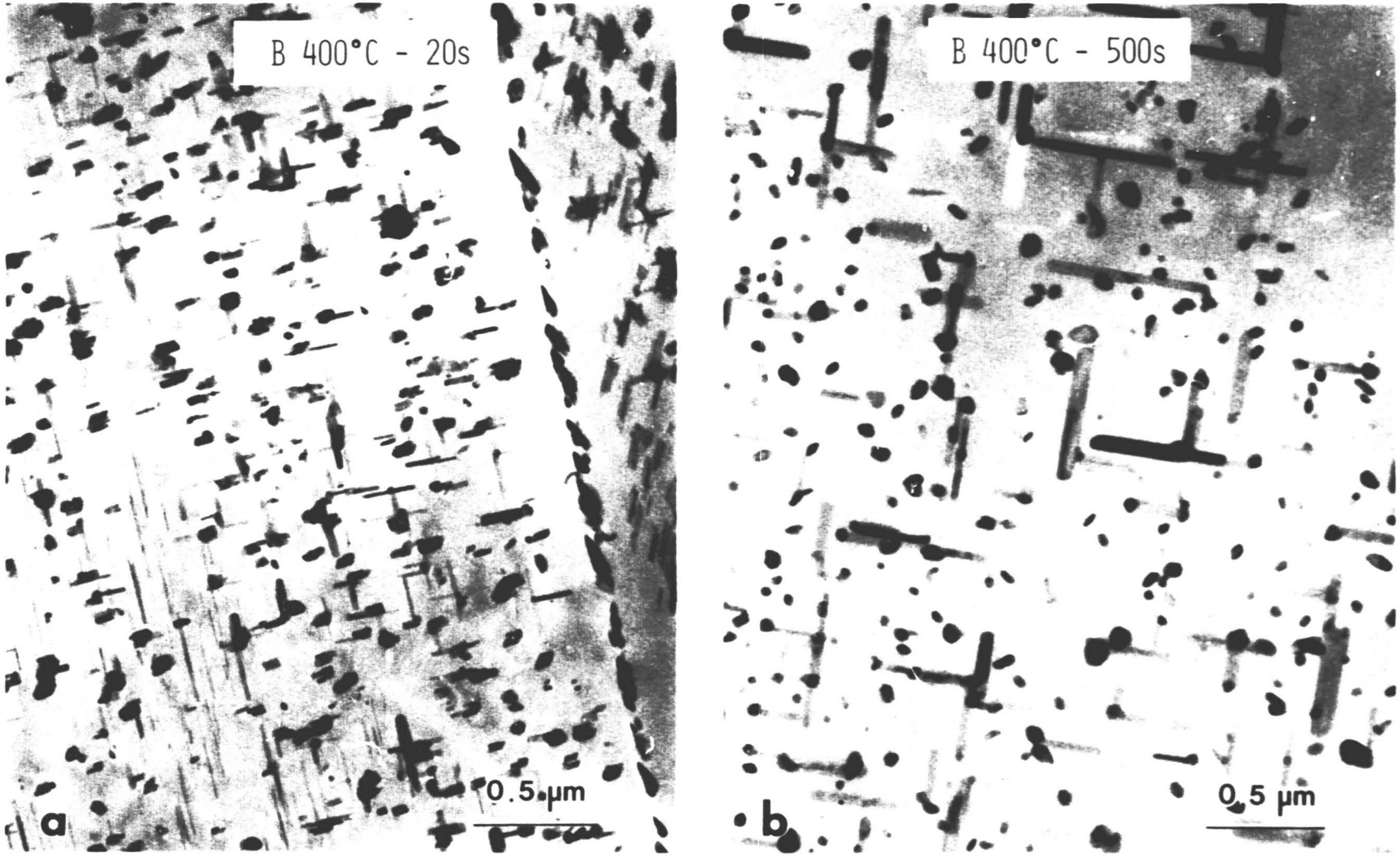

Figure 83. (a-f) Same as Figure 82 but at higher magnification.

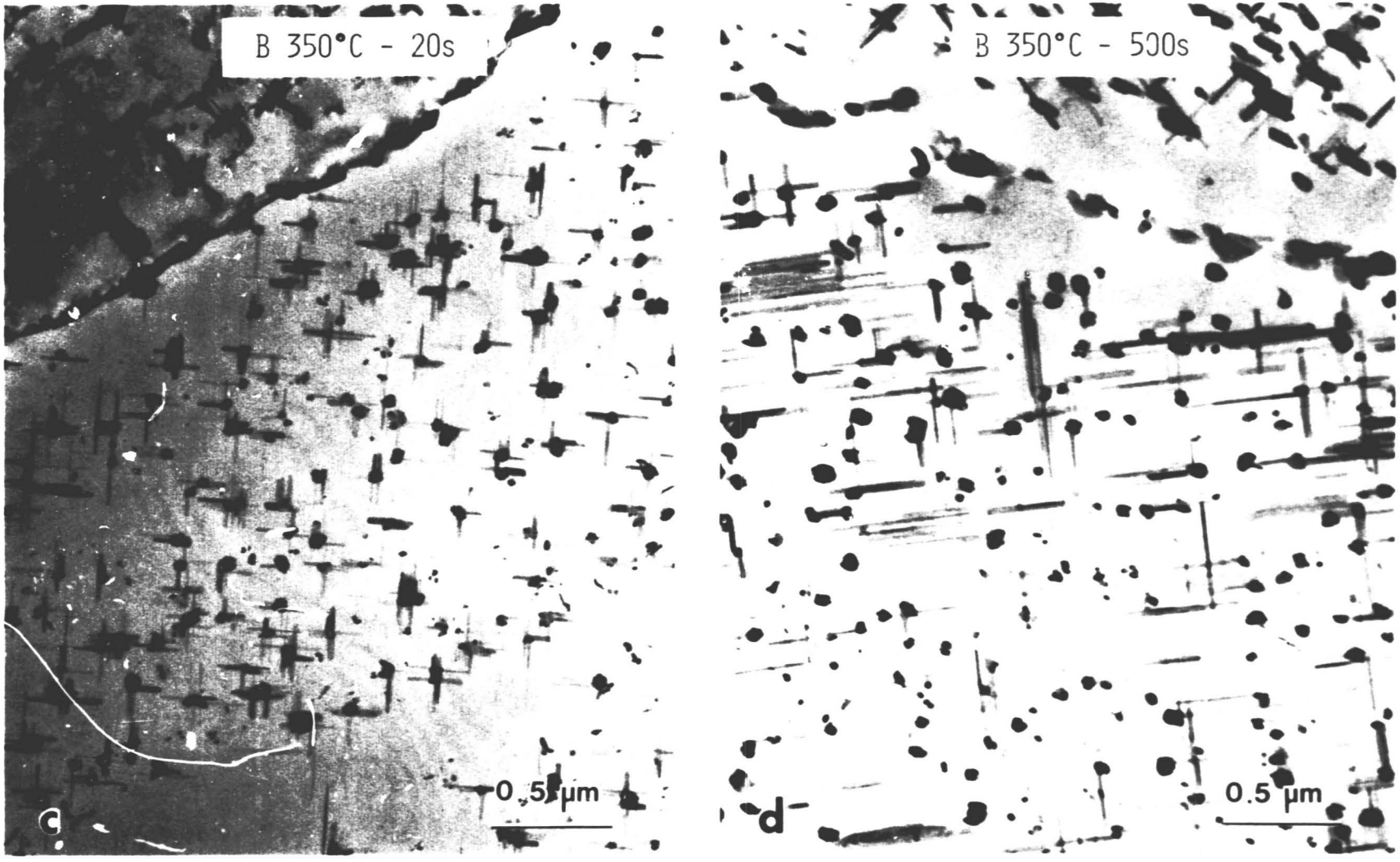

(Figure 83. Continued)

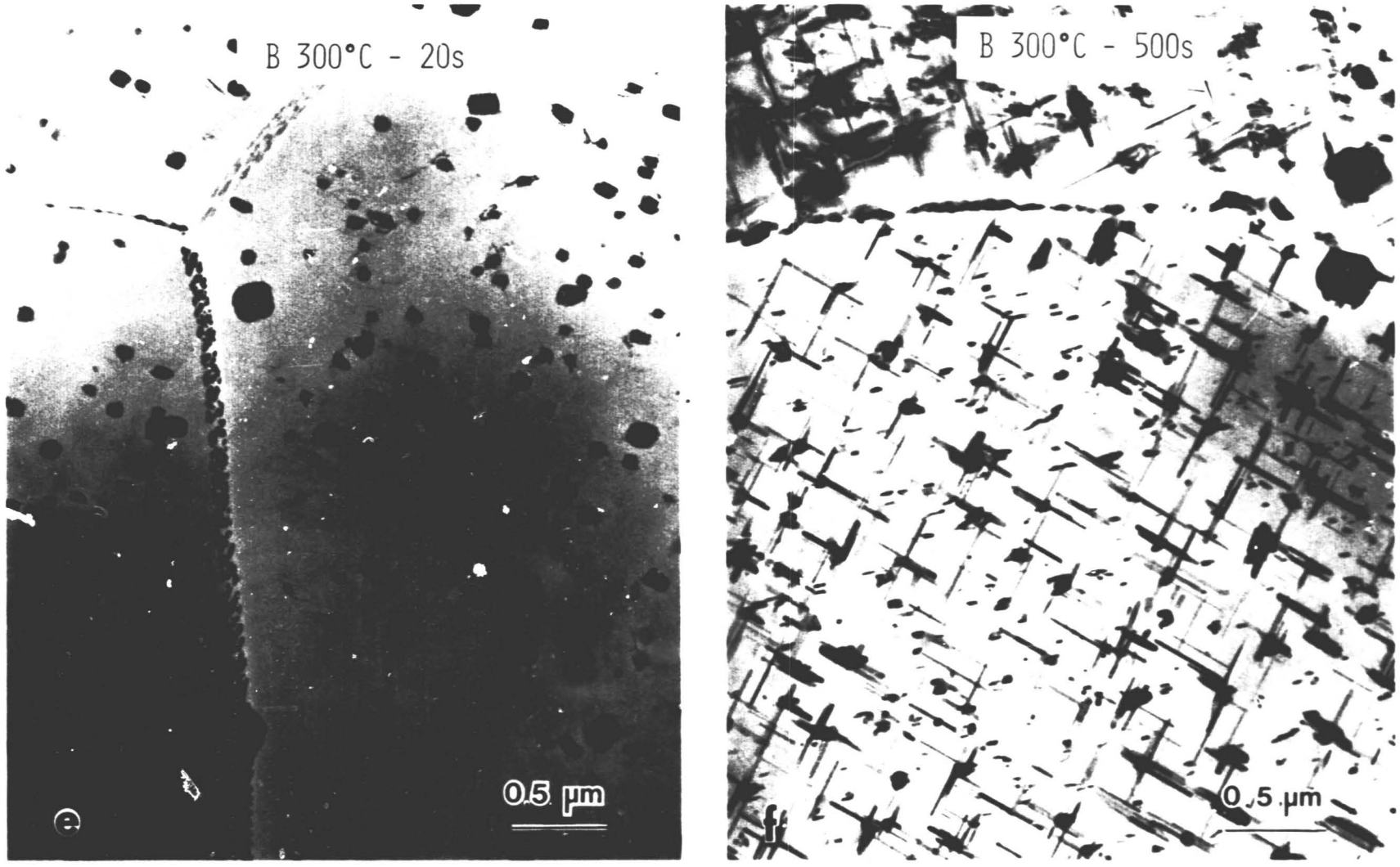

(Figure 83. Continued)

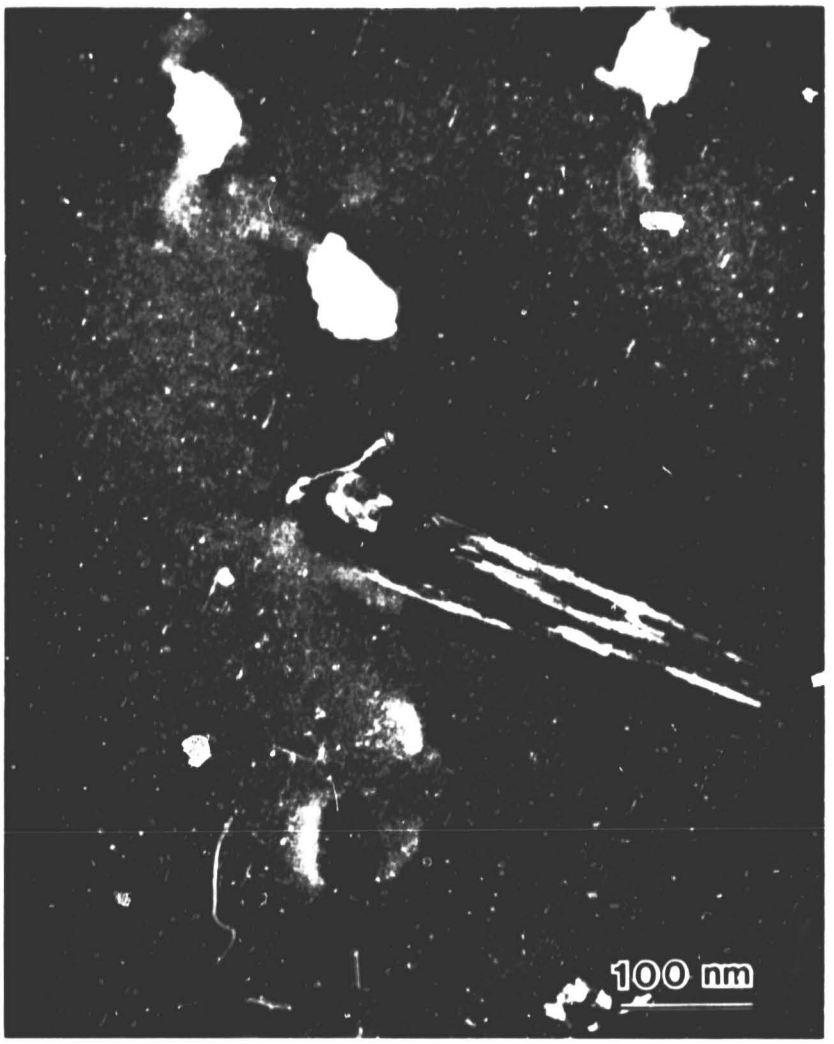

Figure 84. Dark field micrograph showing large heterogeneously nucleated S' precipites at dispersoid particles and at dislocations (bands of adjacent precipitates). Homogeneously distributed precipitates are present in matrix except in vicinity of large heterogeneously nucleated precipitates. Sequence B "pre-aged" at 300°C for 20s.

Figure 85. Optical micrograph of (a) sequence A "pre-aged" at 400°C for 7200 minutes. (b) sequence B "pre-aged" at 400°C for 7200 minutes.

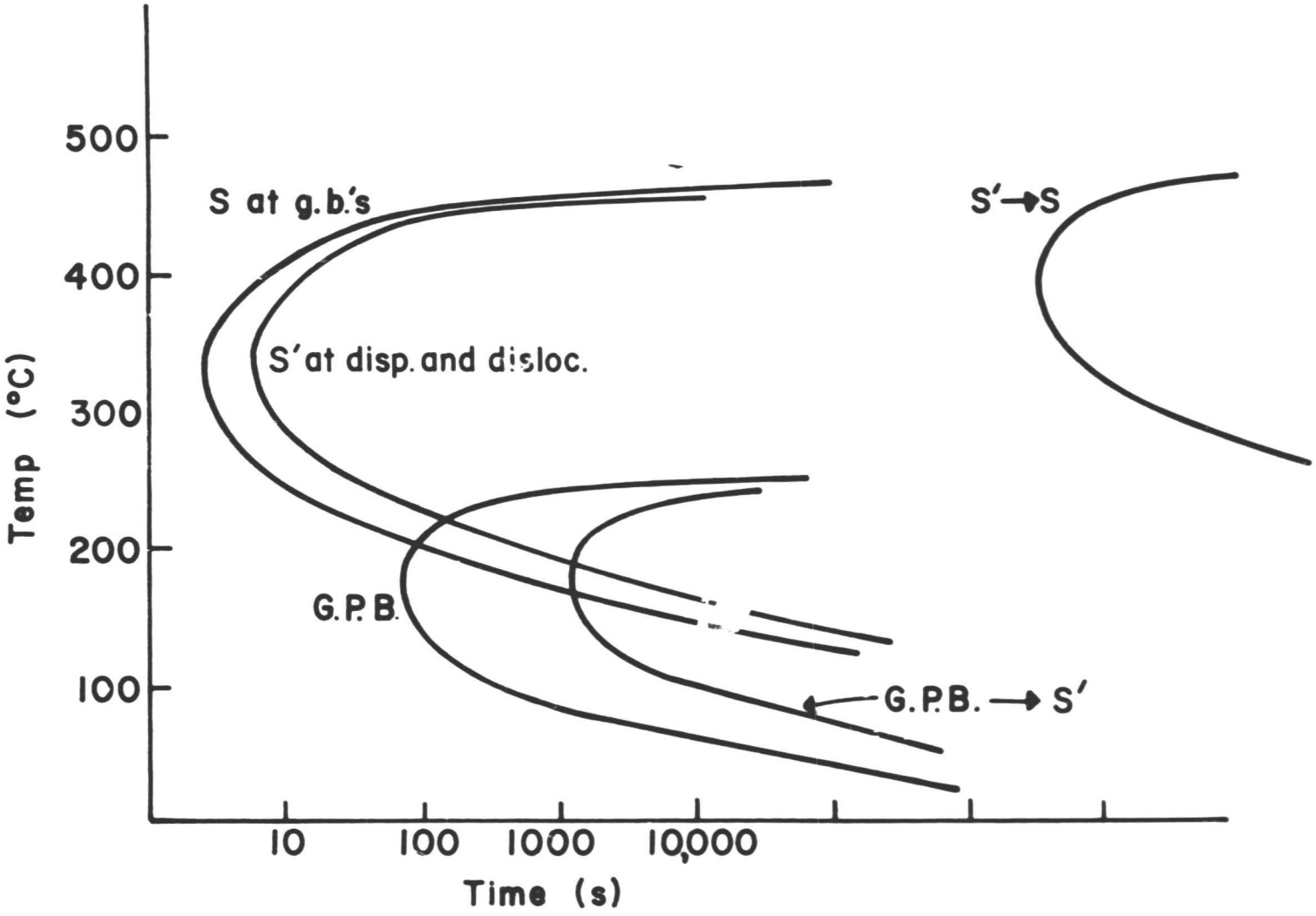

Figure 86. Schematic representation of nucleation curves for sequence B "pre-aging" treatment.

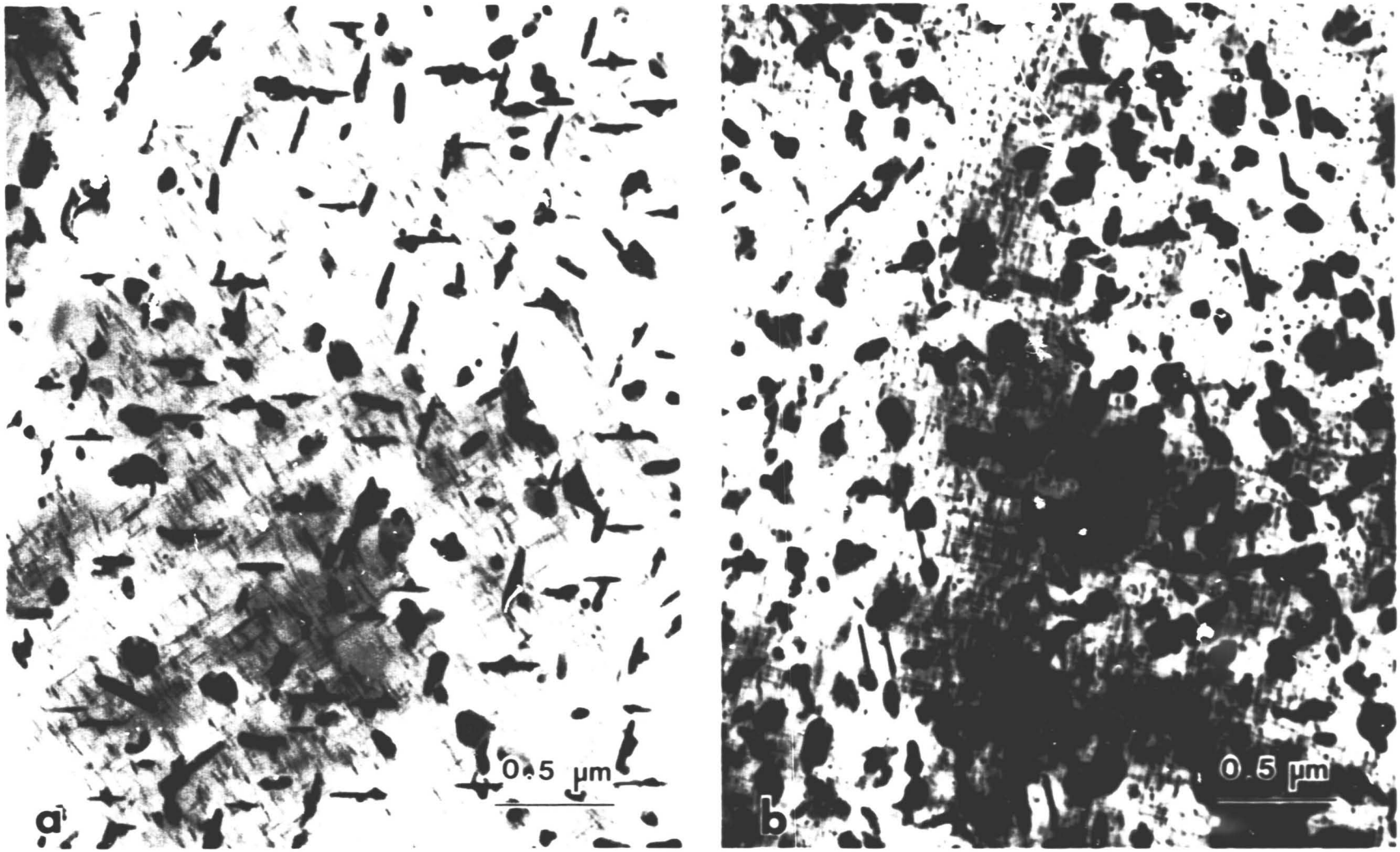

Figure 87. Specimens after sequence A "pre-aging" treatment at 350° for (a) 20s and (b) 109s. Specimens were then processed according to T851 specifications. Small needle shaped precipitates are S' formed during final aging treatment. Many S phase precipitates are surrounded by light (thin) regions.

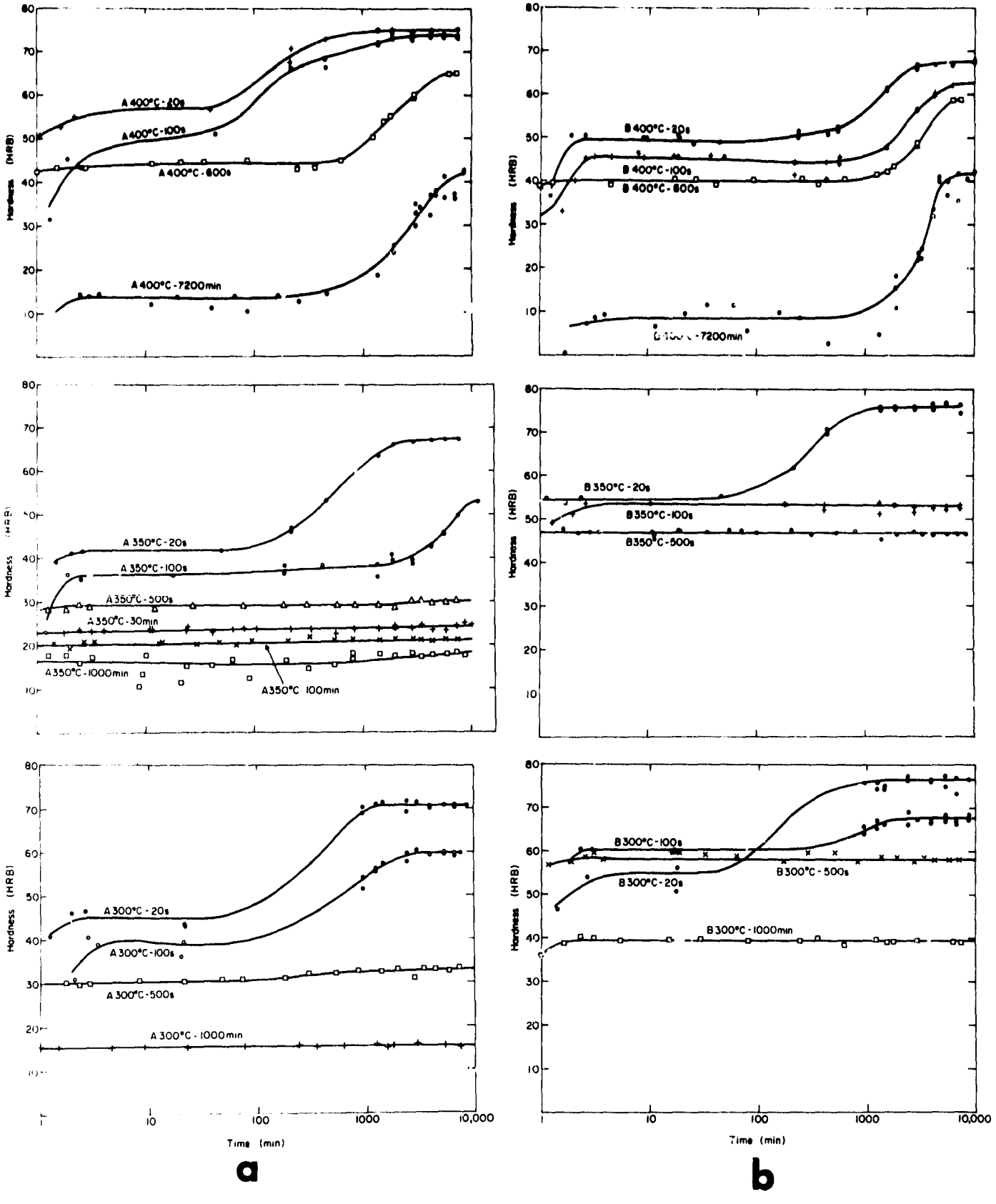

Figure 88. Age-hardening response at room temperature (24-25°C) of "pre-aged" 2024 aluminum alloy specimens. a) Sequence A "pre-aging" treatment. (b) Sequence B "pre-aging" treatment.

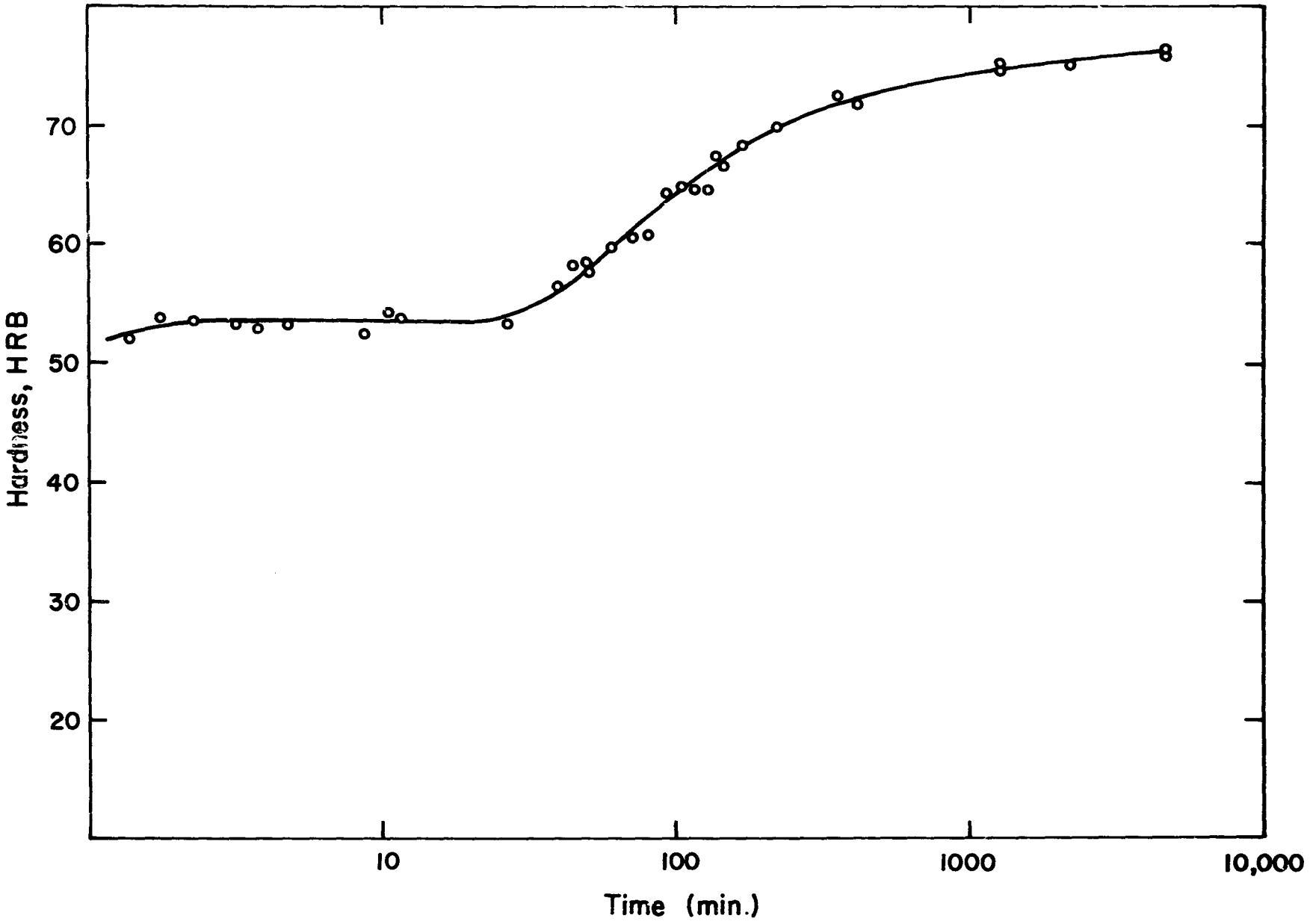

Figure 89. Room temperature (24-25°C) age-hardening behavior of direct quench specimen.

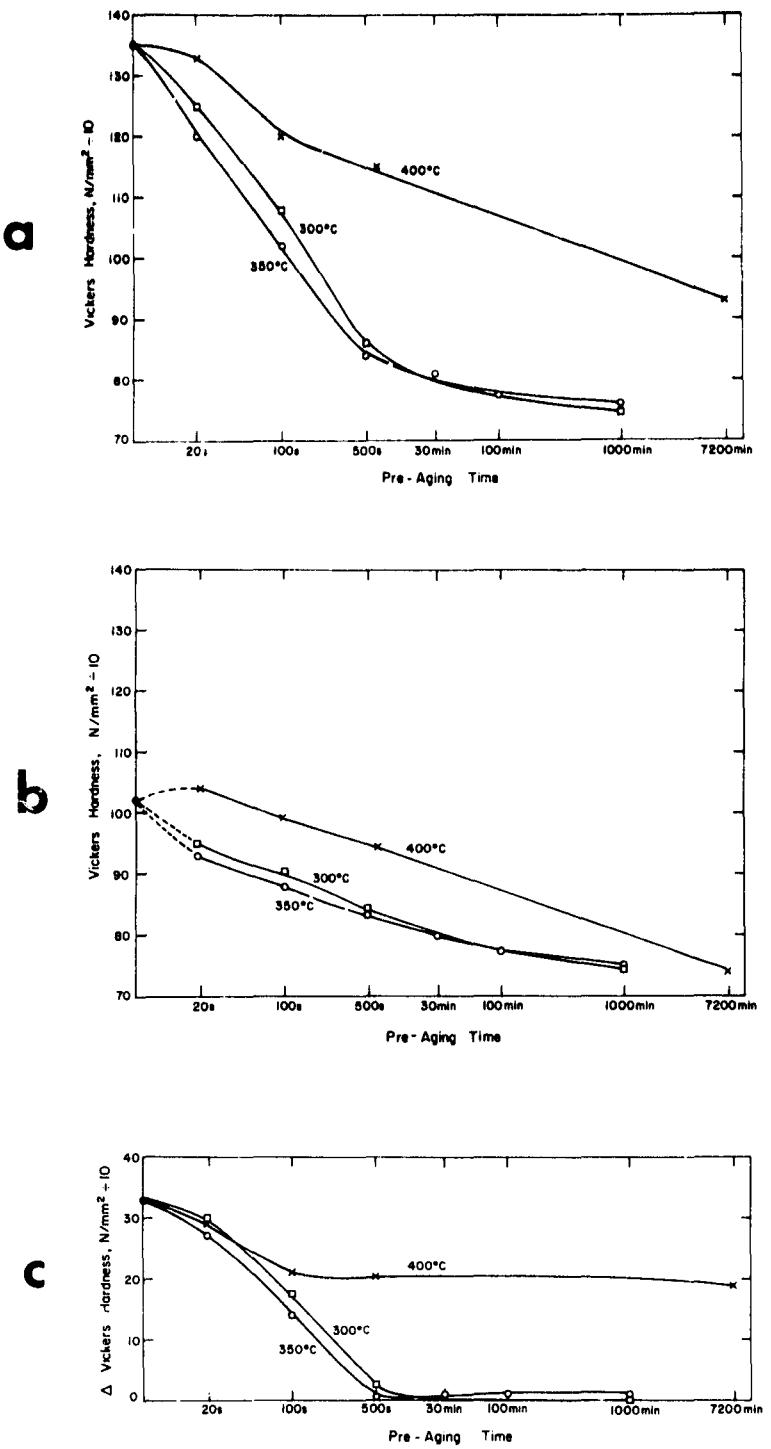

Figure 90. Affect of sequence A "pre-aging" treatment on hardness. (a) Final hardness after room temperature aging (T4). (b) Incubation hardness. (c) Incremental change in hardness due to room temperature aging. Data taken from Figures 88 and 89.

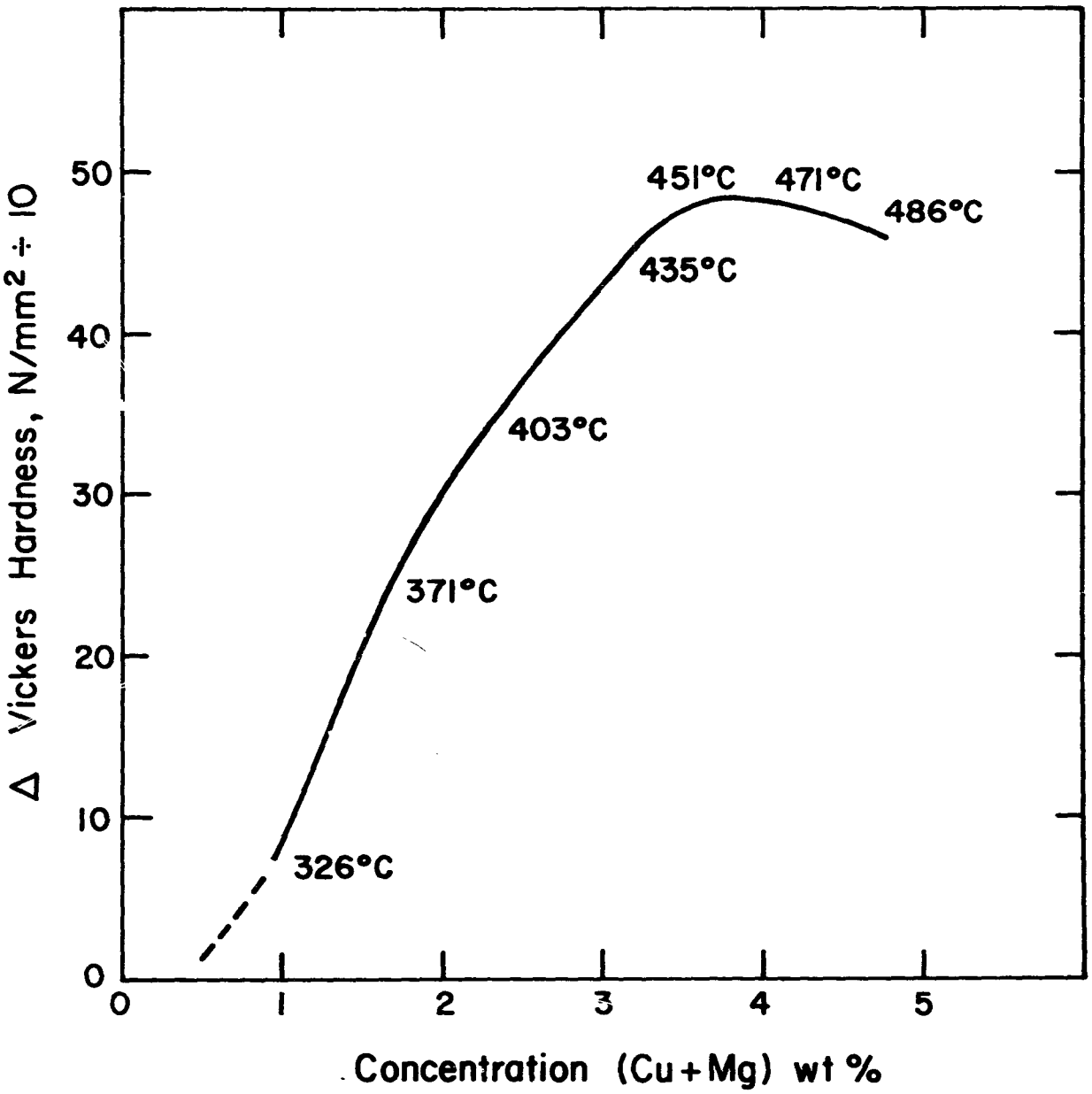

Figure 91. Incremental change in hardness as a function of (Cu+Mg) concentration due to room temperature aging. Data taken from Beton and Rollason (38) Figure 2. Solvus temperatures for the $\alpha/(\alpha+S)$ boundary are indicated.

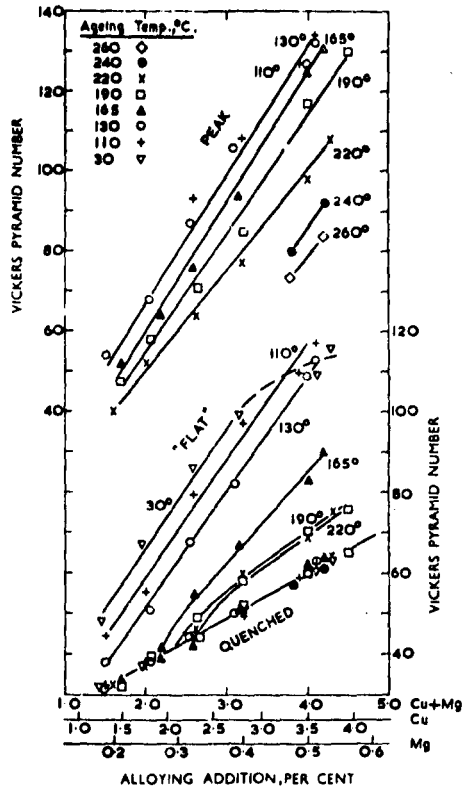

Figure 92. As-quenched and final hardness curves for Al-2.2:1 (Cu+Mg) alloys from Hardy (35) Figure 7.

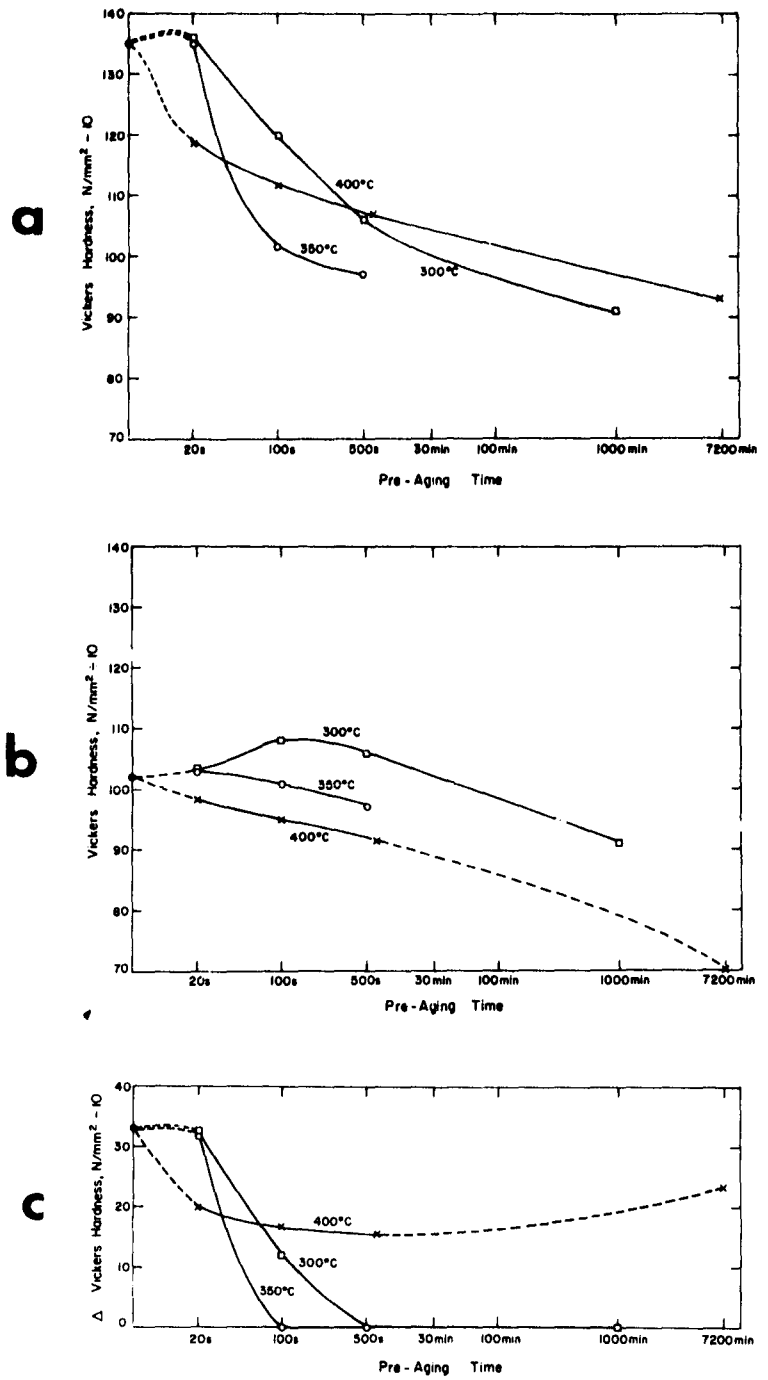

Figure 93. Effect of sequence B "pre-aging" treatments on hardness. (a) Final hardness after room temperature aging (T4). (b) Incubation hardness. (c) Incremental change in hardness due to room temperature aging. Data taken from Figures 88 and 89.

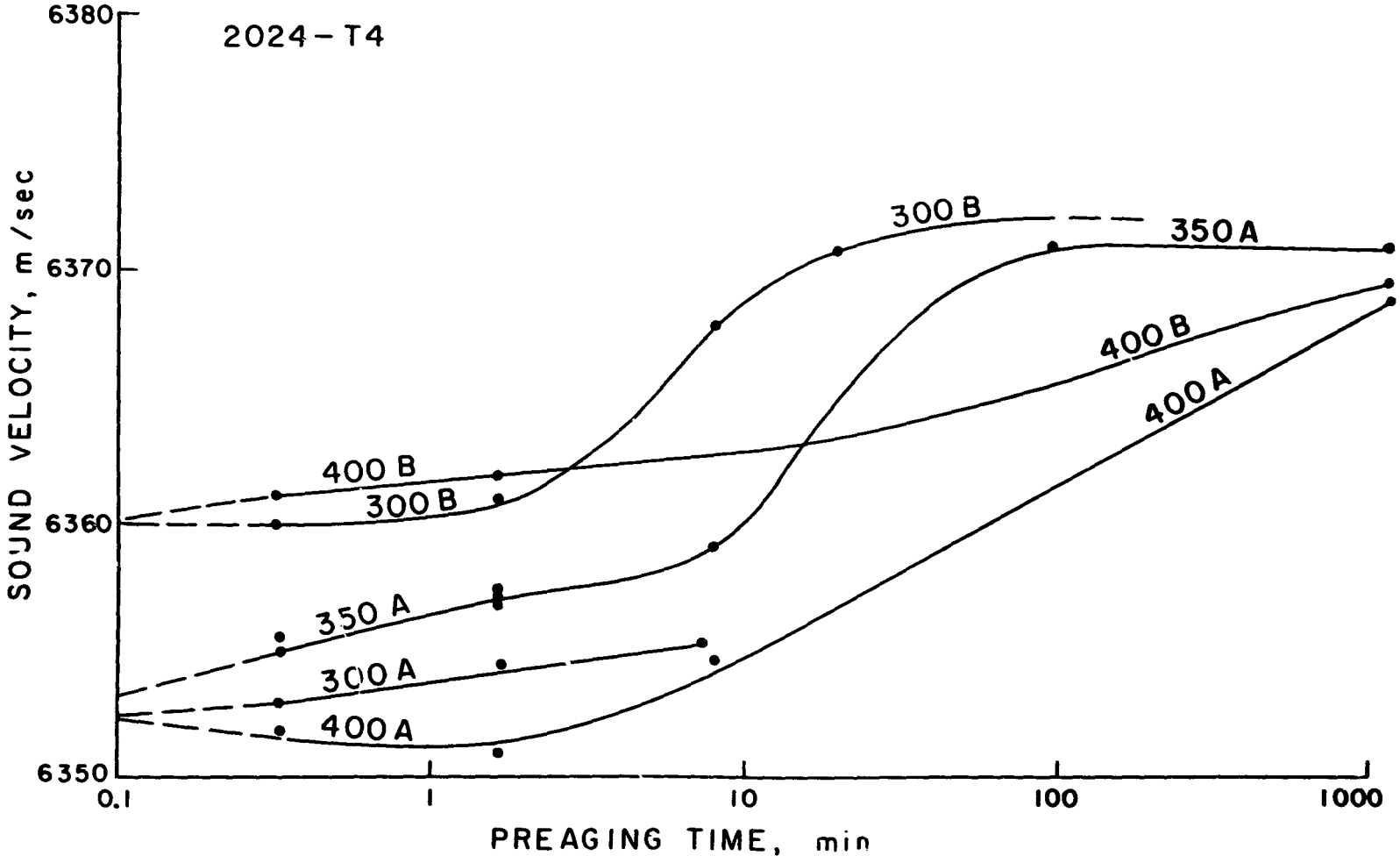

Figure 94. Variation of the sound-wave velocity in 2024-T4 aluminum alloy as a function of "pre-aging" time at different "pre-aging" temperatures and heat treatment sequences.

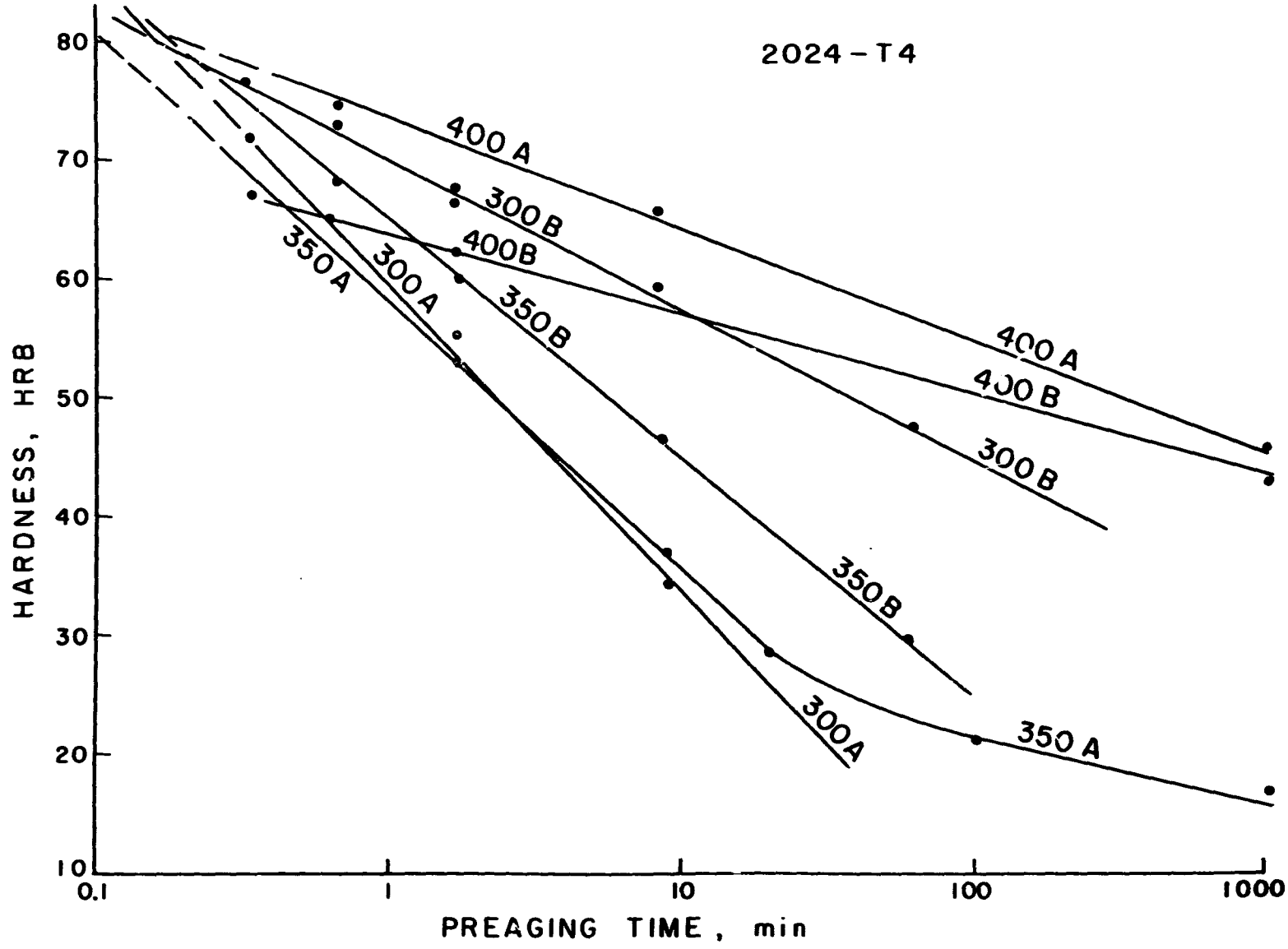

Figure 95. Variation of hardness in 2024-T4 aluminum alloy for different "pre-aging" temperatures and heat treatment sequences.

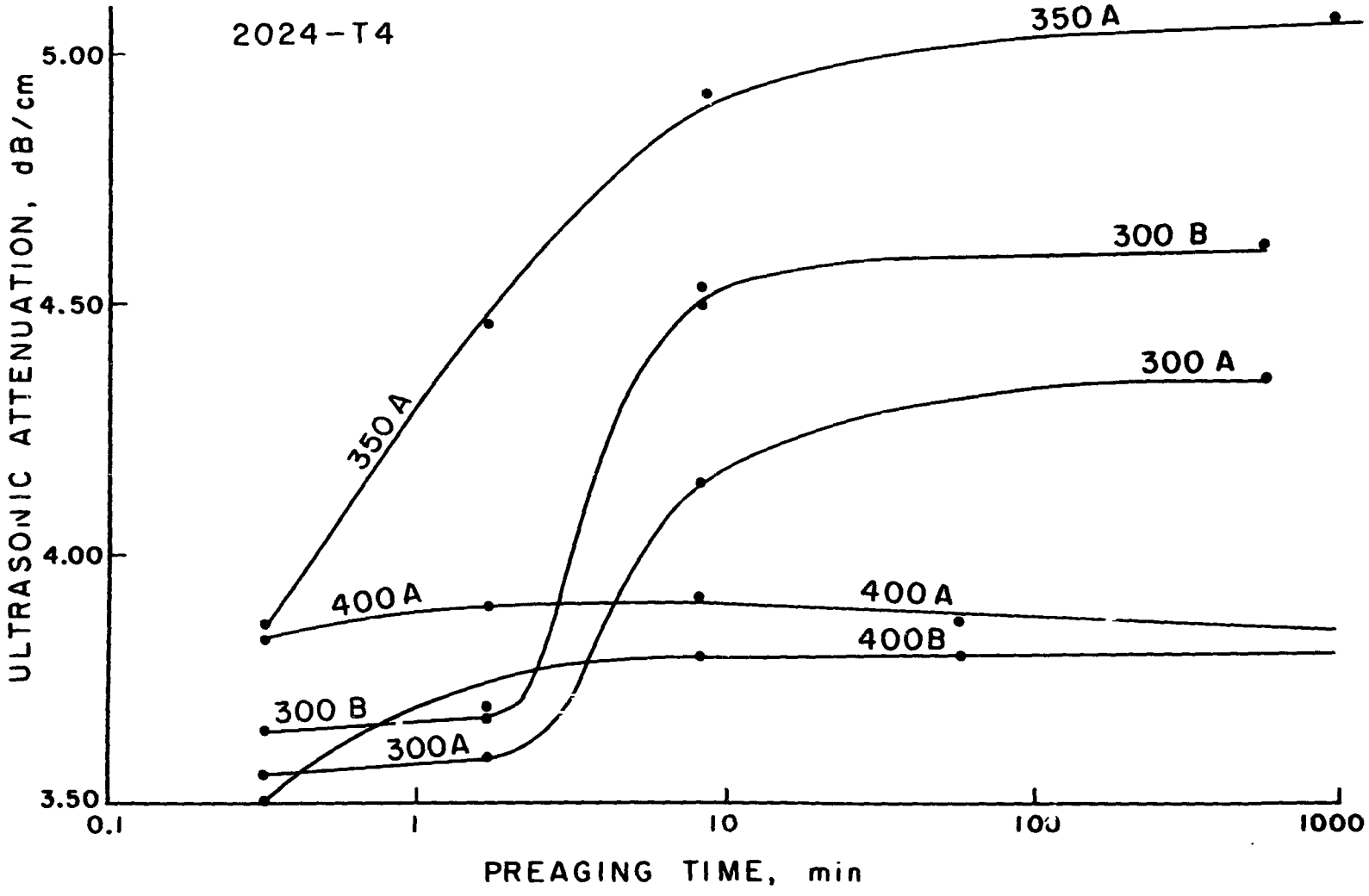

Figure 96. Variation of ultrasonic attenuation in 2024-T4 aluminum alloy with "pre-aging" time for different "pre-aging" temperatures and heat treatment sequences.

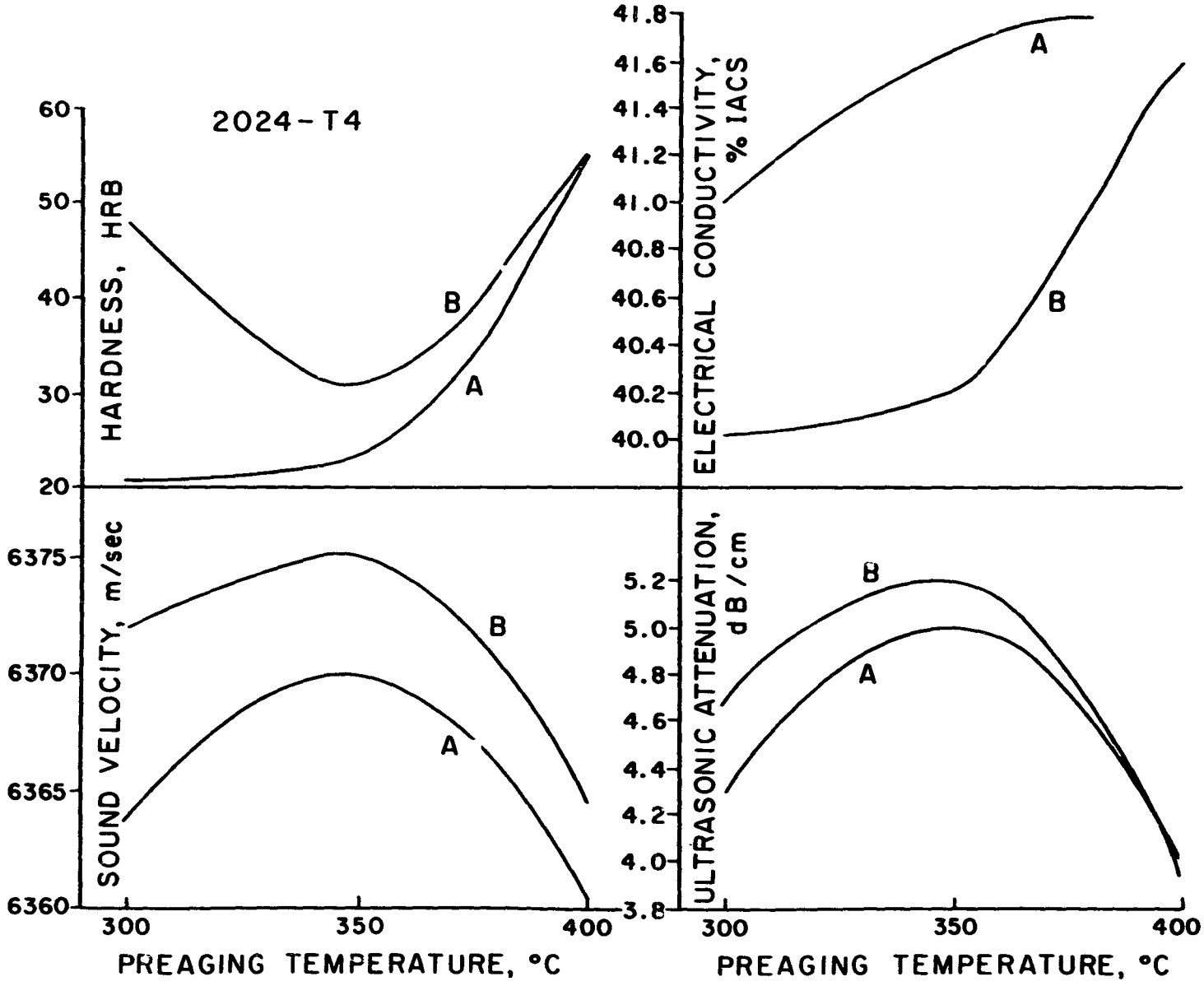

Figure 97. Effect of "pre-aging" temperature and sequence on hardness, sound velocity, ultrasonic attenuation and electrical resistivity of 2024-T4 aluminum alloy after 60 minutes of "pre-aging".

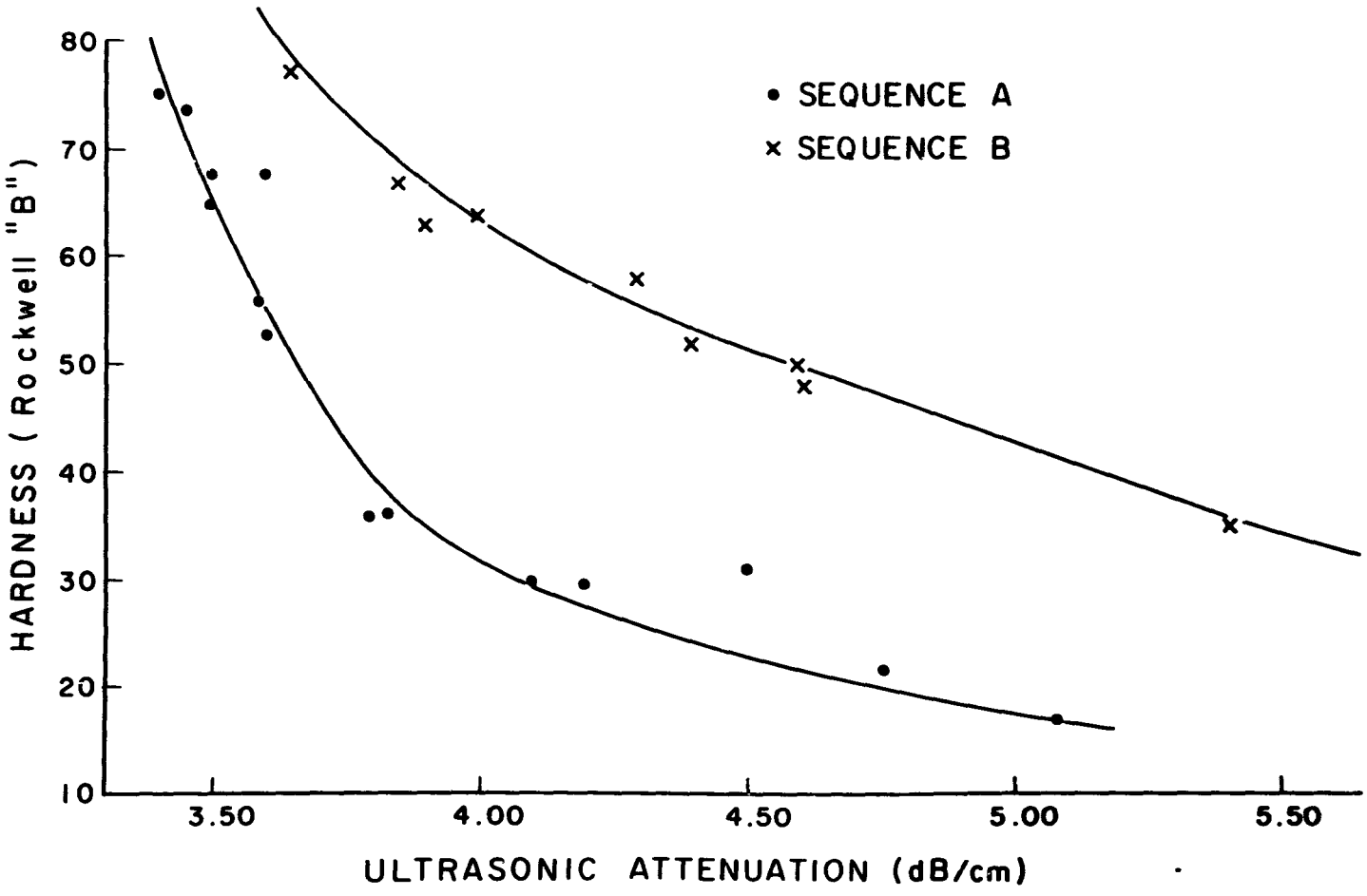

Figure 98. Correlation between hardness and ultrasonic attenuation for 2024-T4 aluminum alloy. Dependence on "pre-aging" treatment sequence.

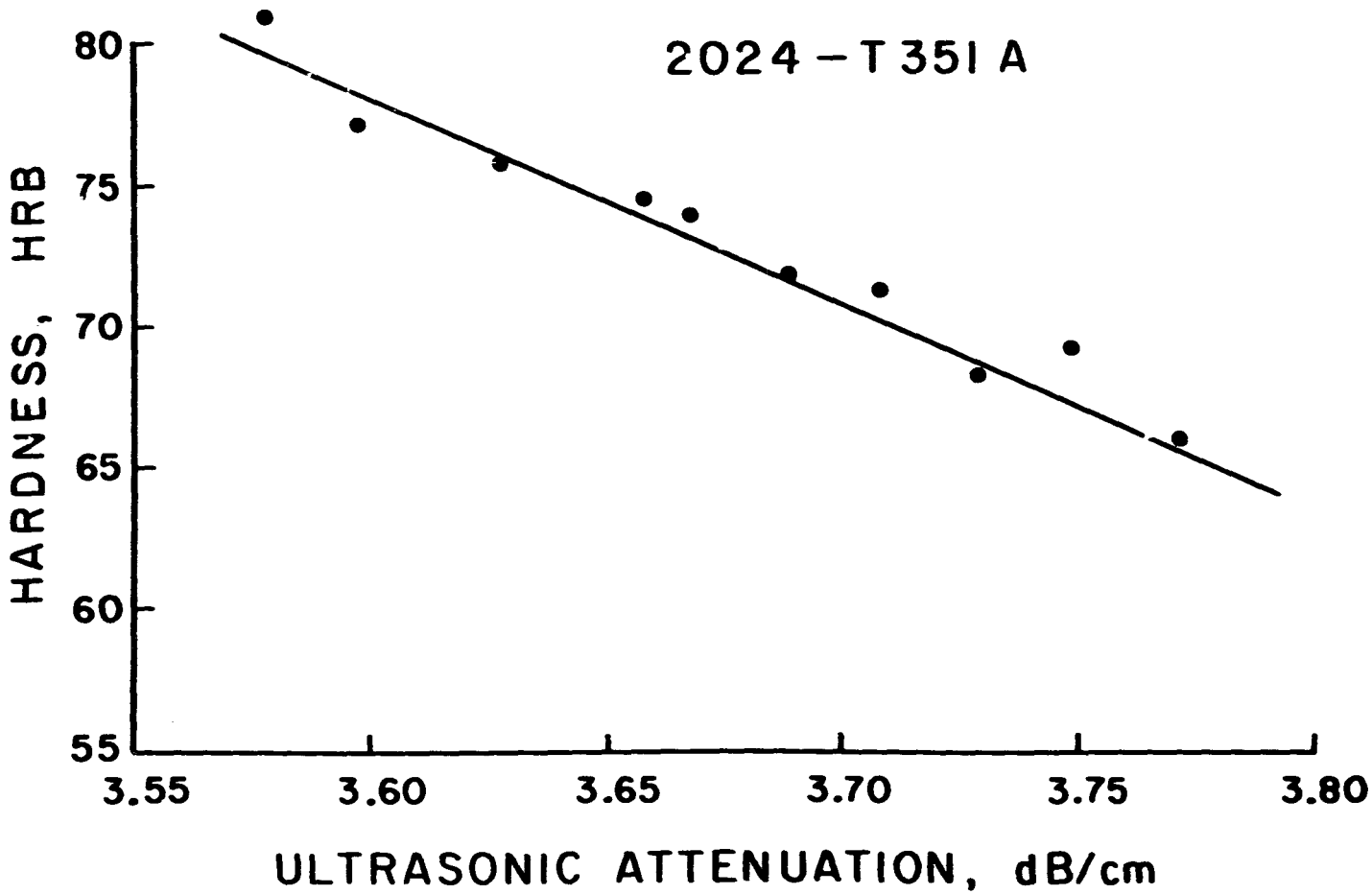

Figure 99. Correlation between ultrasonic attenuation and hardness for 2024-T351 aluminum alloy (sequence A).

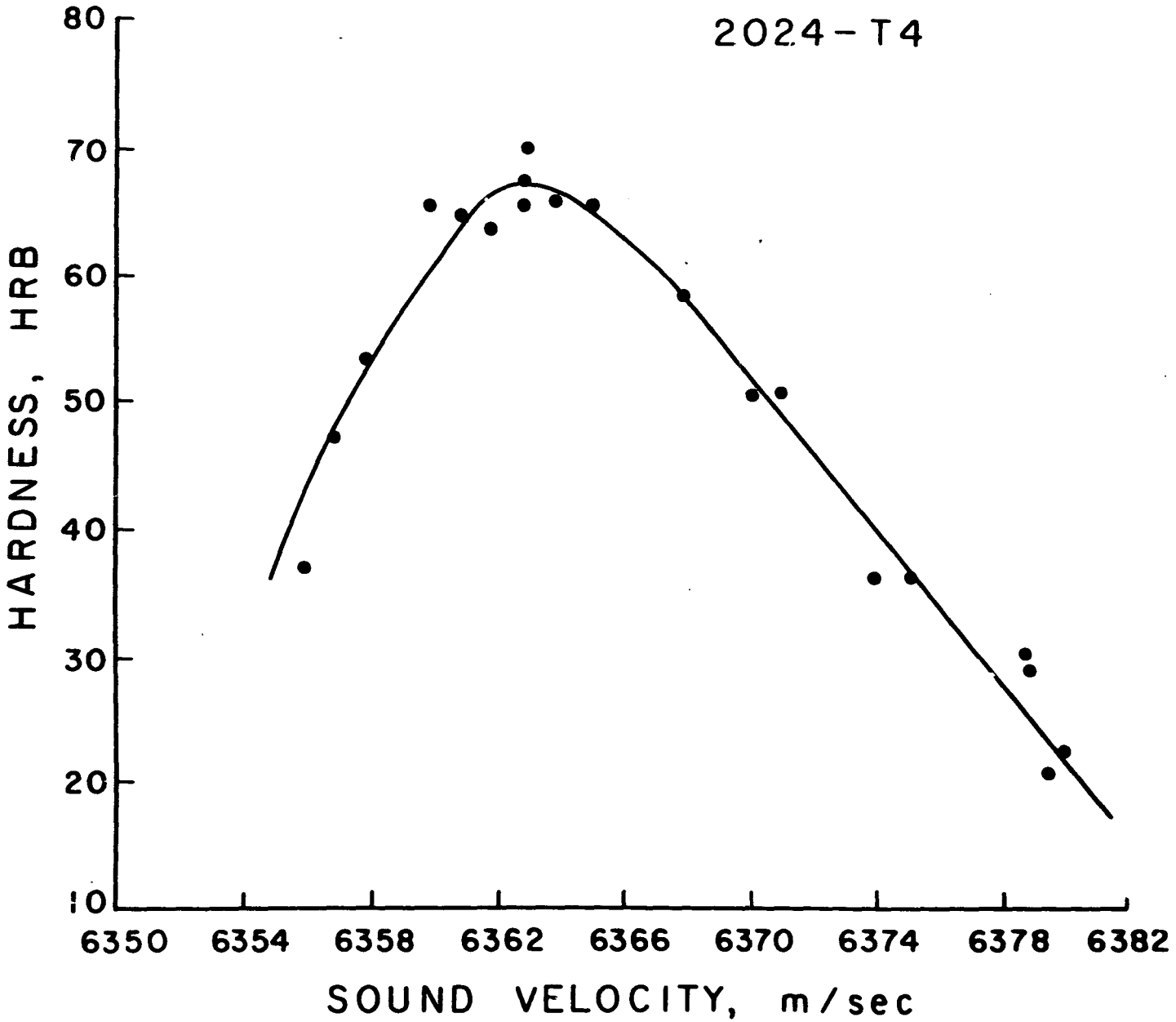

Figure 100. Correlation curve between sound-wave velocity and hardness for 2024-T4 aluminum alloy.

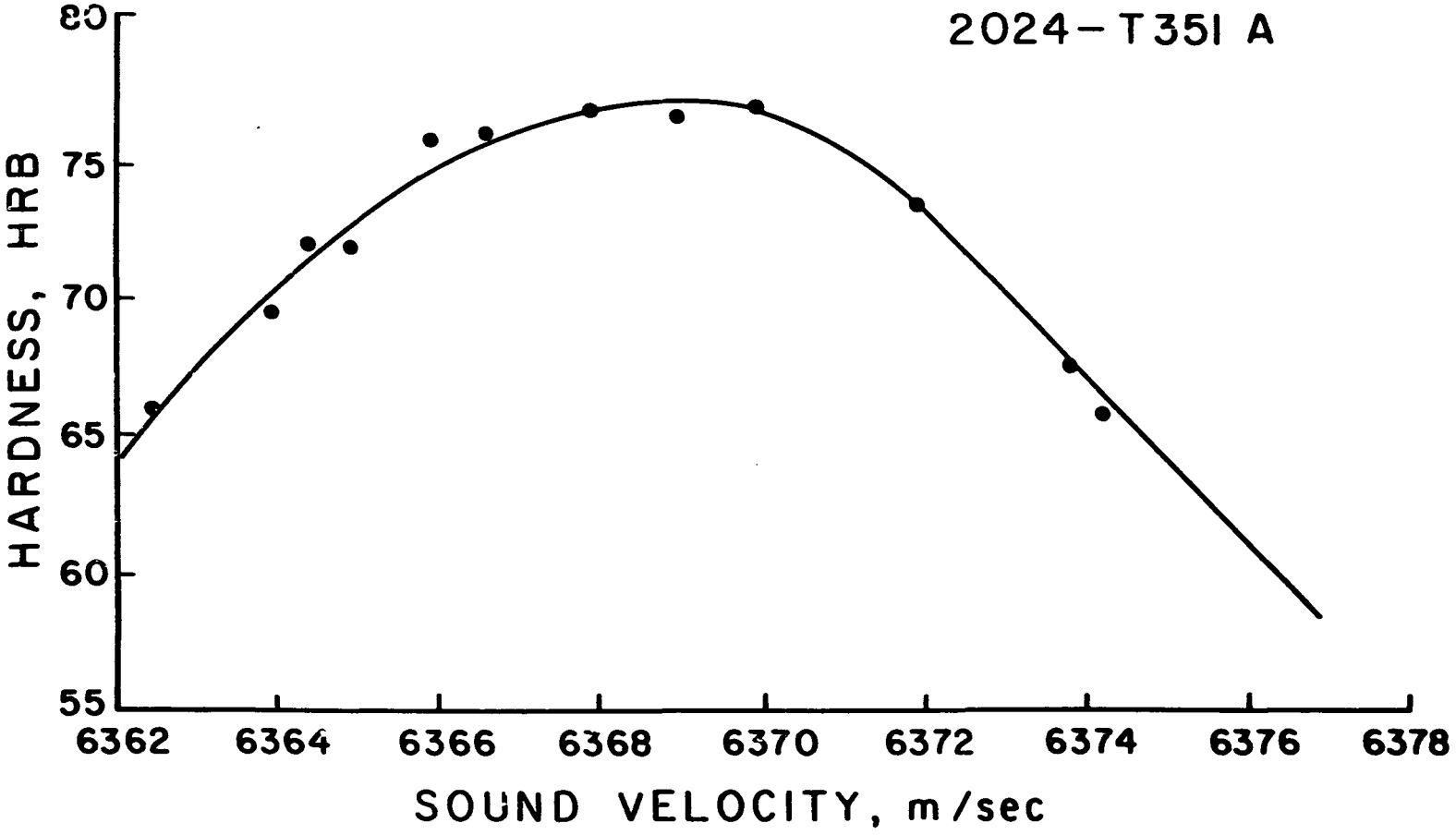

Figure 101. Correlation curve between sound-wave velocity hardness for 2024-T351 aluminum alloy.

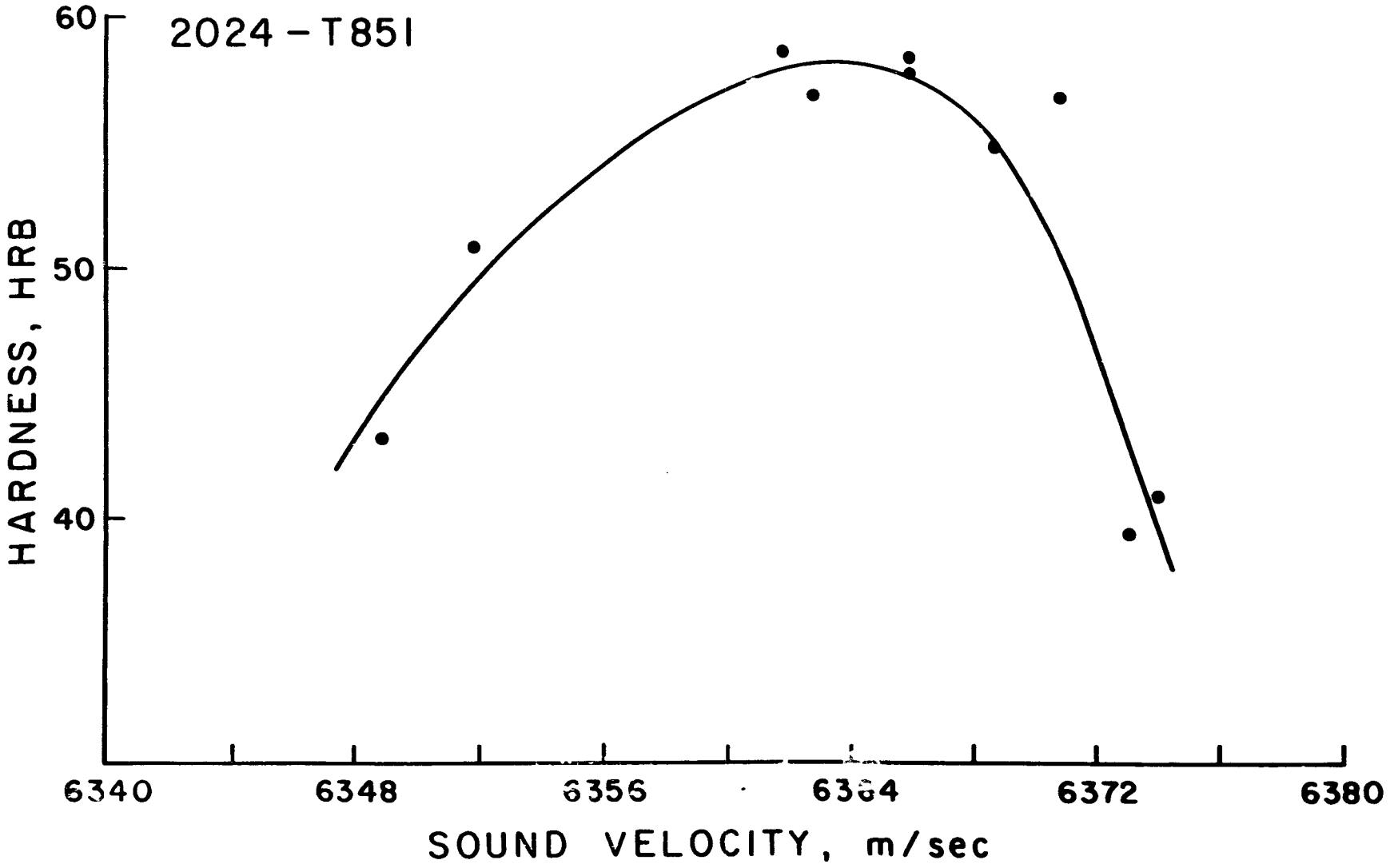

Figure 102. Correlation curve between sound-wave velocity and hardness for 2024-T851 aluminum alloy.

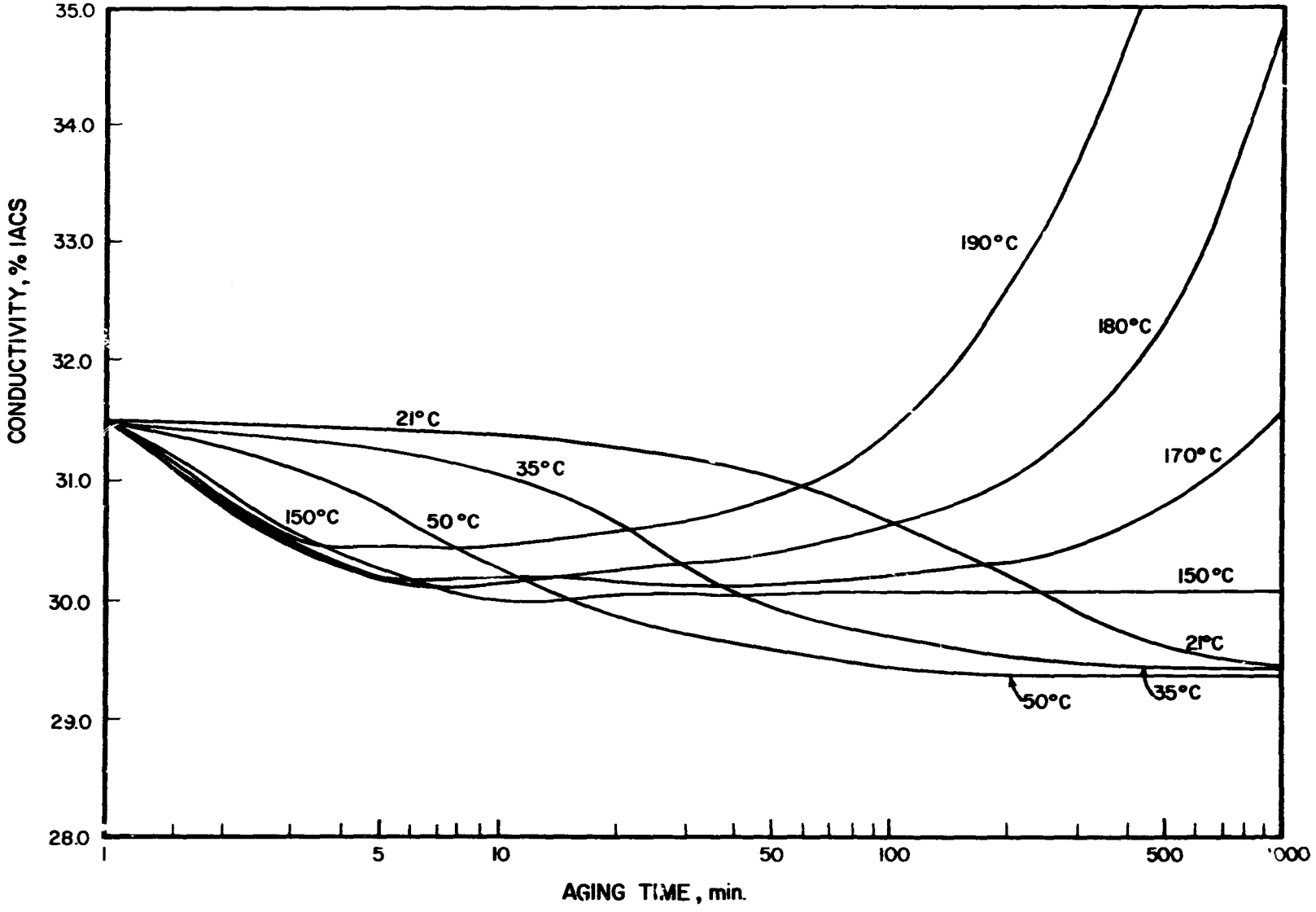

Figure 103. Eddy-current conductivity as a function of aging time, at different aging temperatures, of 2024 aluminum alloy (unstretched).

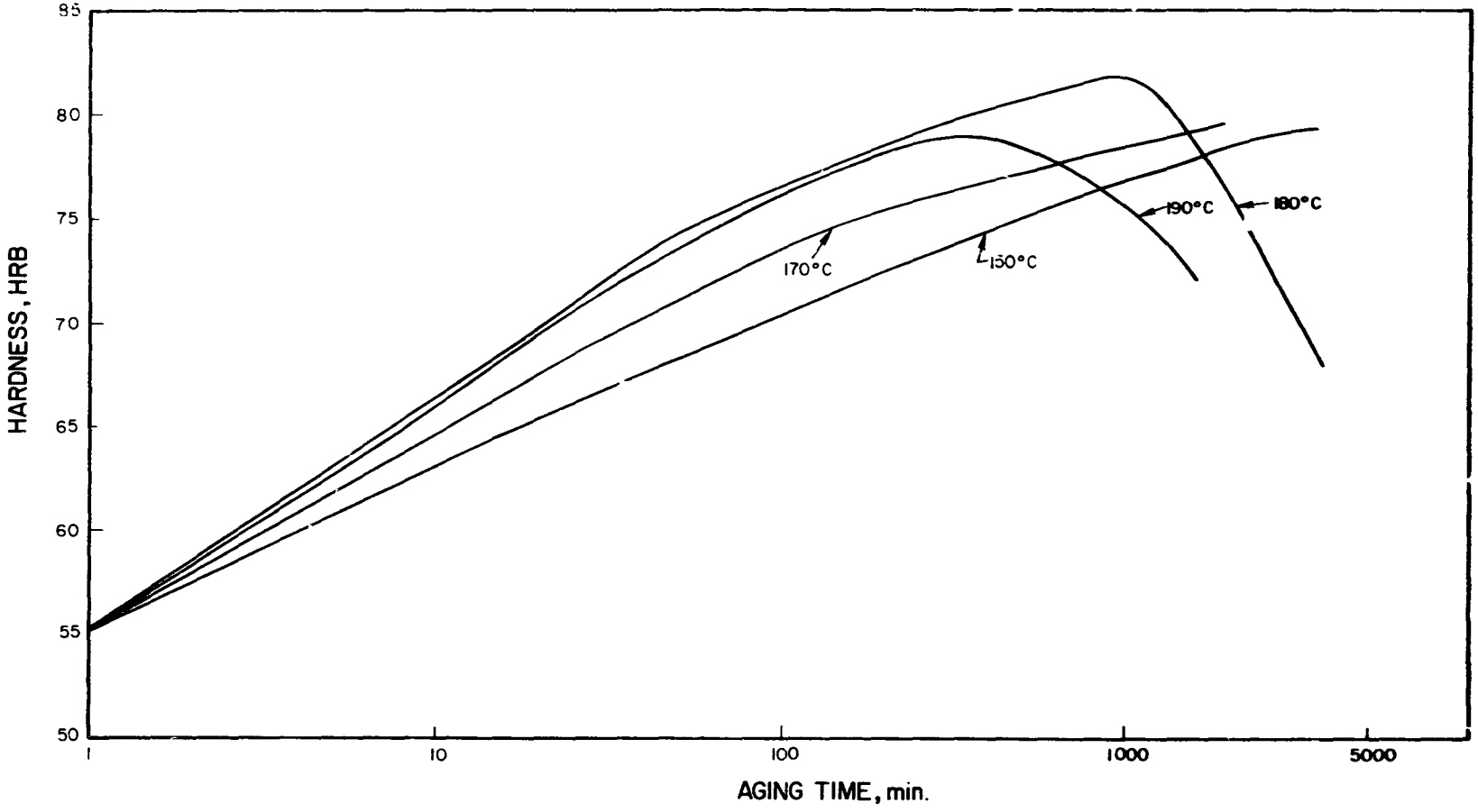

Figure 104. Hardness as a function of aging time, at different aging temperatures, of 2024 aluminum alloy (unstretched).

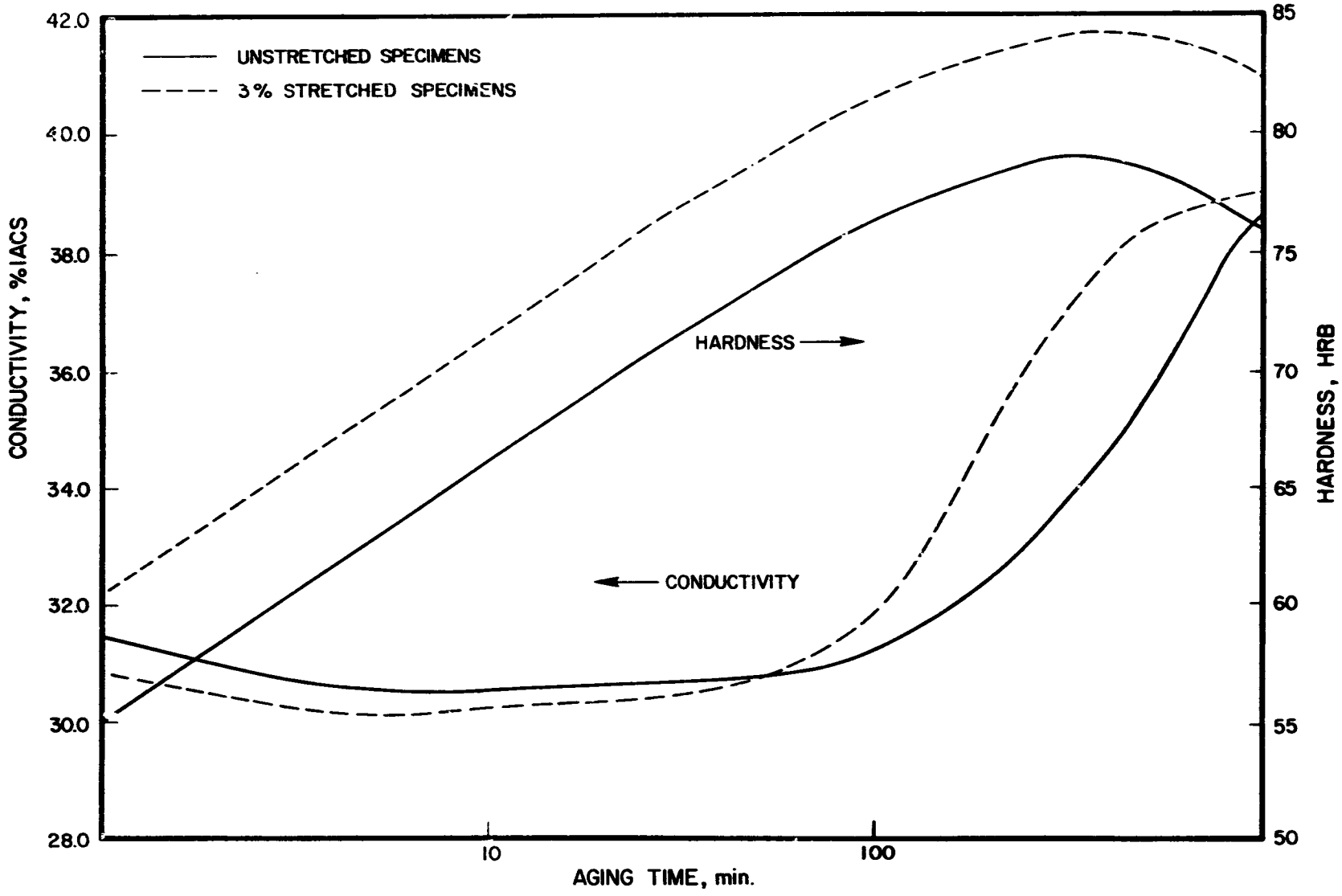

Figure 105. Eddy-current conductivity and hardness as a function of aging at 190 °C of 2024 aluminum alloy (stretched and unstretched).

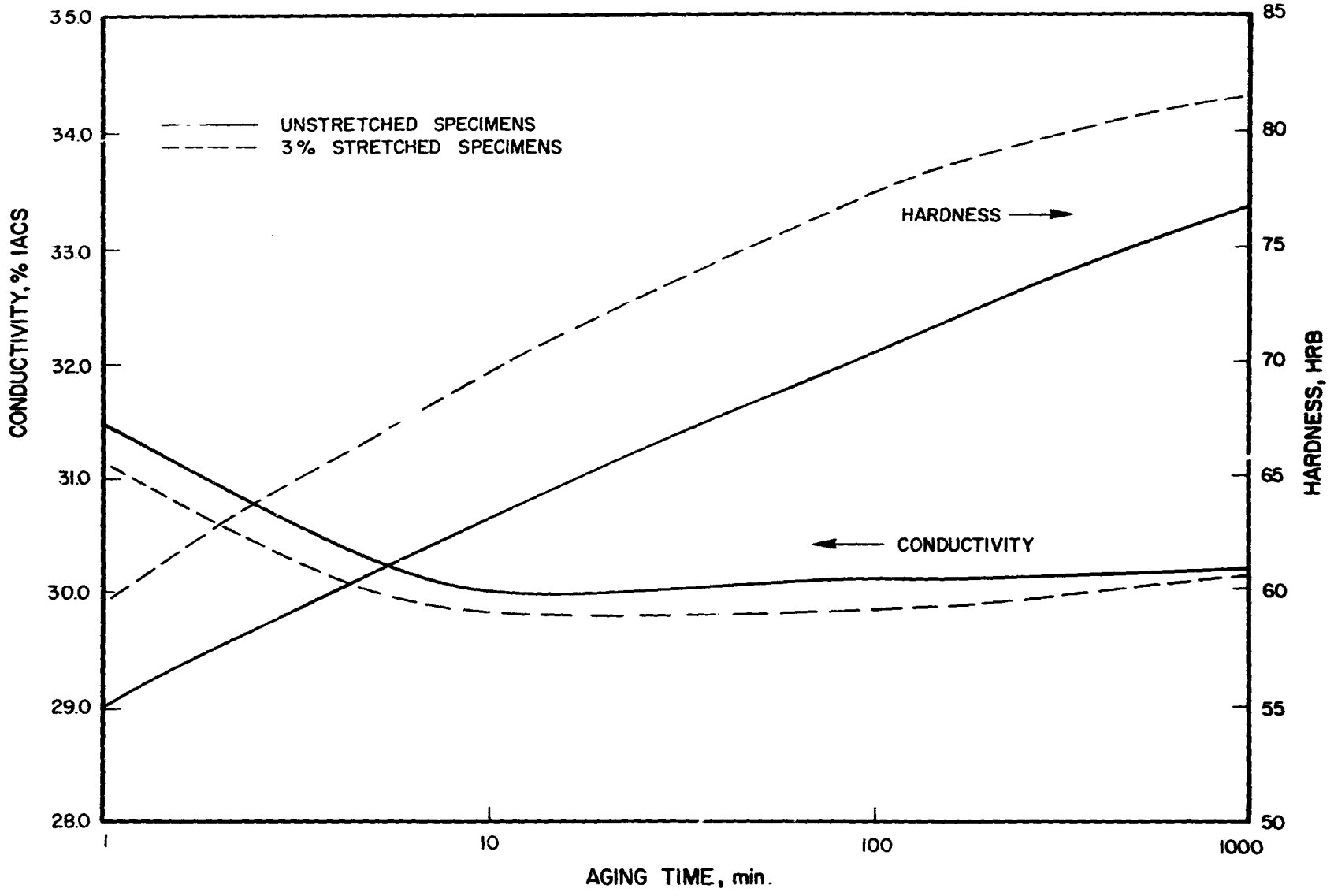

Figure 106. Eddy-current conductivity and hardness as a function of aging time durirg aging at 150 °C, of 2024 aluminum alloy (stretched and unstretche. .

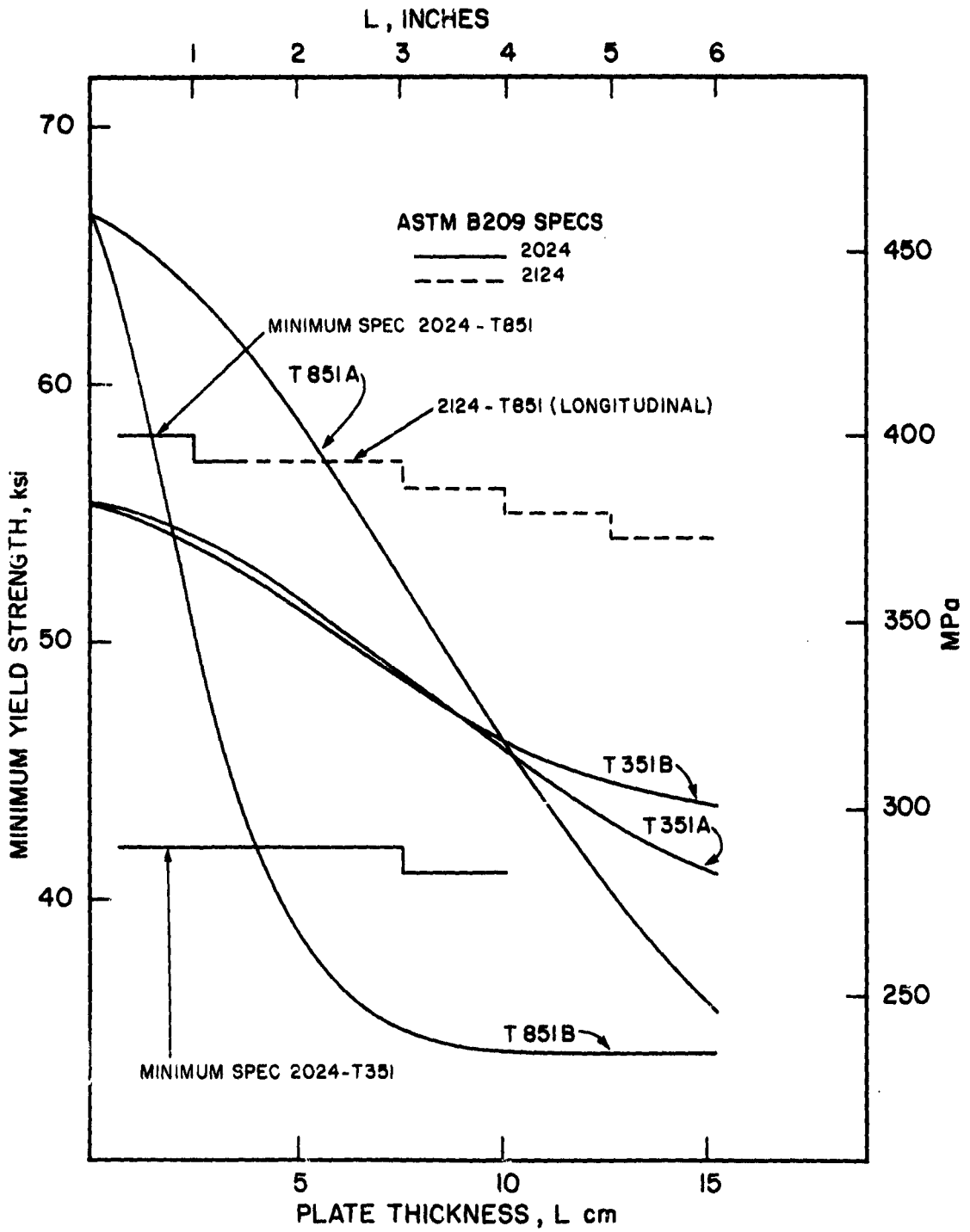

Figure 107. Predicted minimum yield strength in different thickness plates under the "worst case" heat flow conditions for both T351 and T851 using sequence A or B data.

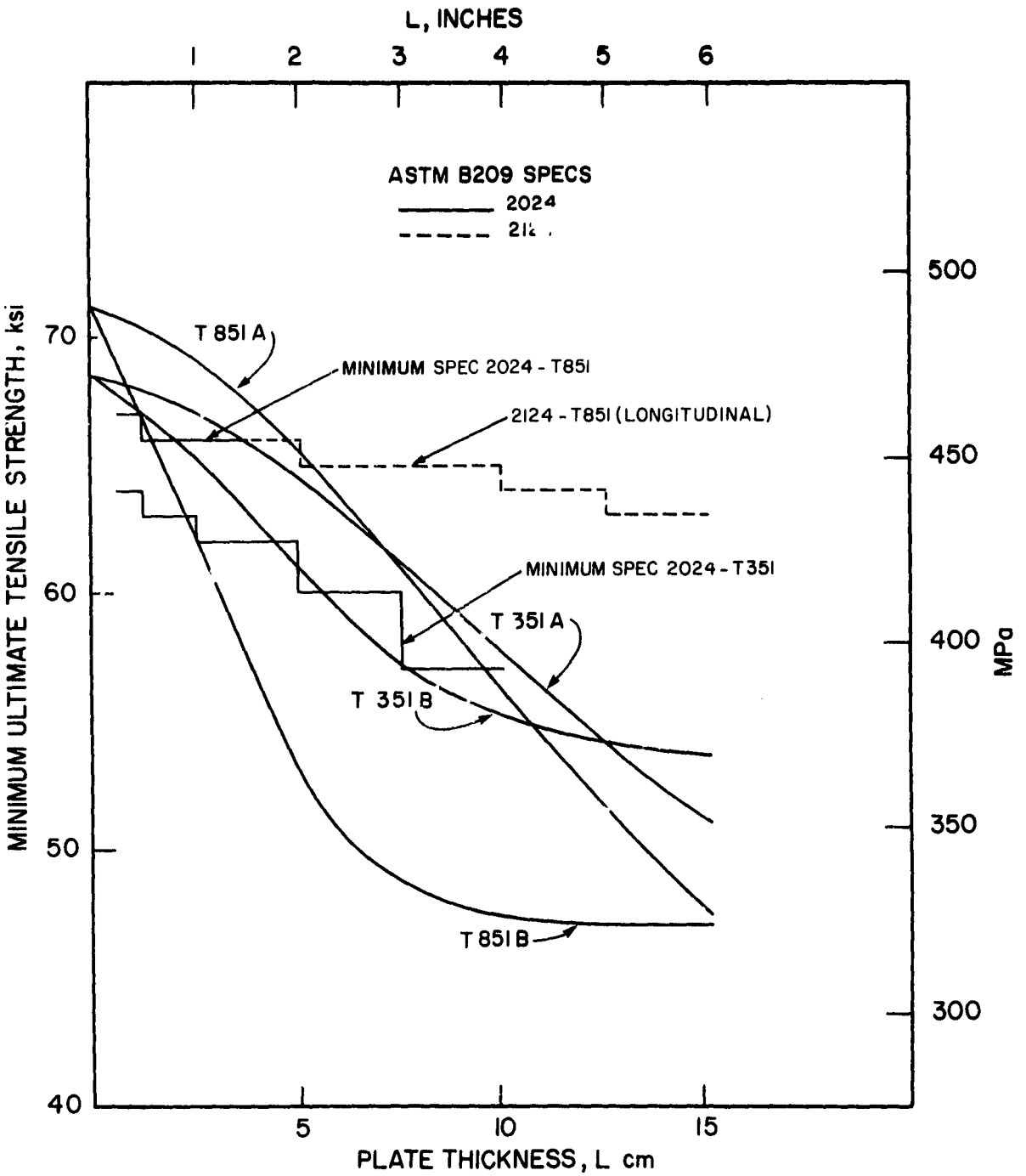

Figure 108. Predicted minimum ultimate tensile strength in different thickness plates under the "worst case" heat flow conditions for both T351 and T851 using sequence A or B data.

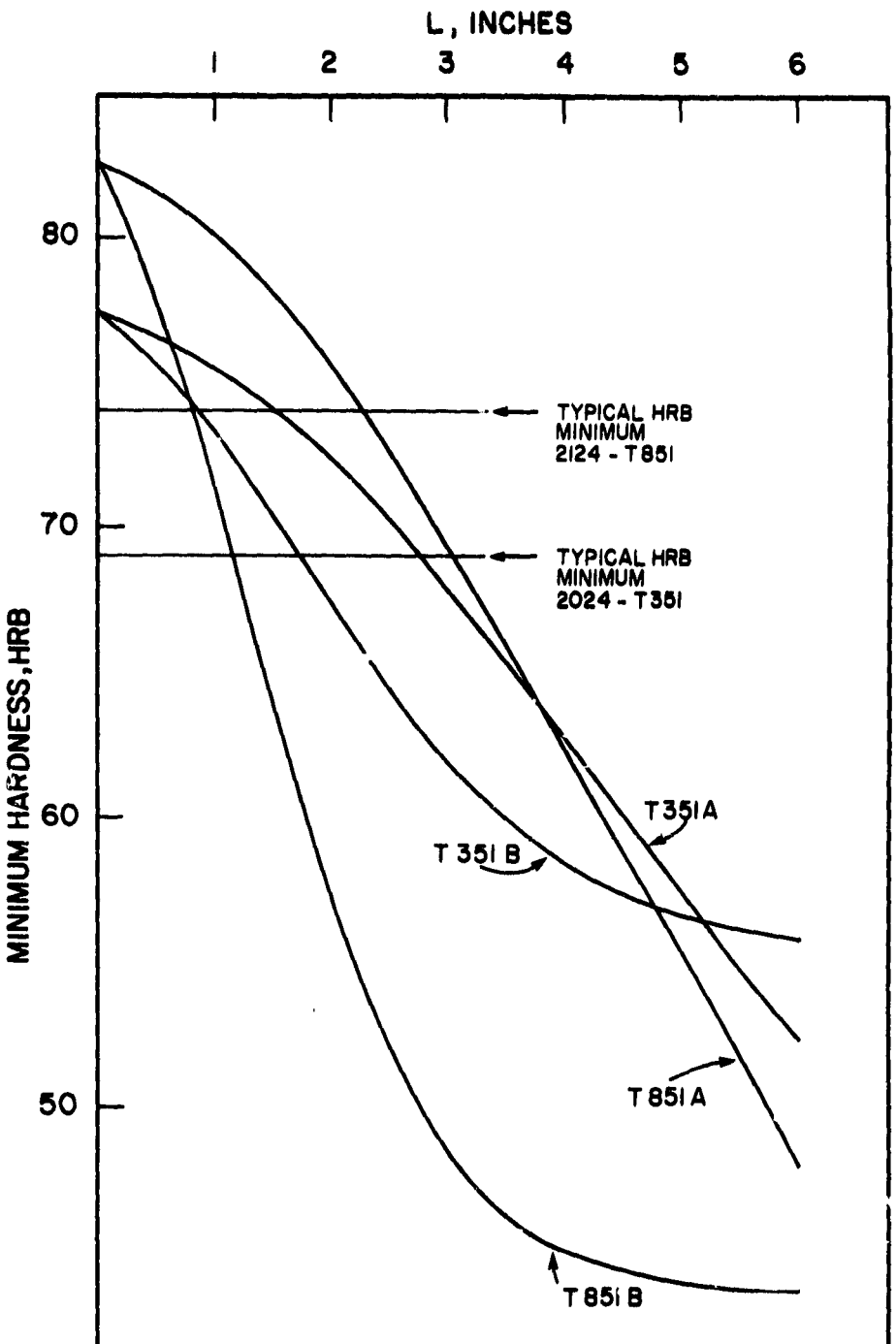

Figure 109. Predicted minimum hardness in different thickness plates under the "worst case" heat flow conditions for both T351 and T851 using sequence A or B data.

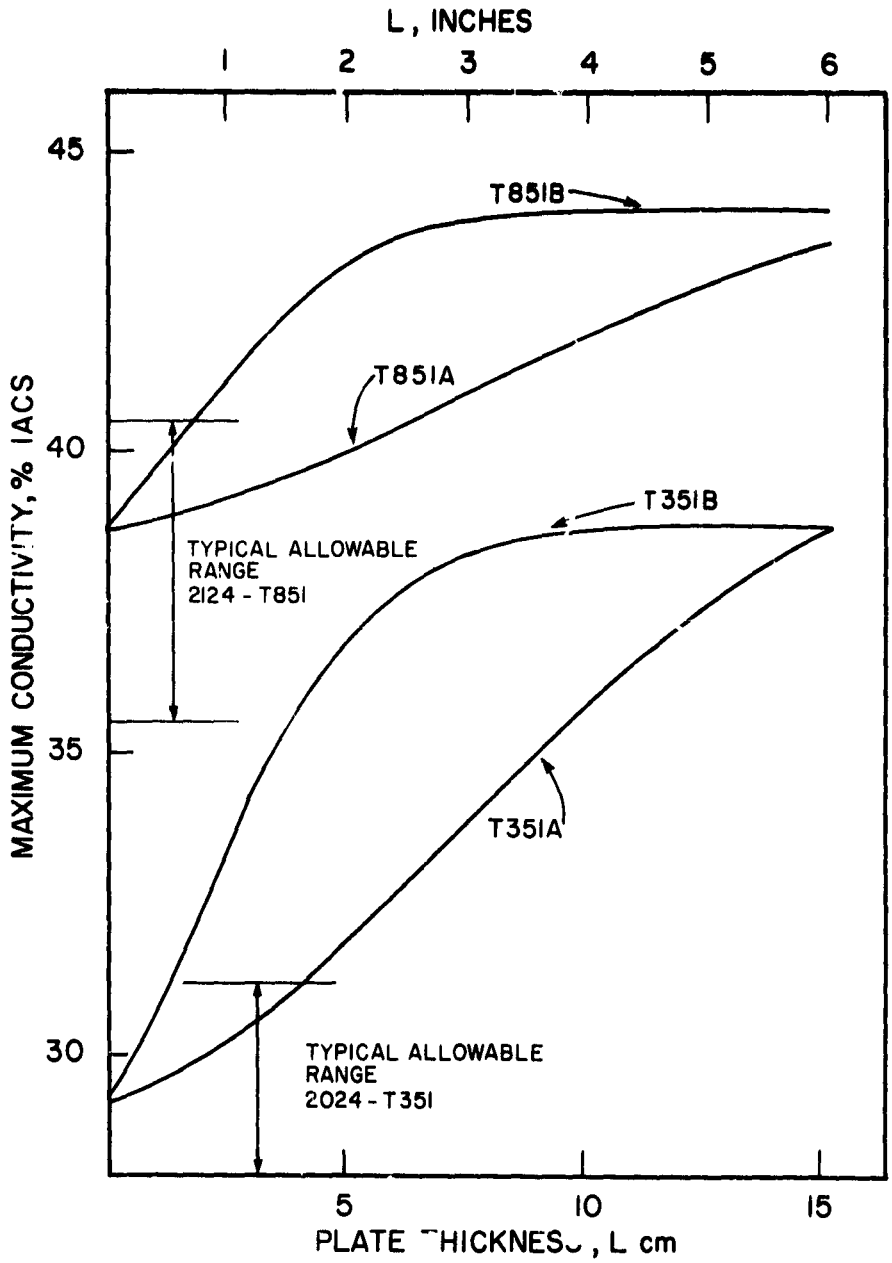

Figure 110. Predicted maximum conductivity in different thickness plates under the "worst case" heat flow conditions for both T351 and T851 using sequence A or B data.

NBS-114A (REV. 2-8-C)

U.S. DEPT. OF COMM. BIBLIOGRAPHIC DATA SHEET (See Instructions)	1. PUBLICATION OR REPORT NO. 83-2669	2. Performing Organ. Report No.	3. Publication Date April 1983

4. TITLE AND SUBTITLE

NBS: Processing/Microstructure/Property Relationships in 2024 Aluminum Alloy Plates

5. AUTHOR(S) L. Ives, L. Swartzendruber, W. Boettinger, M. Rosen, S. Ridder, F. Biancaniello, R. Reno, D. Ballard and R. Mehrabian

6. PERFORMING ORGANIZATION (If joint or other than NBS, see instructions)

NATIONAL BUREAU OF STANDARDS
DEPARTMENT OF COMMERCE
WASHINGTON, D.C. 20234

7. Contract/Grant No.

8. Type of Report & Period Covered

9. SPONSORING ORGANIZATION NAME AND COMPLETE ADDRESS (Street, City, State, ZIP)

NASA
Washington, DC

10. SUPPLEMENTARY NOTES

☐ Document describes a computer program; SF 185, FIPS Software Summary, is attached.

11. ABSTRACT (A 200-word or less factual summary of most significant information. If document includes a significant bibliography or literature survey, mention it here)

Nondestructive evaluation (NDE) using eddy-current conductivity and hardness measurements form an essential part of the quality control of aluminum alloy plates used for aerospace vehicles. The relationships between the NDE measurements and the important mechanical properties are affected by a large number of variables including: chemical composition, cast structure, ingot scalping, solution heat treatment and quenching, mechanical working, and aging treatment. At the request of the National Aeronautics and Space Administration, a number of these relationships has been explored for 2024 aluminum alloy. This work is a continuation of our previous efforts on 2219 aluminum alloy and is motivated by a concern that a number of improperly treated plates with "soft spots" may have been incorporated into aerospace structures. A major result of our research has been a delineation of which alloy tempers and plate thicknesses are most likely to contain "soft spots" due to specific processing errors.

12 KEY WORDS (Six to twelve entries; alphabetical order; capitalize only proper names; and separate key words by semicolons)

Aging; aluminum alloy; eddy-current conductivity; hardness; heat flow; microstructure; nondestructive evaluation; precipitation; processing; segregation; solution heat treatment; ultrasonics.

13. AVAILABILITY

☒ Unlimited
☐ For Official Distribution. Do Not Release to NTIS
☐ Order From Superintendent of Documents, U.S. Government Printing Office, Washington, D.C. 20402.
☒ Order From National Technical Information Service (NTIS), Springfield, VA. 22161

14. NO. OF PRINTED PAGES 268

15. Price $22.00

USCOMM-DC 6043-P80